Nanomaterials for Drug Delivery and Multi-Modal Imaging

Dissertation

zur

Erlangung der naturwissenschaftlichen Doktorwürde
(Dr. sc. nat.)

vorgelegt der

Mathematisch-naturwissenschaftlichen Fakultät

der

Universität Zürich

von

Jennifer Lamb

aus

Großbritannien

Promotionskommision

Prof. Dr. Jason P. Holland (Vorsitz)

Prof. Dr. Greta Patzke

Prof. Dr. Felix H. Zelder

Zürich, 2020

Acknowledgements

First and foremost, I would like to thank Prof. Jason Holland for giving me the opportunity to complete a PhD in his group. Throughout the last four years, Jason has remained both encouraging and passionate about my work, providing an exciting and supportive environment to conduct research. As the first PhD student, I would also like to thank Jason for the fun, team environment he has created by filling the lab with the most amazing co-workers. My fellow PhD students (Faustine, Rachael, Florian, Jose and Melanie) have made the last four years the best! I could not have wished for a better group of people to laugh, stress, problem solve, and (of course) drink with. I would also like to thank the Post-Docs (Malay, Amaury, Dan and Eliane) and Masters students (Larissa, Alan and Patricia) who have been part of the group during my time here, your support has been appreciated.

I have to give a special mention to Rachael. In the last three and a half years we have shared a desk and lab bay, probably spending more time together than with our respective partners. Our tolerance for each other's mess, moaning and madness is outstanding and must be a sign of true friendship.

From a more scientific standpoint, I would like to thank Dr. Thomas Fox for his help with T_1 and T_2 relaxation measurements. I would also like to thank Dr. Marcus Yaffee for his synthesis of nanoparticles and the interesting discussions regarding nanomaterials. Dr. Christoph Salzmann has provided a vital collaboration throughout my PhD by supplying graphene nanoflakes. I am grateful for both the materials and expertise you have given me. Thank you to both the NMR department and MS service for all the measurements and support.

Next, I would like to thank my committee members Prof. Greta Patzke and Prof. Felix Zelder. Firstly, I appreciate both of you taking the time to be a part of my promotion committee, meeting with me each year to offer your expert advice. I would like to thank Prof. Greta Patzke for allowing me to use equipment in your laboratory and I am grateful to Esmeal, Matteo, Rafael and Lucas for your help when acquiring these measurements. As the leader of the CMSZH graduate school, Prof. Felix Zelder allowed me to be part of the retreat organisational committee. Being part of The Orga Team was a fulfilling experience, and my fellow team members made this role very fun indeed.

The Department of Chemistry at UZH has been a welcoming and friendly place to work and this is of course due to the amazing employees. There are numerous people who have been not only colleagues, but also friends. Thank you for all the apero, do-bar, retreat, BBQ fun. I would like to thank the administration team, especially Ramona, for all the organisational support. Also, a big thanks goes the two safety officers who have been present here during my time, Andreas Müller and Ferdinand Wild.

Finally, I would like to thank my friends and family outside of UZH. Moving to Switzerland has been an amazing experience and this is completely due to the people I have met. I would like to thank all the friends I have made here for being my family away from home, you know who you are and you are awesome! I would also like to thank my partner Alex. Alex and I have spent the Coronavirus lockdown in a small apartment, trying our best to finish our PhDs, there is no one else in the world I could have done this with.

To Mum, Dad and Adam. Thank you for everything. Do not worry, there is no place quite like home.

Abstract

Molecular imaging uses techniques to visualise, characterise and measure biological processes at the cellular and molecular level. These techniques can be incredibly sensitive, allowing the detection of small abnormalities at the tissue or cellular level based on molecular differences, and thus providing accurate diagnosis and monitoring of disease, especially in the field of oncology. Image acquisition relies on the use of molecular imaging agents which target and accumulate at biomarker sites, allowing visualisation of the target in comparison to background tissue. Nanomedicine is a field which refers to the use of nanomaterials in a therapeutic or diagnostic setting. Nanomaterials often display unique characteristics, offer structural versatility and act as scaffolds; providing platforms that have the potential to be truly multi-functional. In this thesis, we take advantage of these properties by synthesising and developing tumour-targeted nanomaterial constructs for multi-modal imaging and therapy.

Iron oxide nanoparticles provide MRI contrast, therefore, following radiolabelling with a diagnostic radionuclide, the nanoparticles can be used as multi-modal imaging agents in techniques such as PET/MRI. Chapter 2 in this thesis focuses on the synthesis, characterisation and development of iron oxide nanoparticles for further experiments and applications. Preliminary radiolabelling methods explore classical radiolabelling techniques, where chelates are deployed to bind radionuclides. Subsequent radiolabelling techniques focus on non-classical, chelate-free methods which offer fast and efficient synthesis, superior yields, and have minimal impact to the nanoparticle structure. We explore the versatility of chelate-free radiolabelling on different nanoparticles and also perform kinetic studies to gain an insight into the mechanism by which this process occurs.

Using chemistries established in Chapter 2, Chapter 3 focuses on developing the nanoparticle systems for PET/MR imaging. Nanoparticle constructs are targeted toward an established cancer biomarker, and tested *in vitro* and *in vivo* by using small-animal PET imaging.

Chapters 4 and 5 use graphene nanomaterials as scaffolds to create multi-modal agents. Graphene nanoflakes (GNFs) consist of a graphene sheet approximately 30 nm in diameter with a pristine aromatic system and an edge terminated with carboxylic acid groups. Their high water solubility and relative ease of functionalisation by using carboxylate chemistry means that GNFs are potential scaffolds for the design of multi-modality nanomedicines. Chapter 4 establishes the chemistry and provides a first indication on the flexibility of GNFs as potential theranostic agents. GNFs are multi-functionalised with drug molecules, chelates to bind PET active radionuclides, small-molecule biological targeting vectors and pharmacokinetic modifying groups. Further experiments *in vitro* and *in vivo* were used to evaluate the performance of GNFs in theranostic drug design.

Building from our experience with GNFs functionalised with small-molecule targeting agents, Chapter 5 further utilises GNFs to create targeted constructs for application in PET/MRI. GNFs are multi-functionalised with, chelates to bind PET radionuclides as well as gadolinium complexes for MRI contrast, they are then functionalised with an antibody that is known to bind a specific cancer biomarker. Again, constructs are evaluated *in vitro* and *in vivo* to evaluated their pharmacokinetics and tumour-targeting and to test their potential as PET/MRI agents.

Zusammenfassung

Die molekulare Bildgebung verwendet Techniken zur Visualisierung, Charakterisierung und Messung biologischer Prozesse auf zellulärer und molekularer Ebene. Diese Techniken können unglaublich empfindlich sein und ermöglichen, basierend auf molekularen Unterschieden, den Nachweis kleinster Anomalien in Geweben oder Zellen. Ein solcher Ansatz schafft die Möglichkeit einer präzisen Diagnose und Überwachung von Krankheiten, insbesondere im Bereich der Onkologie.

Diese Bilderfassung beruht auf dem Einsatz von molekularen Bildgebungsmitteln, welche sich an Biomarkerstellen anreichern, wodurch das Ziel- im Vergleich zum Hintergrundgewebe sichtbar gemacht werden kann. Die Nanomedizin ist ein Forschungsgebiet, welcher sich auf die Verwendung von Nanomaterialien mit einem therapeutischen oder diagnostischen Zweck bezieht. Nanomaterialien weisen oft einzigartige Eigenschaften auf, sie bieten strukturelle Vielseitigkeit und fungieren als Gerüst. So bilden sie Plattformen, welche das Potenzial haben multifunktional zu sein. In dieser Arbeit machen wir uns diese Eigenschaften zunutze, indem wir tumorgerichtete Nanomaterialien für die multimodale Bildgebung und Therapie entwickeln und synthetisieren.

Eisenoxid-Nanopartikel bieten MRT-Kontrast, weshalb die Nanopartikel nach der Radiomarkierung mit einem diagnostischen Radionuklid als multimodale Bildgebungsmittel in Techniken wie PET/MRI eingesetzt werden können. Kapitel 2 dieser Arbeit konzentriert sich auf die Synthese, Charakterisierung und Entwicklung von Eisenoxid-Nanopartikeln. Vorläufige Radiomarkierungsmethoden untersuchen klassische Radiomarkierungstechniken, bei welchen Chelate zur Bindung von Radionukliden eingesetzt werden. Nachfolgende Radiomarkierungstechniken konzentrieren sich auf nicht-klassische, chelat-freie Methoden, welche eine schnelle und effiziente Synthese, überlegene Ausbeuten und minimale Auswirkungen auf die Struktur der Nanopartikel bieten. Wir untersuchen die Vielseitigkeit der chelat-freien Radiomarkierung von verschiedenen Nanopartikeln und führen kinetische Studien durch, um einen Einblick in den Mechanismus des Prozesses zu erhalten.

Kapitel 3 konzentriert sich auf die Entwicklung von Nanopartikelsystemen für die PET/MR-Bildgebung unter Verwendung der in Kapitel 2 festgelegten chemischen Verfahren. Nanopartikel-Konstrukte werden auf einen etablierten Krebs-Biomarker ausgerichtet und in vitro und in vivo mit Hilfe der PET-Bildgebung an Kleintieren getestet.

In den Kapiteln 4 und 5 werden Graphen-Nanomaterialien als Gerüst für die Herstellung multimodaler Wirkstoffe verwendet. Graphen-Nanoflocken (GNFs) bestehen aus einer Graphenfolie von etwa 30 nm

Durchmesser mit einem rein aromatischen System und einem Rand, der mit Carbonsäuregruppen umschlossen ist. Ihre hohe Wasserlöslichkeit und die relativ einfache Funktionalisierung durch die Verwendung von Carboxylatchemie bedeutet, dass GNFs potenzielle Gerüste für das Design von multimodalen Nanomedizinprodukten sind. Kapitel 4 schafft die Grundlage für die Chemie und gibt einen ersten Hinweis auf die Flexibilität der GNFs als potentielle Theranostika. GNFs sind multifunktional mit Arzneimittelmolekülen, Chelaten zur Bindung von PET-aktiven Radionukliden, niedermolekularen biologischen Zielvektoren und pharmakokinetisch modifizierenden Gruppen ausgestattet. Weitere in vitro- und in vivo-Experimente wurden durchgeführt, um die Leistung der GNFs beim Design von Theranostika zu bewerten.

Aufbauend auf unseren Erfahrungen mit GNFs, die mit niedermolekularen Vektoren funktionalisiert wurden, werden in Kapitel 5 GNFs weiter genutzt, um zielgerichtete Konstrukte für die Anwendung in PET/MRT zu designen. GNFs werden multifunktionalisiert mit Chelaten zur Bindung von PET-Radionukliden sowie Gadolinium-Komplexen für den MRT-Kontrast. Anschließend werden sie mit einem Antikörper funktionalisiert, von dem bekannt ist, dass er einen spezifischen Krebs-Biomarker bindet. Auch hier werden die Konstrukte in vitro und in vivo evaluiert, um ihre Pharmakokinetik und Tumor-Targeting zu bewerten und ihr Potenzial als PET/MRT-Agenten zu testen.

Abbreviations

[^{18}F]FDG	[^{18}F]-2-fluoro-2-deoxy-D-glucose
APD	Avalanche photodiode
APTES	(3-aminopropyl)triethoxysilane
ATSM	Diacetyl-2,3-*bis*(N^4-methyl-3-thiosemicarbazone)
c-MET	Human hepatocyte growth-factor receptor
CSF	Cerebrospinal fluid
CT	Computed tomography
CVD	Chemical vapour deposition
DFO	Desferrioxamine B
DLS	Dynamic light scattering
DOTA	1,4,7,10-tetraazacyclododecane-1,4,7,10-tetraacetic acid
DTPA	Diethylenetriaminepentaacetic acid
EC	Electron Capture
EMA	European Medicines Agency
EPR	Enhanced permeability and retention
Fab	Antigen-binding fragment
FACS	Fluorescence-activated cell sorting
FDA	Food and Drug administration
FH	Feraheme (FH)
FOV	Field of view
GCPII	Glutamate carboxypeptidase II
GNFs	Graphene Nanoflakes
GO	Graphene oxide
HER2/*neu*	Human epidermal growth factor receptor 2
HGF	Hepatocyte growth-factor (HGF)
HPLC	High-performance liquid chromatography
IARC	International Agency for Research on Cancer
IC	Internal conversion
IT	Isomeric transition
I.V.	Intravenous
KSP	Kinesin spindle protein
log*D*	Distribution coefficient

mAb	Monoclonal antibody
MRI	Magnetic resonance imaging
NAAG	*N*-acetyl-L-aspartyl-L-glutamate
NCI	National Cancer Institute
NMR	Nuclear magnetic resonance
NOTA	1,4,7-triazacyclononane-1,4,7-triacetic acid
PASP	Polyaspartic acid
PD10	Sephadex^{TM} desalting columns
PDT	Photodynamic therapy
PEG	Polyethylene glycol
PEI	Polyethyleneimine
PET	Positron emission tomography
PHA	Pulse height analyser
PMT	Photomultiplier tube
PSA	Prostate specific antigen
PSMA	Prostate specific membrane antigen
PTT	Photothermal therapy
rGO	Reduced graphene oxide
RTK	Receptor tyrosine kinase
SAM	Self-assembled monolayer
SCX	Small cation exchange resin
SEC	Size exclusion chromatography
SF	Scatter factor
SPECT	Single-photon emission computed tomography
SPIONs	Superparamagnetic iron oxide nanoparticles
SPPS	Solid-phase peptide synthesis
SPR	Surface Plasmon Resonance
STM	Scanning tunnelling microscopy
TEM	Transmission electron microscopy
TS	Transition state
US	ultrasound
XPS	X-ray photoelectron spectroscopy
XRD	X-ray diffraction

Table of Contents

Chapter 1: Introduction

1.1 Aims of Chapter

This chapter introduces the main themes and basic concepts used in this thesis as well as providing a brief overview of recent literature.

1.2 Cancer

1.2.1 Statistics

In 2018, 18.1 million new cancer cases (and 9.6 million cancer deaths) were reported worldwide.[1] The International Agency for Research on Cancer (IARC) predicted that the incidence rate will increase to 29.5 million by 2040, demonstrating the ever-growing burden cancer will have on future global society.[2] Despite recent medical advances, cancer remains the leading cause of death in 30-69 year olds in a number of developed countries including both Switzerland and the United States of America (USA).[3] However, early and thorough diagnosis provides patients with the best prognosis possible. Whilst the detection of cancer biomarkers during *in vitro* diagnostics is a valuable tool, it must be combined with companion diagnostic methods to determine the development of the disease and potential spread of the cancer to secondary metastatic sites. These companion techniques include molecular imaging which often target biomarkers *in vivo*.

1.2.2 Cancer biomarkers

The National Cancer Institute (NCI) in the USA defines a biomarker as "a biological molecule found in blood, other body fluids, or tissues that is a sign of a normal or abnormal process, or of a condition or disease."[4] Therefore, a cancer biomarker acts as an indicator that cancer is present in the body, and when combined with other diagnostics tools, can aid the initial diagnosis.[5] However, biomarkers are used throughout all stages of a patients cancer treatment and can be categorised into different types based on their potential use (Table 1).[6,7] Biomarker identification allows clinicians to offer patients an accurate and effective treatment plan which is personalised to the individual.

Table 1.1. Summary of the categories of biomarkers used during cancer diagnosis and treatment.[6] Note: some biomarkers fall into more than one category.

Category	Potential use
Diagnostic	Elevated levels of biomarkers can be indicative of tumour presence
Prognostic	Predicts the disease risk and progression for the patient
Predictive	Indicates the likelihood of a patient responding to a given drug
Pharmacodynamic	Determines an effective drug dose

1.2.3 Examples of biomarkers

In this thesis, biomarkers will be targeted in the development of radiotracers for *in vivo* imaging. Below are examples of biomarkers which are relevant to the research found in later chapters.

Prostate specific membrane antigen (PSMA)

Prostate cancer is the most commonly occurring cancer in European men.[8] For many years, the prostate specific antigen (PSA) played a major role in the diagnosis of prostate cancer. A serum PSA level above 4.0 ng/mL is often considered a sign of prostate cancer, however this is not always the case. Some prostate cancers do not cause an increase in PSA serum concentrations, resulting in a false negative which can potentially lead to the patient not receiving the required treatment. On the contrary, other factors, including aging, can cause an increase in PSA levels, and this can produce a false positive result which could lead to unnecessary biopsies. It would, therefore, be logical that whilst PSA can act as an indication of disease, it should not be used solely when evaluating disease progression. Additional diagnostic methods are required which should ideally monitor alternative biomarkers. Other biomarkers can offer the potential for *in vivo* imaging allowing tumour size to be assessed and metastases to be located, assisting clinicians in prescribing the correct treatment.[9]

Glutamate carboxypeptidase II (GCPII; also known as or *N*-acetyl-L-aspartyl- L-glutamate peptidase I [NAALADase I] or folate hydrolase I) is a membrane-bound glycoprotein enzyme which is predominantly located in the extracellular space.[10] GCPII is found in a number of different tissues including the central nervous system where it known to catalyse the hydrolysis of *N*-acetyl-L-aspartyl-L-glutamate (NAAG) to produce glutamate and *N*-acetyl-L-aspartate (NAA).[11,12] It is also found in the intestine where it catalyses the hydrolysis of folylpoly-γ-L-glutamate ultimately producing folate whilst releasing glutamate in the process.[13,14] GCPII is found in the prostate and this has led to the protein being more commonly known as the prostate specific membrane antigen, PSMA. In this thesis, the term PSMA will be used, however it is important to state that the terms GCPII and PSMA refer to the same, structurally identical protein. Although PSMA is expressed in normal prostate epithelium and tissues including those mentioned above, it is more highly expressed in several prostate cancers and resulting metastatic lesions. Therefore, PSMA can be used a potential biomarker in the diagnosis and monitoring of disease. [15–18]

PSMA is a type II transmembrane protein comprised of 750 amino acids.[19] The first X-ray crystal structures of PSMA were determined in 2005 by Davis *et al.* who elucidated the structure of the extracellular domain (residues 44-750) (**Figure 1.1**).[20] PSMA is a symmetrical dimer with each polypeptide chain containing a protease, an apical and a helical domain. A large cavity lies between the domains where substrate binding can occur. The cavity is a funnel shape which leads down 20 Å from the protein surface. The active site lies at the point in the cavity where two zinc ions

(Zn^{2+}) are present and two binding sites are found; S1 and S1′. As introduced above, the active site of PSMA is responsible for the hydrolysis of substrates to release glutamate. The S1′ site binds to the glutamic acid residue of a compound with very high affinity, whilst the S1 pocket allows the binding of several different structures with a lower affinity.[19–22]

Figure 1.1. The X-ray diffraction crystal structures of an inactive mutant of PSMA (human glutamate carboxypeptidase II) in complex with *N*-acetyl-L-aspartyl-L-glutamate (NAAG) (Data extracted from RCSB PDB. Code: 3BXM).[23]

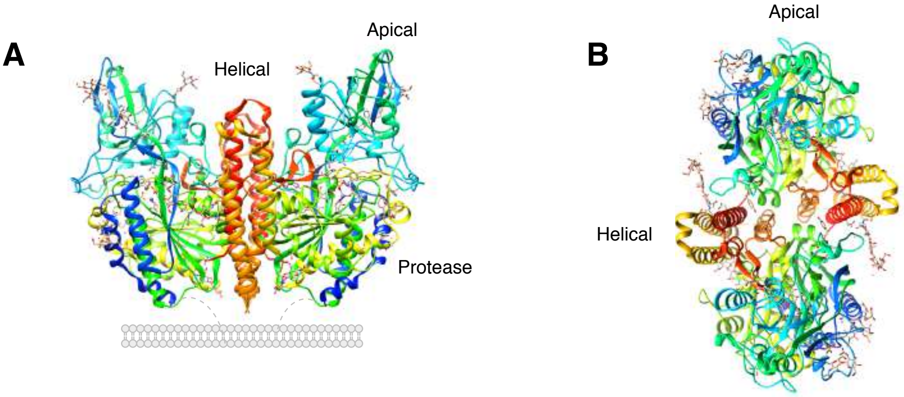

Binding to PSMA can be accomplished *via* two methods: using small, low molecular weight compounds or antibodies. Due to the high affinity of which the S1′ pocket binds glutamate residues, small-molecule inhibitors of PSMA often contain a glutamic acid moiety. Another region of the molecule should bind to the zinc ions and either mimic the transition state (TS) of the hydrolysis reaction or mimic the natural ligand without being susceptible to hydrolysis.[24,25] 2-phosphonomethyl pentanedioic acid (2-PMPA) was the first potent and selective inhibitor of PSMA with an inhibition constant (K_i) of 0.3 nM.[26] The glutarate (pentanedioic acid) portion of the compound is tightly bound to the S1′ pocket, whilst the phosphonate group forms strong dative covalent bonds with the zinc ions (**Figure 1.2B**). The nature of the bonding in the S1′ pocket favours the binding of the (*S*)-enantiomer, this is logical given that this configuration is comparable to L-glutamate.[27] Urea-based compounds are a second class of small-molecules that exhibit PSMA binding. A large number of these compounds are glutamate-urea-lysine (Glu-NH-CO-NH-Lys) analogues, and as with 2-PMPA, the glutarate portion of the molecule binds tightly to the S1′ pocket. The urea mimics the peptide bond found in the natural ligands such as NAAG and the carboxyl group coordinates to a zinc ion.[25] The lysine residue acts as a handle for chemical functionalisation (R-group in **Figure 1.2C**) to attach, for example, a fluorophore for optical imaging, a chelator of Gd^{3+} for MRI imaging and radionuclides for nuclear imaging. [28–31] When an aromatic ^{125}I group (R = 1-carboxy-(4-[^{125}I]iodo-benzoylamino) is present the compound has a K_i value of 0.01 nM which results in significant binding to PSMA expressing tumours. During preclinical SPECT/CT studies an uptake of 34.3 ± 12.7% injected dose per gram of tumour tissue was observed.[30,32]

The murine monoclonal antibody (mAb) 7E11-C5.3 was used for early imaging of PSMA, however, it binds an intracellular epitope of the protein creating issues when imaging viable cells that have intact cell membranes.[33] To overcome this issue, humanised or fully human mAbs that bind to the extracellular region were developed.[34–36] J591 is a notable example of a PSMA binding mAb, and derivatives have been used in both imaging and treatment of PSMA expressing tumours. A number of radioimmunoconjugates were developed including ^{225}Ac-J591, ^{213}Bi-J591 and ^{90}Y-J591 for therapeutic applications and ^{177}Lu-J591 and ^{89}Zr-J591 for medical imaging.[37–41] Despite promising results small-molecules are considered a superior option for developing diagnostic imaging agents since antibodies exhibit long circulation times and poor tumour penetrability, especially for bone metastases.[42]

Figure 1.2. (A) Chemical structure of 2-PMPA with PSMA binding sites highlighted and **(B)** 2-PMPA in complexation with the PSMA active site (Data extracted from RCSB PDB. Code:2PVW).[21] **(C)** Chemical structure of Glu-NH-CO-NH-Lys derivative with the PSMA binding sites highlighted and **(D)** Glu-NH-CO-NH-Lys-NH-1-carboxy-(4-[^{125}I]iodo-benzoylamino in complexation with the PSMA active site (Data extracted from RCSB PDB. Code:3D7H).[43] Note: Hydrogen bonds are represented using blue bonds, whilst bonding to Zn^{2+} (purple) are represented *via* dashed purple bonds.

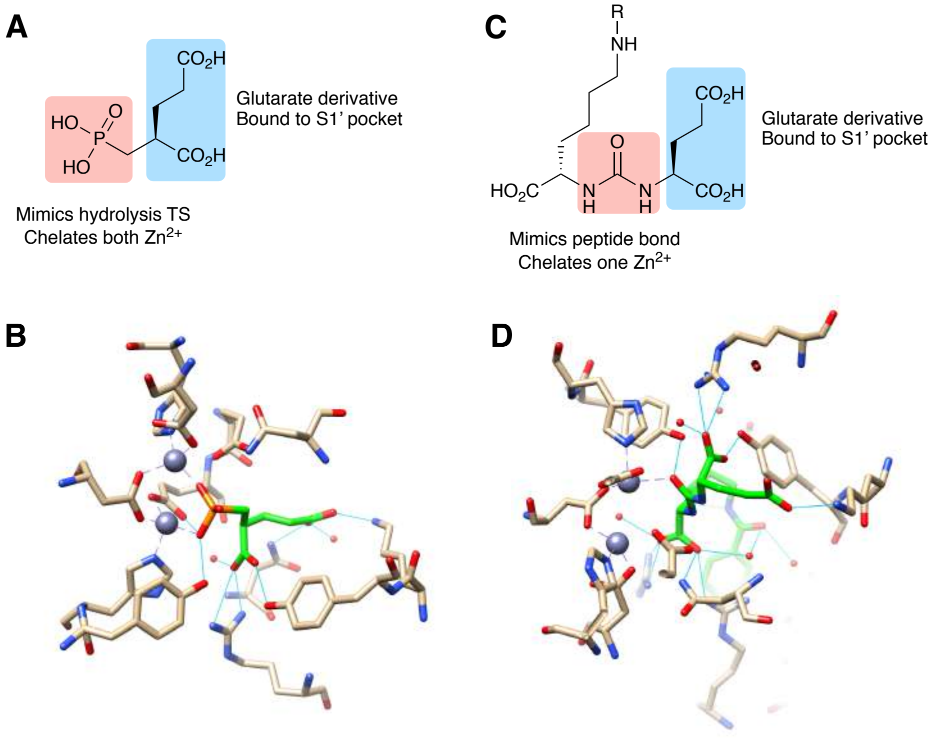

Human epidermal growth factor receptor 2 (HER2/*neu*)

Human epidermal growth factor receptor 2 (HER2/*neu*; also known as ErbB-2) is overexpressed in approximately 20-30% of breast cancers.[44] Although the protein is expressed during embryonic development it is almost undetectable in normal adult tissue. In effected cancer lines, expression of the HER2/*neu* oncogene is significantly amplified which leads to the overexpression of the associated protein; thus making it an ideal target for therapeutics and for imaging.[45] The protein itself is a receptor tyrosine kinase (RTK), a category of proteins which play a critical role in cell proliferation, differentiation and survival. There are over 20 different classes of RTK proteins and HER2/*neu* falls into the ErbB family.[46,47] The ErbB family of proteins reside in the cell surface membrane. Whilst there is no known ligand for HER2/*neu*, other ErbBs respond to polypeptide growth factors in the local environment which cause homo- and heterodimerisation with other ErbB proteins, including HER2/*neu*.[48,49] The dimers then cross-phosphorylate, a process where each protein phosphorylates tyrosine residues on the other. The result is a cascade of downstream signalling which has the potential to alter nucleus transcription events. Alterations in RTK expression and activation can lead to dysregulation of normal cell prosesses.[50,51]

Harari *et al.* stated that, "ErbB-2 (HER2/*neu*) overexpression hotwires the cell cycle."[50] An overexpression of HER2/*neu* causes an increase in downstream signalling, which accelerates cell proliferation, and provides resistance to apoptosis. Overexpression of HER2/*neu* is also thought to increase the motility of cells (the ability of cells to migrate to other tissues) as well as the releasing signals which cause angiogenesis (the development of new blood vessels). Overall, HER2/*neu* overexpression results in a cancer which is incredibly progressive and, before recent advances in medicine, resulted in a very poor prognosis for the patient.[52]

Nowadays, HER2/*neu* positive (+ve) tumours can be treated by using various mAbs including trastuzumab, pertuzumab and margetuximab.[53–55] Trastuzumab is the most commonly used and the formulated drug is known in the clinic as Herceptin®.[55] HER2/*neu* is a transmembrane protein with an extracellular region consisting of approximately 630 amino acids that make up four domains (I-IV **Figure 1.3A**). The antigen-binding fragment (Fab) of trastuzumab binds to the *C*-terminal portion of domain IV (**Figure 1.3B**).[56] The anti-tumour properties are well-known and documented, however, the process by which it occurs is a little less understood and several mechanisms are proposed. The binding of the trastuzumab may cause:

1) Antibody-dependent cellular cytotoxicity (ADCC), a mechanism where an immune effector cell recognises and induces cell lysis;
2) Inhibition of the homo- or heterodimerisation, preventing the initial cross-phosphorylation and downstream signalling from occurring;
3) Blocking the cleavage of the extracellular domain of HER2/*neu*, which inhibits the signalling pathway;
4) Internalisation and subsequent break down of the trastuzumab in the cell.[52,57,58]

Figure 1.3. The X-ray diffraction crystal structures of the extracellular domains of **(A)** rat HER2 which is analogous to human sHER2 (Data extracted from RCSB PDB. Code: 1N8Y) and **(B)** human HER2 complexed with trastuzumab Fab shown in purple (Data extracted from RCSB PDB. Code: 1N8Z).[56]

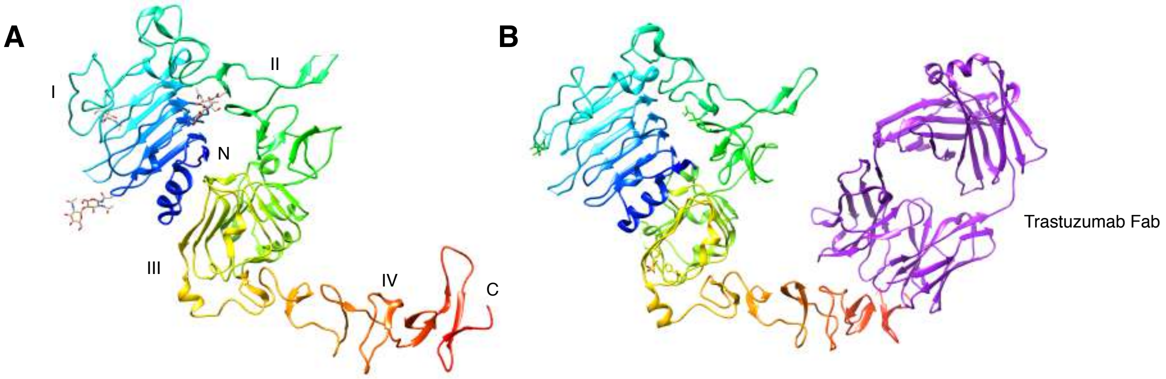

Traditionally, to determine if a patient has a HER2/*neu* +ve tumour, a biopsy must be taken. An immunohistochemistry (IHC) test then detects the HER2 protein and samples are scored by a pathologist, or a fluorescence *in situ* hybridisation (FISH) test detects an upregulation of the HER2 gene in the biopsied lesion. The process of taking the biopsy from a lesion may cause movement of cancer cells to other tissues when extracting the tissue with the needle, inducing tumour metastasis. The biopsy also only removes a small amount of tissue from the primary lesion. Since cancerous lesions are often heterogeneous, the portion of biopsied tissue may not contain HER2/*neu* levels which are representative of all sites of disease. Molecular imaging targets biomarkers *in vivo*, and so can act as a non-invasive method which informs the clinician of biomarker expression throughout all areas of the primary tumour and metastatic lesions.[59] Since trastuzumab is known to bind to HER2/*neu*, it can be modified to create a molecular imaging agent. Conjugating a diagnostic radionuclide to the mAb and administering the radiotracer at microdose levels allows imaging HER2/*neu* expression using techniques such as PET and SPECT. There are multiple reports of zirconium-89 conjugates of trastuzumab, an ideal radioisotope as the long half-life is compatible with the long circulation times of the mAb.[60–64] A number of ^{89}Zr-trastuzumab conjugates have been trailed in the clinic; for example, a 2010 study focussed on the quantification of HER2/*neu* +ve lesions following administration of ^{89}Zr-trastuzumab.[65–67]

Human hepatocyte growth-factor receptor (c-MET)

Similar to HER2/*neu*, the human hepatocyte growth-factor receptor (c-MET) is a RTK protein. It is expressed on the cell surface of normal epithelial cells and is also known to be overexpressed in a number of cancers including colon, gastric, bladder, breast, ovarian, liver, lung, and thyroid.[68] The only known natural ligand for c-MET is the hepatocyte growth-factor (HGF), also known as scatter factor (SF).[69] As with other RTKs, binding of the ligand causes dimerisation of the receptor resulting in tyrosine phosphorylation and the consequential activation of downstream signalling. These signalling events control cellular responses such as proliferation, motility and morphogenesis which are important in facilitating a wide range of biological processes including embryological development, wound healing, tissue regeneration, angiogenesis and growth. As with HER2/*neu*, due to the myriad of cellular responses that c-MET controls, upregulation of this RTK in cancer cells usually results in an aggressive disease which is likely to metastasise.[70]

There are several inhibitors of c-MET which have been developed for therapeutic and imaging purposes.[71] For example, crizotinib (Xalkori®, Pfizer, New York, USA) exhibited an IC_{50} of 8.4 nM *in vitro* using gastric carcinoma cells. Following subsequent successful clinical trials, crizotinib became an European Medicines Agency (EMA) approved drug.[72] HGF itself has also been radiolabelled with ^{64}Cu to produce a potential PET imaging agent.[73] However, due to ability of HGF to accelerate unfavourable cellular responses, other protein-based imaging agents have proved more attractive.[73] As bivalent antibodies can also cause dimerisation and internalisation, and induce downstream signalling, the one-armed antibody onartuzumab (Genentech Inc., South San Francisco, CA) was developed. The monovalent antibody has been studied for the treatment of non-small-cell lung cancer in phase III clinical trials and radiolabelling with zirconium-89 has proved promising in pre-clinical studies.[74,75]

1.3 Molecular Imaging

1.3.1 Medical imaging and biomarkers

Traditional medical imaging methods including X-ray computed tomography (CT), magnetic resonance imaging (MRI), and ultrasound (US) have provided clinicians with detailed anatomical information. These techniques allow the location of tumours to be determined, as well as their size and structure. Molecular imaging uses techniques such as positron emission tomography (PET), single-photon emission computed tomography (SPECT) and optical imaging to visualise, characterise and measure biological processes at the cellular and molecular level.[76,77] This is often achieved *via* the use of molecular imaging agents that target biomarkers. Molecular imaging agents accumulate at biomarker sites and allow visualisation of the target in comparison to background tissue. Providing an effective imaging agent is used, molecular imaging techniques have the potential to be incredibly sensitive techniques by detecting small abnormalities based molecular differences. For example, PET imaging with [^{18}F]FDG (see below for details) can visualise tumours with a volume as small as 80 mm^3.[78] Comparatively, anatomical imaging techniques, such as CT, can only visualise tumours once they are a centimetre in diameter and are unable to characterise the biochemistry of the disease.[79] Therefore, by targeting a specific biomarker, molecular imaging can allow for earlier diagnosis in comparison to traditional imaging techniques.[76,80]

Moreover, molecular imaging can provide benefits when combined with *in vitro* diagnostic assays. Whilst *in vitro* assays are able to aid the diagnostic process, the simple detection of a biomarker in the blood becomes less useful during the treatment of the patient. During the course of treatment, biomarker concentrations may fluctuate in ways that are not representative of the patient response. Therefore, molecular imaging must be used to investigate if treatment is effective on a lesion-by-lesion basis. For example, a patient undergoing treatment can exhibit a partial response to treatment which may result in a decrease in biomarker concentrations in the blood. However, a simple, *in vitro* test cannot determine whether all lesions have decreased in size or whether a heterogeneous response has occurred with some lesions increasing in size whilst others diminish. In this case, molecular imaging can act as a non-invasive method to determine the heterogeneity of response to therapeutics.[81]

1.3.2 Imaging techniques

Positron emission tomography

PET is a nuclear imaging technique which detects and locates radioactive decay events *in vivo*, providing quantitative tomographic images. The steps involved in the acquisition and data processing of a PET image are summarised in **Figure 1.4A**.[82]

Figure 1.4. (A) The steps of image acquisition in PET: 1) Positron (ß$^{+}$) decay event which results in the eventual emission of two γ-photons at ~180^{o}. 2) Photons travel along the line of response (LOR) before reaching detector. 3) Scintillation events converts γ-rays to visible light. 4) Visible light is converted to electrical pulses by a photomultiplier tube (PMT). 5) If the energy of detection is in the correct widow, a coincidence event is registered. 6) Coincident events are stored in the form of a sinogram. 7) Images in real space are reconstructed from sinogram data. **(B)** The arrangement of detectors and the relation between the LORs and the FOV.

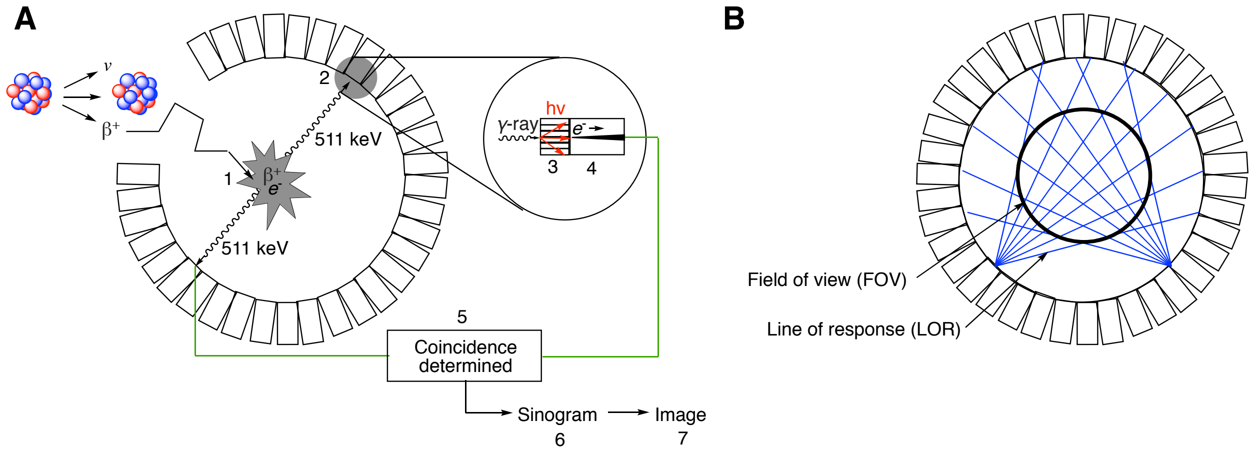

The technology relies on ß$^+$ decay which is explained in detail in section 3.3.1. Briefly, following the administration of a radiotracer containing a positron-emitting radionuclide, it accumulates in tissues. The radionuclide emits a positron which travels through the surrounding tissues losing enough kinetic energy by interaction with the medium. When the positron has lost the majority of its kinetic energy it slows down and interacts which an electron causing both particles (ß$^+$ and e$^-$) to annihilate. Annihilation produces two gamma (γ) photons of 511 keV that propagate at ~180° and their coincident detection is the mechanistic basis of PET.[83]

Detection of the 511 keV photons is facilitated by using a scintillator; a material which when excited by ionising radiation (e.g. X-rays, γ-rays) emits visible or UV photons. Scintillators vary greatly in composition, however, inorganic single-crystal scintillators are most commonly used in PET imaging as their high density and high effective atomic number leads to efficient detection of γ-rays.[84] Lutetium oxyorthosilicates (Lu_2SiO_5[Ce] or LSO) are commonly used scintillation crystals and are considered superior to other inorganic scintillators for a number of reasons. As well as a high density and effective atomic number, they exhibit high light output which optimises resolution. LSO crystals also have a short decay time (40 ns) allowing the detector to run at a high efficiency at higher count rates.[83–85] However, images in this thesis were acquired using a G4 PET/X-ray camera which uses bismuth germanate ($Bi_4Ge_3O_{12}$ or BGO) scintillator crystals. Whilst BGO may not hold some of the advantages of other scintillator crystals, for small animal PET imaging it is ideal. BGO is a lower cost scintillator, has a high stopping power and can be easily fabricated. It also exhibits reduced inter-crystal scatter, improving spatial resolution, and has low intrinsic radioactivity which improves the minimum detectable activity.[86]

The visible light that is emitted from scintillators is converted into an electrical pulse and amplified by photomultiplier tubes (PMTs). The PMT itself is a vacuum tube with a photocathode which releases electrons following the absorption of light. The electrons are accelerated through a series of dynodes which multiply the number of electrons before the electron pulse reaches the anode to which it is attracted. Further amplification occurs until the pulse is detectable by a pulse height analyser (PHA). The PHA facilitates energy discrimination of the signal and ensures that only photons of the correct energy are used for the image construction, removing any data which may have arisen from scattered photons.[83,87] Early PET cameras required one PMT per scintillation crystal, which made production expensive and limited the number of crystals that could be used, in turn limiting the spatial resolution. Nowadays, to overcome these issues, block detection is used. A block detector is a large crystal that is divided into an array of sub-elements by partial cuts and is connected to multiple PMTs. Geometric calculations from the resulting pulses allows the location of the scintillation event within the crystal to be determined and assigned to a particular crystal element.[88]

With the two photons emitted by the annihilation event propagating at ~180° from each other, it is possible to locate their source along a straight line of coincidence known as the line of response (LOR). Put simply, a LOR is the volume of space between opposite detectors. The number of LORs is a function of the PET camera design.[89] Detectors can be arranged in several geometries but state-of-the-art cameras usually use a full ring of detectors in a circular arrangement. This increases the number of LORs and hence improves the field of view (FOV) (**Figure 1.4B**).[90,91] Each detected photon (in the correct energy window) is time stamped (±1 ns) and pairs of photons are considered coincident if they fall into the 'coincidence timing window' (often between 6-12 ns).[92] The data obtained from coincident events are stored in the form of a sinogram for image reconstruction.

The acquisition of the image is reliant on the administration of the radiotracer. [^{18}F]-2-fluoro-2-deoxy-D-glucose ([^{18}F]FDG) is currently the most commonly used radiopharmaceutical for oncological PET studies.[93] The first ^{18}F-labelled FDG for human studies was synthesised in 1976 *via* electrophilic fluorination of 3,4,6-tri-O-acetyl-D-glucal with [^{18}F]F_2.[94] Due to low yields, long reaction times and the development of [^{18}F]F^- production, a new synthetic route was reported in 1986 using nucleophilic substitution (**Figure 1.5A**).[95] This allowed [^{18}F]FDG to be synthesised in high yields with a high purity and in the subsequent years automated synthesis modules were made commercially available.[96]

Figure 1.5. (A) Chemical synthesis of [^{18}F]FDG. **(B)** PET images of a patient recorded 70-90 min. post-injection (left) and 0-90 min post-injection of [^{18}F]FDG. Image reproduced with permission from Rahmim *et al.*, *Eur. J. Nucl. Med. Mol. Imaging*, 2018, **46**, 501–518, Copyright 2018 Springer nature.[97]

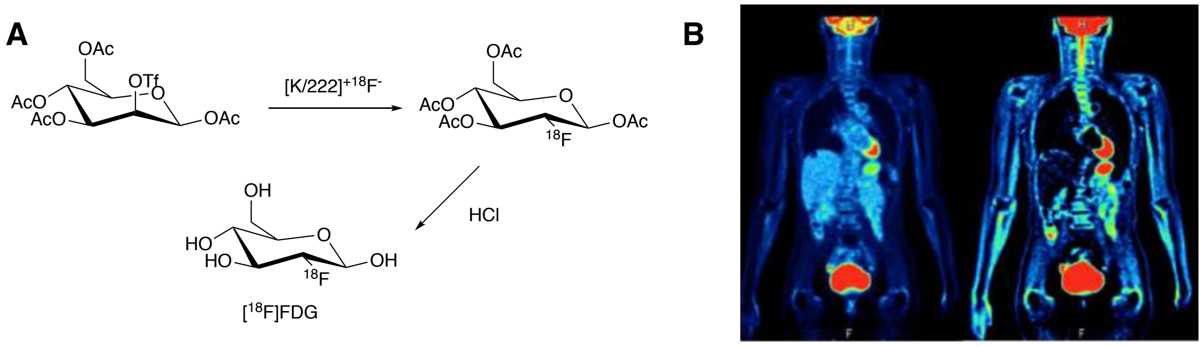

With the structure of [^{18}F]FDG being analogous to glucose it is transported into cells by glucose transporters, however, with no -OH group at the C2 position normal metabolism cannot take place and FDG remains in the cell. Cancer cells are known to exhibit an increased rate of glycolysis and therefore an increased accumulation of [^{18}F]FDG can be observed in tumours providing contrast to background tissue.[98] The biochemical similarities of [^{18}F]FDG with glucose allow it to cross the blood brain barrier, meaning this versatile radiotracer can also be used for imaging tumours in the brain and other neurological diseases.[96]

Magnetic resonance imaging (MRI)

MRI is an imaging technology based on nuclear magnetic resonance (NMR) which produces three dimensional anatomical images of the body. The NMR phenomenon was first discovered by Isidor Isaac Rabi in 1938 which later led to the development of MRI which used NMR technology to create images. For this work Lauterbur and Mansfield shared the 2003 Nobel Prize in Physiology/Medicine. The first human MR images were reported in 1977 and following this, the technology became available in the clinic from the early 1980s.[99,100]

MRI usually images hydrogen nuclei as they are the most common nuclei in biological tissue. An adult human is around 60% water and there is also an abundance of protons in fat, carbohydrates, *etc.* The spins of each proton (I = 1/2) are randomly orientated when no magnetic field is applied. When a magnetic field B_0 is applied across the subject or sample, most spins align with the external magnetic field, whilst a minority of high energy spins align in the antiparallel direction. The result is a net magnetisation in the M_z (longitudinal) direction (**Figure 1.6A**). The rotation of the spin is known as precession and the rate of precession is given by the Larmor frequency (v) seen in **Equation 1.1**. Here, B_0 is the strength of the applied magnetic field and γ is the gyrometric ratio which for a proton is equal to 42.58 MHz/T.

Equation 1.1. The Larmor equation

$$v = \gamma \cdot B_0$$

A radiofrequency (RF) pulse is then applied (**Figure 1.6B**) at the Larmor frequency so that resonance can occur allowing the energy to be transferred from the RF pulse to the protons. The pulse causes a portion of spins to flip to the opposite state diminishing the longitudinal magnetisation (**Figure 1.6D**) and causes the spins to synchronise resulting in a growth of magnetisation in the M_{xy} (transverse) direction (**Figure 1.6C**). As the net magnetisation is flipped from the longitudinal to the transverse plane we denote this as a 90° RF pulse. When the RF pulse is removed, there is a rapid loss of transverse magnetisation, this is known as T_2 or 'spin-spin' relaxation (**Figure 1.6C** to **1.6D**). Following this the high-energy protons in the opposite direction to the applied magnetic field fall back to the low energy state and the longitudinal magnetisation grows again (**Figure 1.6E** to **1.6F**). The energy released during the transition is absorbed by the surrounding tissue as heat energy and therefore this T_1 relaxation is also referred to as 'spin-lattice' relaxation. The T_1 time is the time it takes for the longitudinal magnetisation to return to 63% its original state, whilst the T_2 time is the time it takes for the transverse magnetisation to decrease to 37% of its starting value (**Figure 1.7**).[101]

Figure 1.6. Representation of the orientation of proton spins and resulting net magnetisation during MRI acquisition steps. **(A)** An external field, B_0, causes alignment of the majority of spins. **(B)** A 90° RF pulse then causes **(C)** spins to align the xy plane resulting in the growth of the transverse magnetisation and **(D)** Spins then dephase *via* T_2 relaxation (C →D). The 90° RF pulse also causes **(E)** some spins to flip resulting in a diminishing of the longitudinal magnetisation and **(F)** longitudinal magnetisation regrows *via* T_1 relaxation (E →F).

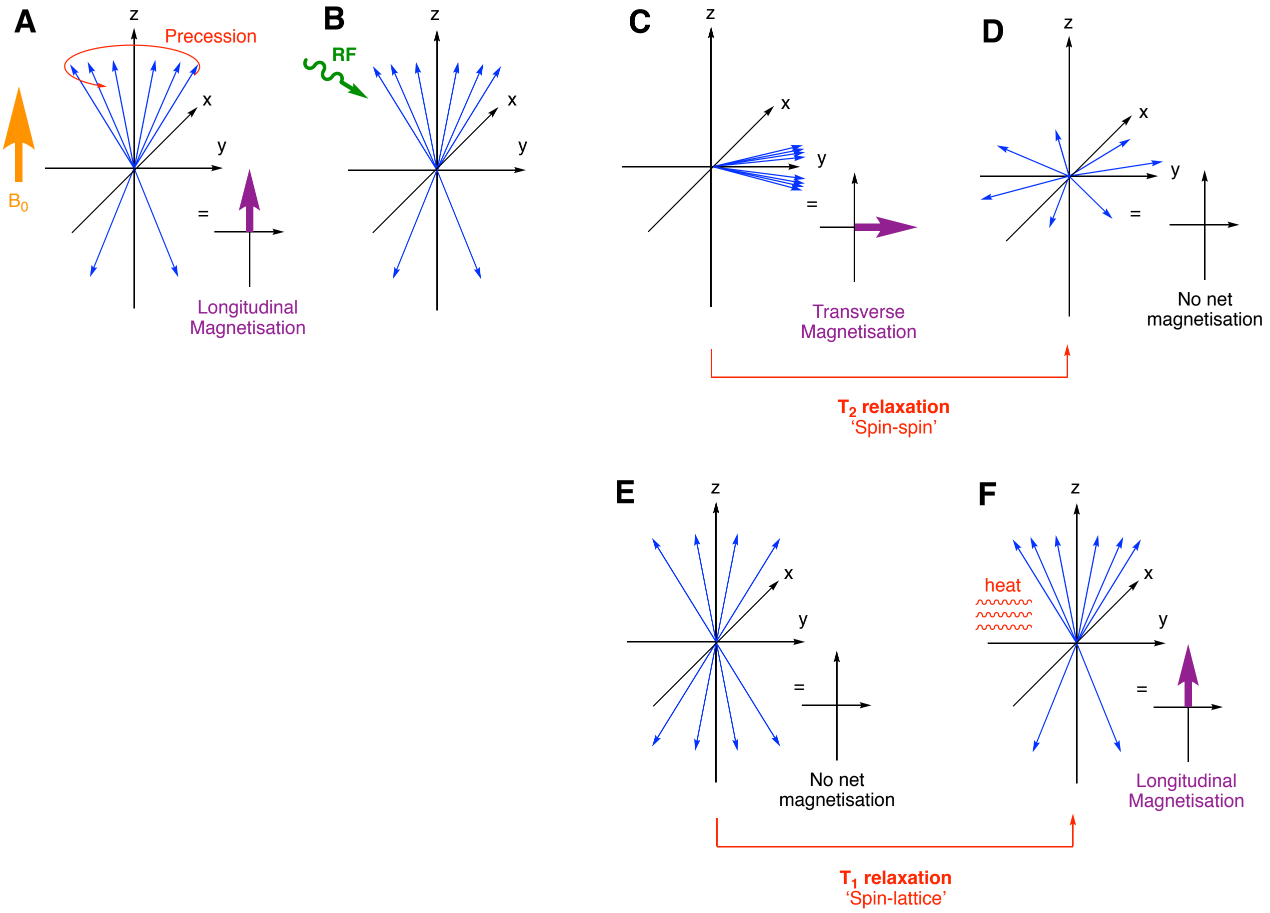

Figure 1.7. Definition of **(A)** T_1 relaxation and **(B)** T_2 relaxation.

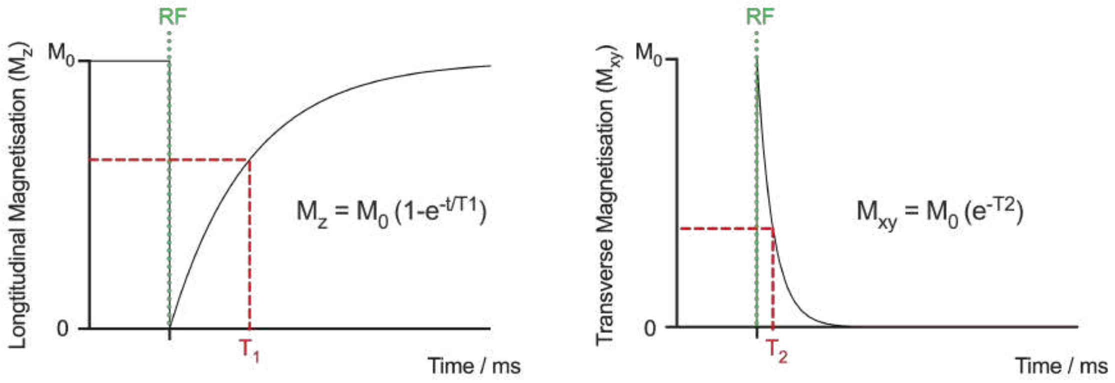

The observed relaxation following a 90° RF pulse is actually denoted as T_2^*. Here, T_2^* is defined as the spin-spin dephasing ("true" T_2 relaxation) plus relaxation that occurs from inhomogeneities in the local magnetic field, ΔB_{inhom} (**Equation 1.2**). These inhomogeneities arise due to the differences in magnetic susceptibility of various tissues, a distribution in chemical shifts and inhomogeneities in the applied magnetic field itself.[102] The result is the observed T_2^* relaxation is significantly faster than T_2.

Equation 1.2. Relationship between T_2^* and T_2.

$$\frac{1}{T_2^*} = \frac{1}{T_2} + \frac{1}{T_2'} \qquad \textit{where} \qquad \frac{1}{T_2'} = \gamma \cdot \Delta B_{inhom}$$

To eliminate the dephasing caused by inhomogeneities, a 180° pulse can be used alongside the 90° pulse in a process known as a spin echo. Following the initial 90° pulse, the protons begin to dephase *via* T_2^* relaxation generating a free induction decay (FID) signal. A 180° RF pulse is then applied which causes the spins to flip to the opposite axis and rephase which causes a second signal peak known as the spin echo. The time between the initial RF pulse and the spin echo is referred to as T_E. To determine the true T_2, multiple 180° pulses are used in a sequence and T_2 is found as the time it takes for the echo amplitudes to decay to 37% (**Figure 1.8**). Following the sequence, time T_R passes before the new 90° pulse is applied.[103–105]

Different tissues exhibit variations in T_1 and T_2 relaxation times due to the different environments of the protons. In general, fluids have longer relaxation times than denser tissues; for example, cerebrospinal fluid (CSF) has T_1 and T_2 times of approximately 4500 ms and 2200 ms respectively, whilst for fat these values are lower at 250 ms and 60 ms.[106] To provide sufficient contrast between tissues the differences can be accentuated by altering the pulse sequence. In a T_1-weighted image, energy is transferred more easily in tissues, such as fat, as heat deposited in the surrounding tissue. This increases the speed spins flip during longitudinal relaxation which decreases T_1 times and is assigned the greyscale colour of white on an image. To accentuate this characteristic, short T_E and T_R times are used as the longitudinal magnetisation recovers more quickly in fat and can be detected. The longitudinal magnetisation in fluids does not recover on this timescale and the regrowth in longitudinal magnetisation is not as observable. This is assigned the greyscale colour of grey/black. In a T_2-weighted image, the protons in tissues such as fat de-phase faster, resulting in a decreased T_2 time which is assigned a greyscale colour of black on the MRI image. On the contrary, protons in substances such as water remain in phase for a longer time and have longer T_2 relaxation times which is assigned a greyscale colour of white. To accentuate these differences, long T_E and T_R times are used, this gives spins ample time to dephase to a position where a greater variance in transverse magnetisation can be observed.[107,108] Despite the inherent differences in T_1 and T_2 relaxation times of certain tissues, contrast agents are often used to further accentuate the differences.

Figure 1.8. (A) Formation of multiple spin echoes from a string of 180° RF pulses. The initial faster decay observed after the 90° RF pulse is due to T_2* effects and the true T_2 decay can be determined from the decrease in amplitude of the spin echoes. **(B)** The resulting pulse sequence.

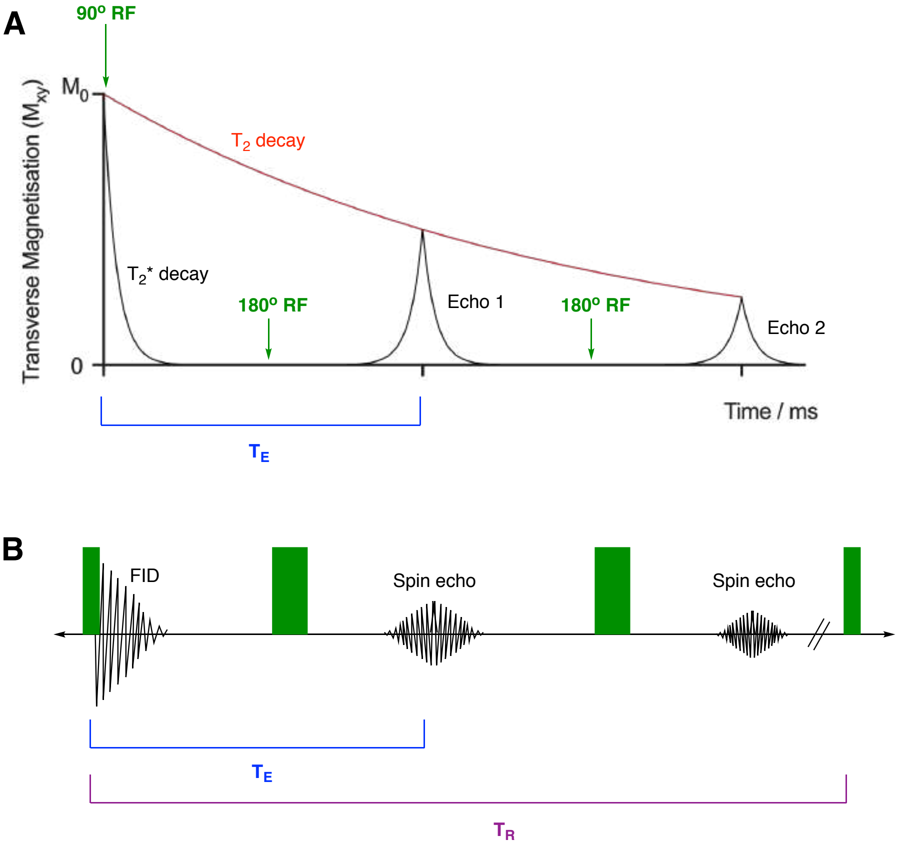

MRI contrast agents

T_1 contrast agents

T_1 contrast agents (also known as positive contrast agents), as the name suggests, catalytically shorten the longitudinal relaxation times of nearby protons and hence increase signal intensity on T_1-weighted images. Gd^{3+} is by far the most commonly used T_1 contrast agent and will therefore be discussed further.[109–111] With seven unpaired electrons in the 4f shell, Gd^{3+} is paramagnetic with a high magnetic moment (7.9 μ_B). It is also in a totally symmetric electronic state (ground state term symbol: $^8S_{7/2}$) which provides a slower electronic relaxation allowing sufficient time for the magnetic state to be transferred to the surrounding bulk water.[112] However, the free, non-complexed Gd^{3+} (found as the aquated $[Gd(H_2O)_9]^{3+}$) is highly toxic and must be bound to chelating ligands. The earliest example is Gd-diethylenetriaminepentaacetic acid $[Gd(DTPA)H_2O]^{2-}$ which was the first MRI contrast agent to enter the clinic marketed as Magnevist® (**Figure 1.9**).[113]

Equation 1.3.

$$\frac{1}{T_i} = \left(\frac{1}{T_i}\right)_0 + r_i[CA] \quad where \quad i = 1 \; or \; 2$$

Figure 1.9. Contrast agent Magnevist® (red) and the variables which effect *r₁*

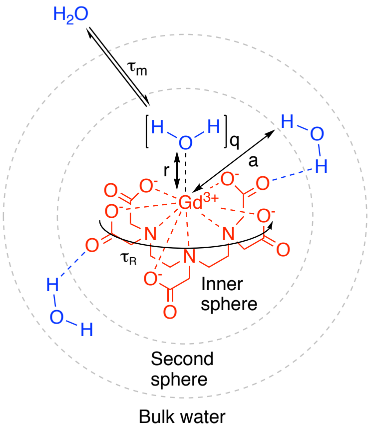

The ability of contrast agents to increase the rate of longitudinal relaxation of surrounding water molecules is known as the relaxivity (r_1). r_1 is described by **Equation 3** where $(1/T_1)_0$ refers to the contrast agent-free solution and [CA] refers to the concentration of the contrast agent.[114] To measure and predict the relaxivity of potential Gd^{3+} based chelators, Solomon–Bloembergen–Morgan (SBM) theory is used. Factors which increase the relaxivity value are (*i*) a greater number of inner sphere water molecules (q), (*ii*) an optimal, but short, water residence time (τ_m), (*iii*) a slow tumbling rate ($1/\tau_R$), (*iv*) interactions with the complex and water molecules in the outer spheres (a), and (*v*) sufficient coordination distance (r) (**Figure 1.9**).[112,114,115]

T_2 contrast agents

T_2 contrast agents catalytically shorten the transverse relaxation times of nearby protons which decreases signal intensity on T_2-weighted images (known as negative contrast agents) (**Figure 1.10**). Iron oxide nanoparticles are the most commonly used T_2 and T_2^* contrast agents. They consist of γ-Fe_2O_3 (maghemite), Fe_3O_4 (magnetite) or α-Fe_2O_3 (hematite), however, magnetite and maghemites are the most commonly used in MR imaging. Magnetite consists of iron (II,III) oxide with 1/3rd of the iron sites are filled with Fe^{2+} ions, and 2/3rd filled with Fe^{3+} (described as $Fe^{2+}Fe^{3+}{}_2O_4{}^{(2-)}$). In aqueous conditions, magnetite slowly oxidises to maghemite which consists solely of iron in the 3+ oxidation state. Both magnetite and maghemite bulk materials are ferrimagnetic but once the nanoparticles reach the size of a single domain they exhibit superparamagnetism. Iron oxide nanoparticles begin to exhibit superparamagnetism at sizes below 20 nm, they are then termed super paramagnetic iron oxide nanoparticles (SPIONs). In the presence of an external magnetic field, SPIONs exhibit strong magnetism which causes inhomogeneities in the local magnetic field. This accelerates the dephasing of the surrounding protons causing an accelerated loss in transverse magnetisation which decrease T_2 signal intensity.[116,117] Whilst concentration still impacts the relaxivity (r_2) of the nanoparticles, their size, shape and coating is also important.

Figure 1.10. T_2-weighted MR images. **(A)** Conventional MRI *versus* **(B)** MRI 24 h post-administration of SPIONs. The arrow highlights the accumulation of the nanoparticles in the lymph node. Image reproduced with permission from *N. Engl, J. Med.,* 2003., **348**, 2491-2499, copyright Massachusetts Medical Society .[118]

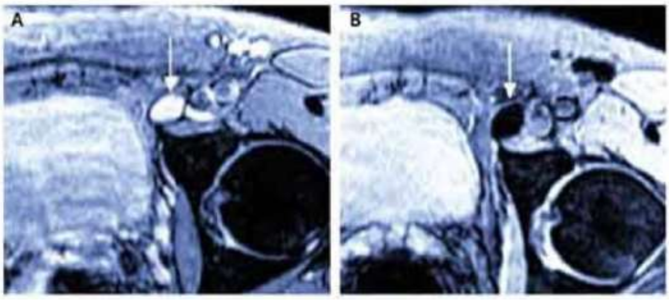

Although nanoparticles must be sufficiently small to qualify as SPIONs (core size <20 nm), larger particles within this range exhibit larger mass magnetisation values, and therefore, produce shorter T_2 relaxation times. For example, this can be seen in the work by Jun *et al.* who observed a darker contrast in T_2-weighted images as the size of SPION is increased (4-12 nm).[119] The effect is due to spin canting and is also known as the inclination effect.[120,121] The magnetic moments of SPIONs arise from the unpaired 3d electrons in the Fe^{2+} and Fe^{3+} atoms. The spins at the octahedral sites and the spins at the anti-parallel tetrahedral sites couple *via* oxygen atoms. Due to the incomplete coordination shells for surface atoms and general disordering of the lattice at the nanoparticle surface, sufficient coupling cannot take place, and the spins are said to be canted. As size decreases the surface area to volume ratio increases and more spins are canted, which decreases the overall magnetic moment of the SPION.[120] Kim *et al.* reported that 93.6% of spins in 3 nm-sized iron oxide nanoparticles are canted, whereas only 38.6% of spins in 12 nm-sized nanoparticles are canted. This results in an increase in magnetic moments with values of 273 and 24800 μ_B for 3 and 12 nm particles respectively.[122] Once a size is reached where canting effects no longer cause a significant difference, T_2 relaxation times decreases with increasing size. As surface area to volume ratio decreases with increasing size there is a reduction in the surface accessibility to water molecules, therefore a decrease in proton exchange rate. SPIONs with a diameter of 22 nm are reported to have faster T_2 relaxation times in comparison to those with a diameter of 30 nm.[123]

The shape of the nanoparticles can also influence the T_2 relaxivity by altering the core size and surface area. A study by Alipour *et al.* indicated that cubic iron oxide nanoparticles exhibit increased relaxivities.[124] Particle coatings can also have an effect on the relaxivity of the nanoparticle. Park *et al*. explored the effect of coating the SPION with PEG chains of varying length. They found that the relaxivity of the SPION decreases as the molecular weight of the PEG increases. The coating both decreases the diffusion rate of the water molecules due the hydrophilicity of PEG and increases the distance between the iron core and the water molecules.[125]

PET/MR imaging

As with all imaging techniques, both PET and MRI have unique advantages and disadvantages. Nuclear imaging techniques such as PET provide functional information and are exceptionally sensitive, requiring just picomoles of radiotracer. However, PET images do not provide anatomical information and offer limited resolution. *Vice versa*, MRI provides high soft-tissue contrast and anatomical information at high resolution but if contrast agents are required, they must be administered at a relatively high concentration. To circumvent some of these issues and to employ the advantages of each imaging moiety, hybrid imaging can be used.[126] PET/MRI multimodal imaging is a relatively new technology which was first introduced to the clinic in 2010 with one of the earliest scanners being installed at the University Hospital Zurich (2011, Discovery PET/CT + MR combo, installed by GE Healthcare).[127] Integrating PET and MRI scanners is particularly challenging as the strong magnetic field can degrade the PMTs on the PET detector and can affect the positron range and spatial resolution. Therefore, early scanners relied on tandem scans where PET and MRI images are acquired sequentially. Nowadays, these issues can be overcome and simultaneous scanners have been developed. The Siemens mMR system was the first commercially available whole-body PET/MRI scanner. PMTs are replaced with solid-state silicon photo sensors known as avalanche photodiodes (APDs) which are not sensitive to the magnetic field.[128]

Figure 1.11. (A) The full body MRI, **(B)** PET image following the injection of ^{68}Ga-DOTA-TOC, and **(C)** the overlaid PET/MRI. Image reproduced with permission from S. A. Esfahani *et al.*, *Am J Nucl Med Mol Imaging*, 2017, **7**, 53–62, copyright AJNMMI 2017. [129]

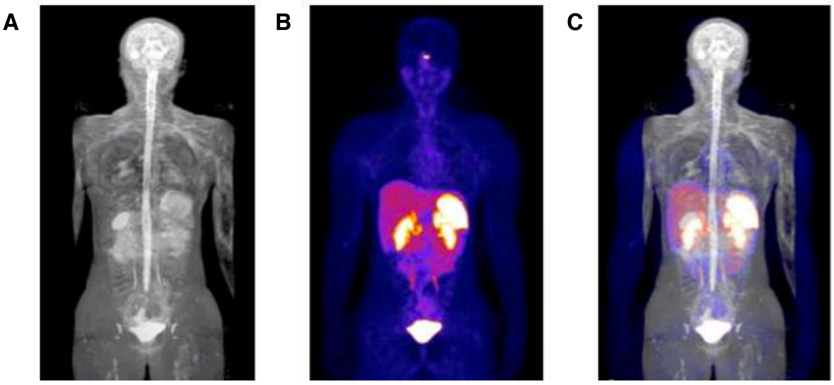

PET/MR imaging agents

In theory, in acquiring a PET/MR image a clinician has three options when deciding how to use potential imaging agents. The first option is to inject a patient with the PET tracer alone and rely on the natural contrast of different tissues in MRI imaging. Whilst this is routinely practiced, it is a non-ideal solution as the addition of a contrast agent would add clarity to the MR image and may, for example, highlight lesions that would not be seen on a normal MRI scan.[130] Secondly, two separate imaging agents could be injected simultaneously into the patient, a T_1 or T_2 contrast agent plus a radiotracer.[131] This can be problematic as the compounds may have different pharmacodynamic and pharmacokinetic profiles which can complicate data obtained from the scan. Potential drug interactions can also not be excluded. Finally, a single dual-modality molecular imaging probe could be injected into the patient. By designing a compound that contains a MRI contrast agent, a radionuclide and a biological targeting vector (**Figure 1.12**), a single biomarker can be imaged with multiple techniques using just one entity. With the introduction of PET/MRI technology research began to focus on the development of hybrid imaging agents. For example, Frullano *et. al.* developed a Gd^{3+} based contrast agent radiolabelled with ^{18}F which targeted the acidic nature of tumours.[132] Shen *et al.* used superparamagnetic manganese ferrite ($MnFe_2O_4$) nanoparticles as the MRI detection unit which also act as a scaffold to conjugate the targeting vector arginine-glycine-aspartic acid (RGD)-peptide and a ^{64}Cu complex.[133] Despite the increased research into the development of dual PET/MRI probes, there has been little progress in solving concentration-related issues in the design if the multimodal imaging agents. Whilst PET requires only picomoles of radiotracer, MRI contrast agents often require the administration of millimoles of material. Small-molecule probes offer little solution to this issue with their limited loading capacity. However, nanotechnology may offer a solution to this problem as nanoparticles, and similar materials, offer a large surface or volume for functionalisation.[134] Using nanotechnology to overcome these issues forms a large basis of this thesis and will be discussed in more detail in **Section 1.5**.

Figure 1.12. Design of multi-modal PET/MR imaging agent.

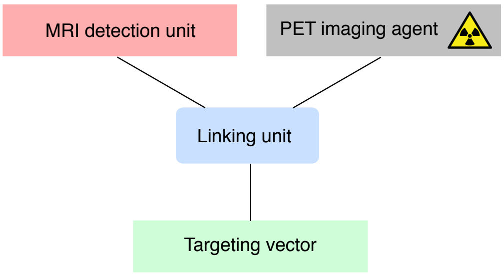

1.4 Radionuclides in nuclear medicine

1.4.1 Laws of radioactive decay

Radionuclides are unstable due to an excess of nuclear energy. The transition to a stable state involves the emission of ionising radiation in a process known as radioactive decay. The rate at which radioactive decay progresses follows classic first-order kinetics where the decay rate ($-dN/dt$) is proportional to number of radioactive atoms (N) multiplied by the decay constant (λ) of the radioactive species (**Equation 1.4A**). When $N = N_0$ at $t = 0$, we can integrate to obtain **Equation 1.4B**.[135] Half-life ($t_{1/2}$) is frequently used to describe the time required for half the radioactive atoms to decay ($N_{t_{1/2}} = N_0/2$). Hence, when $t = t_{1/2}$ **Equation 1.4C** applies. During practical measurements of radioactivity, the measured quantity of $\lambda \cdot N$ is referred to as the activity (A). Therefore, **Equation 1.4A** holds and A can be described by **Equation 1.4D**. The SI unit for activity (A) is the Becquerel, where 1 Bq = 1 decay s^{-1}.[136]

Equation 1.4. (A) Decay rate and **(B)** the corresponding integrated rate law. Definitions of **(C)** half-life and **(D)** activity.

A. $-\frac{dN}{dt} = \lambda \cdot N$ **B.** $N = N_0 \cdot e^{-\lambda t}$ **C.** $t_{1/2} = \frac{\ln 2}{\lambda}$ **D.** $A = A_0 \cdot e^{-\lambda t}$

1.4.2 Radiopharmaceuticals

There are a large number of radionuclides used in nuclear medicine and a selection of these are highlighted in **Table 1.2**. Therapeutic radiopharmaceuticals deliver cytotoxic ionising radiation to tumour sites, resulting in the death of local cells. Radionuclides used in α-therapy decay *via* the emission of a high-energy helium nucleus known as a α-particle. Radionuclides used in ß-therapy are neutron rich and undergo isobaric ($ß^-$) decay. Here, a neutron is converted into a proton, a $ß^-$ particle (e^-) and an anti-neutrino.[137] Diagnostic radiopharmaceuticals depend on the use of radionuclides at very low concentrations (nM to pM) to perform non-invasive imaging.[138]

Table 1.2. A selection of common radionuclides used as radiopharmaceutics.[139–143]

Radionuclide	Half-life	Decay mode	Application
^{177}Lu	6.7 d	$ß^-$ (100%)	ß-therapy
^{225}Ac	10.0 d	α (100%)	α-therapy
^{67}Ga	3.3 d	EC	SPECT
^{68}Ga	67.7 min	$ß^+$	PET
^{111}In	2.8 d	EC (100%)	SPECT
^{89}Zr	78.4 h	EC (77%), $ß^+$ (23%)	PET
^{18}F	110 min	$ß^+$ (97%), EC (3%)	PET
^{11}C	20.4 min	$ß^+$ (99.8%), EC (0.2%)	PET
^{64}Cu	12.7 h	EC (44%), $ß^+$ (17%), $ß^-$ (39%)	PET, SPECT
^{99m}Tc	6.01 h	IT	SPECT

1.4.3 Decay modes related to diagnostic radiopharmaceuticals used in PET and SPECT

ß⁺ decay

PET imaging relies on ß⁺ decay. Here, a proton rich radionuclide decays when a proton is converted into a neutron (n), a positron (ß⁺) and a neutrino (ν) (**Equation 1.5**). The equation shows that the products are heavier by 2 electron masses. The energy which is equivalent to this mass balance is 1.022 MeV, therefore, for positron decay to occur, the radionuclide must have a transition energy (known as the Q-value) greater than this value. Additional energy is transferred as kinetic energy to the positron, the neutrino, and to the daughter nuclide. The positron travels a random walk path length before it loses enough energy that it can interact with an electron (511 keV). This matter-antimatter interaction causes annihilation of both particles and releases two γ-photons of 511 keV at ~180°.[83,136]

Equation 1.5. Scheme of ß⁺ decay.

$$p \rightarrow n + \beta^{+} + \nu$$

Electron capture

Similar to ß⁺ decay, electron capture (EC) occurs when a radionuclide is proton rich. However, when the transition energy (Q-value) is less than 1.022 MeV, ß⁺ decay cannot take place. In this case, an electron from the inner shell of the radionuclide is captured by the nucleus and the proton decays to a neutron releasing a neutrino in the process. The empty position from the inner shell is then filled by electrons from higher shells and this causing the emission of X-rays. Some nuclides which undergo EC produce a daughter nuclide which is in an excited state. When this falls to its ground state it releases γ-rays which can be detected in SPECT imaging. Other nuclides emit an electron, this process is known as Auger electron emission and can be used in therapeutic applications.[144]

Equation 1.6. Scheme of electron capture.

$$p + e^{-} \rightarrow n + \nu$$

Isomeric transition (IT)

Isomeric transition occurs when an radionuclide in an excited (nuclear) state de-excites to a metastable or ground state without change in the number of neutrons or protons. Transitions are facilitated via γ-ray emission or internal conversion (IC). IC is a process where an orbital electron enters the nucleus and absorbs the energy from the excited state before being emitted from the atom.[144]

1.4.4 Radionuclides used as diagnostic radiopharmaceuticals

Gallium-68

Gallium-68 decays primarily *via* ß$^+$ emission, allowing it to be an ideal candidate for PET imaging. The half-life of ^{68}Ga is 67.71 min which provides sufficient time for production of the tracer and performing the PET imaging whilst minimising the radiation exposure to the patient. Following a ^{68}Ga PET scan a patient must wait a minimal time to be activity free and can typically be released from hospital on the day of the procedure. As can be seen from the decay diagram (**Figure 1.13**), ^{68}Ga decays through 89% positron emission. This high positron abundance allows for a reduction in the administered dose and shorter scan times. However, positrons produced from the largest branch of the positron emission (amounting to 87.7%) have a maximum energy of 1.9 MeV. This energy is considerably higher than the energy of positrons emitted from many other clinically relevant PET radionuclides, which explains the relatively low resolution of ^{68}Ga PET as positrons travel a longer range before annihilation occurs (**Table 1.3**).[145,146] Despite this draw back, ^{68}Ga still remains a desirable nuclide for PET imaging because of its easy accessibility and relatively low cost due to the development of the ^{68}Ge/^{68}Ga generator. In the generator-based production of ^{68}Ga, the parent nuclide ^{68}Ge decays to ^{68}Ga through electron capture with a half-life of 270.9 days. Germanium-68 is produced by using a cyclotron and then is absorbed onto a stationary solid-phase, which in modern commercial generators is often composed of titanium(IV) oxide or tin(IV) oxide. The ionic differences between ^{68}Ge(IV) and ^{68}Ga(III) are then exploited to achieve separation of the daughter radionuclide from the parent, and the ^{68}Ga^{3+} ions are eluted with a hydrochloric acid solution (typically 0.1-1 M). The breakthrough of ^{68}Ge(IV) in modern generators is usually very low.[147,148] However, removal of ^{68}Ge along with other contaminants including ^{68}Zn(II) (the final decay product) and Fe(III) (a general chemical impurity and radiochemical 'poison') remains important. There are several established methods for the removal of these impurities; in our facility, we use a small cation exchange resin (SCX) and a highly ionic (of ~5 M NaCl in 0.1 M HCl) solution to elute purified ^{68}GaCl$_3$(aq.).[148–150]

Finally, the chemistry of ^{68}Ga is versatile with Ga^{3+} behaving similar to high-spin Fe^{3+} and readily forming 6-coordinate octahedral complexes. As Ga^{3+} acts as a hard Lewis acid, chelates are designed to contain hard Lewis bases to produce thermodynamically stable complexes. High thermodynamic stability is essential to prevent ligand exchange in the blood serum as gallium can transchelate to the iron transport protein transferrin.[151] Also, due to the short half-life of ^{68}Ga, fast formation kinetics are necessary for a successful chelator.[152–154] For example, the commonly used desferrioxamine-B (DFO) coordinates *via* the oxygen atoms in its hydroxamate groups binding the Ga^{3+} ion with high affinity (formation constant, log *ß* = 28.2) with reaction times less than 5 minutes.[152,155] However, chemistry performed with Ga^{3+} is often limited due its strong tendency to hydrolyse in aqueous conditions. The precipitation of Ga(OH)$_3$ is reported to occur at a pH as low as 3.3.[156] Such a low pH is often not necessary when producing radiotracers due to the nanomolar concentrations, however, until the Ga^{3+} is coordinated, reactions must remain under acidic conditions.[156]

Figure 1.13. The decay scheme of ^{68}Ga, data extracted from the Laboratoire National Henri Becquerel.[146]

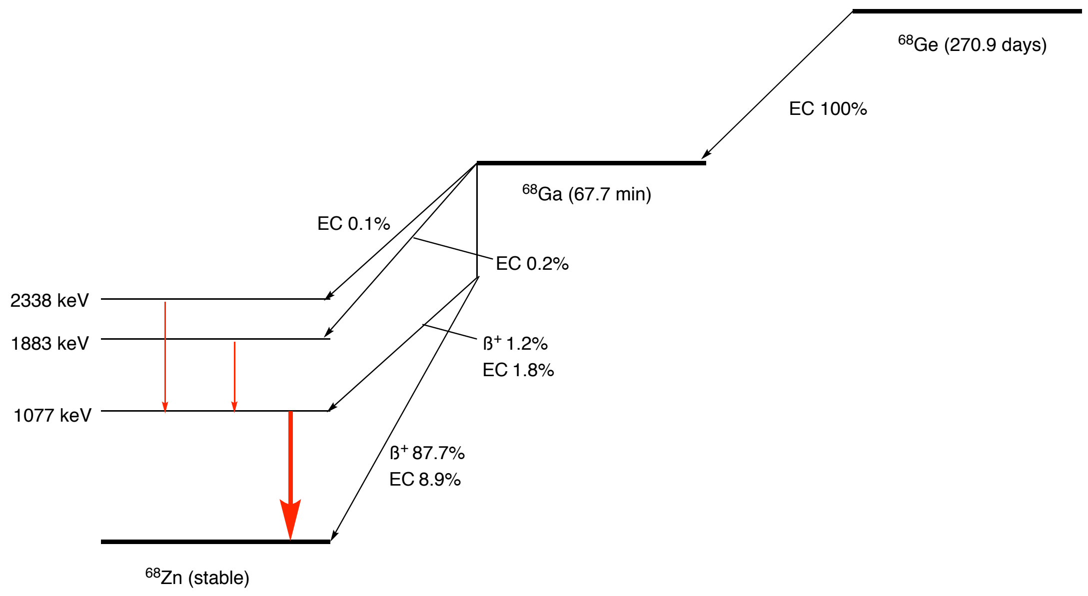

Zirconium-89

Compared with ^{68}Ga, the positron emitting radionuclide ^{89}Zr has a long half-life of 78.4 h. Whilst this may expose the patient to a prolonged radiation dose, it does allow for PET images to be taken at later time points, allowing larger biomolecules such as antibodies to circulate and accumulate in target tissue. The decay of ^{89}Zr results in a positron energy of 0.9 MeV. This relatively low energy improves image resolution compared with nuclides that emit higher energy positrons. As can be seen in the decay scheme in **Figure 1.14A**, 23% of decay is *via* $ß^+$ emission, whilst 77% is *via* electron capture. This decay is initially to a short-lived ^{89m}Y ($t_{1/2}$ = 15.6 s) species, before IT produces the ^{89}Y ground state releasing a γ-ray of 909 keV.[157] Due to release of the high energy, highly penetrating γ-rays in almost 100% of the decay pathways, increased shielding for transport and handling is required to work with ^{89}Zr safely. It may also limit the dose which can be given to patients. As only 23% of decay events result in positron emission this may cause problems as higher doses may be required, however, this could potentially be overcome by using longer scan acquisition times.[158] ^{89}Zr is produced by using a cyclotron, coupled with either a ^{89}Y(p,n)^{89}Zr or ^{89}Y(d,2n)^{89}Zr reaction. Fortunately, the metal target ^{89}Y is 100% naturally abundant, is commercially available and is inexpensive when compared with other target materials such as enriched ^{64}Ni (used in the production of ^{64}Cu, *vide infra*). Typically, ^{89}Y(p,n)^{89}Zr produces higher yields, however, both reactions produce several radioactive impurities such as ^{88}Zr which has a half-life of 83.4 days. Purification is usually achieved by using a hydroxamate resin column with oxalic acid as the eluent where the suspected isolated species is $[^{89}\text{Zr}][\text{Zr(oxalate)}_4]^{4-}$. The oxalate can then be converted to the chloride by using an anion exchange column to produce $ZrCl_4$.[159,160]

Figure 1.14. (A) The decay scheme of ^{89}Zr, data extracted from the Laboratoire National Henri Becquerel.[157] **(B)** Complexation of $^{89}Zr^{4+}$ with DFO with the calculated structure. Reproduced with permission from J. P. Holland.[161]

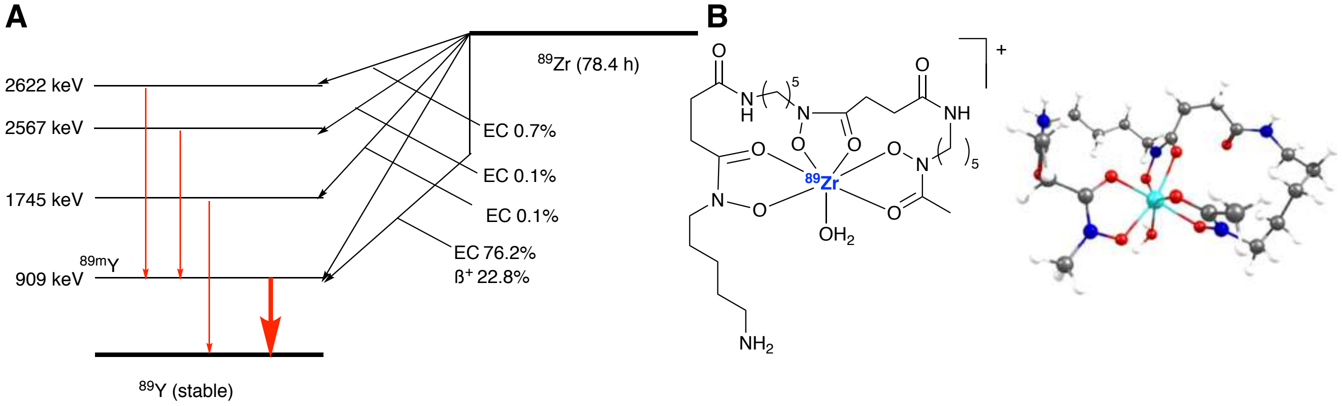

Due to the long half-life of ^{89}Zr, its main application in imaging is immuno-PET. As Zr^{4+} displays low affinity for non-specific binding to protein, chelates are conjugated to the antibody (or protein targeting vectors) prior to ^{89}Zr labelling. The chelate must provide high thermodynamic and kinetic stability *in vivo* whilst also facilitating high radiochemical yields. Similar to Ga^{3+}, Zr^{4+} is a hard Lewis acid, and therefore, the chemistry is dominated by the binding of oxygen, nitrogen and anionic ligands. With its relatively large ionic radius (87 pm) and empty d-orbitals ([Kr]d^0), Zr^{4+} exhibits coordination numbers from 6 through to 8.[161,162] DFO is a common chelate for Zr^{4+}.[163] DFT calculations show the most stable mode of binding is coordination through the hydroxamate groups with one H_2O molecule coordinating in an axial position to form a 7-coordinate complex (**Figure 14B**).[161]

Copper-64

PET imaging with ^{64}Cu provides high resolution images due to the low energy of the emitted positrons (E_{max} = 0.65 MeV). Its half-life of 12.7 h means that it may decay substantially before an antibody clears sufficiently from the blood pool and accumulates at its target. However, this half-life is ideal for smaller molecules such as peptides. ^{64}Cu is an interesting nuclide because of its multiple decay modes (**Figure 1.15**). ^{64}Cu can be described as a potential theranostic radionuclide; $ß^+$ decay provides PET capabilities whilst $ß^-$ decay and EC (and associated emission of Augur electrons) offer therapeutic potential.[164] Similarly to ^{89}Zr, ^{64}Cu is also cyclotron produced, most often by the ^{64}Ni(p,n)^{64}Cu transmutation reaction. Unlike other radionuclides discussed above, (e.g. $^{68}Ga^{3+}$) copper is readily reduced under acidic conditions. It is also a softer Lewis acid and can form complexes with chelates bearing softer N and S donor atoms. To make use of the versatile properties of ^{64}Cu, diacetyl-2,3-*bis*(N^4-methyl-3-thiosemicarbazone) (ATSM) is often used as a chelate to deploy the nuclides potential theranostic properties.[165] It is a tetradentate ligand binding to the ^{64}Cu(II) centre *via* the thiosemicarbazide groups.[166] On entry into a hypoxic cancer cell (acidic conditions) the ^{64}Cu(II) centre is reduced to ^{64}Cu(I). The [^{64}Cu(I)-ATSM]$^-$ complex is not stable in the cell and dissociates by a proton-mediated pathway, trapping the ^{64}Cu(I) in the cell and allowing potential imaging and therapeutic action.[167,168]

Figure 1.15. The decay scheme of ^{64}Cu, data extracted from the Laboratoire National Henri Becquerel.[169]

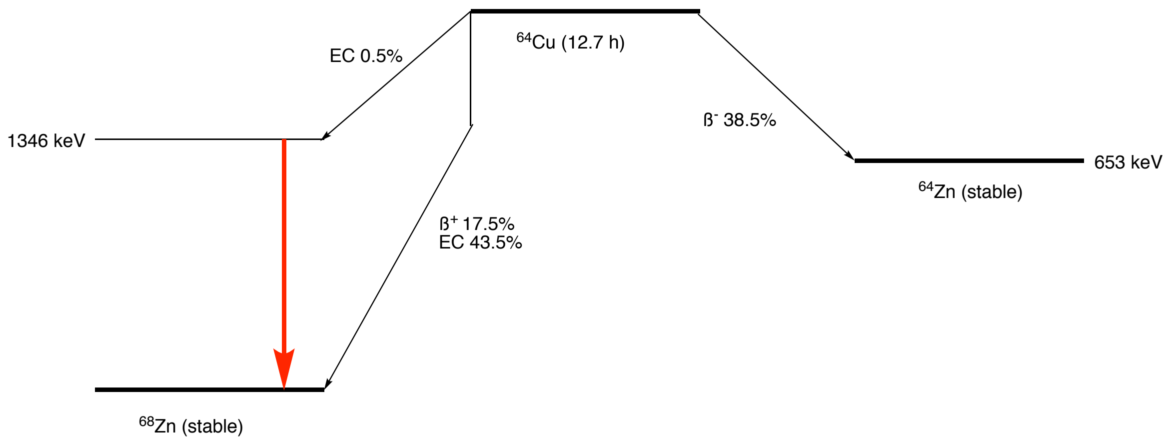

Indium-111

^{111}In decays 100% by EC to a ^{111m}Cd excited state level (417 keV), this then decays *via* a two-step γ-emission (E_1 =171 keV, E_2 =245 keV).[170] As there is no positron emission, ^{111}In cannot be used in PET imaging. However, after ^{99m}Tc it is the second most commonly used radioisotope in SPECT imaging. Unlike ^{99m}Tc, ^{111}In must be produced by using a cyclotron, nevertheless it is popular in the clinic due to its long half-life ($t_{1/2}$ = 67.32 h). This half-life makes ^{111}In ideal to conjugate to antibodies for use in immuno-SPECT.

^{111}In is stable in aqueous conditions in a +3 oxidation state. As a hard metal ion, chelates that contain hard donor atoms show greater stability. 1,4,7,10-tetraazacyclododecane-1,4,7,10-tetraacetic acid (DOTA) and diethylenetriaminepentaacetic acid (DTPA) are commonly used to complex ^{111}In^{3+} ions. Whilst the macrocycle DOTA may provide improved thermodynamic stability, heat is required to form the complex which may be problematic when working with heat sensitive constructs, such as mAbs. Therefore, DTPA is often used preferentially. Also, similar to ^{68}Ga^{3+}, ^{111}In^{3+} ions are prone to hydrolysis and radiolabelling reaction must be carried out under acidic conditions to avoid the formation of insoluble In(OH)$_3$.[171,172]

Figure 1.16. The decay scheme of ^{111}In, data extracted from the Laboratoire National Henri Becquerel.[170]

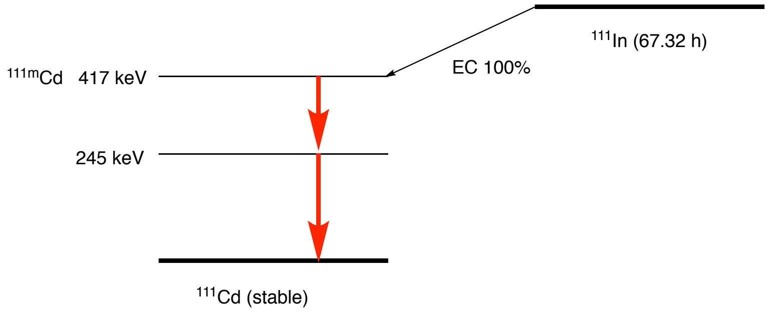

Selection of radionuclide

Table 1.3 shows the properties of commonly used PET radionuclides. Here, the listed properties are key when determining which nuclide should be incorporated into the radiotracer. Firstly, the half-life should be appropriate for the circulation time of the radiotracer, whilst minimising exposure of the patient to radioactivity. Therefore, longer circulating constructs such as radiolabelled antibodies require longer-lived nuclides such as ^{89}Zr ($t_{1/2}$ = 78.4 h), whilst agents with faster PK profiles such as many small-molecules or peptides should ideally be radiolabelled with radionuclides such as ^{11}C ($t_{1/2}$ = 20.4 min), ^{18}F or ^{68}Ga. Second, it is important to consider the abundance of $ß^+$ decay. High branching ratios of $ß^+$ decay allow a lower effective dose to be administered and reduce the exposure of patient to other forms of decay. Third, it is important to consider the energy associated with emitted $ß^+$. High energy $ß^+$ travel a further distance before annihilation. Therefore, those radionuclides with a larger $ß^+$ range generally result in low resolution PET images. Finally, the chemistries of the radionuclide must be considered. Metalloradionuclides can be beneficial because they can usually form metal-chelate complexes quickly and in mild conditions. That said, radionuclides such as ^{11}C form covalent bonds with the radiotracer providing stability, however, they may require a more complicated synthesis with harsher conditions. Overall, a radionuclide should be selected based on the ease of radiotracer synthesis, compatibility of decay properties and availability.

Table 1.3. Radionuclides commonly used in PET imaging and their characteristics (R_{max} and R_{min} refer to the $ß^+$ range in water). Data extracted from Conti *et al*.[173]

Radionuclide	Half-life / min	Major $ß^+$ Branch / %	E_{max} / MeV	E_{mean} / MeV	R_{max} / mm	R_{min} / mm	Production
^{68}Ga	67.8	87.7	1.90	0.84	9.2	3.3	Generator
^{89}Zr	4704	22.7	0.90	0.40	3.8	1.3	Cyclotron
^{64}Cu	762	17.5	0.65	0.28	2.5	0.7	Cyclotron
^{11}C	20.4	99.8	0.96	0.39	4.2	1.2	Cyclotron
^{18}F	110	96.9	0.63	0.25	2.4	0.6	Cyclotron

1.5 Nanotechnology in medicine

In 1959, Richard Feynman delivered a lecture titled, 'There's Plenty of Room at the Bottom' which was an introduction to what we now call nanotechnology.[174] Whilst there is no unique universally accepted definition of nanotechnology, it can be broadly defined as, '*the manipulation and study of materials at the molecular and atomic level between the dimensions of 1-100 nm*'.[175] At this scale, the properties of matter can differ from both the bulk materials and single atoms or molecules.[175] Nanotechnology is truly an interdisciplinary field; from materials science and physics, to mechanical engineering and chemistry.[176] The materials produced are incredibly versatile with unique characteristics such as interesting optical, magnetic and electrical properties. This versatility results in nanotechnology being used in several different applications across a wide range of industries, including medicine. Here, we use the term nanomedicine which refers to the use of nanomaterials in therapeutic or diagnostic applications.[177] A large proportion of these applications are based in the field of oncology and include the use of nanomaterials as tumour targeted drug delivery vehicles, imaging agents and heat therapy vectors.[178,179]

Nanoparticles possess a variety of intrinsic properties which make them suitable for potential use in the diagnosis or therapy of cancer. For example, some iron oxide nanoparticles are superparamagnetic and can alter T_2 relaxation times in MR imaging.[180] Gold nanoparticles exhibit surface plasmon resonance allowing photothemal therapy.[181] Nanoparticles can also act as scaffolds for drug molecules, targeting vectors or imaging moieties. For example, nanoparticles can be radiolabelled with ^{89}Zr for PET imaging, or loaded with cisplatin for chemotherapy treatment.[182,183] However, nanomaterials are challenging materials to work with. The complexity of constructs often leads to problems with complete and thorough characterisation, batch-to-batch reproducibility and stability. That said, overall, nanomaterials are versatile, adaptable materials with a range of intrinsic properties and functionalisation options. This allows scientists to create multi-modal nanomaterials which can be used simultaneously in multiple applications. This thesis will focus on nanomaterials as multi-modal PET imaging agents; specifically, PET/MR imaging agents and theranostic agents for use in PET imaging.

1.5.1 Design of nanomaterials as multi-modal PET imaging agents

Properties influencing circulation times *in vivo*

Figure 1.17. Summary of properties which effect the biocompatibility and circulation abilities of nanoparticles.[184] Scale bars are estimated and not to scale.

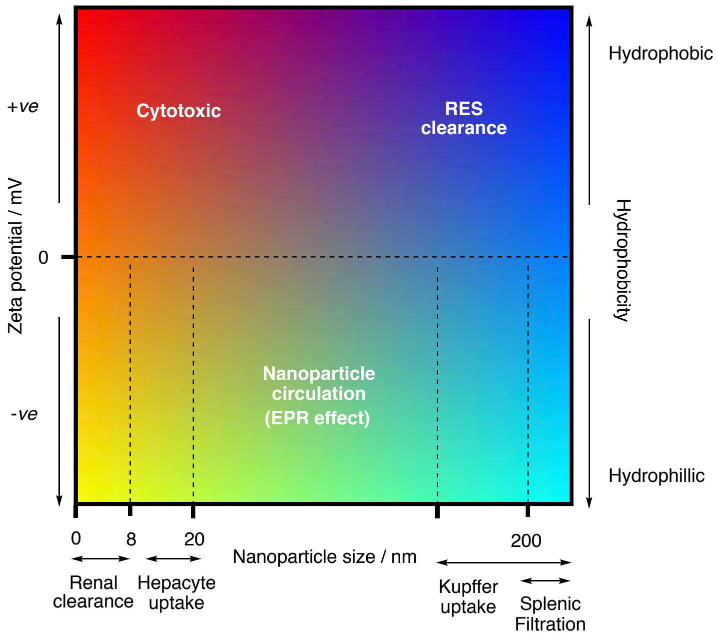

A major challenge in the development of nanomedicines is the delivery of the nanomaterial to the tumour. A nanoparticle may exhibit favourable properties *in vitro* but this is redundant if the particles are unable to circulate *in vivo*. The circulation time of a nanoparticle is largely determined by: (*i*) the size, (*ii*) the surface charge of the particle, also known as the zeta-(ζ-)potential, and (*iii*) the hydrophobicity (or solubility).[184]

The size of nanomaterials is fundamental to their use in nanomedicine. Particles at the nanoscale exhibit a surface area which is orders of magnitude larger than the bulk material. Not only does this give some nanoparticles interesting magnetic and electronic properties, but it also provides more sites for functionalisation. It follows that the smaller the nanoparticle, the greater the nanoparticle surface area and the greater the loading capacity of the particle. However, if particles are too small they are unable to circulate for a significant length of time as particles smaller than 8 nm are excreted rapidly *via* the renal system.[185] On the other hand, larger particles are sequestered and excreted by the hepatic system. Splenic filtration removes particles larger than 200 nm whilst Kupffer cells located in the liver rapidly take up nanoparticles greater then 150 nm in diameter. Smaller particles escape uptake by Kupffer cells by diffusion out of the sinusoids through the fenestrae. Here, the smaller nanoparticles then reach the hepatocytes, which rapidly phagocytise particles with a diameter between 10-20 nm.[186,187] This complex filtration system of the liver has a detrimental effect on nanoparticle circulation. It tends to be unavoidable with 30-99% of injected nanoparticles sequestering in the liver.[188] By careful control of nanoparticle size this sequestering effect can be minimised.

The thin layer of aqueous ions surrounding a charged nanoparticle is referred to as the electrical double layer (EDL) (**Figure 1.18**). As the name implies, the EDL comprises of two layers, with the first being known as the Stern layer. Here, nanoparticles with a net charge will have a layer of ions of the opposite charge tightly bound to the surface. The second, more diffuse layer is then found. This has the same charge as the nanoparticle surface and is known as the slipping layer where exchange with the bulk takes place. The ζ-potential is the electrostatic potential of the slipping plane. For nanoparticles to be stable in solution, ζ-potential values should be greater than ±30 mV. At these values the electrostatic repulsion is high enough to prevent aggregation.[189,190] However, the surface charge of the nanoparticles is not only significant for particle stability, but also affects the fate of the nanoparticles *in vivo*. Particles with a positive ζ-potential are more likely to induce aggregation of platelets and cause haemolysis.[191] To avoid these cytotoxic effects, anionic nanoparticles with a ζ-potential >30 mV should be used, which promotes circulation and prevents aggregation.[184,185]

Figure 1.18. Depiction of the EDL solvating nanoparticles.[192]

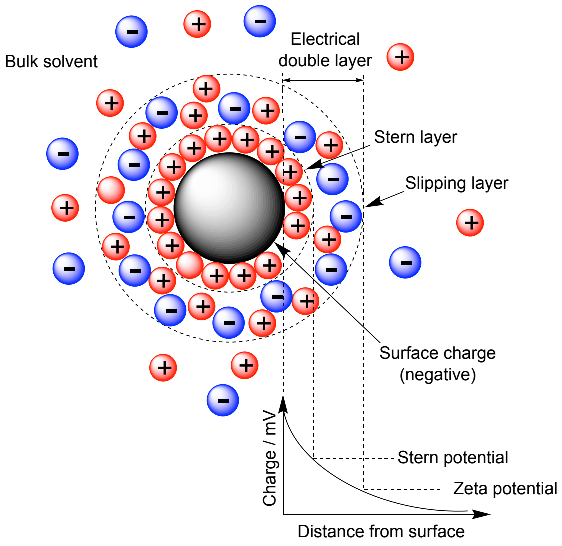

The final characteristic which is important to biocompatibility and circulation is the hydrophobicity of the nanoparticles. Hydrophobic nanoparticles are rapidly removed from the bloodstream by cellular components of the reticuloendothelial system (RES) (*i.e.* ingested by the macrophage system).[193] However, uptake into tumour sites relies on prolonged circulation times, therefore, hydrophilic coatings, such as polyethylene glycol (PEG) or dextran sugars are used. PEG aids dispersion of the nanoparticles in the bloodstream and lowers the

ζ-potential decreasing the cytotoxicity of the nanoparticle.[184,185] **Figure 1.17** (*vide supra*) summaries how the properties above influence the circulation of the nanoparticles *in vivo*. Overall, the system is complicated and it is difficult to obtain nanoparticles that possess sufficient circulation times. However, if nanoparticles are anionic, hydrophilic and between the sizes of 20 to 150 nm there is an increased possibility of an extended blood pool half-life. This longer circulation time may allow a nanoparticle to accumulate in a tumour *via* non-specific or specific uptake.

Tumour uptake of nanoparticles

Often nanoparticles exhibit tumour uptake because of the enhanced permeability and retention (EPR) effect.[194] Due to the rapid proliferation of cancer cells, blood vessels in tumours are irregular. They lack the detailed branching that leads from large vessels to smaller capillaries which results in abnormal vessel structure with large pores. The growth of the cancer cells also compresses lymphatic vessels, consequently, the only functional lymphatic drainage occurs at the periphery of the tumour. Nanoparticles can extravasate through the large vessel pores into the tumour and the lack of lymphatic drainage leads to their increased retention, which is the basis of the EPR effect.[195] Whilst nanoparticles can be designed to achieve EPR driven uptake, this phenomenon does not target a specific biomarker. By incorporating a biological targeting vector into the nanoparticle structure, nanoparticles can be specifically targeted towards a biomarker, giving nanoparticles the potential to be used in molecular imaging.

Radiolabelling methods

There are a number of restrictions and requirements that should be considered when radiolabelling nanomaterials for PET imaging. Due to the short-lived nature of several radionuclides used in nuclear medicine, radiolabelling will ideally be fast and carried out in the final step of the synthesis. This ensures an optimal amount of radioactivity is present for administration into the patient. The radiolabelling should also minimise changes to the physical, chemical, or biologic properties of the nanoparticles to prevent changes in stability of the nanoparticles which could result in aggregation. Radiolabelling should also avoid alterations in the specific binding to the biological target and changes in the pharmacokinetics of the nanoparticles *in vivo*. Reaction conditions will also ideally be mild and at physiological pH. This will avoid exposing nanomaterials to conditions which may cause aggregation or a change in the oxidation state of metal ions. Finally, the radiolabelling method should provide a stable product to avoid loss of activity from the construct *in vivo*, which may produce false images which would be detrimental to the diagnosis of disease.[192,196]

Currently, there are a number of different methods used for radiolabelling of nanomaterials. In 2018, we published a review detailing current radiolabelling methods for multimodal nuclear imaging agents.[192] Here, we divided radiolabelling methods into two categories; classical and non-classical methods (**Table 1.4**).

Classical radiolabelling methods use a chelate or prosthetic group to radiolabel the nanoparticle. The surface of the particle is modified directly. **Figure 1.19A** shows examples of this type of radiolabelling using thiol-mediated binding to gold nanoparticles, silylation of surface hydroxyls, and bisphosphonate binding to iron oxide particles.[192,197,198] Similarly, the coating of the nanoparticle can be modified to attach a chelate or prosthetic group to the coating of the nanoparticle by a covalent bond. For example, the carboxymethyl dextran coating of the Food and Drug Administration (FDA) approved iron oxide nanoparticle Feraheme can be modified with DFO for ^{89}Zr labelling (**Figure 1.19B**).[199] The advantages and disadvantages of classical radiolabelling are summarised in **Table 1.4**.

Figure 1.19. Classical radiolabelling methods. **(A)** Particle surface modification **(B)** Particle coating modification. Modified from Lamb *et al. J. Nucl. Med.,* 2018*, **59**,* 382-390 (awarded the Alavi-Mandell prize 2019).[192]

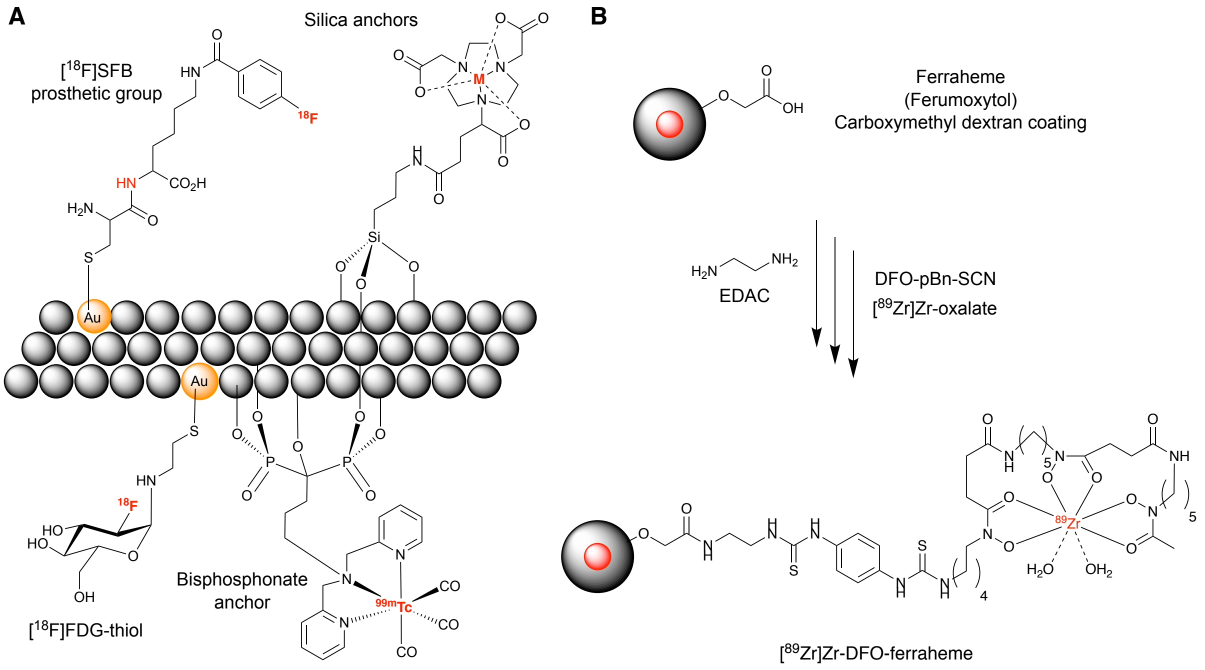

Table 1.4. Non-classical and classical nanoparticle radiolabelling methods.

Radiolabelling method	Advantages	Disadvantages
Classical radiolabelling methods ○ Particle surface modification ○ Particle coating modification	○ Covalent attachment of anchoring groups to the nanoparticle provides kinetic and thermodynamic stability. ○ The radionuclide is either covalently bound to a prosthetic group or tightly bound in a multi-dentate ligand, this providing further stability. ○ High stability ensures activity remains associated with nanomaterial *in vivo*. ○ Radiolabelling of chelate can be achieved prior to nanoparticle conjugation, this can minimise the exposure of the nanoparticles to harsh reaction conditions.	○ Can often require a multi-step radiolabelling reaction producing lower specific activities and radiochemical yields. ○ Addition of a lipophilic prosthetic groups or chelate can have adverse effects on toxicity and/or the pharmacokinetic profile by altering the surface charge of the nanoparticles. ○ May reduce the specific binding of the nanoparticle to its biological target.
Non-classical radiolabelling methods ○ Radiochemical doping ○ Physisorption ○ Direct chemisorption ○ Isotope exchange ○ Cation exchange ○ Particle beam/reactor activation ○ Cavity encapsulation	○ Generally, does not affect the physical and biochemical properties of the nanoparticles. Avoiding the use of bulky groups during radiolabelling has minimal effects on the stability of nanoparticles, preventing aggregation. It also prevents the change in the pharmacokinetic properties *in vivo*. ○ Methods are versatile. For example, they are not reliant on the coordination chemistry of the radionuclide. ○ Often only requires a single step, radiolabelling reaction. This provides increased radiochemical yields and specific activities.	○ Lack of chelate/covalent bonds may result in lower kinetic and thermodynamic stability. ○ The exact chemical nature of many intrinsic radiolabelling methods are not fully understood.

Non-classical radiolabelling methods do not require a chelate or prosthetic group. This is often referred to as the intrinsic radiolabelling of a nanomaterial. Non-classical radiolabelling methods are illustrated in **Figure 1.20** with the general advantages and disadvantages summarised in **Table 1.4** (*vide supra*). Earlier methods of intrinsic radiolabelling of nanoparticles often relied on radiochemical doping. This involved the addition of 'hot-plus-cold' precursors, where small amounts of radionuclide are added during particle fabrication.[200] The method is based on protocols defined in the Fajans-Paneth-Hahm law of radioactive coprecipitation (as described in Otto Hahn's 1936 work, *Applied Radiochemistry*).[201] The law describes the coprecipitation of a radioactive element in the presence of larger amounts of carrier metal, producing nanoparticles where the radionuclide resides either within the crystal lattice or on the surface of the nanoparticle. This method has been widely established producing doped nanoparticles using a number of radiotracers including, ^{64}Cu, ^{65}Zn, ^{68}Ga, ^{111}In, ^{141}Ce, ^{153}Sm and ^{198}Au.[202–212]

More recently, a new method for nanoparticle radiolabelling has emerged.[213–217] It involves the direct chemisorption of the radionuclide onto the nanoparticle surface. This phenomenon was first reported in 2013. Following early reports of the uptake of arsenic ions onto iron oxide surfaces, Chen *et al.* studied the uptake of As^{3+} and As^{5+} onto the surface of magnetite (Fe_3O_4) to produce *As-SPIONs (where * = 71, 72, 74, 76).[213,223] Since this initial report, the chemisorption technique has been used with a number of different radionuclides and nanoparticles.[214–222] A detailed description of the literature and the chemical nature of the chemisorption of radionuclides will be presented Chapter 2.

Figure 1.20. Summary of non-classical nanoparticle radiolabelling methods. Reproduced from Lamb *et al.*[192]

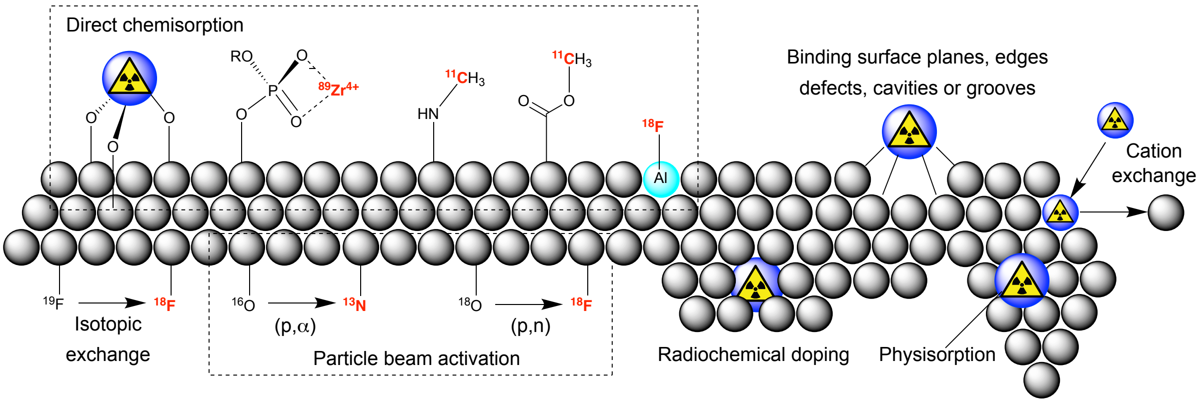

1.6 Nanomaterials as PET/MRI agents

As discussed in section 2.2.3, the introduction of PET/MRI technology led to an increased research focus on the development multi-modal imaging agents. Administering one multifunctional tracer gives an indication that the same target is being imaged as opposed to simultaneously administering two tracers that exhibit differential PK profiles. Nanomaterials are good candidates when designing PET/MRI agents as they offer a platform to create, multifunctional, multi-component structures.

1.6.1 Inorganic nanoparticles as PET/MRI agents

A large number of different nanomaterials are used to create PET/MRI agents; however, the field is largely dominated by inorganic nanoparticles. Inorganic nanoparticles used as PET/MR agents are usually inherently MR active and they are then radiolabelled with a positron-emitting radionuclide.

SPIONs

Superparamagnetic iron oxide nanoparticles (SPIONs) are the most commonly used materials used in the construction of PET/MR imaging agents. As introduced in **Section 1.3.2**, SPION coatings can have adverse effects on the T_2 relaxation properties on the nanoparticles. However, coatings are often necessary to ensure biocompatibility of the nanoparticle. To avoid biocompatibility problems, some research has focused on modifying clinically approved particles. This limits any cytotoxic effects and simplifies the process of good manufacturing practice (GMP) quality control tests. Feraheme (also known as Ferumoxytol) is a clinically approved drug for the treatment of anaemia, and is comprised of an iron oxide core with a polyglucose sorbitol carboxymethylether coating (a modified dextran). Thorek *et al*. modified these nanoparticles with DFO to chelate ^{89}Zr (**Figure 1.19B**), creating a radiolabelled tracer to target lymph node metastasis. Metastases in the lymph nodes are usually the initial indication of the spread of many cancers, and particularly prostate cancer. Current technology to obtain specimens from the lymph nodes relies on using SPECT imaging with ^{99m}Tc colloids, however, this does not provide anatomical information. By combining PET and MR capabilities ^{89}Zr-ferumoxytol overcomes the soft-tissue contrast problems and precisely delineates nodes in the axillary drainage models.[199] In a similar example, de Rosales *et al*. functionalised Endorem, a dextran coated SPION. Here, two dithiocarbamate bisphosphate ligands (dtcbp) were used, where the bisphosphonate anchors bind to the nanoparticle iron oxide surface and whilst two dithiocarbamate chelate ^{64}Cu. The [^{64}Cu][Cu(dtcbp)$_2$-Endorem] accumulates in the popliteal lymph nodes and this can then be imaged, the PET/MR provides spatial and anatomical information and also indicated that the construct is stable *in vivo*.[224]

Although using clinically approved nanoparticles as a starting point for constructing multi-modal imaging agents offers some advantages, synthesis of the particles provides enhanced freedom and control in the design. **Table 1.5** shows various synthetic methods used to produced SPIONs. In general, SPIONs should be designed in a way to provide a maximum magnetic moment to shorten T_2 relaxation times, whilst using a coating and size that provides biocompatibility and adequate circulation times. Previously highlighted examples (*vide supra*) rely on the non-specific delivery lymph nodes which allows biopsies to be taken to determine the presence of disease. However, they do not provide specific uptake directly into tumour sites. One of the earliest works to overcome these problems was published by Lee *et al.* in 2008.[225] Here they synthesised iron oxide nanoparticles with a core size of 5 nm which when coated with polyaspartic acid (PASP) obtained particles with a hydrodynamic diameter of 45 ± 10 nm. The resulting nanoparticles gave T_2 relaxation times comparable to Feridex, a clinical drug similar to Feraheme.[226] The PASP coating gave the nanoparticles a desirable ζ-potential of -50 mV and provided both carboxylate and amino groups to functionalise the nanoparticles. The chelate DOTA was conjugated to allow for ^{64}Cu labelling, along with cyclic arginine-glycine-aspartic (RGD) peptide which targets integrin $\alpha_V\beta_3$ positive tumours. The nanoparticle conjugates are reported to specifically bind to $\alpha_V\beta_3$ positive cell lines *in vitro*. During *in vivo* PET and MR imaging, non-targeted nanoparticles were found to accumulate in the $\alpha_V\beta_3$ positive tumour xenografts *via* the EPR effect. However, this uptake could be increased with the addition to the RGD targeting group. In small-animal PET imaging (**Figure 1.21**), an increased tumour uptake was observed when the targeting peptide is present on the nanoparticle surface. These results provide an encouraging precedent for the use of nanomaterials in PET/MR molecular imaging.[225]

Figure 1.21. Decay-corrected whole-body coronal PET images of nude mouse bearing human U87MG tumour at 21 h after injection of 3.7 MBq of **(A)** ^{64}Cu-DOTA-IO and **(B)** ^{64}Cu-DOTA-IO-RGD. This research was originally published in JNM. Lee et al., *J Nucl Med*, 2008, **49**, 1371-1379, copyright SNMMI .[225]

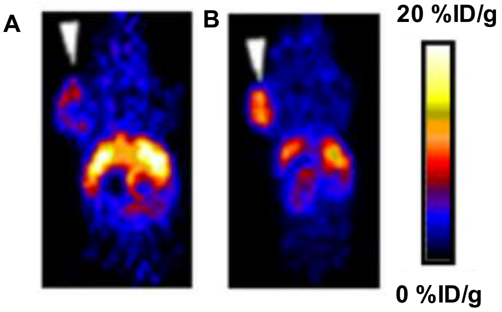

Following this early example, several SPIONS decorated with biological vectors and chelators were developed as potential PET/MRI agents.[227–231] A notable example from 2016 uses a Glu-NH-CO-NH-Lys derivative to target SPIONs towards tumour lines which overexpress PSMA. Radiolabelling with ^{68}Ga was achieved by conjugating a DOTA derivative to the nanoparticle coating which allowed PET imaging. PET and MR imaging in mouse models showed favourable uptake in 22Rv1 (PSMA +ve) cell line *versus* the PC-3 (PSMA -ve) cell line xenografts.[227]

Despite advances in the use of nanoparticles in PET/MR imaging, these examples all require the use of a chelate or prosthetic group to radiolabel. Although this provides thermodynamic and kinetic stability, the use of these classical radiolabelling methods often has disadvantages outlined in **Table 1.4**. Due to these disadvantages, it has become desirable to investigate chelate-free methods of radiolabelling nanoparticles, often referred to as intrinsic labelling. The intrinsic radiolabelling of SPIONs has been demonstrated by our group, here we reported the heat-induced chemisorption of ^{64}Cu, ^{111}In, and ^{89}Zr onto Feraheme.[183] Also, Burke *et al.* intrinsically radiolabelled iron oxide nanorods with ^{68}Ga to produce intrinsically radiolabelled potential PET/MRI agents.[232] However, to our knowledge, an intrinsic radiolabelled SPION bearing specific biological targeting vectors have not been reported. With the desire for molecular imaging to be used regularly during diagnosis and treatment of cancers, the development of such constructs will be advantageous to the field. Therefore, one of the aims of the thesis is to develop an intrinsic radiolabelled targeted SPION.

Manganese nanoparticles

Manganese is an interesting element when considering the design of PET/MR agents as it itself can be both PET and MR active. The isotopes ^{51}Mn, ^{52m}Mn and ^{52g}Mn all emit positrons during their decay hence can be used as PET agents. Whilst, Mn(II) is paramagnetic and enhances the longitudinal relaxation of surrounding protons, hence it is a T_1 contrast agent.[233] Therefore, Mn isotopes can be used directly for PET/MR applications. For example, Lewis *et al.* produce $^{52}MnCl_2$ which they co-inject alongside $^{nat}MnCl_2$ to reach the higher concentrations required for MR imaging.[234] Manganese nanoparticles are typically defined as MnO, MnO_2 or Mn_3O_4 and example of synthesis methods can be found in **Table 1.5**. Zhan *et al.* synthesised Mn_3O_4 particles coated with polyethyleneimine (PEI) and the chelate NOTA is conjugated to bind ^{64}Cu for PET functionality.[235] Mn_3O_4@PEG nanoparticles can also be intrinsically radiolabelled *via* the chemisorption of ^{89}Zr onto the nanoparticle surface.[236] This demonstrates the versatility of the chemisorption method of radiolabelling and indicates that an intrinsically radiolabelled, targeted manganese nanoparticle would be a viable option in the design of PET/MR imaging agents.

Gadolinium nanoparticles

Gadolinium oxide (Gd_2O_3) nanoparticles offer a platform in which to deliver high molecular weight compounds whilst offering a high concentration of Gd(III). However, due to the toxicity of the Gd(III), particles must remain stable to prevent leaching of the ions. Gd_2O_3 particles with a PEG coating have shown stability in physiological conditions and (when the diameter = 2.2 nm) exhibited longitudinal relaxivities over 2-fold that of Gd-DOTA.[237] Despite these favourable properties there are few examples of Gd_2O_3 used as potential PET/MR agents. However, Ai *et al*. attempted to create a multi-modal radiotracer by using intrinsically labelled Gd_2O_2S:Eu. The nanoparticles where synthesised and coated with PEG to improve biocompatibility. Radiolabelling then occurred *via* a chelate-free route with ^{89}Zr where a RCY ~75% was achieved. Whilst the particles are not specifically targeted, [^{89}Zr]Zr-Gd_2O_2S:Eu-PEG exhibits gamma ray-induced radioluminescence whilst the Gd(III) acts as a T_1-weighted MRI agent. Therefore, this particle is PET and MRI active whilst also having the potential to be used in radioluminescence imaging.[238]

Table 1.5. Examples of synthesis methods of inorganic oxide nanoparticles used in the construction of PET/MR imaging agents.

Particle Composition	Synthesis method	Size of bare nanoparticle / nm	Nanoparticle coating	Size of coated particle / nm
Iron oxide – magnetite (Fe_3O_4)	Co-precipitation[239]	12	-	-
	Microwave assisted synthesis (aqueous conditions)[240]	12 ± 2	Poly(sodium 4-styrenesulfonate) (PSSS)	13.4 ± 1.5
			Sodium polyphosphate (SPP)	10.1 ± 1.5
	Microwave assisted, high pressure, sol-gel (organic conditions)[241]	5.5 ± 0.9	-	-
	High-temperature[242]	-	Oleic acid and oleylamine	4
	Electrochemistry.[243]	7.6	Poly(vinylpyrrolidone) (PVP) and polyethyleneimine (PEI)	9.2
	Sono-precipitation[244]	-	3-aminopropyl-triethoxysilane (APTES)	11.6
Manganese oxide - MnO	High-temperature, sol-gel [245]	37	PET	
	Thermal decomposition[246]	-	PET	
	Microwave, polyol[247]	-	Poly(acrylic acid) (PAA) and PVP	10
Gadolinium oxide - Gd_2O_3	Colloidal precipitation[248]	2-5	-	-
	Colloidal precipitation followed by mediated seed growth[237]	4.6	Polysiloxane shell	6

1.6.2 Organic nanoparticles as PET/MR imaging agents

Whilst organic based nanomaterials used as potential PET/MRI agents are not intrinsically MR active, they facilitate the combination of radionuclides and MR active structures.

Liposomes

Liposomes are spherical-like structures constructed from phospholipids that self-assemble to form bilayers. Liposomes are versatile structures, and by altering the lipids used in the synthesis they can range in size (30 nm to 2.5 µm), surface charge, fluidity of bilayer, and assembly conditions. They are biocompatible and can both encapsulate materials or incorporate compounds onto the surface by the modification of the phospholipids.[249] For this reason they have become a focal point in the design of multi-modal PET/MR imaging constructs. Previous work has seen the encapsulation of maghemite SPIONs with the phospholipid heads modified with a NODAGA chelate for ^{68}Ga radiolabelling and FDG for cancer cell targeting.[250] However, this approach produced liposomes with a diameter of 100-300 nm and although PEG was used to try to avoid liver uptake, *in vivo* images showed high accumulation in the hepatic system with little tumour uptake.[250] Abou *et al.* offered a different approach which allowed the intrinsic radiolabelling of the liposomes. ^{89}Zr was added during the formation of the liposomes, this caused the $^{89}Zr^{4+}$ to coordinate to the phosphate groups on the phospholipid heads in the bilayer whilst the constructs were targeted towards neuroendocrine tumours *via* human somatostatin receptor subtype 2 (SSTr2).[251]

Dendrimers

Dendrimers are macromolecules at the nanometre scale. They tend to be comprised of an organic framework that consists of a number of structures branching out from a central core. The elaborate branching structure provides a platform for chemically modification in a variety of ways. Therefore, dendrimers can be multi-functionalised to form multi-modal nanomedicines.[252] Li *et al*. produce a porphyrin based dendrimer to produce a multi-functional material. The nanoporphyrin combines PET and MRI functionalities, and can also be used to integrate a number of different functions including, near-infrared fluorescent imaging, photothermal therapy (PTT), photodynamic therapy (PDT) and targeted drug delivery. The PET/MRI capabilities originated from the structures intrinsic ability to bind ^{64}Cu(II) and Gd(III). The metals ions bind within the structure which consists of linear polyethylene glycol (PEG) and dendritic oligomers of a porphyrin analogue and cholic acid. Whilst no targeting vector is present, a significant amount of tumour uptake was observed for dendrimers which were cross linked with additional cysteine groups. This brought the size of the nanoparticles to approximately 32 nm which allowed for longer circulation times resulting in enhanced tumour uptake.[253]

Nano-sized carbon allotropes

Graphene

Graphene based nanomaterials have become increasingly popular in recent years in the field of nanomedicine. Aside from pristine graphene, graphene oxides (GO) and reduced graphene oxides (rGO) are commonly used in the design of a multi-modal agent. Covalent modification of pristine graphene is often chemically challenging; disrupting the delocalised network is highly thermodynamically unfavourable whilst steric hindrance arises from the lattice deformation that occurs following hybridisation of a carbon atom from sp^2 to sp^3.[254] Therefore, the presence of oxygen containing groups in rGO and GO offers sites for modification, and also improve the hydrophilicity of the constructs. Shi *et al.* took advantage of this method to modify rGO with polyethylene glycol (PEG), a tumour targeting antibody (anti-CD105 antibody TRC105) and the ^{64}Cu chelator NOTA, creating a potential positron emission tomography (PET) imaging agent.[255] Similarly, an elegant example of chelate-free labelling saw the direct radiolabelling on the GO surface with ^{18}F replacing oxygen atoms *via* a cyclotron induced $^{18}O(p,n)^{18}F$ reaction.[256] In spite of significant tumour uptake, these examples do not demonstrate multimodal PET/MRI capabilities. In a rare example, Xu *et al.*, synthesised an iron oxide nanoparticles-rGO conjugate. This was then modified with NOTA (which was radiolabelled with ^{64}Cu) on the perimeter of the first PEG shell, which was further modified with the addition of a second PEG shell. This second PEG shell helped to prevent non-specific interactions between graphene nanostructures and proteins. This allowed longer circulation times *in vivo.* An elimination half-life of 27.7 h provided adequate time for tumour uptake *via* the EPR effect. This can be observed in both the PET and MRI images (**Figure 1.22**).[257] Despite successful tumour uptake, this binding is not specific. During this thesis, work was carried out on functionalisation and tumour-targeting of graphene nanoflakes for potential use in PET/MR imaging (**Chapter 5**).

Figure 1.22. (A) Serial coronal PET images of 4T1 tumour-bearing mice at different time points post-injection of ^{64}Cu-NOTA–RGO–IONP–^{1st}PEG–^{2nd}PEG. Tumours are indicated by yellow arrowheads. **(B)** T_2-mapped MR images acquired pre-injection at 3 h and 24 h time points following intravenous injection of NOTA-RGO-IONP-^{1st}PEG-^{2nd}PEG. Image reproduced from Xu *et al.*, *Nanoscale*, 2016, **8**, 12683–12692, with permission from The Royal Society of Chemistry.[257]

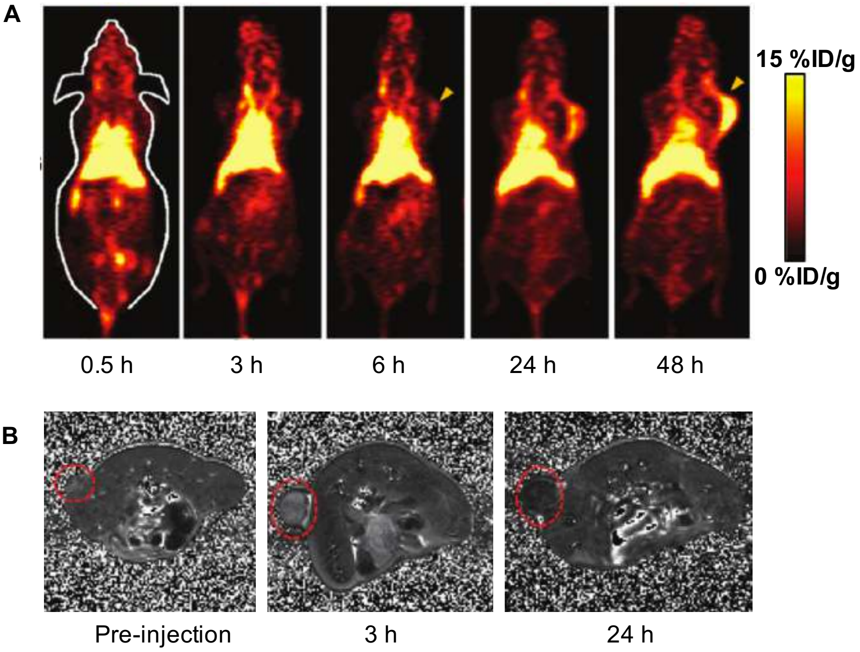

Carbon nanotubes

In a different approach, Cisneros *et. al.* used carbon nanotubes to synthesise potential PET/MRI agents.[258] Nanotubes have the ability to encapsulate materials within the tube cavity, hence the experiment focused on the encapsulation of Gd(III) and ^{64}Cu into ultra-short single-walled carbon nanotubes (US-SWCNTs). Gd(III) and ^{64}Cu where loaded into US-SWCNTs *via* sonication and dispersed in solution using a surfactant. Stability tests indicated no significant leakage of Gd(III) or ^{64}Cu over 7 days. PET images in mice indicated uptake in the liver and lungs, and it was speculated that this accumulation arises due to interactions with surfactant peptides in the lungs. T_1 studies of non-radioactive Cu-Gd-US-SWCNT gave relaxivity values of 52.7 mM^{-1} s^{-1} which is greater than the r_1 value of the clinically used Magnevist proving the real potential of the nanotubes. The undesirable property of these nanotubes is their poor aqueous solubility so it is not possible to administer the drug *in vivo* at a concentration sufficient to obtain a MRI contrast image. Future research in this area should focus on the dispersion of the compounds into water to exploit their full potential as PET/MRI agents.

Nanodiamonds

Despite the flexibility that comes with the use of carbon nanotubes as multi-modal imaging agents some research has suggested significant cytotoxicity of the materials due to their ability to accelerate oxidative stress and alter the morphology of cells.[259] Nanodiamonds are promising materials as biocompatibility has been proven.[260] Whilst PET/MR nanodiamond agents have yet to be developed, carboxylated nanodiamonds have been conjugated to a Gd-DOTA derivative to produce constructs which provide T_1 contrast for stand-alone MRI.[261] Nanodiamonds have also been functionalised with a ^{18}F prosthetic group for potential PET imaging.[262]

Fullerenes

Finally, fullerenes have potential to be used as nano-sized carbon allotropes in PET/MRI. Fullerenes are carbon spheres, forming cage-like structures that can be directly modified or encapsulate materials. Luo *et al*. encased Gd_3N into a C_{80} cage to provide MRI activity. The cage was then oxidised and the radiolabelled with the positron emitting ^{124}I, with the iodo-group attaching directly to the cage in the ortho-position relative to the formed hydroxyl group. This produced a water soluble fullerene for PET/MR imaging.[263] Whilst this is one of the few examples involving fullerenes as PET/MRI agents it highlights the potential of these materials.

1.6.3 Outlook for the development of nanomaterials as PET/MRI agents

The development of nanomaterials as PET/MR imaging agents is relatively new field of research. However, this brief review of the literature demonstrates that growth has been both rapid and diverse, using a large range of different materials and radiolabelling methods. Despite this, with the introduction of molecular imaging, it has been more vital than ever to produce imaging agents which are specifically targeted. Therefore, this thesis will investigate a range of nanomaterial radiolabelling methods, both classical and non-classical, and combine this with the specific targeting of known cancer biomarkers.

1.7 Nanomaterials as theranostic PET agents

Theranostics combine both therapeutic and diagnostic capabilities into a single modularity. For this to be possible, a platform is needed which allows the linking of different components, and due to versatility of nanomaterials they are often the obvious choices when designing theranostic compounds. As before nanomaterials can be either be classically or non-classically radiolabelled providing the diagnostic, PET imaging capability. The therapeutic component can then be incorporated into the nanoparticles in different ways. Drug molecules can be loaded onto the nanoparticle *via* surface modification or encapsulation into their structures. Nanomaterials can also have therapeutic properties themselves making them ‘intrinsically therapeutic’.

1.7.1 Drug loaded nanomaterials

In the design of theranostic nanomaterials, a number of researchers have decorated the surface of the materials with drug molecules post nanomaterial synthesis. A simple example uses the modified dextran coating on SPIONs to covalently attach Quercetin *via* amide bond formation. Quercetin has chemotherapeutic properties and the resulting nanoparticles show anti-cancer properties *in vitro*. However, these particles have not been radiolabelled for PET imaging.[264] In a more sophisticated example, Chen *et al.* used electrostatic interactions to decorate silica nanoparticles with the anti-cancer drug doxorubicin (DOX).[265] As the nanoparticles are mesoporous, the drug molecules reside in the channels as well as the surface allowing for a greater loading capacity. Due to the nature of the electrostatic interactions between the SiO_2 particles and DOX, acidic conditions protonate the silanols in the nanoparticles and results in the dissociation of the drug. Therefore, as nanoparticles enter the acidic environment of cancer cells the drug is released and *ex vivo* tumour analysis showed that this was able to reduce tumour size. The nanoparticles were also radiolabelled with ^{64}Cu using the NOTA chelate and antibody targeted towards the CD105 biomarker which is over expressed in several cancer lines.[265] In a similar example, SPIONs have been loaded with DOX by incorporating the DOX molecules into the polymer coating. Particles have then been modified with a radiolabelled mAb to produce a therapeutic construct capable of PET/MRI imaging.[266]

Other nanomaterials encapsulate therapeutics into the core of their structure. Liposomes are particularly suitable materials for this as they can both encapsulate materials and withstand surface lipid modifications. Li *et al*. produce multifunctional theranostic material by loading DOX, therapeutic radionuclides ^{186}Re/^{188}Re and diagnostic ^{99m}Tc into the core of the liposomes. They also modified the lipid heads with fluorescent dyes and metal chelators to chelate Gd^{3+} and $^{64}Cu^{2+}$. This producing a final compound which is capable of diagnostic PET, SPECT and NIR imaging as well as therapeutic chemo- and radio- therapy.[267] Ferritin cages can also be used to encapsulate drug molecules (DOX) as well as radionuclides (^{64}Cu) demonstrating their potential as theranostic agents for PET imaging.[268,269]

1.7.2 'Intrinsically' therapeutic nanoparticles

Photodynamic therapy (PDT) relies on a photosensitiser (PS) which resides at the tumour site and then produces reactive oxygen species (ROS) following excitation using light of a particular wavelength. The ROS oxidise molecules within the cell, leading to cell death.[270] A large range of nanomaterials are used as PS carriers, such as mesoporous silica nanoparticles loaded with the PS chlorin e6 and radiolabelled with ^{64}Cu.[271] However, some nanomaterials are able to generate ROS by their own means. For example, fullerenes absorb light in the UV to visible region due to their conjugated π-system. Excitation of fullerenes forms the long-lived triplet state, which can generate ROS. Multi-modal fullerenes PS are able to combine this PDT capability with imaging moieties. Shi *et al.* conjugated iron oxide nanoparticles to the fullerene surface for PDT and MR imaging.[272] However, a similar construct towards PET imaging has not yet been developed. Whilst, nanomaterials capable of PDT have not yet been labelled with a positron emitting radionuclide, there is plenty of scope for this to be achieved. For example, cuprous oxide nanoparticles, carbon nanotubes, gold nanorods and titanium oxide nanoparticles are just some of the nanoparticles capable of PDT.[273–276]

Photothermal therapy (PTT) is another treatment option where nanomaterials are used. Light energy absorbed by nanoparticles, can be released as luminescence or heat. Following location of nanomaterials in the tumour site, laser light at a specified wavelength can be used to induce localised heating due to the presence of the nanomaterials. By combining this with PET imaging produces a theranostic agent where the location of laser light application can be determined from the obtained PET image.[277] Zhou *et al.* produced folic acid targeted CuS nanoparticles labelled with ^{64}Cu without the use of a chelate. This was achieved *via* the radiochemical doping method, where 'hot-plus-cold' $CuCl_2$ was used. *In vivo* and *in vitro* analysis indicated tumour uptake and thermal ablation on irradiation with a NIR laser.[278] In a final example, Cheng *et al*. develop a fully multi-functional theranostic platform combining gold nanospheres capable of PTT with mesoporous silica nanoparticles loaded with DOX. The complete construct is radiolabelled using a DOTA mediated ^{64}Cu labelling producing a PET imaging agent with chemo- and photothermal-therapeutic effects.[279]

1.8 Aims of Thesis

This thesis aims to explore the use of nanomaterials as multi-modal agents for use in PET imaging. Chapters 2 to 5 aim to investigate the synthesis, drug loading, biological targeting and radiolabelling of different nanoparticles. Some of these constructs are then investigated *in vitro* and *in vivo*.

Chapter 2 focuses on the synthesis and characterisation of iron oxide nanoparticles. A selection of iron oxide nanoparticles are synthesised or acquired and compared using various chemical and physical characterisation methods. The aim is to synthesise nanoparticles that are appropriately sized, offering potential circulation *in vivo* whilst shortening the T_2 relaxation times of surrounding protons. Following successful synthesis, nanoparticles must be coated appropriately to allow dispersion in aqueous solution. Again, the effects of nanoparticle coatings are evaluated *via* the characterisation of the products using size analysis, surface charge determination and relaxivity measurements. Once nanoparticles have been fully characterised, radiolabelling methods are investigated. Initially, chelate based methods are explored by utilising traditional gold-thiol interactions and investigating the photoconjugation of photo-activatable chelates to the surface. Following this, intrinsic, chelate-free radiolabelling methods are explored with various methods and kinetic parameters studied. In later chapters, these particles and radiolabelling techniques are used in application-based projects.

Chapter 3 uses iron oxide nanoparticles to create multi-modal agents for potential application in PET/MRI. By utilising the nanoparticles and radiolabelling methods established in Chapter 2, MRI active nanoparticles can be radiolabelled with $ß^+$ emitting radionuclides for PET imaging. Constructs are then targeted towards PSMA to aid the specific uptake of nanoparticles in prostate tumours.

Chapter 4 aims to produce a tumour-targeted theranostic agent by using a novel graphene-based nanomaterial. The nanomaterials are used as scaffolds to load drug molecules for therapeutic action and a chelate to bind a $ß^+$ emitting radionuclides. Similarly to Chapter 3, the constructs are targeted towards cancer cells using a small-molecule, PSMA binding vector. Despite successful results *in vitro*, *in vivo* analysis indicates poor tumour uptake due to rapid excretion. To avert poor pharmacokinetics, Chapter 5 explores the binding of antibodies to the graphene nanomaterials. Multi-modal graphene nanomaterials are constructed *via* the addition of gadolinium agents to shorten T_1 relaxation times whilst a secondary chelate binds $ß^+$ emitting radionuclides, this producing a PET/MRI agent. We aim to then bind the constructs to an antibody targeting a biomarker over-expressed in specific cancers. The overall goal is to produce a construct that accumulates in tumour tissue and provides contrast and visualisation in MR and PET imaging.

Chapter 2: Nanoparticle synthesis and radiolabelling

2.1 Aims of chapter

This chapter focuses on the fundamental chemistry of nanoparticle synthesis and radiolabelling. Multiple types of iron oxide nanoparticles are synthesised and characterised. Classical and non-classical radiolabelling methods are then explored.

2.2. Nanoparticle synthesis and characterisation

2.2.1 Introduction

Feraheme® (FH; ferumoxytol) is an FDA-approved iron oxide nanoparticle used in the treatment of anaemia. It is composed of a magnetite SPION core and a carbohydrate coating, polyglucose sorbitol carboxymethylether. Particles have an average chemical formula of $Fe_{5874}O_{8752}C_{11719}H_{18682}O_{9933}Na_{414}$ which implies a molecular weight of 796 kDa and an overall size of 17-31 nm.[280] Transmission electron microscopy (TEM) analysis of FH by Bullivant *et al.* found a core size diameter of < 5 nm.[281] This gives the nanoparticles favourable magnetic properties leading to a T_2 relaxivity (r_2) of 98.45 mM^{-1} s^{-1} showing the potential of the particles to be used as MRI contrast agents. Whilst the surface of FH can be modified to create multi-modal agents, we wanted to study a range of particles to investigate radiolabelling methods and biological applications.[199] Therefore, it was desirable to synthesise iron oxide nanoparticles with a range of coatings.

Table 5 seen in chapter 1, highlights some of the ways in which nanoparticles can be synthesised. An extensive review of the literature by Wu *et al.* indicates that the most successful methods are: co-precipitation, thermal decomposition, hydrothermal synthesis, microemulsion, and sonochemical synthesis.[282] These methods produce small, monodisperse particles. Whilst details on the complete synthesis of FH remain proprietary, the magnetite core is synthesised via the co-precipitation method followed by addition of the coating. This is a technique also utilised by our group. Co-precipitation is well-established as the conventional synthesis route and reports date back to 1981.[239] It involves the precipitation of ferric (Fe^{3+}) and ferrous (Fe^{2+}) ions in a 2:1 ratio in aqueous, basic conditions. The pH of the solution is then lowered and the mixture is heated to induce the nucleation of the magnetite nanoparticles.[283] The process is highly dependent on the reaction conditions; changes in the temperature and ionic strengths of solutions influence the final size and morphology of the nanoparticles.[284–286]

Scheme 2.1. Co-precipitation synthesis of Fe_3O_4 (Fe_2O_3:FeO) nanoparticles.

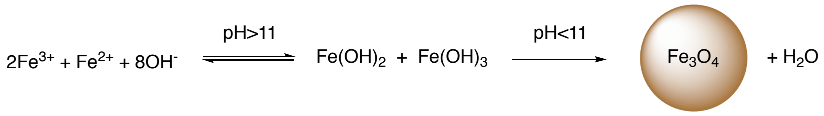

By altering reaction conditions, the co-precipitation synthesis method offers a certain degree of flexibility when designing the properties when nanoparticle constructs. However, this also makes reproducing results and synthesising monodisperse nanoparticles difficult. Therefore, the thermal decomposition acts as suitable alternative toward the synthesis of magnetite nanoparticles. Sun and Zeng report an innovative example using $Fe(acac)_3$ which is heated to high temperatures (265 °C) using diphenylether as the solvent. Here, 1,2-hexadecanediol is used as a reducing agent to provide Fe^{2+}, whilst oleylamine and oleic acid are used to cap and coat the surface of the nanoparticles. This produces monodisperse, size-controlled nanoparticles with a diameter of 4 nm.[287] However, these nanoparticles can only be dispersed in non-polar organic solvent which is a major disadvantage of this synthesis method. Therefore, further surface modification is required in order to disperse the nanoparticles in the aqueous solution for biological applications.

In this section both the co-precipitation and thermal decomposition routes toward iron oxide nanoparticle synthesis are investigated. Particles are characterised by using several different methods. The hydrodynamic diameter of the nanoparticles was obtained by using dynamic light scattering (DLS). This method relies on the Brownian motion of the nanoparticles, *i.e.* the random movement of particles due to their interactions with solvent molecules. Due to their relative size, larger particles have a slower Brownian motion and the dependence of this velocity (D ($m^2\ s^{-1}$); known as the translational diffusion coefficient) on size can be calculated via the Stokes-Einstein equation (**Equation 2.1**). Here $d(H)$ (m) is equal to the hydrodynamic diameter, k ($m^2\ kg\ s^{-2}\ K^{-1}$) is the Boltzmann constant, T (K) is the temperature, and η ($kg\ m^{-1}\ s^{-1}$) is viscosity of the liquid. The translational diffusion depends not only on the core and coating size of the nanoparticle, but also on the solvation shell which is determined by a number of factors such as surface structure and charge.[288] Therefore, DLS measurements determine the hydrodynamic diameter of the nanoparticles as opposed to TEM which measures the core size of the particles. In TEM a beam of electrons passes through the sample. Due to the shorter de Broglie wavelength of electrons, the image obtained is at a much higher resolution than a conventional light microscope, which is described by Abbe's equation (**Equation 2.2**). Here, the maximum resolution is defined as the wavelength of the image forming radiation (λ), in this case the electron beam, over the numerical aperture ($n\ sin\alpha$) of the system.

Equation 2.1. Stokes-Einstein equation describing the hydrodynamic diameter, $d(H)$, obtained from the translational diffusion coefficient, D.

$$d(H) = \frac{kT}{3\pi\eta D}$$

Equation 2.2. Abbe's equation describing the maximum resolution, d (nm), from the wavelength of image forming radiation, λ (nm) and the numerical aperture, $n\ sin\alpha$.

$$d = \frac{0.612\lambda}{n\ sin\alpha}$$

The composition of the nanoparticles was characterised by using X-ray diffraction (XRD), spectroscopic assays and induction-coupled plasma mass spectrometry (ICP-MS). As detailed in the introduction, the ζ-potential of nanomaterials is important for their stability and fate *in vivo*. Therefore, this was measured by using a Malvern Zetasizer which passes an electrical current across the nanoparticle sample. Finally, the T_2 relaxation times of the nanoparticles was obtained by using on a NMR spectrometer.

2.2.2 Results and discussion

Characterisation of Feraheme®

Whilst characterisation data could be obtained for FH through the specification information and various publications, the hydrodynamic diameter was confirmed *via* DLS measurements to be 34.6 ± 13.7 nm. This size and relatively large error margin corresponds to the manufacturers size specifications of FH (17-31 nm). Whilst the surface charge of the nanoparticles is not reported by the manufacturer, we found the ζ-potential was -62.4 ± 3.52 mV. This highly negative value is expected due to the polyglucose sorbitol carboxymethylether coating which is a modified dextran. This carboxymethyl dextran is highly anionic, and therefore, produced nanoparticles which exhibit a highly negative ζ-potentials. Finally, the T_2 relaxation times were obtained for FH. This was found to be 0.11 ± 0.2 ms which equates to a relaxivity of 507 ± 78.1 $mM^{-1}\ s^{-1}$. We cannot directly compare obtained relaxivity values to those found in the literature. Literature relaxation times are usually obtained using a 1.5 or 3.0 T MRI machines whereas a 11.74 T, 500 MHz NMR was used in this study to obtain relaxation times. However, as the measured relaxivity describes the relationship between iron concentration to relaxation times, r_2 values are a valid way to compare synthesised nanoparticles to the FDA approved FH directly.

Synthesis of magnetite nanoparticles via the co-precipitation method

Reaction conditions

Fe_3O_4 nanoparticles were obtained via the standard co-precipitation method described above. Fe^{2+} and Fe^{3+} ions in the form iron(III) chloride and iron(II) chloride were precipitated in aqueous ammonia solution. The pH was reduced by the addition of nitric acid and then the nucleation process was carried out by heating the solution to reflux. As explained above, the size of the resulting nanoparticles is highly dependent on reaction conditions used. We investigated the effect of altering the ammonia or nitric acid concentrations and reaction times in a number of different screening reactions (**Figure 2.1**).

Figure 2.1. Effects of altering the **(A)** concentration of ammonia used during precipitation, **(B)** the concentration of nitric acid used during nucleation, and **(C)** the reaction time on the hydrodynamic diameter of the Fe_3O_4 nanoparticles produced by the co-precipitation method.

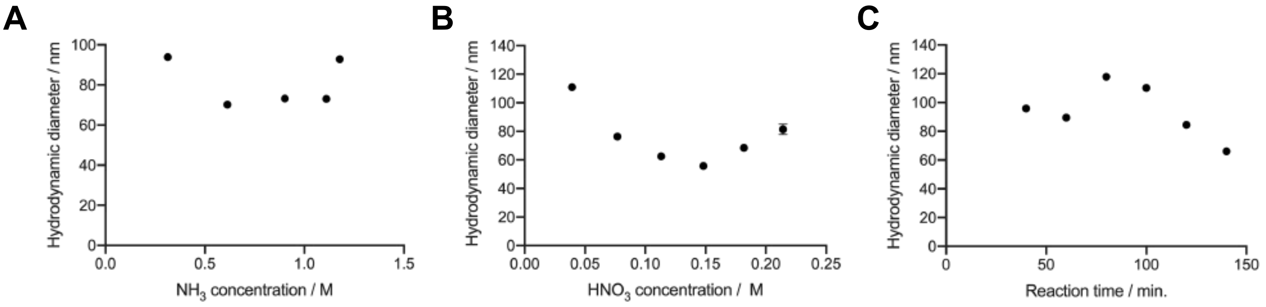

Characterisation of nanoparticles

By selecting the conditions which gave the smallest nanoparticles, we were able to produce nanoparticles with a hydrodynamic diameter of 26.51 ± 10.19 nm (**Figure 2.2A**) and a diameter of 11.31 ± 4.19 nm (**Figure 2.2C**). The obtained XRD pattern (**Figure 2.2C**) indicated that the major phase present was magnetite. This allowed us to determine we had produced Fe_3O_4 nanoparticles without further oxidation to Fe_2O_3.

Figure 2.2. Representative characterisation data for Fe_3O_4 nanoparticles synthesised by co-precipitation **(A)** a DLS profile of particles in water ($d(H)$ = 26.51 ± 10.19 nm). **(B)** TEM image of nanoparticles (d(TEM) = 11.31 ± 4.19 nm). **(C)** Experimental XRD pattern of dried particles overlaid with the magnetite standard pattern (ICSD collection code: 27899)

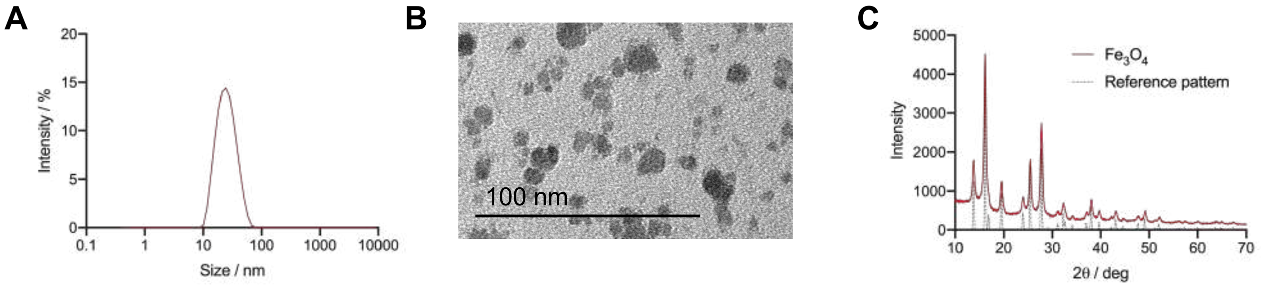

Finally, we determined the iron concentration of the Fe_3O_4 by using a spectroscopic assay. This method is based on measuring the absorbance of iron thiocyanate complexes.[289] Briefly, the nanoparticles are dissolved in strong acid (10 M HCl) to produce a solution of Fe^{2+} and Fe^{3+} ions. Ammonium persulfate was then added which oxidises the Fe^{2+} ions to Fe^{3+} which are then complexed by thiocyanate ligands forming $[Fe(SCN)_6]^{3-}$ (ε = 14100 M^{-1} cm^{-1})(**Scheme 2.2**). This complex has a characteristic absorbance in the UV-visible spectrum with a peak at 466 nm. Therefore, by constructing a calibration plot at known iron concentrations (**Experimental**; **Figure 6.1**), we were able to determine the total concentration of iron in the initial nanoparticle solution (**Figure 2.3**). With this we were able to determine that Fe_3O_4 contained 12.72 ± 0.04 mmol iron per gram of nanoparticle. This means that the nanoparticles are 70.9 ± 0.2% iron by mass. If particles were pure Fe_3O_4 the maximum iron percentage would be 72.4%. This difference can be attributed to the incomplete drying of the nanoparticles before the determination process, along with a small amount of oxidation of the magnetite to maghemite over time. This determination of iron content allowed us to calculate the relaxivity of Fe_3O_4. A T_2 relaxation time of 0.49 ± 0.03 ms was determined which was adjusted for iron content to determine a relaxivity (r_2) of 160 ± 9.2 mM^{-1} s^{-1}. Relaxivity was decreased compared to FH due to increased core size.

Scheme 2.2. Summary of the iron determination process. The oxidation of Fe^{2+} to Fe^{3+} with ammonium persulfate is highlighted in the box.

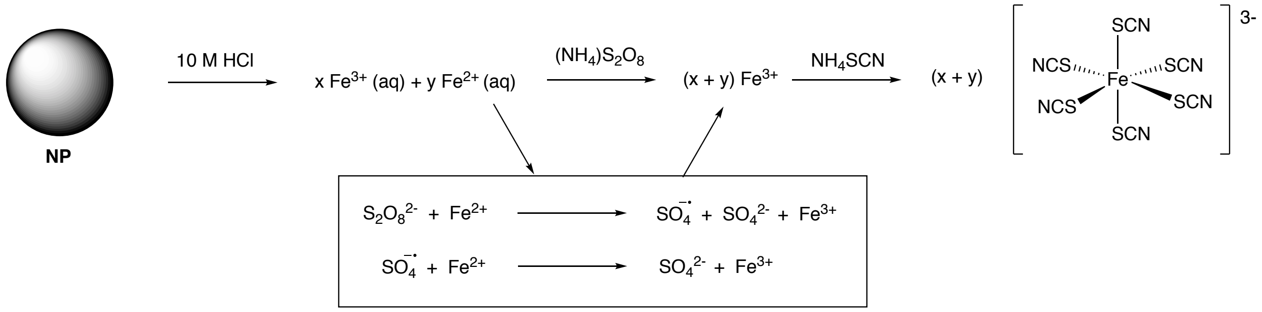

Figure 2.3. **(A)** Representative image of the $[Fe(SCN)_6]^{3-}$ solutions which are formed when different amounts of iron oxide nanoparticles are used. Left-to-right 1:3 dilution from 0.1 mg mL^{-1}. **(B+C)** Plots for the determination of iron content in nanoparticles. **(B)** UV-vis spectrum (350-650 nm) for a variety of $[Fe(SCN)_6]^{3-}$ solutions (produced from the dissolution of nanoparticles) with the λ_{max} = 466 nm. **(C)** Particle concentration vs. absorbance at λ_{max} = 466 nm.

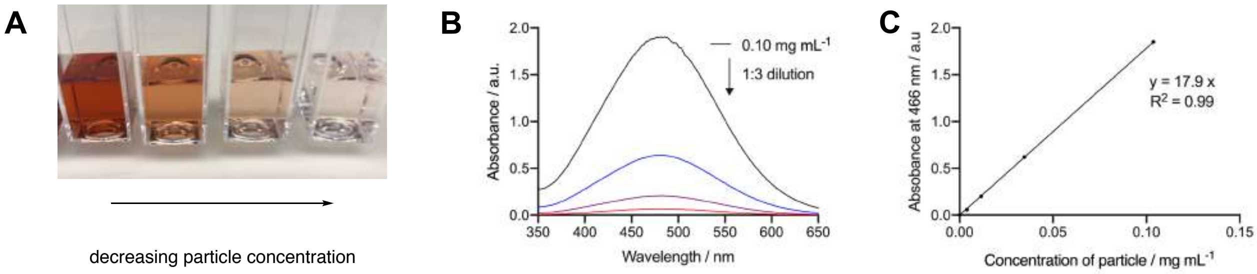

Synthesis of magnetite nanoparticles via thermal decomposition

Reaction conditions

Fe_3O_4@OA was obtained by using an adapted method based on the thermal decomposition route.[287] High temperatures and a mixture of the surfactants oleic acid and oleylamine were used to produce SPIONs dispersed in hexane. This synthesis method is termed 'thermal decomposition' because of the thermal instability of the Fe(III) acetylacetonate precursor.[290] A recent publication from Lak *et al.* indicated that complete dissociation of the acetylacetonate occurs at temperatures >90 °C.[291] Following decomposition, a portion of Fe(III) is reduced to Fe(II) by using 1,2-hexandecanediol. The precise mechanism of this reduction is unknown; however, a proposed scheme is given in **Scheme 2.3**, whereby oxidation of the diol facilitates the reduction of Fe(III).

Scheme 2.3. Proposed reactions that facilitate the reduction of Fe(III) by using 1,2-hexandecanediol.[290,291]

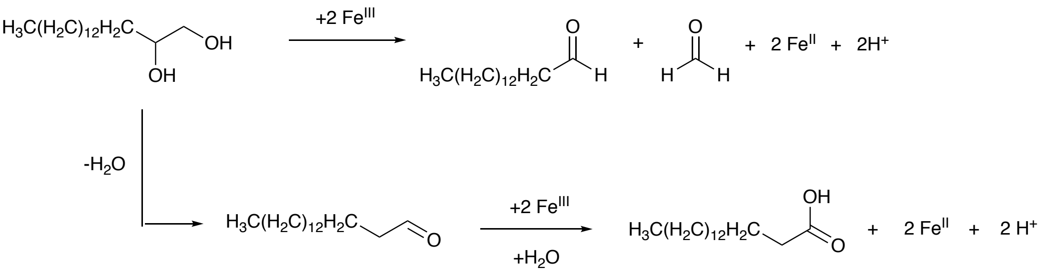

The partial Fe(III) reduction increases the number of suitable monomers in solution. This allows the nucleation process to occur, forming magnetite seed crystals. As these form the monomer concentration drops and particle growth occurs. These steps are known as the LaMer mechanism which can be summarised in three stages; 1) monomer accumulation, 2) homogenous nucleation, and 3) diffusion-controlled growth. We found that heating an iron and surfactant solution simultaneously before combining the two created particles which were smaller. This method is known as the hot-injection synthesis method and is commonly used during the synthesis of a variety of nanoparticles.[292] By shortening the time frame in which monomer accumulation occurs there is a quick burst of nucleation which then causes growth to occurs from seed crystals that have similar sizes. This, in turn, leads to a decrease in size distribution of the nanoparticles.[292] Following successful synthesis, particles were precipitated in ethanol and dispersed in hexane to remove impurities.

Characterisation of nanoparticles

At this stage, the particles were then characterised by using DLS, TEM and XRD analysis. DLS found a hydrodynamic diameter of 8.95 ± 3.98 nm (**Figure 2.4A**) when the particles are dispersed in hexane. A diameter of 6.79 ± 3.41 nm was observed with TEM (**Figure 2.4B**). The XRD pattern of the same nanoparticles (**Figure 2.4C**) indicated that magnetite was the major phase present.

Figure 2.4. Representative characterisation data for Fe_3O_4@OA. **(A)** A DLS profile of particles in hexane (8.95 ± 3.98 nm). **(B)** A TEM image of nanoparticles (6.79 ± 3.41 nm). **(C)** XRD pattern of dried particles. (magnetite standard: ICSD collection code: 27899)

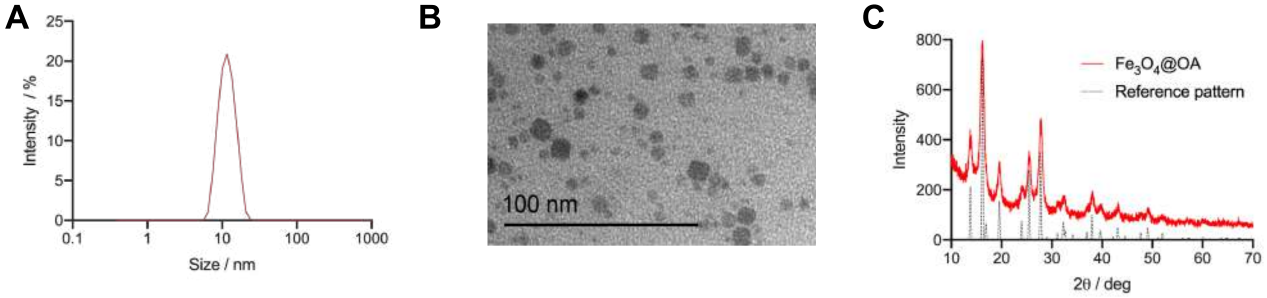

Functionalisation of Fe_3O_4@OA

Due to hydrophobic nature of the oleic acid and oleylamine surfactants, the nanoparticles are only stable in non-polar solvents and aggregate in aqueous solution. Therefore, to disperse the SPIONs into a desirable solvent the surface ligands must be replaced. This was achieved by using two methods creating Fe_3O_4@$Al(OH)_3$ and Fe_3O_4@APTES nanoparticles. The first, based on works from Cui *et al.*, involved the use of aluminium chloride to create an aluminium hydroxide coating on the surface.[293] The initial sign of successful functionalisation is the ready dispersion of the nanoparticles in water, indicating successful displacement of the hydrophobic oleic acid and oleylamine surface ligands. To confirm this functionalisation, the IR spectrum was obtained which indicated a broad OH stretching mode (3029 cm^{-1}) and deformation mode (1553 cm^{-1}) with a disappearance of the CH stretches at 2846 and 3794 cm^{-1}. Particles were further characterised by TEM and showed a minor increase in particle size, d(TEM) = 10.6 ± 2.47 nm, which can be assigned to the presence of the $Al(OH)_3$ coating. However, DLS measurements showed that there was a significant increase in the hydrodynamic diameter ($d(H)$ = 113 ± 51.3 nm) due to the solvation shell of the water molecules. The ζ-potential of the particles was +52.8 ± 6.14 mV, which, at first, seemed surprising given the presence of hydroxide groups in the coating. However, this highly positive surface potential arises due to the Al^{3+} ions present at the surface and a similar ζ-potential was reported from Cui *et al*. Iron content measurements indicated that particles contained 11.3 ± 1.1% iron (by mass). These findings were supported by the long T_2 relaxation time (6.52 ± 0.01 ms), which corresponds to a r_2 value of 74.5 ± 0.1 mM^{-1} s^{-1}. The relaxivity is relatively poor (see **Table 1**) when compared with other nanoparticles investigated in this chapter. It can be assumed that the $Al(OH)_3$ coating protects the iron oxide core and limits the proximity of the surrounding water molecules.

The second functionalisation method involved the use of (3-aminopropyl)triethoxysilane (APTES) to displace the hydrophobic surfactants and to coat the nanoparticles, creating Fe_3O_4@APTES. In a similar way approach to the synthesis of Fe_3O_4@Al(OH)$_3$, the initial indication of successful functionalisation by ATPES was the dispersion of nanoparticles into water without the aggregation. IR measurements indicated the presence of both Si-O (1283 cm^{-1}) and Si-C bonds (1396 cm^{-1}). TEM images showed a minor increase in the core size of the nanoparticle with a diameter of d(TEM) = 11.4 ± 7.47 nm. However, again the hydrodynamic diameter exhibited a dramatic increase (d(H) = 102 ± 68.2 nm) due to the extended aqueous solvation shell. Similarly, the ζ-potential of the Fe_3O_4@APTES nanoparticles was positive (+46.4 ± 9.19 mV) which was expected due to the primary amines at the surface. T_2 relaxation times were very fast (0.39 ± 0.01 ms), corresponding to a high relaxivity (r_2 = 611 ± 15.3 mM^{-1} s^{-1}). Whilst the nanoparticles exhibit a similar d(H) to the Fe_3O_4@Al(OH)$_3$nanoparticles, the APTES coating is less dense, hence water molecules are at a closer proximity to the nanoparticle surface. Therefore, it is the small core size in combination with the organic coating efficiently accelerates relaxation of water molecules.

Scheme 2.4. Dispersion of Fe_3O_4@OA into aqueous solution using either a Al(OH)$_3$ or APTES coating.

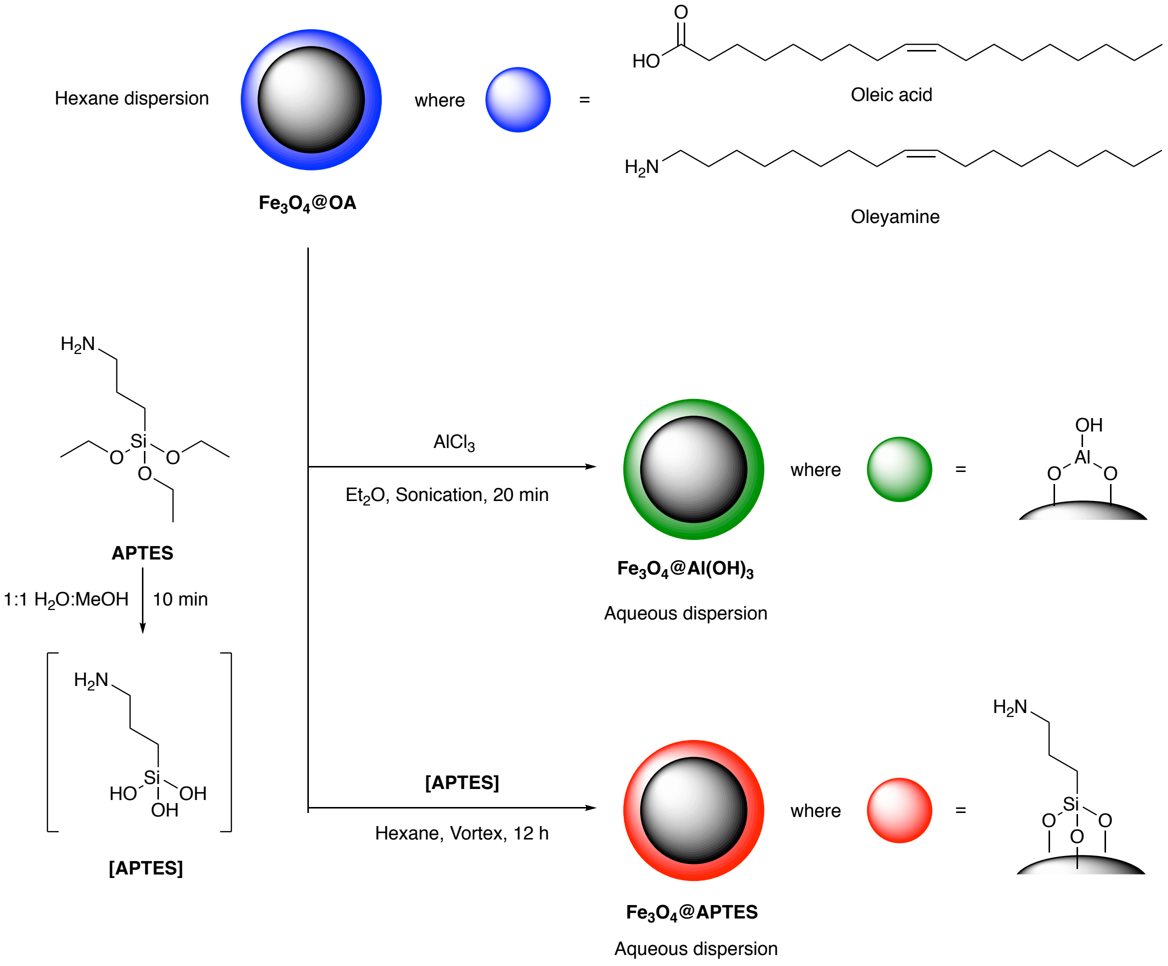

Figure 2.5. Characterisation data for Fe_3O_4@APTES and Fe_3O_4@Al(OH)$_3$ **(A)** IR spectrum of Fe_3O_4@Al(OH)$_3$ (black), Fe_3O_4@OA particles (blue) and Fe_3O_4@APTES (red) **(B)** TEM image of Fe_3O_4@Al(OH)$_3$ nanoparticles (10.6 ± 2.5 nm). **(C)** DLS profile of Fe_3O_4@Al(OH)$_3$ (113.0 ± 51.3 nm). **(D)** TEM image of Fe_3O_4@APTES nanoparticles (11.4 ± 7.5 nm). **(E)** DLS profile of Fe_3O_4@APTES (102.0 ± 68.2 nm).

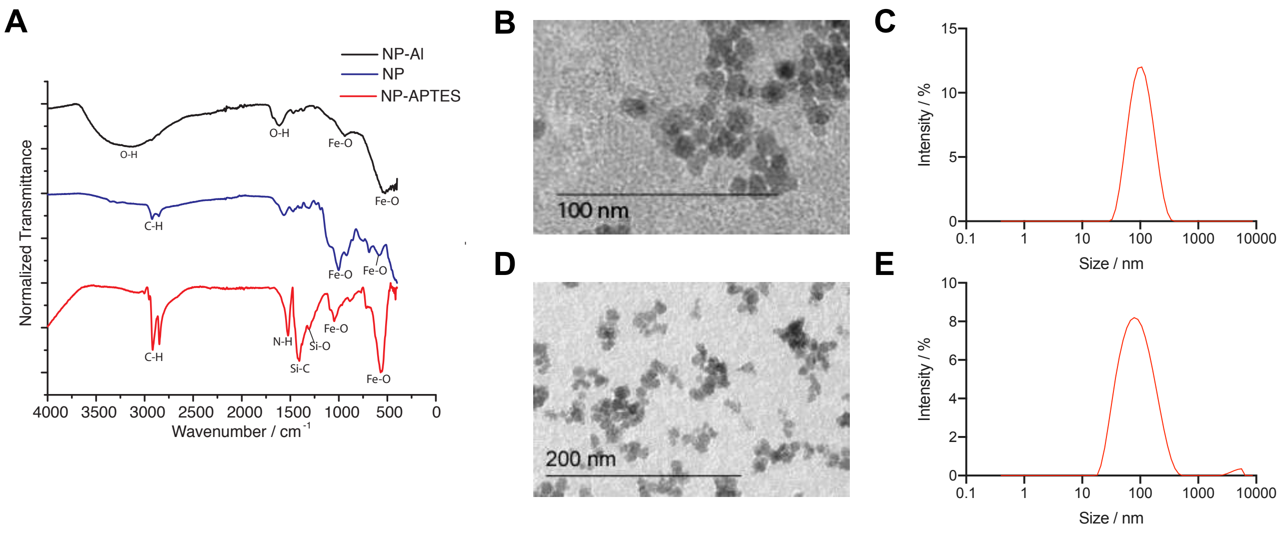

Characterisation of Fe_2O_3@Au nanoparticles

Fe_2O_3@Au nanoparticles were kindly synthesised and characterised by Dr. Marcus Yaffee at the University of Zurich. The particles consist of a maghemite core with an Au(0) coating with a diameter measured by TEM of d(TEM) = 17.8 ± 4.3 nm and a hydrodynamic diameter of $d(H)$ = 51.4 ± 25.3 nm (**Figure 2.6**). ICP-MS analysis determined the composition of metal ions in the nanoparticles; a content of 19% iron and 81% gold (by mass of metal ion) was found, this corresponds to ~8.5 Au atoms for each Fe_2O_3 component. This suggests that the particles have a relatively thick Au coating encasing a comparatively small maghemite core. This explains the relative long T_2 relaxation time (24.68 ± 0.01 ms) and low r_2 relaxivity (11.8 ± 0.01 $mM^{-1}\ s^{-1}$) in comparison to other nanoparticles reported in this chapter. The Au(0) coating protects the iron core from direct contact and reaction with the water, shielding the surrounding water molecules from the maghemite core. The dense, thick, Au(0) coating provides more shielding than the thinner, lighter Al(OH)$_3$ or APTES coatings, hence poorer transverse relaxation properties are observed for the Fe_2O_3@Au nanoparticles.

Figure 2.6. Representative characterisation data for Fe_2O_3@Au. **(A)** A DLS profile of the particles in water (51.4 ± 25.3 nm). **(B)** TEM image of nanoparticles (17.8 ± 4.31 nm). **(C)** Image of Fe_2O_3@Au dispersion.

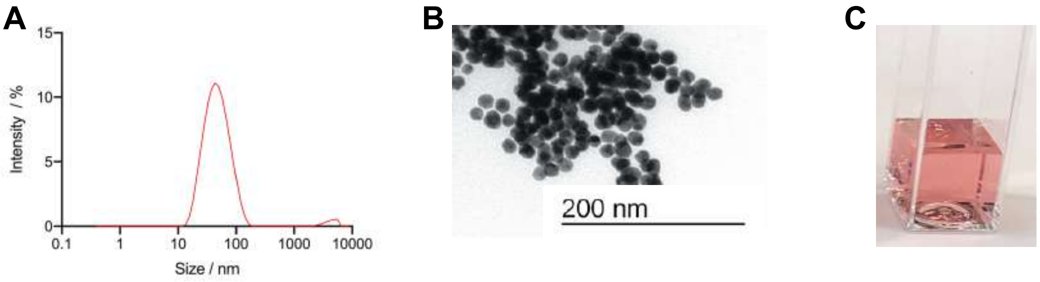

Visual inspection provided an immediate indication that the gold atoms were coating at the surface of the nanoparticles (**Figure 2.6C**). Unlike iron oxide nanoparticles (which appear brown) and similarly to other gold nanoparticles, the Fe_2O_3@Au nanoparticles exhibit a pink/red colour due to the presence of the surface plasmon resonance (SPR). The free conduction electrons (*d* electrons) in solid gold oscillate collectively in the presence of light and are known as a plasmon. Plasmons can be excited in the bulk and at the surface, however, at the nanoscale, only surface plasmons are expected which is the case for gold nanoparticles. At a specific wavelength of light, surface plasmons resonate causing the strong absorbance or scattering of light giving rise to the strong observed colour. For gold nanoparticles this results in an absorbance maximum (λ_{max}) of around 510-570 nm in the UV-visible spectrum. The resonance frequency is strongly dependent on a number of conditions including the size and shape of the nanoparticles, therefore, modification or aggregation of the nanoparticles can be observed from changes in the absorption spectra.[294] This phenomena is well-demonstrated by Haiss *et al.* who showed that λ_{max} red-shifts from 525 to 579 nm as particle diameter increases from 32 to 108 nm.[295] As expected, the Fe_2O_3@Au nanoparticles have an λ_{max} of 520 nm.

2.2.3 Summary

Table 1 summarises the nanoparticles synthesised and characterised during this section of the thesis. These particles will be further modified in following sections of the thesis.

Table 1. Summary of nanoparticles and their characteristics. N.B. Data is incomplete for Fe_3O_4@OA as these particles are not soluble in aqueous solution.

Particle	Diameter, *d*(TEM) /nm	Hydrodynamic size, *d*(*H*) / nm	ζ-potential / mV	T_2 relaxation time / ms	r_2 relaxivity/ mM^{-1} s^{-1}
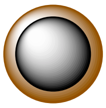 **FH**	> 5 [281]	34.6 ± 13.7	-62.4 ± 3.52	0.11 ± 0.02 ms	507 ± 78
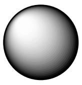 **Fe_3O_4**	12.31±5.19	26.5± 10.2	38.1 ± 0.9	0.49 ± 0.03 ms	160 ± 9.2
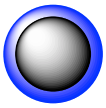 **Fe_3O_4@OA**	8.95 ± 3.98	-	-	-	-
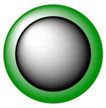 **Fe_3O_4@Al(OH)$_3$**	10.6 ± 2.47	113 ± 51.3	52.8 ± 6.14	6.52 ± 0.01	74.5 ± 0.12
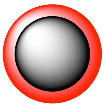 **Fe_3O_4@APTES**	11.4 ± 7.47	102 ± 68.2	46.4 ± 9.19	0.39 ± 0.01	611 ± 15.3
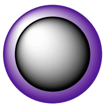 **Fe_2O_3@Au**	17.8 ± 4.31	51.4 ± 25.3	-32.0 ± 11.4	24.68 ± 0.01	11.8 ± 0.01

2.3 Radiolabelling of nanoparticles

2.3.1 Introduction

As introduced in **Chapter 1**, methods for radiolabelling nanoparticles can be classified as classical or non-classical. The former routes typically involve the use of a chelate or prosthetic group and the latter methods explore the intrinsic, chelate-free radiolabelling. This section of the thesis we aimed to explore a range of radiolabelling methods whilst addressing some unanswered questions in the field and identifying the best methods to create targeted radiolabelled compounds (see **Chapter 3**).

Chelate-based methods use known chemistries to produce kinetically and thermodynamically stable complexes.[296,297] The complexation of radiometals using macrocyclic or acyclic chelators is a heavily researched and developed topic, and a number of ideal chelates for particular radionuclides have been established.[154,156,298–301] For example, DOTA is known as an ideal chelator of $^{111}In^{3+}$, whilst thermodynamic parameters are promising (log K = 23.9), the kinetic inertness of the complex also prevents metal dissociation *in vivo*. [298] Similarly, NOTA (1,4,7-triazacyclononane-1,4,7-triacetic acid) is known to form complexes with $^{68}Ga^{3+}$ (log K = 31.0) and $^{64}Cu^{2+}$ (log K = 23.3) which remain stable under physiological conditions.[156,302]

Despite the stability offered by using radiometal chelators, these methods may not be optimal when radiolabelling nanoparticle constructs. Incorporating a chelate as part of the nanoparticle structure typically requires multi-step reactions and results in the addition of bulky groups which may compromise the biological targeting and pharmacokinetics. Non-classical, chelate-free methods aim to avoid the use of these groups by taking advantage of the intrinsic reactivity and properties of nanoparticles. An example of chelate-free radiolabelling is the direct chemisorption of the radionuclide onto the iron oxide nanoparticle surfaces, and this is becoming a popular radiolabelling method. Since the first report of this phenomena by Chen *et al.* (synthesis of *As-SPIONs (where * = 71, 72, 74, 76)), several publications have highlighted the versatility of the technique [183,196,213,232,303–305] Madru *et al.* radiolabelled PEGylated SPIONs with ^{68}Ga whilst and Chakravarty *et al.* labelled SPIONs with ^{69}Ge and our group demonstrated that Feraheme® could be labelled with ^{64}Cu, ^{89}Zr and ^{111}In when heated.[183,304,305] The mechanism by which this radiolabelling occurs is not fully understood, however, electron paramagnetic resonance (EPR) studies performed by our group pointed towards a surface interaction with the oxide layer.[183] The EPR spectra of Cu^{2+} labelled of Feraheme® exhibited the a Cu^{2+} signal which would be lost if the Cu^{2+} ions were incorporated into the superparamagnetic core of the nanoparticle. This initial speculation of the radiometal binding mode was supported by recent findings from Patrick *et al*.[306] They carried out several experiments with both magnetite and maghemite nanoparticles and ^{89}Zr and ^{111}In radionuclides to determine that the radionuclide mineralised onto the surface of the nanoparticles.[306] ^{57}Fe Mossbauer spectroscopy indicated that iron atoms remained in the same environment following the radiolabelling process. This suggested that no sub-lattice modification takes place and radiolabelling only takes place at the surface of the particles. X-ray photoelectron spectroscopy (XPS) then confirmed this result and indicating the presence of In with a 3+ oxidation state assigned as In_2O_3, and Zr with a 4+ oxidation state assigned as ZrO_2 at the particle surface. Time-of-flight secondary ion mass spectroscopy (ToF-SIMS), ICP-MS and XRD were then used to further support the theory of radiometal binding *via* the surface oxide layer which they termed surface mineralisation.

This section reports our experimental work investigating the chemical and radiochemical scope of the radiomineralisation technique using the nanoparticles introduced in **Section 2.1**. Whilst the chemical interaction is now understood to occur *via* mineralisation, the kinetics of this process has not been studied. Our previous work indicated there were differences in binding when labelling Feraheme® with a range of metals ions (Zr^{4+}, Tb^{3+}, Eu^{3+}, In^{3+}, Cu^{2+}, Co^{2+}, Ni^{2+}, Mn^{2+} and Zn^{2+}). Therefore, kinetic data were measured from the radiolabelling of Fe_3O_4 and FH with both ^{68}Ga and ^{111}In radionuclides. The aim of this was to determine if the nature of the particle coating or the choice of radionuclide affects the mineralisation process. As control studies and for direct comparison with the chelate-free methods, we also investigated the use of several classical radiolabelling methods. Finally, a novel thiol-mediated uptake of ^{64}Cu radionuclides onto gold surfaces was studied.

2.3.2 Results and discussion - Classical radiolabelling methods

Functionalisation of Fe_2O_3@Au with a dithiolane chelate derivative

Basic principles

As introduced in the previous section, the Fe_2O_3@Au nanoparticles comprise of maghemite core with a gold coating. Due to the strong affinity between gold and sulphur, the coating of the nanoparticles can be modified by the chemisorption of thiols and disulphides onto the surface to form a self-assembled monolayer (SAM). Therefore, we decided to use a chelate derivatised with a dithiolane group to the append a radionuclide onto the nanoparticle construct. The dithiolane group is speculated to have an increased stability compared with a single thiol due to the 'didentate' effect of the two sulphur atoms conjugating to the surface.[307] When modified with dithiolane derivatives we observed a small but significant red shift in the SPR of the Fe_2O_3@Au-dithiolane-R nanoparticles where λ_{max} increased from 520 nm to 524 nm (**Figure 2.7**). This minor shift provided the first indication of a successful modification of the nanoparticle resulting in a small change in the surface electron distribution.

Figure 2.7. (A) Surface modification of Fe_2O_3@Au nanoparticles, and **(B)** electronic absorption spectra showing the shift in absorption maximum as the nanoparticles are modified with a dithiolane derivative (lipoic acid).

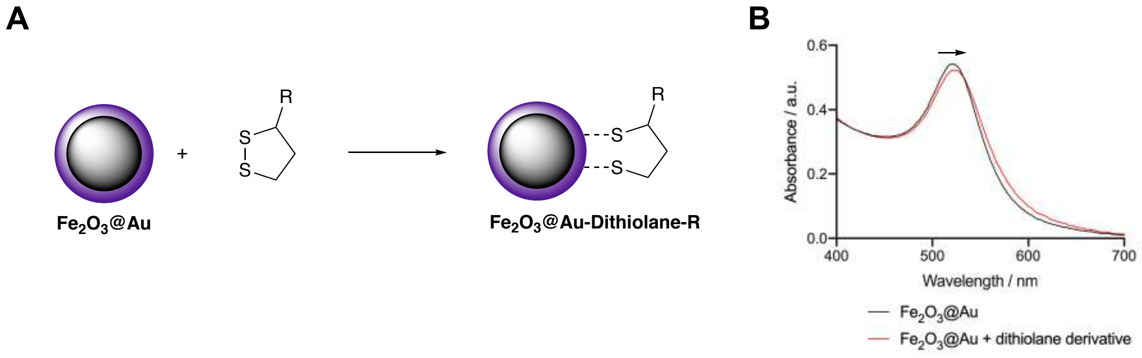

The exact bonding mode of the dithiolane to the gold surface is unknown. Whilst early experiments established that S-S bond breaks the during surface functionalisation, the exact chemical transformation at the surface, and the resulting structure, is not fully understood.[308] Due to the uneven surface of the nanoparticle surface, it is believed that the final structure is polymorphic, hence it is difficult to elucidate. However, it has been shown by DFT, X-ray diffraction and STM that thiols tend to bind an adatom (an atom which lies on the crystal surface) as RS-Au-SR.[309,310] In this structure the sulphur atoms can be considered as sp^3 hybridised forming a bond to the adatom, to the gold surface and to the R group, plus an additional lone pair. Evidence for this bonding mode is provided by Knoppe *et al.* (and other publications from the same group) who report chirality in thiol-functionalised gold nanoclusters.[311–313] However, the system cannot be as simple as that proposed in **Figure 2.8B**, as the reduction of the disulphide bond requires two electrons, and therefore, the oxidation of two gold atoms (**Figure 2.8A**). Recent work by Carro *et al.* used DFT calculations to probe the ionic nature of the bond between the sulphur atom and the adatom. They suggested a more dynamic system, where sulphur atoms would reform disulphides at the surface and bond to multiple adatoms, thus providing electrons to satisfy the oxidation states.[314]

Figure 2.8. Proposed binding method of dithiolane derivatives to the gold surface.

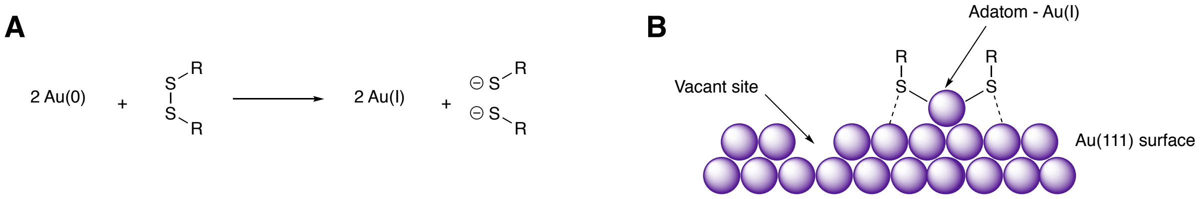

Synthesis and radiolabelling of chelate

The dithiolane derivative (compound **2**) was synthesised from a DOTAGA-PEG_4 chelate. DOTOGA is an established chelator of Ga^{3+} facilitating radiochemistry with ^{68}Ga. Due to the larger cavity size of DOTA compared to other macrocyclic chelates that contain fewer atoms in the ring (*e.g.* NOTA (formation constant with Ga^{3+} : log *K* = 31.0)) the formation constant is lower (log *K* = 21.3).[156] However, unlike chelates such as NOTA, DOTAGA provides up to 8 donor atoms.[296] This allows DOTAGA to form coordination complexes with therapeutic radionuclides ^{90}Y and ^{177}Lu providing flexibility in the system once fully developed.[153] For ease of functionalisation, lipoic acid (LA) was selected as the dithiolane derivative for coupling to DOTAGA-PEG$_4$-NH$_2$. As a dietary supplement used throughout the world, LA is commercially available, inexpensive, and can be modified easily to facilitate functionalisation of DOTAGA-PEG$_4$-NH$_2$. The activated *N*-hydroxysuccinimide (NHS) ester was formed before the addition of the DOTAGA-PEG$_4$-NH$_2$ to obtain DOTAGA-PEG$_4$-NH-LA (**2**) via amide bond formation. Following the successful synthesis of compound **2**, the natural gallium species was synthesised and characterised by using MS and UPLC. The retention time of ^{nat}Ga-**2** on a reverse-phase C18 column served as a reference for characterising the analogous ^{68}Ga compound.

Scheme 2.5. Chemical synthesis of DOTA-GA-PEG$_4$-NH-LA and complexation to natural gallium(III).

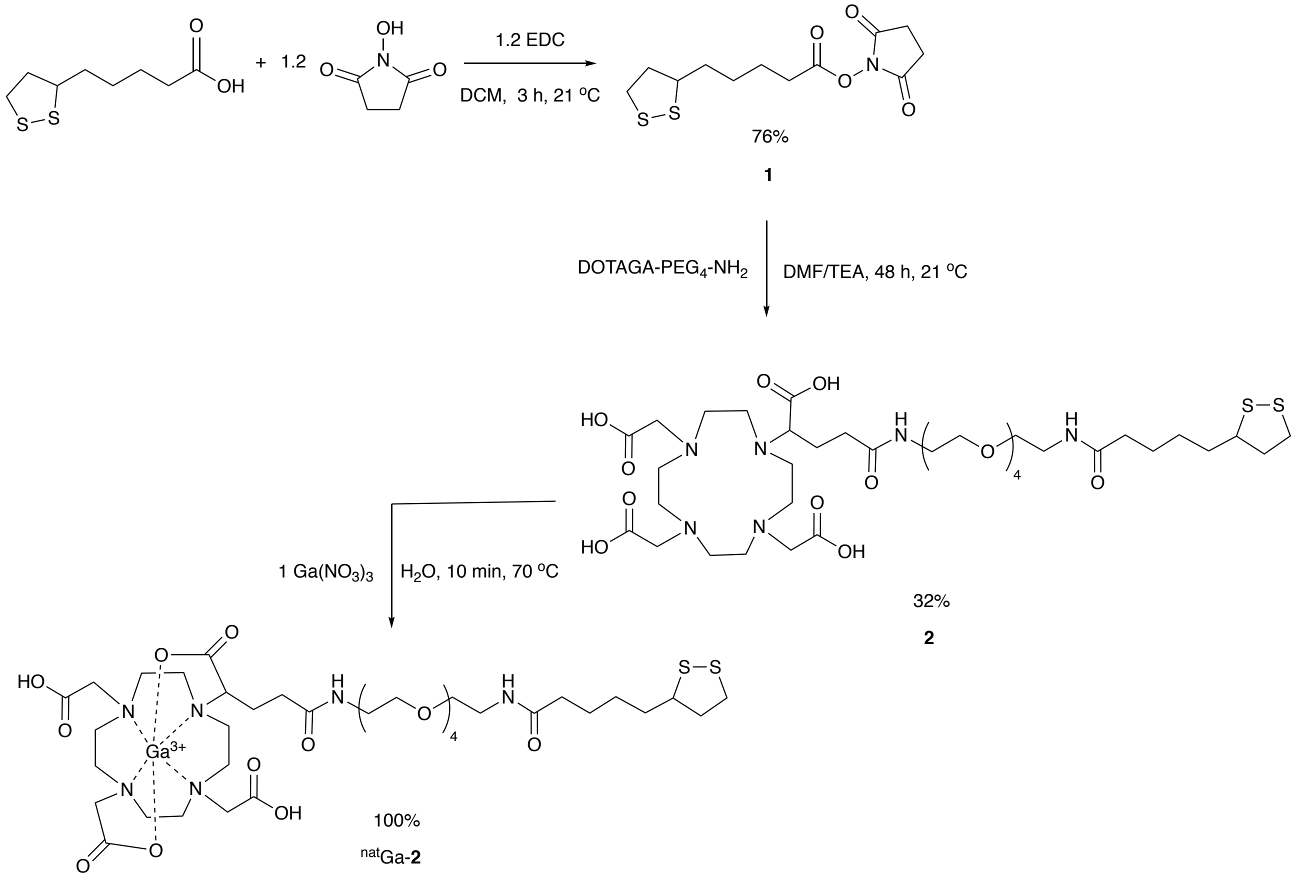

The radiosynthesis of [^{68}Ga]Ga-DOTAGA-PEG$_4$-NH-LA ([^{68}Ga]Ga-**3**) was achieved in a reaction time of 10 min at 70 °C (**Scheme 2.6**) with a RCC >99% (*n* = 5). Acetate buffer was used to ensure pH4.4, minimising the formation of insoluble gallium(III) hydroxide. Due to the slow radiolabelling kinetics of DOTA chelates, a temperature of

70 °C is required to form the metal complex.[296] The reaction was monitored by radio-TLC and after 10 min no free ^{68}Ga was observed (**Figure 2.9**). Radio-UPLC was used to further characterise the product, confirming that [^{68}Ga]Ga-**2** was synthesised as the elution time (R_t = 6.24 min) was equivalent to that of ^{nat}Ga-**2**.

Scheme 2.6. Radiochemical synthesis of [^{68}Ga]Ga-DOTA-GA-PEG$_4$-NH-LA.

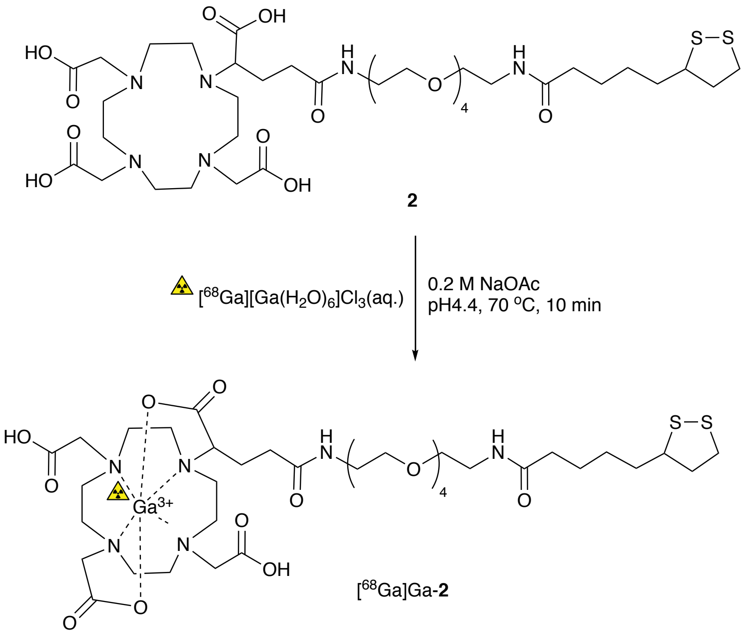

Figure 2.9. Radiochemical characterisation data for [^{68}Ga]Ga-**2** ([^{68}Ga]Ga-DOTAGA-PEG$_4$-NH-LA). **(A)** Radio-iTLC with silica gel as stationary phase and citrate buffer (1 M, pH 4.5 CHECK) as the mobile phase. **(B)** Radio-UHPLC with C18 column stationary phase and 5-95% MeCN in H$_2$O (0.1% TFA) as the mobile phase.

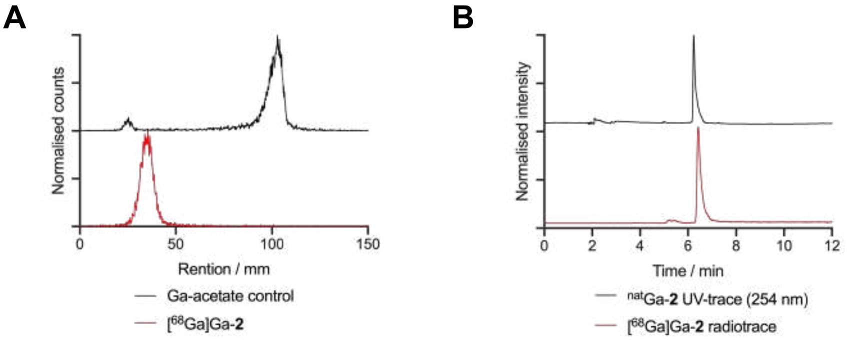

*Functionalisation of Fe$_2$O$_3$@Au with [^{68}Ga]Ga-**2***

Following the successful synthesis of the ^{68}Ga-radiolabelled chelate, [^{68}Ga]Ga-**2**, the reaction mixture was neutralised and then used to functionalise the Fe$_2$O$_3$@Au nanoparticles (**Scheme 2.7**). It was found that the reaction proceeded quickly with a high RCC (>97%, *n* = 3). By using an unusual TLC eluent (MeOH/H_2O 1:1 with 0.5% HCl) we were able to move the radiometal complex ([^{68}Ga]Ga-**2**) to the solvent front whilst radiolabelled nanoparticles remained at the baseline (R_f = 0.0 – 0.1) (**Figure 2.10A**). Further characterisation by PD10-SEC (Sephadex^{TM} desalting column-Size exclusion chromatography) indicated a RCP of 94% (*n* = 1) (**Figure 2.10B**). Control studies where performed to establish whether it was in fact the LA, dithiolane moiety binding to the surface of the [^{68}Ga]Fe_2O_3@Au-Ga-**2** nanoparticles. [^{68}Ga]Ga-DOTAGA-PEG$_4$-NH$_2$ (^{68}Ga-**3**) was synthesised in a RCC of 98%. This control compound features the same DOTAA chelate and PEG$_4$ linker as compound **2** but without the LA group. When neutralised and added to the Fe_2O_3@Au nanoparticles, no significant radiolabelling was observed using PD10-SEC chromatography (**Experimental**; **Scheme 6.2**). This demonstrated that the binding of [^{68}Ga]Ga-DOTAGA-PEG$_4$-NH-LA to the Fe_2O_3@Au nanoparticles was mediated by the dithiolane group.

Scheme 2.7. Radiochemical synthesis of [^{68}Ga]Fe_2O_3@Au-Ga-**2**.

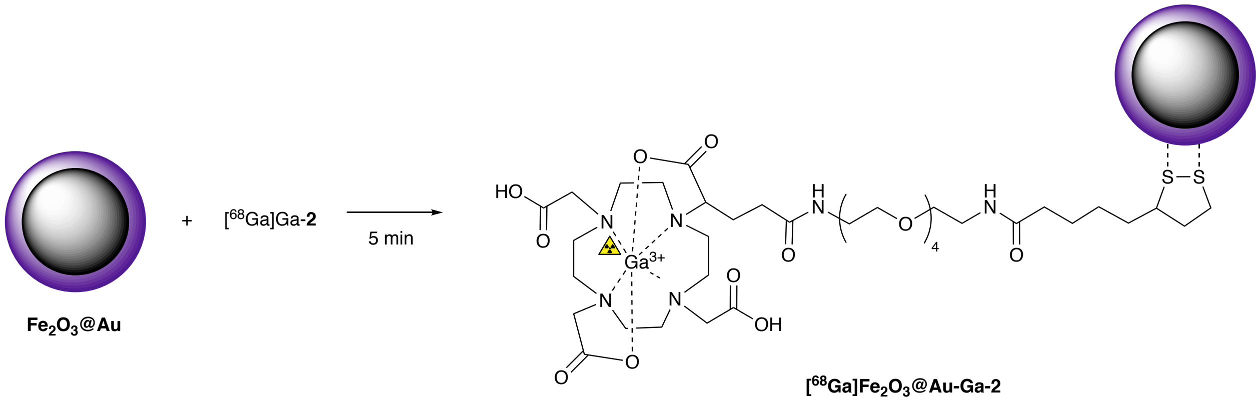

Figure 2.10. Radiochemical characterisation data for [^{68}Ga]Fe_2O_3@Au-Ga-**2**. **(A)** Radio-iTLC with silica gel as a stationary phase and MeOH/H_2O 1:1 with 0.5% HCl as the mobile phase. **(B)** PD10-SEC profile with water as eluent. **(C)** RCC to [^{68}Ga]Fe_2O_3@Au-Ga-**2** product with changing concentration of [^{68}Ga]Ga-**2** (in order to find maximum loading capacity).

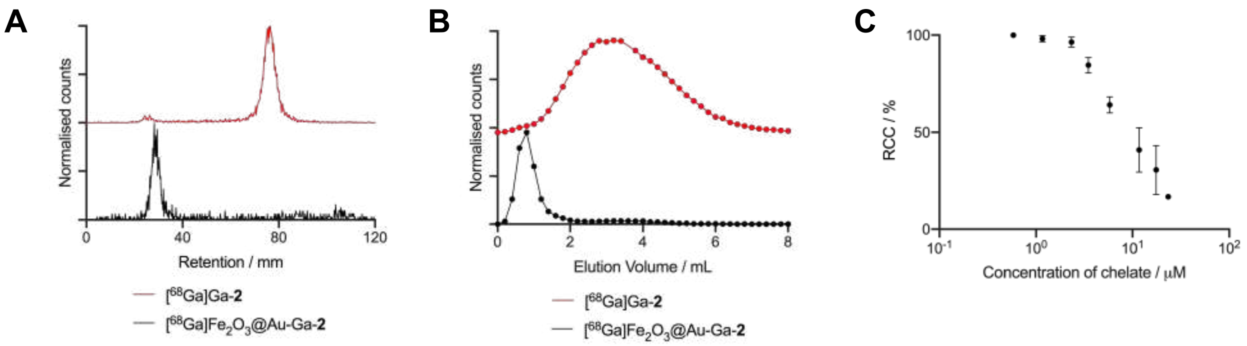

It was important to ascertain the maximum loading capacity of the nanoparticles to achieve the best possible specific activity. Therefore, we carried out a titration experiment, increasing the amount of radiolabelled chelate with respect to the nanoparticle. We found that a 2.33 µM concentration of [^{68}Ga]Ga-**2** saturated a solution of nanoparticles with a Au(0) concentration of 0.54 mM (**Figure 2.11**). We then used this concentration to extract kinetic data by taking samples of the reaction of mixture at various time points. As the reaction proceeded so quickly, reliable data could only be achieved by cooling the reactions to 4 ^{o}C to slow down the rates of conversion. By fitting the obtained data to a second-order rate law, a rate constant of k_2 = 6.25 (±1.2) x 10^{-2} M^{-1} s^{-1} was obtained. These data demonstrates how quickly the final radiolabeling step takes place, which is essential when working with short-lived radionuclides such as ^{68}Ga. From generator elution, radiolabelled nanoparticles can be produced in <20 min.

Figure 2.11. Kinetic data showing **(A)** the change of RCC over time during the synthesis of [^{68}Ga]Fe_2O_3@Au-Ga-**2**, and **(B)** the corresponding linear plot of 1/[[^{68}Ga]Ga-**2**] concentration *versus* time in seconds.

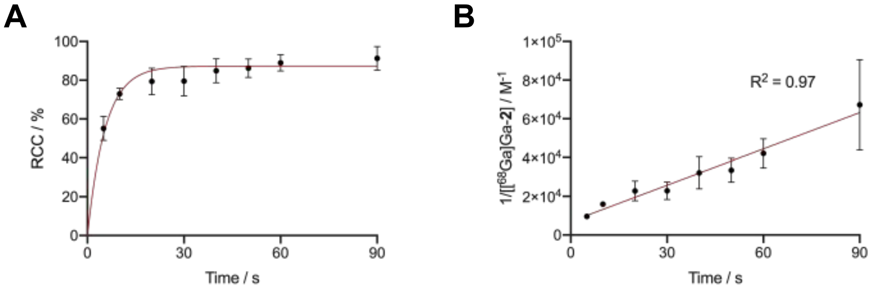

Photoconjugation of a radiolabelled photo-activatable complex to nanoparticle surface

Basic Principles

Recently, our group demonstrated the light-induced bioconjugation of photoactivatable chelates to mAbs. Here, photoactivatable chelates are radiolabelled and conjugated to protein lysine residues *via* a light-induced activation of an arylazide (ArN_3) group on the complex.[63,315–317] The proposed mechanism for this conjugation is given in **Scheme 2.8**. Following light absorption (typically with λ_{max} 365 – 395 nm), dinitrogen is released to produce a short-lived, singlet, open-shell nitrene. This nitrene undergoes a series of reactions where intramolecular rearrangement first produces an bicyclic benzazirine and finally a ketenimine species. The ketenimine is a powerful electrophile that can be attacked by a strong nitrogen-based nucleophile to produce a 2-azepin product.[63] Hydrolysis of the ketenimine competes with the nucleophile producing a azepin-2-ol species or the corresponding tautomers. Remarkably, experimental and computational data indicate that primary amines react preferentially over background quenching processes. To create radiolabelled mAbs the ε-amine group of lysine residues at the surface acts as the nucleophile producing the radiolabelled constructs.

Scheme 2.8. Proposed mechanism of the nucleophilic addition following photoactivation of an ArN_3.

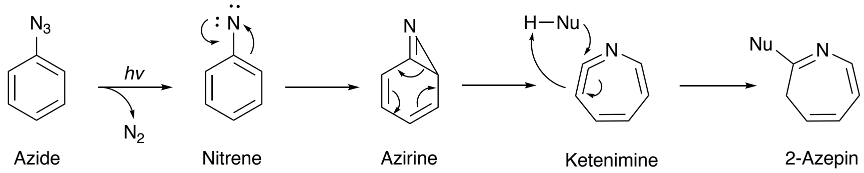

We hypothesised that by using amine-functionalised nanoparticles, we could conjugate radiolabelled photoactivatable chelates to the surface. Initially, we considered using the previously synthesised Fe_3O_4@ATPES. However, due to the positive ζ-potential of the nanoparticles, they were not stable at the optimum pH required for the photoconjugation. As the reaction depends on the nucleophilic attack of the primary amine ($pK_a \sim 10.5$), a pH >7.5 is necessary to produce sufficient deprotonation.[316] Therefore, we produced FH@APTES nanoparticles through hydrolysis of the APTES before overnight agitation with FH. The modified coating of FH providing sufficient stability at the required pH. Following synthesis and purification of FH@APTES, functionalisation was measured by using a Kaiser assay to determine the amount of amine present on the nanoparticle surface. This concentration of amine was found to be 31.5 mM in a 1 mg mL^{-1} sample of nanoparticle. The chelate selected for photoconjugation was a previously synthesised DOTA-PEG_4-ArN_3, kindly donated by Larissa Eichenberger.[316]

Photoconjugation to FH@APTES

DOTA-PEG_4-ArN_3 was radiolabelled with ^{68}Ga using previously described methods to produce [^{68}Ga]Ga-DOTA-PEG_4-ArN_3 with a RCC > 99% and a RCP of 98% (**Figure 2.12**). This was then used for further photoconjugation reactions where FH@APTES was irradiated with the chelate at 365 nm for 10 min at pH8. Due to aggregation of the nanoparticles a pH>8 could not be used, however more basic condition would ideal for the photoconjugation as it would promote the deprotonation of the free amine (pK_a ~10.5).[316] Initial photoconjugation reactions used a chelate concentration of 2.2 mM with an amine concentration of 22.5 mM. At this concentration and pH negligible radiolabelling was observed with a RCC of 1.4%. Hydrolysis reactions can compete with the nucleophilic addition of the amine and subsequent nanoparticle conjugation. Decreasing the concentration of the chelate by 100-fold, increased the RCC to 4.1% (**Figure 2.13A**). The product was then purified *via* PD10-SEC to obtain [^{68}Ga]Ga-DOTA-PEG_4-APTES-FH with a RCP of 97%. To ensure that the radiolabelling was occurring *via* photoconjugation, several control experiments were carried out. FH particles with no APTES functionalisation (no amine) were irradiated with [^{68}Ga]Ga-DOTA-PEG_4-ArN_3 ('RCC' = 1.3%) and FH@APTES was incubated with [^{68}Ga]Ga-DOTA-PEG_4-ArN_3 in the dark ('RCC' = 0.7%) (**Figure 2.13B**). These both produced negligible conjugation to the nanoparticles, as did irradiation of the chelate alone ('RCC' = 0.8%) (**Experimental**; **Figure 6.12**).

Figure 2.12. Radiochemical characterisation data for [^{68}Ga]Ga-**4** ([^{68}Ga]Ga-DOTA-PEG$_4$-ArN$_3$). **(A)** Radio-iTLC with silica gel as stationary phase and citrate buffer as the mobile phase. **(B)** Radio-UHPLC with a C18 column stationary phase and 5-95% MeCN in H$_2$O as the mobile phase.

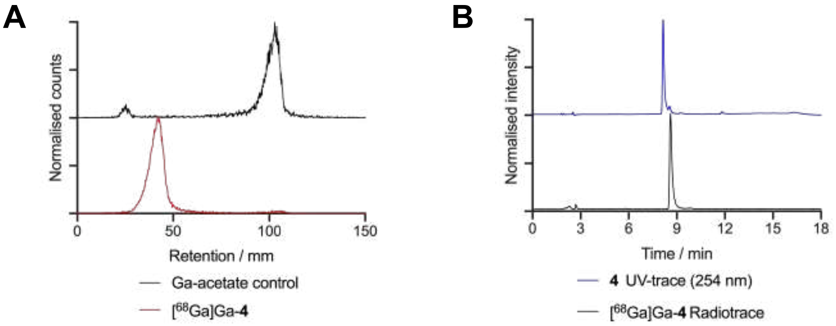

Scheme 2.9. Chemical synthesis of [^{68}Ga]Ga-DOTA-PEG$_4$-ArN$_3$ and photoconjugation to FH@APTES.

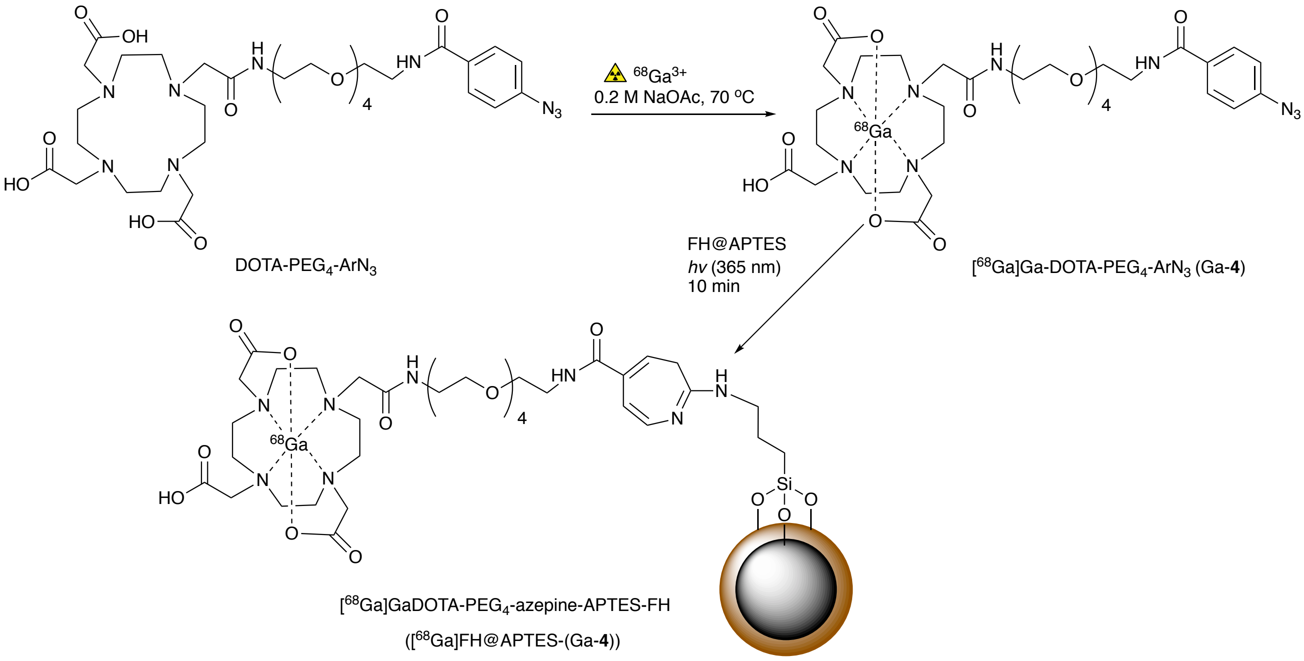

Figure 2.13. SEC-PD10 radiochemical characterisation data for **(A)** [^{68}Ga]FH@APTES-(Ga-**4**) and **(B)** Control reactions where [^{68}Ga]Ga-DOTA-PEG$_4$-ArN$_3$ and FH@APTES were incubated with no irradiation and [^{68}Ga]Ga-**4** and FH (no amine) are irradiated.

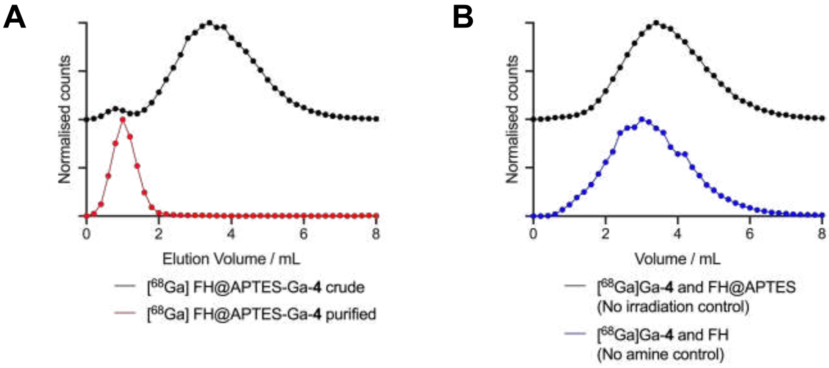

Photoconjugation to Fe$_3$O$_4$@Alendronate

Whilst FH@APTES could be radiolabelled by photoconjugation methods, the RCC was still relatively low at 4.1%. We hypothesised that whilst the dextran modified coating was providing stability at the required pH, its steric bulk was affecting the reactivity of the primary amines. Therefore, we modified the Fe$_3$O$_4$ nanoparticles synthesised by the co-precipitation method with alendronate, a method which has been previously reported to functionalise the surface of iron oxide nanoparticles.[318] Functionalisation was achieved via overnight agitation of the particles with alendronate followed by PD10-SEC purification, the amine content of the Fe$_3$O$_4$@Alendronate nanoparticles was determined to be 4.9 mM of amine in a 1 mg mL^{-1} solution of nanoparticle. The ζ-potential was determined to be -48.6 ± 7.9 mV which imbues the nanoparticles with the required stability at the pH necessary for photoconjugation.

Figure 2.14. Production obtained from the photoconjugation of [^{68}Ga]Ga-DOTA-PEG$_4$-ArN$_3$ to Fe$_3$O$_4$@Alendronate.

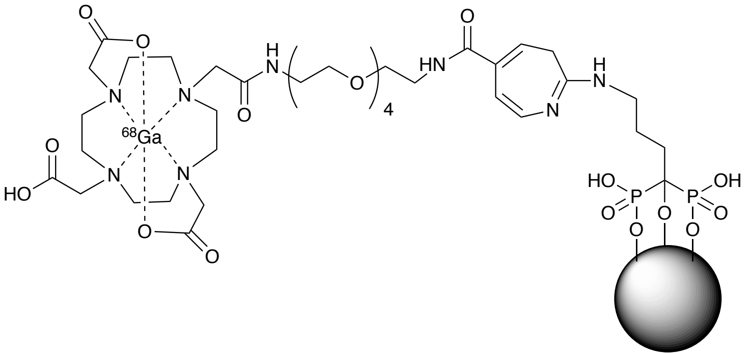

[^{68}Ga]GaDOTA-PEG$_4$-azepine-Alendronate-Fe$_3$O$_4$

([^{68}Ga]Fe$_3$O$_4$@Alendronate-(Ga-**4**))

The photoconjugation was carried out by using the same conditions as before, with irradiation at 365 nm for 10 min at pH8. However, due the slightly lower amine concentration on the Fe_3O_4@Alendronate nanoparticles in comparison to FH@APTES, the chelate concentration was lowered further. Here, a chelate concentration of 70 µM was present in the reaction with an amine concentration of 4.9 mM resulting in a RCC of 7.4 ± 0.3% (*n* = 3). Purification by PD10-SEC yielded [^{68}Ga]Ga-DOTA-PEG$_4$-azepine-Alendonate-Fe_3O_4 (**Figure 2.14**) in a decay-corrected RCY of 6.0 ± 0.2% (*n* = 3) and a RCP of 91% (*n* = 1)(**Figure 15A**). Again, controls were carried out analogous to those in the previous example (**Figure 2.15B**). Both the no amine ('RCC' = 1.6%) and no irradiation ('RCC' = 1.7%) indicated negligible conjugation, demonstrating the radiolabelling of Fe_3O_4@Alendronate with [^{68}Ga]Ga-DOTA-PEG$_4$-ArN$_3$ was occurring *via* a photochemical process.

Figure 2.15. PD10-SEC radiochemical characterisation data for, **(A)** [^{68}Ga]Fe_3O_4@Alendronate-(Ga-**4**), and **(B)** control reactions where [^{68}Ga]Ga-DOTA-PEG$_4$-ArN$_3$ and FH@Alendronate were incubated with no irradiation and [^{68}Ga]Ga-DOTA-PEG$_4$-ArN$_3$ and Fe_3O_4 (no amine) are irradiated.

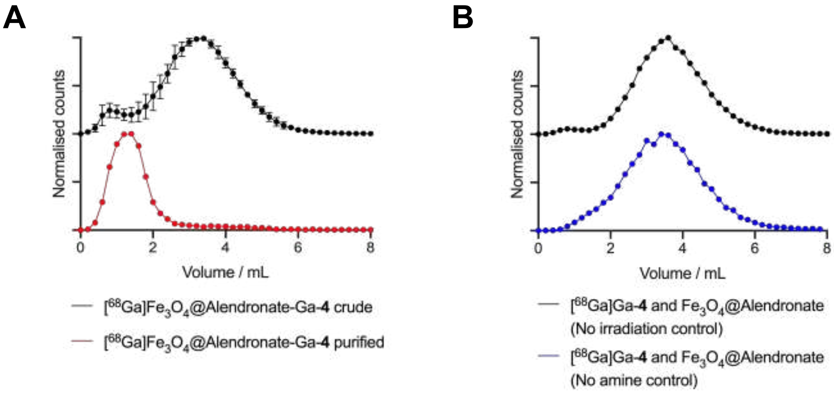

2.3.3 Results and discussion - Intrinsic radiolabelling of iron oxide nanoparticles

Radiomineralisation of nuclides onto nanoparticle surfaces

The intrinsic radiolabelling of a range of nanoparticles (**Figure 2.16**) has been tested using $^{68}Ga^{3+}$. Due to the gold coating of the Fe_2O_3@Au nanoparticles, chelate-free radiolabelling was not possible. However, an alternative method using ^{64}Cu ions is presented in section 3.3.2. All other nanoparticles could be radiolabelled intrinsically with $^{68}Ga^{3+}$.

Figure 2.16. Nanoparticles used for intrinsic radiolabelling.

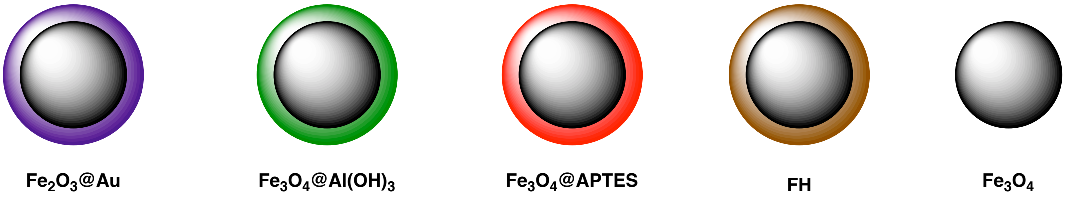

Fe_3O_4@$Al(OH)_3$ and Fe_3O_4@ATPES radiolabelling

Initially, nanoparticles synthesised using the thermal decomposition route (Fe_3O_4@$Al(OH)_3$ and Fe_3O_4@ATPES) were tested. Whilst the particles have the same iron oxide core, due to the difference in coatings, different temperatures were necessary to allow complete radiolabelling. At room temperature, Fe_3O_4@ATPES could be radiolabelled in 10 min at pH4.4 with a RCC of 98.2%. In contrast, the radiolabelling of Fe_3O_4@$Al(OH)_3$ at room temperature (10 min, pH4.4) only resulted in a RCC of 37.2% and elevated temperatures of 70 °C (10 min, pH4.4) were required to obtain a reasonable RCC of 96.1%.

Figure 2.17. Radio-iTLC for the intrinsic radiolabelling of, **(A)** Fe_3O_4@$Al(OH)_3$, and **(B)** Fe_3O_4@ATPES. Silica gel was used as the stationary phase and citrate buffer (1M, pH4.5) as the mobile phase.

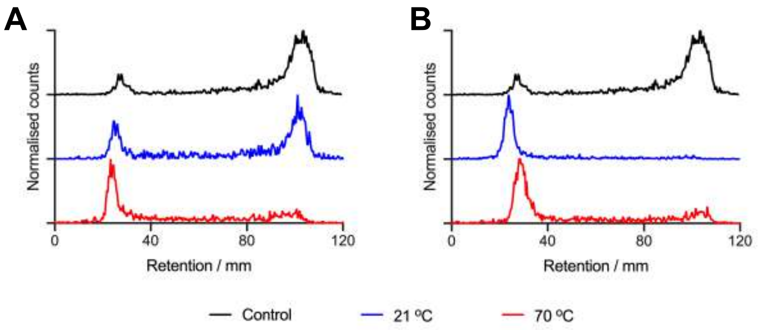

FH and Fe_3O_4 radiolabelling with $^{68}Ga^{3+}$

Next, we compared the radiolabelling of FH and Fe_3O_4. This study was carried out in more depth to investigate the effects of the nanoparticle coating and to gain some insight into the kinetics of the intrinsic radiolabelling. As expected, heating the nanoparticles in the presence of $^{68}Ga^{3+}$ led to incorporation of the radionuclide on the nanoparticle surface. Alternative TLC conditions were required due to the migration of the nanoparticles to the solvent front when using a standard citrate solution as the running buffer. For Fe_3O_4 we used a 1:1 H_2O:MeOH mixture acidified with 1% HCl. This moved any free $^{68}Ga^{3+}$ whilst ensuring that the radiolabelled nanoparticles remained at the baseline. Conversely, we used H_2O to move FH particles, whilst $^{68}Ga^{3+}$ remained at the baseline. When radiolabelling the nanoparticles with $^{68}Ga^{3+}$ at 70 °C for 10 min, these TLC conditions allowed us to determine a RCC of >98% (*n* = 3) for both nanoparticle constructs. We then used these established TLC conditions to determine the change in RCC over time with differing reaction temperatures (**Figure 2.18A, D, G & J**).

Figure 2.18. (A-C) Data associated with $^{68}Ga^{3+}$radiolabelling of Fe_3O_4 ; **(A)** Change in RCC over time, **(B)** associated second-order kinetics plot and **(C)** Eyring plot. **(D-F)** Data associated with $^{68}Ga^{3+}$radiolabelling of FH ; **(D)** Change in RCC over time, **(E)** associated second-order kinetics plot and **(F)** Eyring plot. **(G-I)** Data associated with $^{111}In^{3+}$radiolabelling of Fe_3O_4 ; **(G)** Change in RCC over time, **(H)** associated second-order kinetics plot and **(I)** Eyring plot. **(J-L)** Data associated with $^{111}In^{3+}$radiolabelling of FH ; **(J)** Change in RCC over time, **(K)** associated second-order kinetics plot and **(L)** Eyring plot.

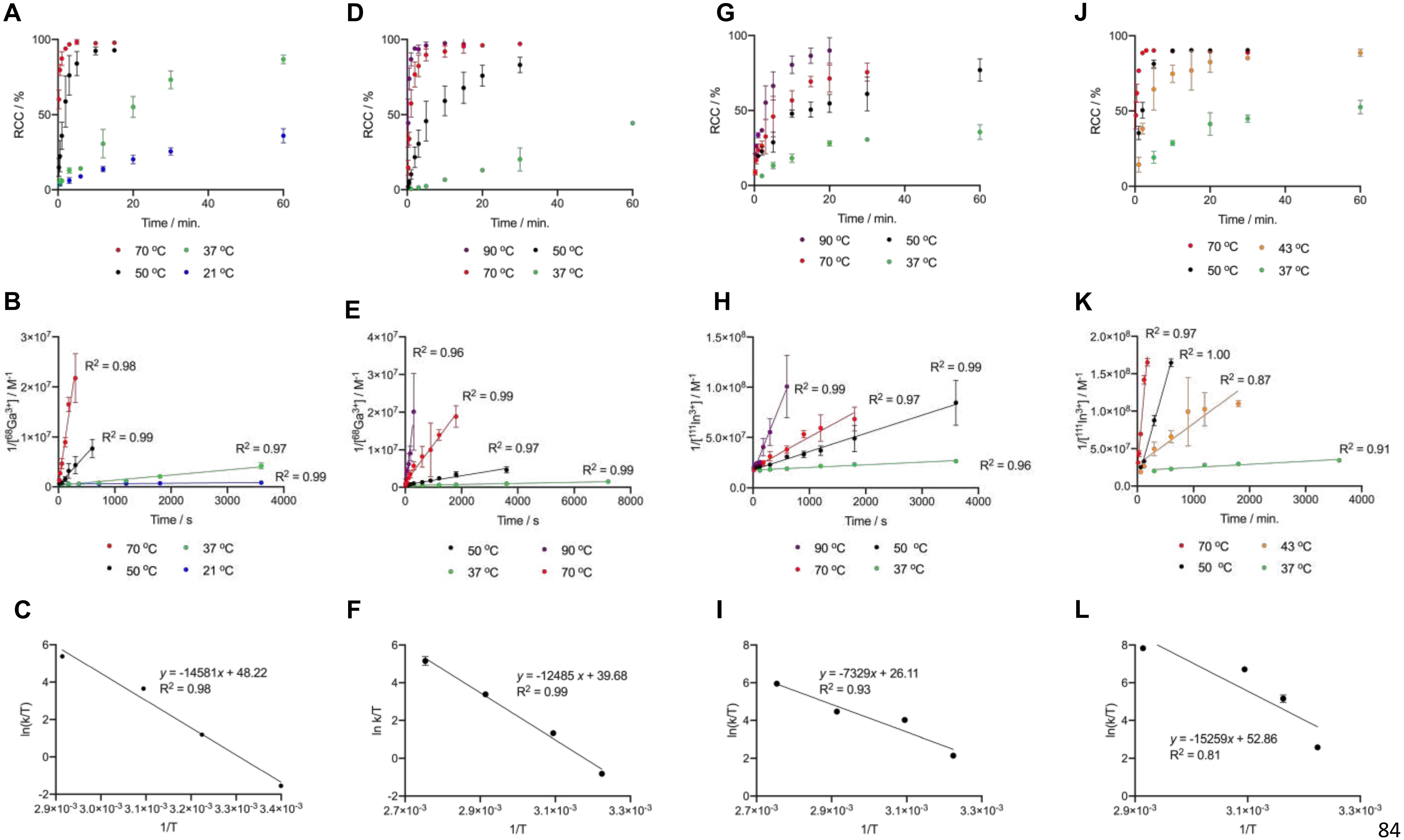

Kinetic interpretation of the data

It was initially assumed that reactions would follow pseudo-first-order kinetics. If we consider a particle with a diameter of 12.3 nm (diameter of Fe_3O_4), and we assume a spherical structure, this would equate to a volume of ~974 nm^3 and a surface area of ~475 nm^2. Magnetite has an inverse spinel structure with a unit cell formula of $(8Fe^{3+})(8Fe^{2+} + 8Fe^{3+})\ 32O^{2-}$ which equates to a volume of 0.59 nm^3. Each face of the unit cell has 8 O atoms at the surface and a surface area of 0.69 nm^2. From this we are able to deduce that there are 5.3×10^4 O atoms in the nanoparticle with 5.5×10^3 O atoms at the surface. Therefore ~10% of oxygen atoms reside at the nanoparticle surface. Each reaction contained 0.1 mg of iron, which would equate to 1.79 µmol iron and 2.4 µmol oxygen. With 10% of oxygen atoms at the surface, this would result in 0.24 µmol of surface oxygen atoms available in the reaction. Each reaction contained 0.19 nmol of Ga atoms which was calculated from obtaining the molar activity. With a 10^3-fold excess of surface oxygen atoms compared to Ga, an initial assumption of pseudo first-order is not unreasonable but the particle concentration is considerably lower. However, results proved otherwise. By fitting data to both pseudo-first-order and second-order kinetics, it was found that the experimental data reproducibly favoured second-order rate constants with increased regression coefficient (R^2) values (**Table 2.2**). From this second-order fitting, bimolecular (k_2 / $M^{-1}\ s^{-1}$) rate constants were obtained (**Figure 2.18**, **Table 2.3**). Transition state theory was applied and data were fitted using the Eyring equation (**Equation 2.2**) to obtain transition state energies.

Table 2.2. R^2 values when fitting data from, **(A)** FH, and **(B)** Fe_3O_4 radiolabelling with $^{68}Ga^{3+}$.

A

Temperature / °C	1st order fitting R^2	2nd order fitting R^2
90	0.36	0.96
70	0.79	0.99
50	0.72	0.97
37	0.99	0.99

B

Temperature / °C	1st order fitting R^2	2nd order fitting R^2
70	0.85	0.98
50	0.81	0.99
37	0.97	0.97
21	0.97	0.99

Equation 2.2. Linear Eyring equation.

$$\ln\left(\frac{k}{T}\right) = \frac{-\Delta H^{\ddagger}}{RT} + ln\left(\frac{k_B}{h}\right) + \frac{\Delta S^{\ddagger}}{R}$$

FH and Fe_3O_4 radiolabelling with $^{111}In^{3+}$

To further investigate the process of chelate-free radiolabelling we also measured the radiolabelling kinetics with $^{111}In^{3+}$. Again, radio-iTLC conditions were established that allowed separation of the free $^{111}In^{3+}$ and the radiolabelled nanoparticles (**Experimental**; **Section 6.2.2**). Using this method, reactions were monitored at different temperatures and the data obtained were fitted by using both first-order and second-order rate equations. As with $^{68}Ga^{3+}$ labelling, R^2 values proved higher when data were fitted to a second-order kinetic profile, and therefore, this model was used to find associated rate constants (**Table 2.3**).

Thermodynamic transition state parameters

Table 2.3 summarises the measured rate constants obtained and the corresponding thermodynamic transition state parameters from the kinetics studies on $^{68}Ga^{3+}$ and $^{111}In^{3+}$ radiolabelling of FH and Fe_3O_4. Whilst further experiments would be required to draw concrete conclusions, these initial data allows us to speculate on the factors affecting radiomineralisation.

Table 2.3. Rate constants associated with intrinsic radiolabelling of Fe_3O_4 and FH. Transition theory was used to calculate transition energies with $\Delta G^‡$ calculated at 298.15 K.

Nanoparticle	**Radionuclide**	**Temperature / °C**	**Rate constant / M^{-1} s^{-1}**	**$\Delta H^‡$ / kJ mol^{-1}**	**$\Delta S^‡$ / J K^{-1} mol^{-1}**	**$\Delta G^‡$ / kJ mol^{-1}**
Fe_3O_4	$^{68}Ga^{3+}$	70	7.46×10^4	121.2 ± 11.3	203.36 ± 36.9	60.6 ± 22.2
		50	1.25×10^4			
		37	1.02×10^3			
		21	6.25×10^1			
FH	$^{68}Ga^{3+}$	90	6.31×10^4	103.8 ± 6.66	132.6 ± 20.3	64.3 ± 12.1
		70	1.01×10^4			
		50	1.21×10^3			
		37	1.37×10^2			
Fe_3O_4	$^{111}In^{3+}$	90	1.39×10^5	60.9 ± 12.1	19.5 ± 36.5	55.1± 22.9
		70	3.00×10^4			
		50	1.80×10^4			
		37	2.65×10^3			
FH	$^{111}In^{3+}$	70	8.64×10^5	126.9 ± 43.2	241.9 ± 134.7	54.7 ± 19.4
		50	2.65×10^5			
		43	5.51×10^4			
		37	4.10×10^3			

There is a positive enthalpy of activation ($\Delta H^{\ddagger}$) associated with $^{68}Ga^{3+}$ and $^{111}In^{3+}$ radiolabelling of both Fe_3O_4 and FH**.** This was expected as our previous experiments had established that this was a heat-induced radiolabelling.[319] We can largely assign the positive enthalpy of activation to the energy required to de-solvate the $^{68}Ga^{3+}$ and $^{111}In^{3+}$ aqua complexes, $[^{68}Ga][Ga(OH_2)_6]^{3+}$ and $[^{111}In][In(OH_2)_6]^{3+}$. However, this does not explain the differences in $\Delta H^{\ddagger}$ observed between the Fe_3O_4 and FH nanoparticles when comparing the identical radionuclides. When observing the activation enthalpy for $^{68}Ga^{3+}$ radiolabelling it was found to be larger for the non-coated Fe_3O_4 nanoparticles ($\Delta H^{\ddagger}$ = 121.2 ± 11.3 kJ mol^{-1}) compared to the coated FH ($\Delta H^{\ddagger}$ = 103.2 ± 6.7 kJ mol^{-1}). A reasoning behind this can be found when we look at little closer at the ζ-potentials of the nanoparticles. The ζ-potentials of Fe_3O_4 and FH are -62.4 ± 3.5 and +38.1 ± 0.9 respectively. Whilst the carbohydrate coating of FH may cause a physical barrier between the radionuclide and the metal oxide surface, the negative charge of the coating is attractive to the metal cation and there is a reduction in electrostatic repulsion between the metal cation and the nanoparticle surface. As the carbohydrate coating is not present in the Fe_3O_4 nanoparticles, there is increased electrostatic repulsion between the nanoparticle surface and the metal cation resulting in an increased $\Delta H^{\ddagger}$. The radiolabelling of Fe_3O_4 with $^{111}In^{3+}$ resulted in a lower $\Delta H^{\ddagger}$ (60.9 ± 12.1 kJ mol^{-1}) in comparison to $^{68}Ga^{3+}$. $^{111}In^{3+}$ is a softer Lewis acid than $^{68}Ga^{3+}$ and the smaller charge-to-size ratio reduces the electrostatic repulsions felt due to the positive ζ-potential of the nanoparticles.

As radiolabelling is an associative mechanism, a negative entropy of activation ($\Delta S^{\ddagger}$) might be expected. However, a positive $\Delta S^{\ddagger}$ is observed for all experiments. This can mainly be attributed to two factors; (*i*) the de-solvation of the $^{68}Ga^{3+}$ and $^{111}In^{3+}$ aqua complexes and (*ii*) the disruption to the EDL solvation shell surrounding the nanoparticle surface. We could assume a greater change in $\Delta S^{\ddagger}$ for $[^{68}Ga][Ga(OH_2)_6]^{3+}$ de-solvation due to the hard water ligands binding tightly to the hard Ga^{3+} centre, however, there are no distinct patterns when comparing $\Delta S^{\ddagger}$ for $^{68}Ga^{3+}$ and $^{111}In^{3+}$ radionuclides. Therefore, we chose to investigate the disruption to the EDL solvation shell by monitoring the change surface charge. To do this we measured ζ-potential at different time points following the addition of Ga^{3+} and In^{3+} to FH and Fe_3O_4 (**Figure 20**). There is a dramatic increase in ζ-potential when Fe_3O_4 is labelled with Ga^{3+} which explains the increased entropy of activation ($\Delta S^{\ddagger}$). As the ζ-potential increases there is an alteration in the solvation shell resulting in a large rearrangement of solvation molecules during the transition state. The $\Delta S^{\ddagger}$ value is less pronounced with FH as the coating shields surrounding water molecules and prevents major changes of the solvation shell, causing a smaller change in transition state entropy with $\Delta S^{\ddagger}$ = 19.5 ± 36.5 J K^{-1} mol^{-1}. These properties of In^{3+} also cause a subtle change in the ζ-potential as it mineralises on the surface. This results in a smaller disruption of the solvation shell and a smaller $\Delta S^{\ddagger}$ in comparison to $^{68}Ga^{3+}$ labelling. Unfortunately, it is a little more difficult to draw conclusions from the $^{111}In^{3+}$ labelling of FH. Due to the increased pH of the FH nanoparticles, an acetate buffer was necessary as the formation of the insoluble $In(OH)_3$ was observed. Therefore, this reaction has a large $\Delta S^{\ddagger}$ (241.9 ± 134.7 J K^{-1} mol^{-1}) associated, however, this is likely due to the dissociation of the indium acetate complex.

Figure 2.20. Change in the ζ-potential of, **(A)** Fe_3O_4, and **(B)** FH over time at room temperature with following the addition of $^{68}Ga^{3+}$ and $^{111}In^{3+}$.

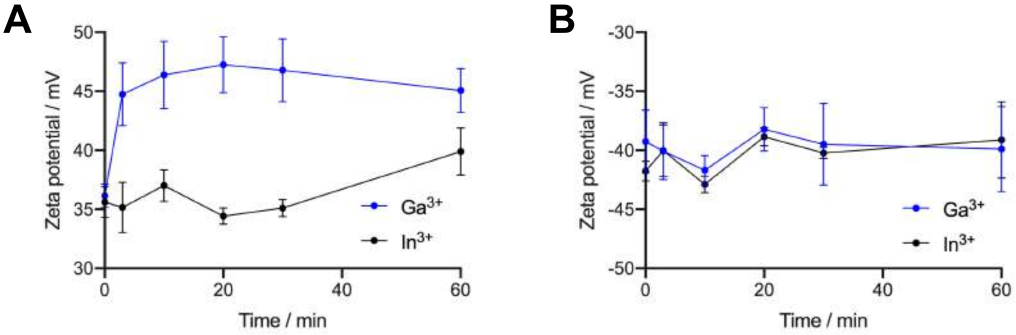

Thiol mediated radiolabelling of Fe_2O_3@Au

Basic Principles

Due to the Au coating of the Fe_2O_3@Au, surface radiomineralisation onto the iron oxide cannot occur and intrinsic radiolabelling with $^{68}Ga^{3+}$ ions could not be achieved by using the same methods described above. Zhao *et al*. have reported chelate-free radiolabelling of gold nanoparticles, although this was achieved via the radiochemical doping ('hot plus cold' precursor) method.[210] To our knowledge, there are no reports of the chemisorption of radionuclides onto the surface of pre-fabricated gold nanoparticles. Therefore, we sought to develop a method to achieve the chelate free radiolabelling of Fe_2O_3@Au.

Research from the group of Thomas Bürgi (University of Geneva) demonstrated the thiol mediated exchange of metal ions between stoichiometrically discrete gold nanoclusters with the molecular formula $Au_{38}(SC_2H_4Ph)_{24}$.[320,321] They discovered that the gold nanoclusters acquire small concentrations of silver atoms through interactions with the thiol groups present in the structure of the clusters. Based on these observations, we hypothesised that intrinsic radiolabelling of Au nanoparticles could occur via a thiol-mediated process.

Radiolabelling with $^{64}Cu^{2+}$

Initially, we established whether radiolabelling could be achieved without thiol functionalisation. Bare Fe_2O_3@Au nanoparticles were incubated with $^{64}Cu^{2+}$. After 60 min, radio-iTLC indicated confirmed radioactivity remained unbound and did not associate with the nanoparticle surface (**Figure 2.23**). Following this, we functionalised the Fe_2O_3@Au particles with thiol PEG which provided the surface thiol groups necessary whilst also offering stability. Incubation (1 h at 21 °C) of Fe_2O_3@Au with CH_3-PEG_n-SH (where n = 800) prior to treatment with $^{64}Cu^{2+}$ indicated successful radiolabelling. By using radio-iTLC, it was established that the radioactivity remained associated with the nanoparticles (**Figure 2.21A**); with 50 mM DTPA as the mobile phase 'free' $^{64}Cu^{2+}$ migrated to the solvent front whilst the nanoparticle product ([^{64}Cu]Fe_2O_3@Au-(-S-PEG_n-CH_3)-Cu) remained at the baseline. To determine the best reaction conditions varying temperatures were tested with aliquots taken at various time points (**Figure 2.21B**). It was found that at temperatures between 4 - 37 °C, RCCs increased between 0 - 60 min, whilst at 50 °C, RCCs increased until 20 min, when the nanoparticles precipitated from solution. Following the study, it was determined that the highest RCC occurred when heating at 37 °C for 1 h (RCC = 91.1 ± 1.8%, RCP = 85.3 ± 8.6%; *n* = 2) (**Figure 2.22B**) and 50 °C for 20 min (RCC = 93.3 ± 1.2%, RCP = 93.3 ± 1.2%; *n* = 2)(**Figure 2.22A**). Due to the increased RCP of the crude product at 50 °C for 20 min, the product was purified giving the radiolabelled product with a RCY of 74.8% and RCP of 99.6% (**Figure 2.22C**). Finally, it was necessary to establish that binding was not occurring *via* complexation to free thiol groups. Therefore, control reactions were performed by incubating $^{64}Cu^{2+}$ with CH_3-PEG_n-SH. Radio-iTLC confirmed that the activity did not associate with the CH_3-PEG_n-SH and remained free $^{64}Cu^{2+}$ (**Figure 2.23**).

Scheme 2.10. Thiol-mediated ^{64}Cu-radiolabelling of Fe_2O_3@Au. In the presence of thiolate species.

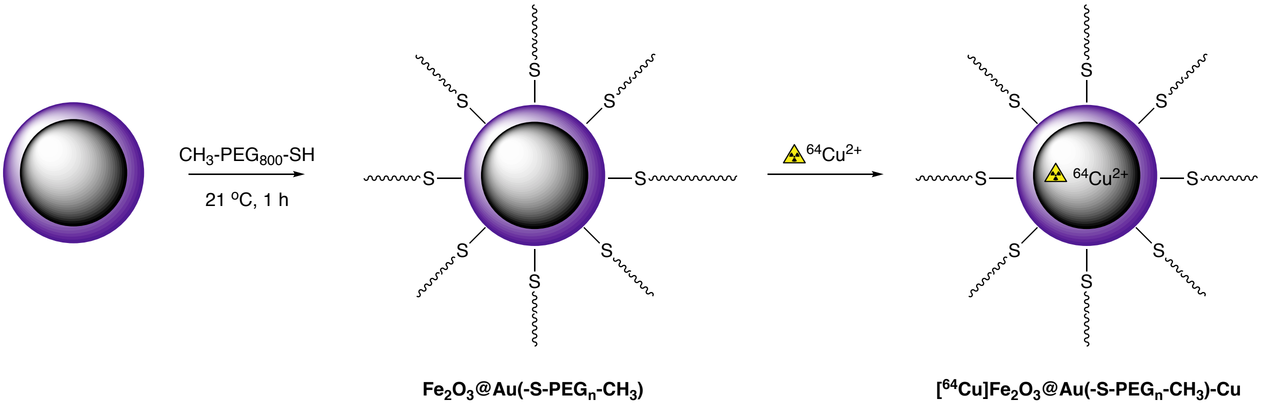

Figure 2.21. (A) Radio-iTLC for the thiol-mediated intrinsic radiolabelling of Fe_2O_3@Au(-S-PEG$_n$-CH$_3$) with $^{64}Cu^{2+}$. Silica gel as stationary phase and 50 mM DTPA as the mobile phase. **(B)** RCCs with differing temperatures and reaction times.

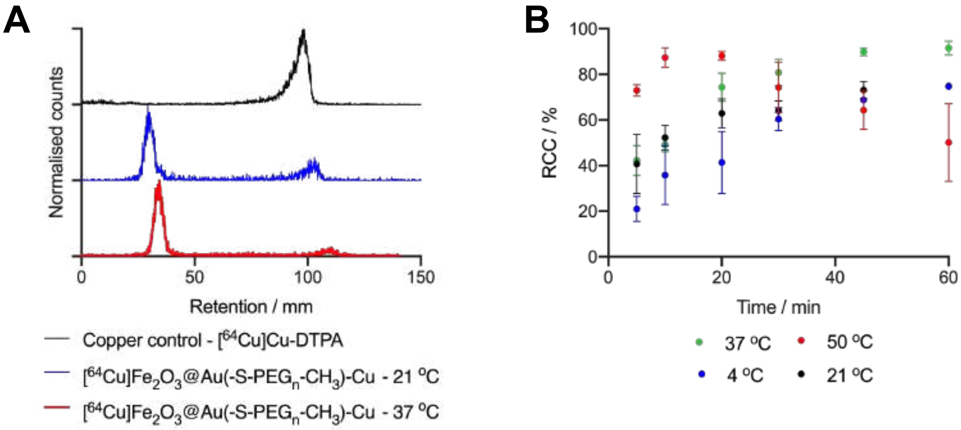

Figure 2.22. PD10-SEC profiles of crude reactions at, **(A)** 50 °C for 20 min, and **(B)** 37 °C for 1 h. **(C)** PD10-SEC profiles of purified product obtained from the reaction at 50 °C for 20 min.

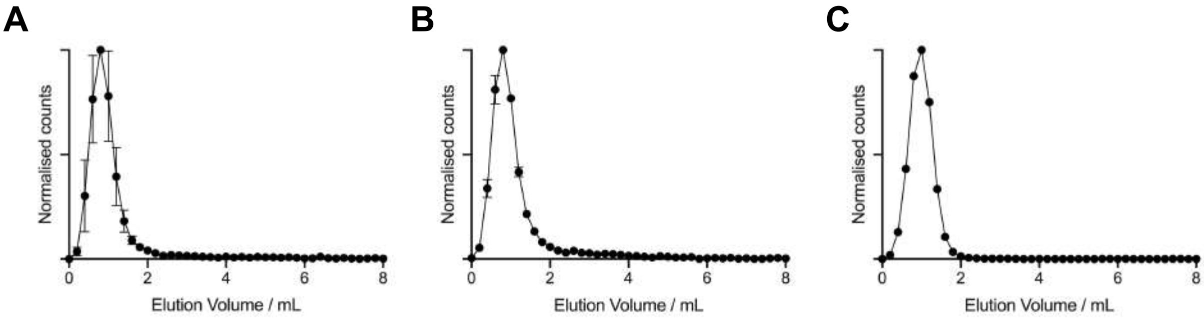

Figure 2.23. Control studies for thiol-mediated radiolabelling. Radio-iTLC of **(A)** Bare Fe_2O_3@Au and $^{64}Cu^{2+}$ and **(B)** CH_3-PEG$_{800}$-SH with $^{64}Cu^{2+}$. Silica gel as stationary phase and 50 mM DTPA as the mobile phase.

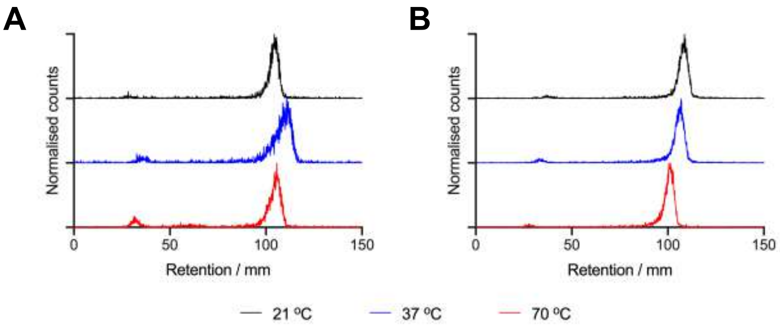

Summary

These experiments have demonstrated the thiol-mediated uptake of $^{64}Cu^{2+}$ radiometal ions into Fe_2O_3@Au(-S-PEG$_n$-CH_3) nanoparticles. Whilst the incorporation of other radionuclides has not been attempted, previous works demonstrate the uptake of Ag atoms, which indicates that this method has the potential to act as a versatile method to intrinsically label gold nanoparticles.[320]

2.4 Conclusion

Here, we have presented studies on the synthesis and characterisation of a variety of nanoparticle structures and their corresponding radiolabelling methods. Nanoparticles were synthesised by using the co-precipitation and thermal decomposition routes. For the latter, surface modifications allowed the transfer of nanoparticles from a dispersion in organic solvent to an aqueous phase, which was necessary for the subsequent radiochemistry and any potential biological applications.

Initially, classical radiolabelling routes were explored. Fe_2O_3@Au nanoparticles were labelled with a high RCC and RCP when using a disulphide, chelate-based method. FH and Fe_3O_4 nanoparticles were radiolabelled by using a photoconjugation method. To our knowledge, this is the first study of its kind, and data demonstrate that photoradiolabelling methods can potentially be adapted for use with nanoparticles. However, this photoconjugation route produced very low yields and further optimisation is required.

Chelate-free, intrinsic methods of radiolabelling were also investigated. Nanoparticles could be radiolabelled without the use of a chelate or prosthetic group which produces minimal change to the nanoparticle structure or properties. Our kinetic studies of $^{68}Ga^{3+}$ and $^{111}In^{3+}$ surface mineralisation have indicated that nanoparticles can be radiolabelled with high RCC in <5 min. This is beneficial as rapid radiolabelling in the final step of synthesis is an ideal method for making radiotracers with short-lived radionuclides. We have also developed a method for allowing the chelate-free radiolabelling of gold nanoparticles where thiols mediate uptake of the radionuclide, again fast reaction times and high RCCs highlight the benefits of employing this technique.

Overall, we have synthesised and investigated several nanoparticle constructs and explored methods by which to radiolabel them. In Chapter 3 we use these develop constructs to produce radiolabelled, biologically targeted nanoparticle constructs.

Chapter 3: Functionalised nanoparticles as targeted multi-modal PET/MR imaging agents

3.1 Aims of the chapter

Due to recent developments in PET/MRI technology, there is now a need for the development of multi-modal imaging agents. By combining PET and MRI capabilities into one construct, it would be possible to administer only one contrast agent into a patient as opposed to two. This prevents unreliable results due to differing pharmacokinetics and pharmacodynamics of the two contrast agents. As mentioned in the introduction, iron oxide nanoparticles are of importance in the design of PET/MR imaging agents due to their ability to accelerate the T_2 relaxation times of nearby protons. They can also be radiolabelled with a positron emitting radionuclide *via* classical or non-classical methods for PET imaging.

In this chapter, we utilised both the classical and non-classical radiolabelling methods which were developed in **Chapter 2**. Specifically, experiments used the ^{68}Ga-DOTGA-PEG$_4$-LA conjugation to Fe_2O_3@Au nanoparticles and the chelate free ^{68}Ga radiolabelling of the Feraheme® (FH). ^{68}Ga is an ideal radionuclide because it is readily available from a commercial ^{68}Ge/^{68}Ga generator and the relatively short half-life of ^{68}Ga minimises radiation exposure to the patients. A major aim of this work was to synthesise biologically targeted nanoparticles. For this purpose, we chose to target the nanoparticles towards PSMA. Here, we report the synthesis of two PSMA-targeted, radiolabelled nanoparticle constructs. This research is key in the development in PET/MR imaging agents for molecular imaging.

3.2. PSMA targeting

As introduced in **Chapter 1** (**Section 1.2.3**), PSMA is a transmembrane glycoprotein that is over-expressed in a number of prostate cancers.[24] Despite antibody binding being a possibility, small-molecule binders tend to be more favourable when developing diagnostic imaging agents as they exhibit shorter circulation times and increased tumour penetrability.[42] A large number of reported small-molecule binders belong to the group of urea-based compounds including Glu- NH-CO-NH-Lys analogues which are potent PSMA binders. For example, [^{68}Ga]Ga-Glu-NH-CO-NH-Lys(Ahx)-HBED-CC, which is commonly known as ^{68}Ga-PSMA-11, has a dissociation constant (K_d) value of 2.89 ± 0.55 nmol L^{-1} when binding to PSMA-expressing LNCaP cells.[322,323] Therefore, we selected small-molecule Glu-NH-CO-NH-Lys derivatives to target our nanoparticle constructs.

The synthesis of Glu-NH-CO-NH-Lys (**9**) is typically achieved *via* a resin-based approach.[324] However, solid-phase peptide synthesis (SPPS) is often only suitable for producing small quantities of product due to the use of expensive resins and preparative HPLC purification. Therefore, by modifying a published resin based synthesis, we devised a route where larger quantities of compound **9** could be obtained by simply purifying each product at each synthetic step (**Scheme 3.1**).[324] The Glu-NH-CO-NH-Lys residue contains two chiral centres. Due to the shape of the PSMA binding pocket the *S*,*S* (L-Glu, L-Lys) configuration exhibits binding, whilst the *R*,*R* enantiomer (D-Glu, D-Lys) and the

R,S (D-Glu, L-Lys) and *S,R* (L-Glu, D-Lys) diastereoisomers are reported as non-binders.[325] To obtain the *S,S*-configuration, the naturally occurring L-glutamic acid and L-lysine were used as starting materials. For compatibility with the triphosgene-mediated urea formation, a benzyl carbamate group (CBz) was used to protect the amine group in the lysine side chain. This CBz group allows selective deprotection, leaving the *t*-butyl carboxylic acid protecting groups in place. This produced compound **8** (in an overall yield of 11%), the *tris*-*t*-butyl protected Glu- NH-CO-NH-Lys residue where the free amine is available for further conjugation. The *t*-butyl groups can be removed by using acidic conditions to produce the fully deprotected compound **9**. These compounds are further used during this chapter to selectively targeted nanoparticles towards PSMA expressing cells.

Scheme 3.1. Chemical synthesis of Glu-NH-CO-NH-Lys, **9.**

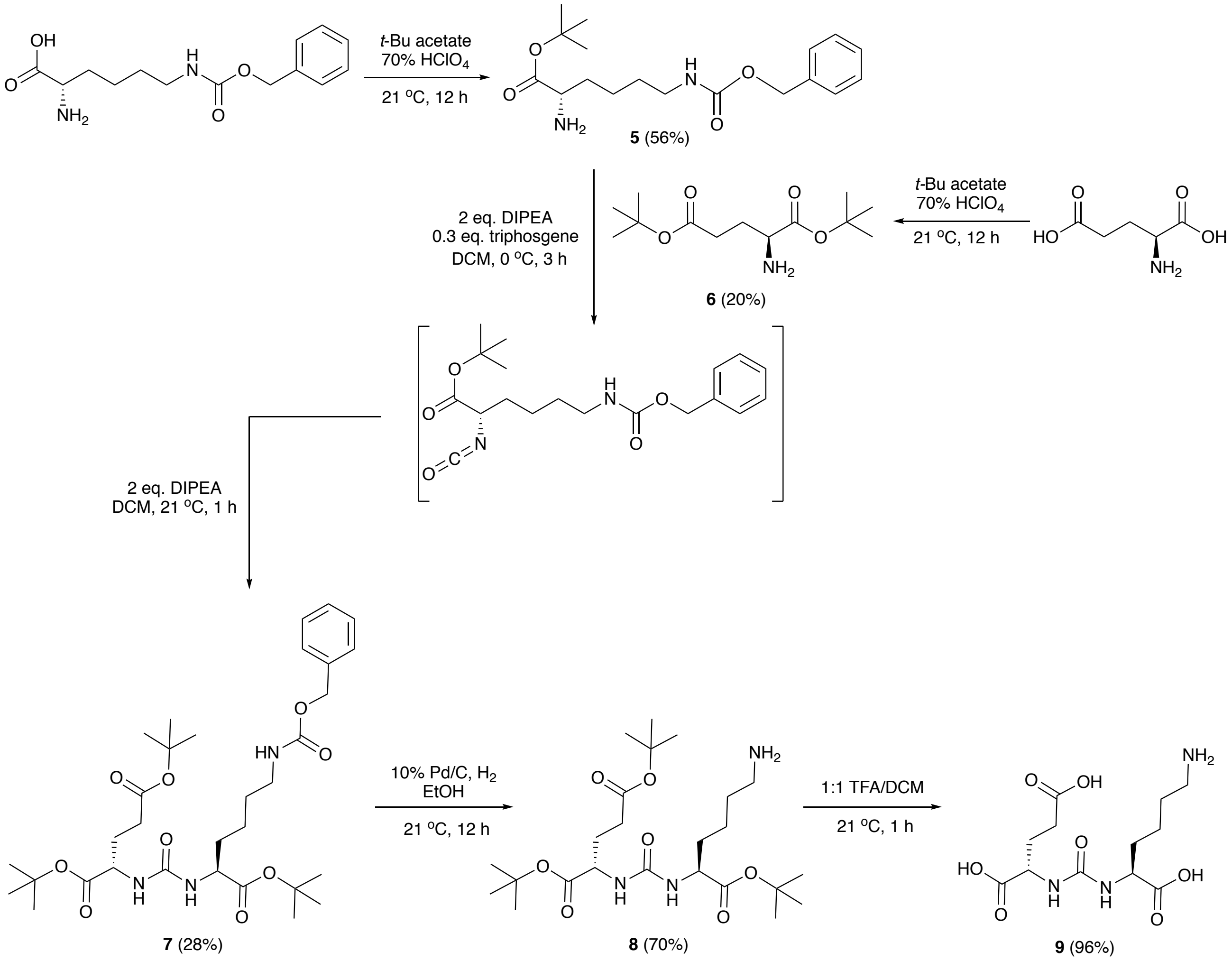

3.3 Chelate conjugated, ^{68}Ga radiolabelled, PSMA targeted gold coated iron oxide nanoparticles for PET/MR imaging

3.3.1 Introduction

In chapter 2, we introduced the Fe_2O_3@Au nanoparticles and their radiolabelling with a DOTAGA lipoic acid derivative ([^{68}Ga]Ga-**2**). Radiolabelling was easily achieved with high RCC and RCP. Whilst a two-step synthesis was necessary, the product could be obtained quickly in only 20 minutes from generator elution. Also, the disulphide interaction with gold was initially selected due to the reported strength of the Au-S bond and resistance to dissociation (Au-S bond dissociation energy, D^{o}_{298} = 418 ± 25 KJ mol^{-1}).[326–328] The radiolabelled Fe_2O_3@Au construct, therefore, became an ideal candidate to modify further for biological applications.

3.3.2 Results and discussion

Synthesis and Characterisation

As we had established the success of radiolabelling using a lipoic acid moiety, it was logical to functionalise compound **9** by using the same NHS activated lipoic acid (**Chapter 2**). The final compound, **10**, was obtained and characterised by NMR and HR-MS before functionalising the Fe_2O_3@Au NPs (**Scheme 3.2**). Since the maximum disulphide loading capacity of Fe_2O_3@Au was established previously by using [^{68}Ga]Ga-**2**, we worked at this total disulphide concentration with a 1:1 ratio of [^{68}Ga]Ga-**2** and **10**. Whilst we had established that the reaction was completed with [^{68}Ga]Ga-**2** in around 60 s, we incubated the reaction at room temperature for 5 min to ensure complete conjugation of compound **10** to the Fe_2O_3@Au NPs. Characterisation of [^{68}Ga]Fe_2O_3@Au-(Ga-**2**)-**10** by radio-iTLC gave a RCC >94% (*n* = 3), and PD10-SEC chromatography indicated a RCP of 95% (**Figure 3.1**).

Scheme 3.2. (A) Chemical synthesis of the Glu-NH-CO-NH-Lys lipoic acid derivative (Glu-NH-CO-NH-Lys-LA, **10**) **(B)** Modification of nanoparticles with [^{68}Ga]Ga-**2** and **10** to obtain [^{68}Ga]Fe_2O_3@Au-(Ga-**2**)-**10**.

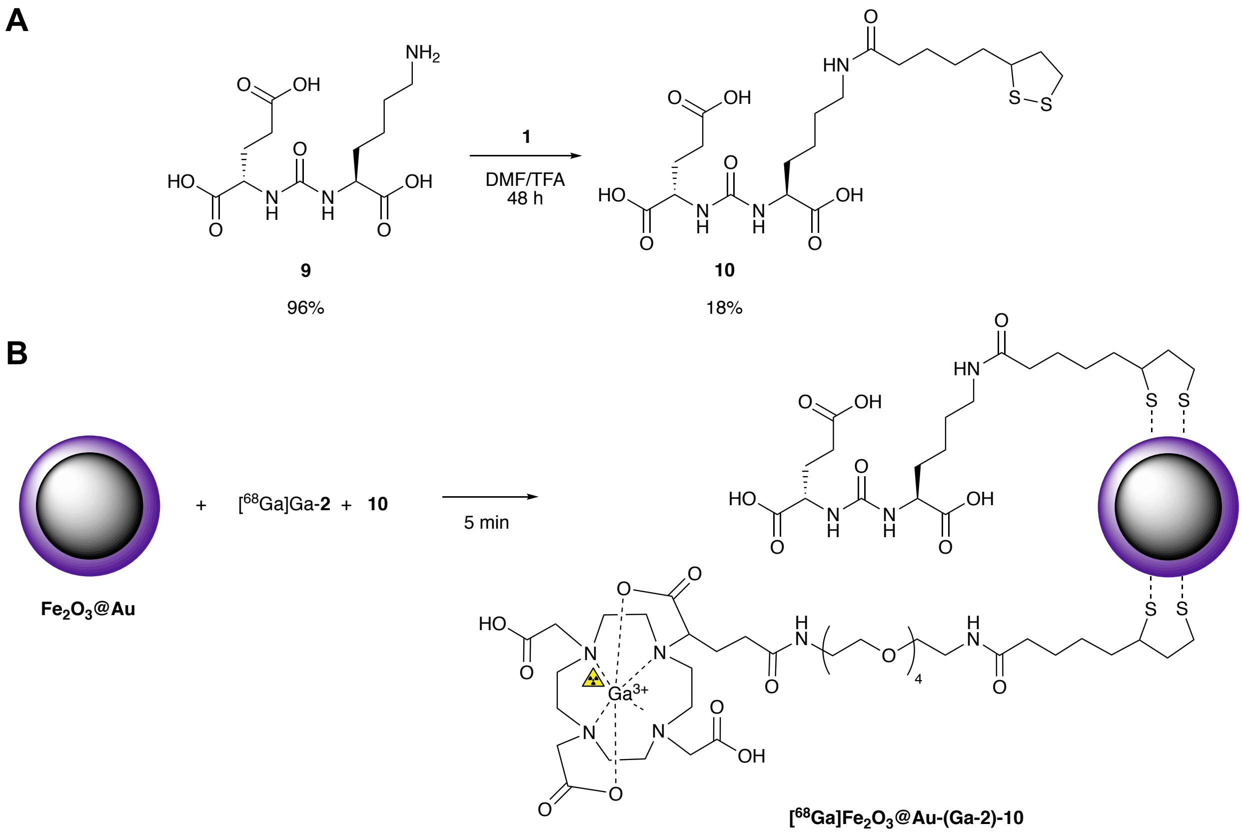

Figure 3.1. Radiochemical characterisation data for [^{68}Ga]Fe_2O_3@Au-(Ga-**2**)-**10** **(A)** Radio-iTLC with silica gel as stationary phase and MeOH/H_2O 1:1 with 0.5% HCl as the mobile phase. **(B)** PD10-SEC with water as the eluent.

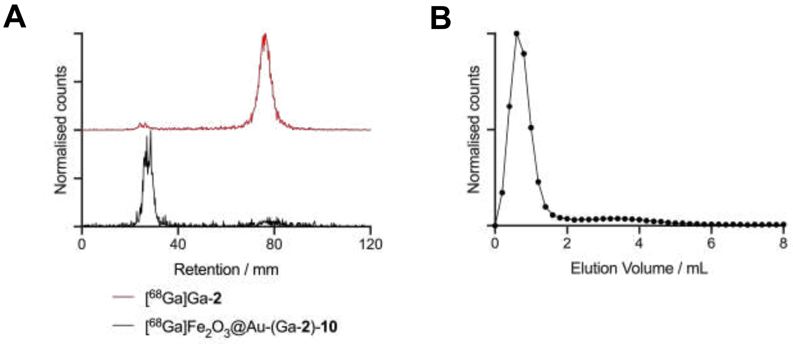

Figure 3.2. Structures of **(A)** [^{68}Ga]Fe_2O_3@Au-(Ga-**2**) and **(B)** [^{68}Ga]Fe_2O_3@Au-(Ga-**2**)-**10** used in further studies.

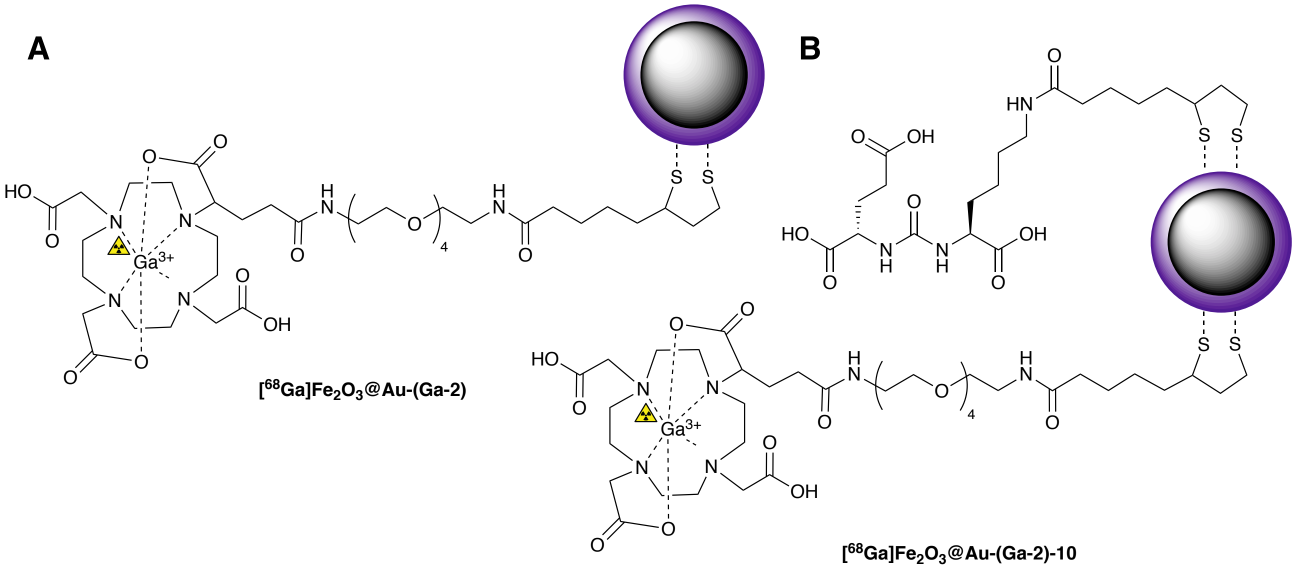

Following the successful synthesis of [^{68}Ga]Fe_2O_3@Au-(Ga-**2**)-**10**, we obtained two constructs for further characterisation and biological evaluation (**Figure 3.2**). [^{68}Ga]Fe_2O_3@Au-(Ga-**2**) was loaded with the same amount of [^{68}Ga]Ga-**2** to obtain equal specific activities for both constructs (12.1 kBq μg^{-1}). DLS analysis of the corresponding non-radiolabelled ('cold') constructs showed modification of the nanoparticle surface had little effect on the hydrodynamic diameter (**Figure 3.3** and **Table 3.1**). Repeated measurements were also taken 24 hours after functionalisation, indicating the stability of the functionalised nanoparticles in water with respect to aggregation over time. Functionalisation causes slight changes in T_2 relaxation times. Whilst these are only small variations, addition of the diamagnetic Ga^{3+} subtly decreased the T_2 relaxation time of the Fe_2O_3@Au-(Ga-**2**) construct in comparison to the bare Fe_2O_3@Au. In contrast, the Fe_2O_3@Au-(Ga-**2**)-**10** construct showed a slight increase in T_2 relaxation time. We postulate that this may be due to saturated disulphide layer limiting the proximity of the water molecules with the NP surface. ζ-potential measurements do not vary significantly and exhibit large errors, but the observed trends in the measured mean values are indicative of functionalisation. Functionalisation with Ga-**2** causes a decrease in ζ-potential with addition of the electronegative carboxylic acid and PEG groups, and this is further decreased with the addition of compound **10**.

Figure 3.3. DLS profiles of constructs

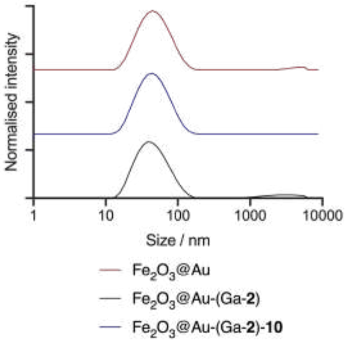

Table 3.1. Characterisation data for [^{68}Ga]Fe$_2$O$_3$@Au-(Ga-**2**) and [^{68}Ga]Fe$_2$O$_3$@Au-(Ga-**2**)-**10** (Fe$_2$O$_3$@Au present for comparison).

Compound	Hydrodynamic diameter / nm	ζ-potential / mV	T$_2$ relaxation time / ms
Fe$_2$O$_3$@Au	48.6 ± 25.0	-33.7 ± 14.7	24.86 ± 0.01
Fe$_2$O$_3$@Au-(Ga-2)	49.7 ± 24.53	-40.6 ± 10.4	23.70 ± 0.01
Fe$_2$O$_3$@Au-(Ga-2)-10	45.7 ± 22.3	-42.5 ± 13.3	28.77 ± 0.02

Stability studies

Whilst particles are stable in water, it was noticed that the nanoparticle constructs begin to aggregate in salt solutions (saline or PBS) over significant periods of time (>24 h). Stable Fe$_2$O$_3$@Au nanoparticles exhibit a pink/red appearance due to the SPR effect.[329] Following addition of saline or PBS particles appear black (**Figure 3.4A**) indicating aggregation of the nanoparticles. It was established that the addition of protein stabilised the nanoparticles *via* the formation of a protein corona.[330] When nanoparticles are exposed to protein, a dynamic, multi-layered 'cloud' is formed around the surface. This acts as a surfactant and prevents aggregation when nanoparticles are exposed to a highly ionic solution. **Figure 3.4** shows that the addition of fetal bovine serum (FBS) at concentrations of 10% and 1% stabilises the nanoparticles, preventing aggregation. The formulation at 1% was then used for further biological assays.

Figure 3.4. (A) Visible aggregation of the nanoparticles following addition of saline and PBS. Photograph was taken 24 hours after addition of solutions and samples were vortexed before immediately before to re-disperse aggregated particles. **(B)** UV-visible spectra recorded between 500-600 nm. Samples exhibit strong absorbance around 530 nm unless aggregated.

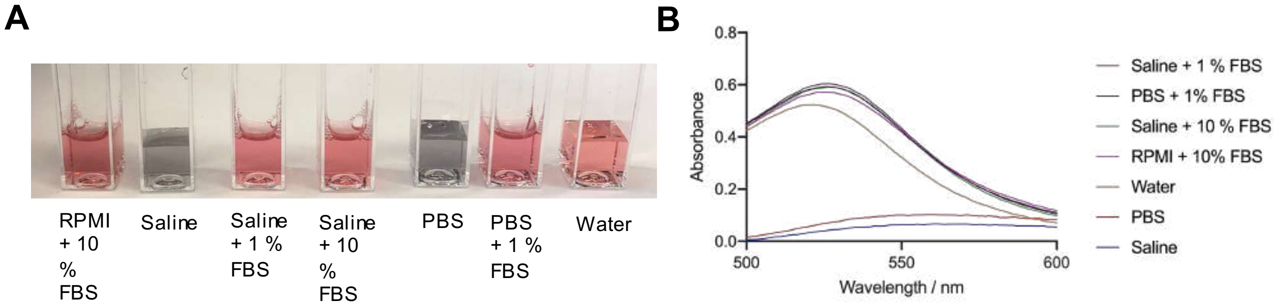

Prior to biological assays, it was important to establish the stability of the functionalised nanoparticles in physiologically relevent conditions. By incubating in different media, we were able to determine if free ^{68}Ga^{3+} or chelate bound ^{68}Ga^{3+} ([^{68}Ga]Ga-**2**) dissociated from the nanoparticle construct (**Figure 3.5**). Standard solutions of saline and PBS (both with the addition of 1% FBS) saw negligible dissociation of activity from the nanoparticles. An EDTA solution (pH7.1, 25 mM) was used as a chelate challenge and again, minimal loss of activity was observed. Due to the presence of disulphides and thiols *in vivo* it was important to establish their potential to displace [^{68}Ga]Ga-**2**. For this we used a solution of cysteine (25 mM) at a concentration far in excess of that found *in vitro* and *in vivo*.[331–333] We found that the majority of the activity remain bound to the particles. However, the greatest dissociation was seen at 2 h for [^{68}Ga]Fe_2O_3@Au-(Ga-**2**)-**10**. Here, 59% of activity remained bound. The greater loss was attributed to this nanoparticle having a more saturated surface than [^{68}Ga]Fe_2O_3@Au-(Ga-**2**), hence more displacement of the [^{68}Ga]Ga-**2** took place. Although a significant amount of dissociation is observed, both constructs remain relatively intact at the 1 h time point. Given the short half-life of ^{68}Ga, this time frame is acceptable for cell assays and *in viv*o imaging.

Figure 3.5. RCP over time of [^{68}Ga]Fe_2O_3@Au-(Ga-**2**) and [^{68}Ga]Fe_2O_3@Au-(Ga-**2**)-**10** when incubated with, **(A)** saline +1% FBS, **(B)** 25 mM EDTA, **(C)** PBS 1% FBS and **(D)** 25 mM cysteine for 2 h at 37 °C.

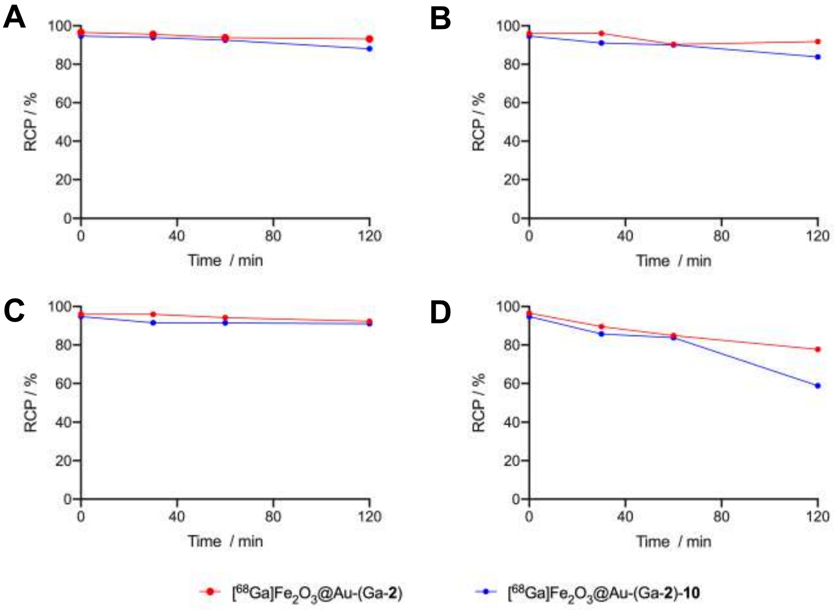

Cellular assays

Following successful synthesis and stability studies, the specific binding of the radiolabelled nanoparticles on PSMA-expressing cells was investigated. LNCaP cells are human prostate cancer cells derived from a metastatic site and are known to over express PSMA.[334] When incubating LNCaP cells (PSMA +ve) with [^{68}Ga]Fe_2O_3@Au-(Ga-**2**) and [^{68}Ga]Fe_2O_3@Au-(Ga-**2**)-**10** we observed an increase in uptake associated with the Glu- NH-CO-NH-Lys containing construct, [^{68}Ga]Fe_2O_3@Au-(Ga-**2**)-**10** (**Figure 3.6**). This is an initial indication that specific uptake is observed when the Glu-NH-CO-NH-Lys is present. It also acts as a positive indication that modification with **10** was successful, which was to be expected given that the chemistry of the conjugating group was identical to that of [^{68}Ga]Ga-**2**. To further investigate the specificity of the cellular uptake, a parallel experiment with the addition of 0.1% sodium azide was performed. Azide inhibits phagocytosis, preventing the internalisation of the nanoparticles. When azide was present, an approximate 3-fold decrease in uptake was observed for both [^{68}Ga]Fe_2O_3@Au-(Ga-**2**) and [^{68}Ga]Fe_2O_3@Au-(Ga-**2**)-**10**, which indicated a large proportion of nanoparticle uptake is due to phagocytosis of the nanoparticles. A blocking study was also carried out where cells were pre-incubated with the free PSMA ligand (Glu-NH-CO-NH-Lys, **9**). This prevents the binding of [^{68}Ga]Fe_2O_3@Au-(Ga-**3**)-**10** causing an approximate 2-fold decrease in comparison to the non-blocked sample. Finally, we compared the binding of the nanoparticles on LNCaP (PSMA +ve) cells with that observed on PC-3 (PSMA -ve) cells which do not express the PSMA protein. When using PC-3 cells (highlighted in blue, **Figure 6**), no significant difference was observed in the binding of [^{68}Ga]Fe_2O_3@Au-(Ga-**2**) and [^{68}Ga]Fe_2O_3@Au-(Ga-**2**)-**10**, indicating that the cellular association was non-specific. Also by comparing [^{68}Ga]Fe_2O_3@Au-(Ga-**2**)-**10** in LNCaP (PSMA +ve) and PC-3 (PSMA -ve) cell lines, we observed an approximate 2.5-fold decrease when PSMA is not present.

Figure 3.6. Cellular binding assay of [^{68}Ga]Fe_2O_3@Au-(Ga-**2**) and [^{68}Ga]Fe_2O_3@Au-(Ga-**2**)-**10** with the LNCaP (PSMA +ve) and PC-3 (PSMA –ve) cell lines. Data given as activity bound per 1 mg mL^{-1} of protein. Where stated cell media contained 0.1% azide and protein content was measured using a BCA assay. For the LNCaP cell line: [^{68}Ga]Fe_2O_3@Au-(Ga-**2**) *versus* [^{68}Ga]Fe_2O_3@Au-(Ga-**2**)-**10**, $p \leq 0.01$. When azide was present: [^{68}Ga]Fe_2O_3@Au-(Ga-**2**) *vs.* [^{68}Ga]Fe_2O_3@Au-(Ga-**2**)-**10**, $p \leq 0.05$. Blocking assay with the LNCaP (PSMA +ve) cell line pre-treated with free Glu-NH-C(O)-NH-Lys ligand (5 μM) before addition of radiotracers. For [^{68}Ga]Fe_2O_3@Au-(Ga-**2**)-**10**: blocked vs. non-blocked: $p \leq 0.01$. Comparison of cell lines: PC-3 *versus* LNCaP [^{68}Ga]Fe_2O_3@Au-(Ga-**2**)-**10**, $p \leq 0.01$; [^{68}Ga]Fe_2O_3@Au-(Ga-**2**), ns. Note: Student's *t*-test analysis: ns = not significant, * = *P*-value <0.05, ** = *P*-value <0.01, *** = *P*-value <0.001.

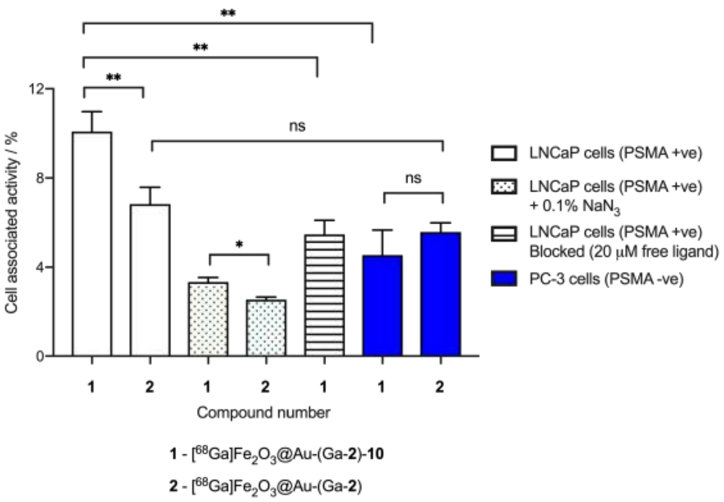

***In vivo* studies**

Following the success of the cellular assays, the distribution of the PSMA-targeted [^{68}Ga]Fe_2O_3@Au-(Ga-**2**)-**10** was evaluated *via* the acquisition of PET images (**Figure 3.7**). For ethical reasons, an initial pilot study was performed by using a single athymic nude mouse bearing a subcutaneous LNCaP tumour. Unfortunately, no significant tumour uptake was observed. By 30 min the majority of activity was found in liver where it remained, with very little change observed at 3 h. Activity can also be seen in the bladder which is indicative of chelate dissociation or demetallation of the $^{68}Ga^{3+}$ from the nanoparticle. However, the excretion of activity by the renal pathway was minimal in comparison to the retention of activity in the liver allowing us to conclude that the particles remain relatively stable whilst in the blood pool. It can be assumed that liver uptake is due to macrophage uptake, particularly phagocytic Kupffer cells. Whilst the surface charge is already negative this could be improved further by, for example, the addition of a PEG coating. Furthermore, the presence a protein corona may alter the surface charge *in vivo* and this may flag the constructs to macrophages. Due to the rapid blood pool clearance, and dominant sequestration of the activity in the liver observed in the pilot study, no further imaging experiments were performed on these constructs.

Figure 3.7. Coronal PET images recorded at 30 min and 3h post-administration of [^{68}Ga]Fe_2O_3@Au-(Ga-**2**)-**10** in a mouse bearing an LNCaP tumour, T = tumour.

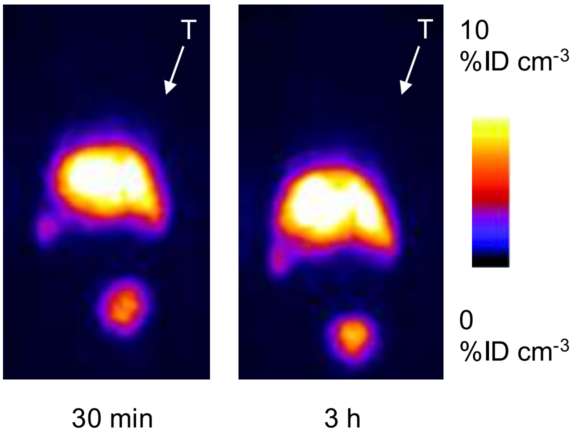

3.3.3 Conclusion

In summary, we have synthesised Fe_2O_3@Au nanoparticles targeted towards PSMA and radiolabelled with ^{68}Ga using a DOTAGA-PEG derivative. Whilst promising radiochemical and cellular results were obtained, imaging *in vivo* proved unsuccessful. Whilst a small PEG chain is conjugated to the nanoparticles, experimental evidence indicated that this is insufficient to prevent clearance from the blood pool and uptake *via* the macrophage system causing accumulation and retention of the activity in the liver. To improve this, a longer polymer PEG chain coating could be used, which would hopefully allow delivery to the tumour site.

3.4. Chelate free, ^{68}Ga radiolabelled, PSMA targeted Feraheme® nanoparticles for PET/MR imaging

3.4.1 Introduction

Following the successful chelate free ^{68}Ga radiolabelling of FH, we chose this method to develop a biologically targeted, chelate-free radiolabelled nanoparticle. To modify the nanoparticles, we chose to use a bisphosphonate anchor. Bisphosphonates are known to have a high affinity for metals and can even coordinate to numerous different metal ions forming complexes.[335] They are also known to conjugate to the surface of iron oxide nanoparticles.[336] Therefore, research focused on the synthesis of a Glu-NH-CO-NH-Lys bisphosphonate derivative. The resulting compound was used to modify FH before subsequent radiolabelling and biological studies.

3.4.2 Results and discussion

Synthesis of small molecules

Scheme 3.3. Synthesis of the PEGylated ethyl protected bisphosphonate, **13**, NH_2-CH_2-CH_2-PEG_4-C(O)NH-$C(PO(OEt)_2)_2$.

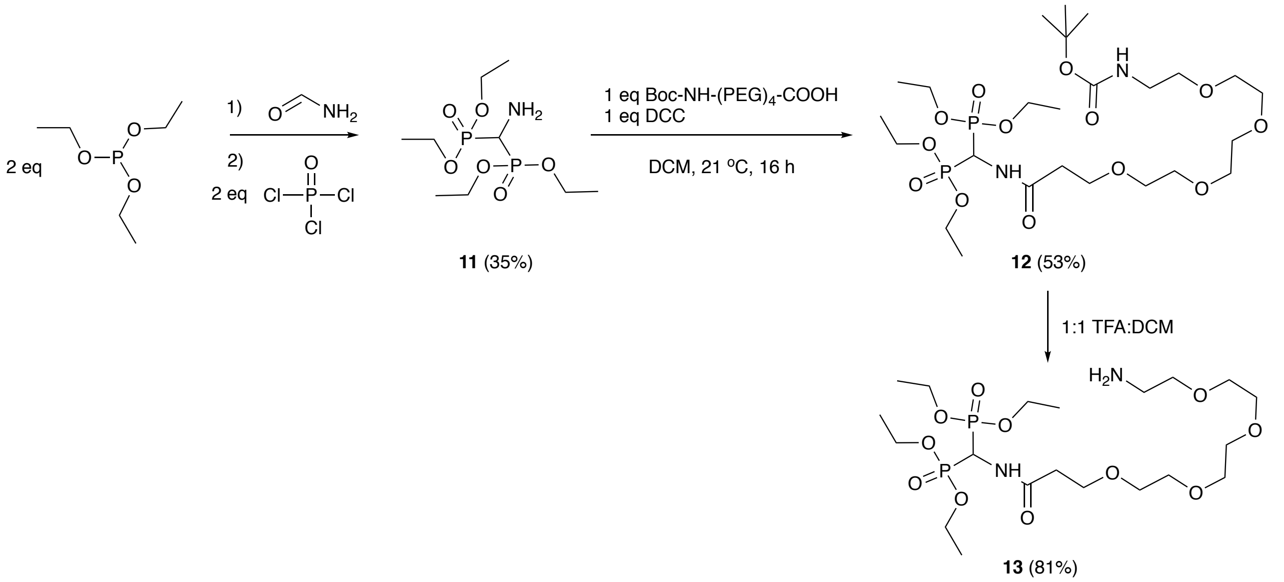

To allow for easier purification, the ethyl protected bisphosphate (**11**) was first synthesised by using literature methods.[337] An amide coupling was then performed to conjugate a *tert*-butyloxycarbonyl (BOC) protected PEG_4 linker. Following deprotection, compound **13** was obtained in 81% yield which provided a basis for further modification at the free amine. Two derivatives of **13** were synthesised, the first being the Glu-NH-CO-NH-Lys in the *S,S* (L-Glu, L-Lys) configuration (**Scheme 3.4**). A urea linkage between **9** and **13** was synthesised by using the triphosgene-generated isocyanate intermediate of **9**. This was attacked by the free amine of **13** creating **14** *via* nucleophilic addition. Following deprotection of the *tert*-butyl groups in acidic conditions, the bisphosphonate groups were deprotected by using bromotrimethylsilane (TMBS). This yielded the final compound **16** in an overall yield of 31%. The second derivative of **13** synthesised was the negative control, featuring the *R*,*R* enantiomer (D-Glu, D-Lys) of Glu-NH-CO-NH-Lys. In this configuration, no binding to PSMA is reported. In analogous conditions **21** was synthesised (**Experimental**; **Scheme 6.11**).

Scheme 3.4. (A) Chemical synthesis of the functionalisation of the PEGylated bisphosphonate with the PSMA binding motif (BP-(PEG)$_4$-NH-CO-Glu-NH-C(O)-NH-Lys). **(B)** Chemical structure of the inactive *R*,*R*-enantiomer.

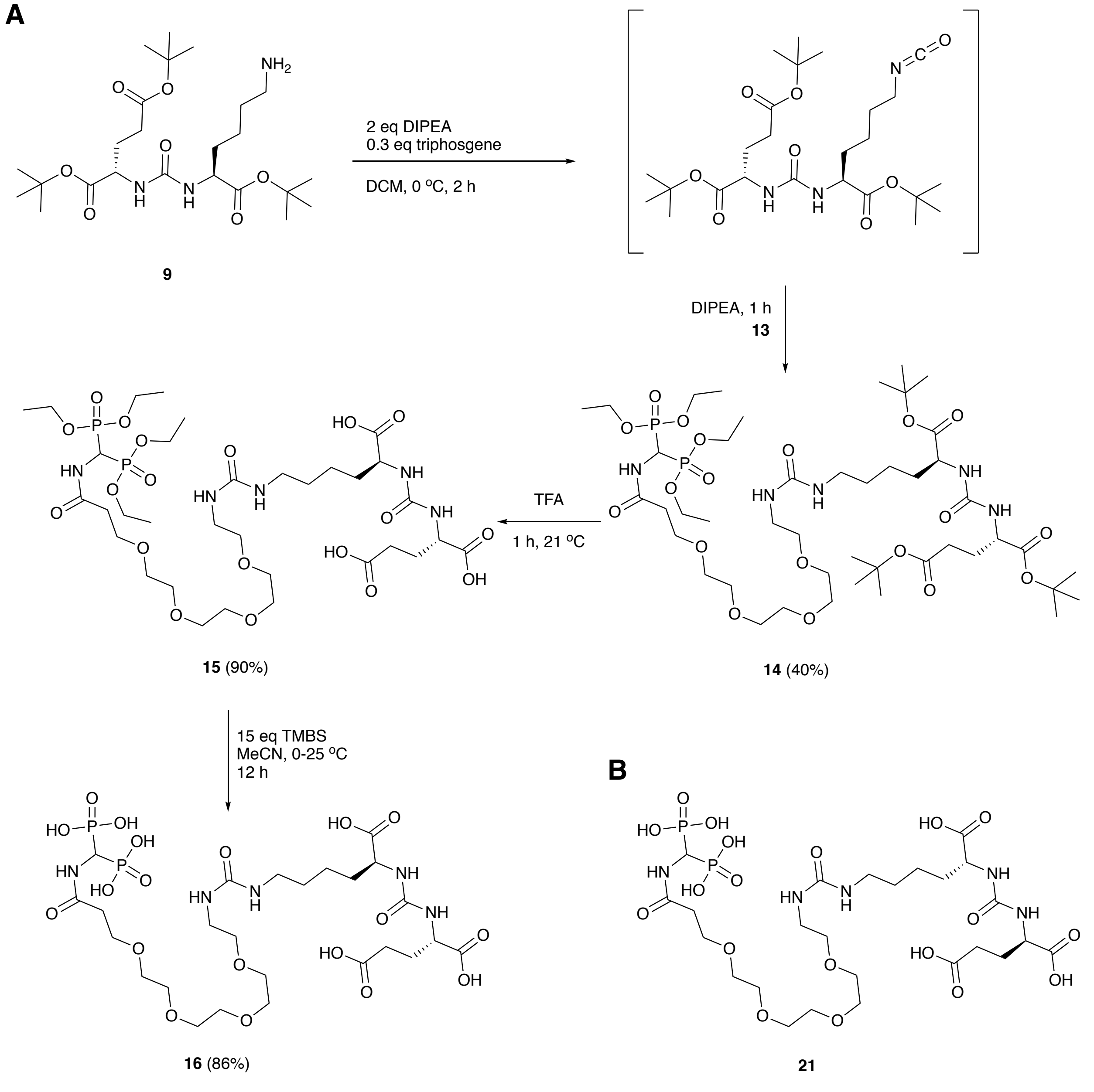

Functionalisation of FH

Following the successful synthesis of the bisphosphonate Glu- NH-CO-NH-Lys derivatives, compounds **16** and **21** were used to modify FH nanoparticles. After overnight reactions and PD10-SEC purification, FH-**16** and FH-**21** were obtained. ICP-MS measurements and ζ-potentials were initially used to establish successful modification. ICP-MS analysis indicated that phosphorous was present in comparison to non-functionalised FH particles. FH-**21** contained 2.99 ± 0.11 μg of phosphorous per 1 mg of iron compared with FH which only contained 0.049 ± 0.001 μg. Secondly, ζ-potential measurements indicated lower ζ-potentials when functionalised with the **16** and **21** (**Table 3.2**). This is expected due to the addition of both the bisphosphonate group and the carboxylated PSMA groups. Interestingly, ζ-potentials differ before and after PD10-SEC, for example, bare FH goes from -57.8 ± 6.29 mV to -7.51 ± 0.54 mV. This is partially due to the fact saline is used as the eluent, hence, this highly ionic solvent alters the solvation shell. However, this decrease could also be due to a break-down in the dextran coating. Unfortunately, we did not study the stability of the coating towards Sephadex® material used as the stationary phase in the PD10 column; however, this could be a possible cause for the dramatic increase in ζ-potential.

Table 3.2. ζ-potential measurements of FH, FH-**16** and FH-**21**. This highlights the importance of dispersant and the effects of exposing the nanoparticles to PD10-SEC.

Particle type	Before/after PD10-SEC	Dispersant	ζ-potential / mv
FH	Before	Water	-57.8 ± 6.29
FH	After	Saline	-7.51 ± 0.54
FH-**16**	After	Saline	-17.0 ± 0.52
FH-**21**	After	Saline	-15.3 ± 1.59

Figure 3.8. Hydrodynamic diameter of FH-**16** (20.22 ± 5.99 nm) and FH-**21** (21.05 ± 6.41 nm)

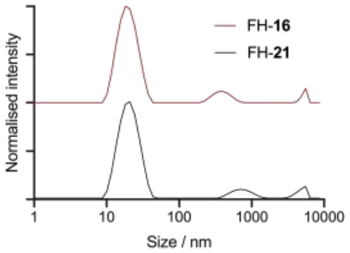

Radiochemistry

Radiolabelling was achieved in 20 min with gentle heating (70 °C) of the nanoparticles. For both FH-**16** and FH-**21**, a RCC >98% was achieved and RCP >94% (**Figure 3.9**). This provided high specific activities of 1.15 MBq μg^{-1} for [^{68}Ga]FH-**16**-Ga and [^{68}Ga]FH-**21**-Ga. The radio-mineralisation process facilitates this high loading of $^{68}Ga^{3+}$ ions onto the nanoparticle surface. Therefore, this method of non-classical chelate-free radiolabelling provides high specific activities with high RCCs and RCPs in a simple, one-step synthesis. The stabilities of the [^{68}Ga]FH-**16**-Ga and [^{68}Ga]FH-**21**-Ga constructs were evaluated by incubation in saline, PBS and EDTA (40 mM, pH7.1) (**Figure 3.10**). Constructs remained stable when incubated with saline and PBS for 2 h at 37 °C, with minimal dissociation of activity from the nanoparticle surface. The chelate challenge showed a considerable amount of dissociation (50%) when particles were exposed to EDTA. However, up to 1 h this loss is negligible, and the concentration is considerably higher than any conditions that would be experienced *in vivo*.

Figure 3.9. Radiochemical characterisation data for [^{68}Ga]FH-**16**-Ga and [^{68}Ga]FH-**21**-Ga. **(A)** Radio-iTLC data with silica gel as stationary phase and citrate buffer as mobile phase. RCCs were extracted and found to be 99.1 ± 0.5% for [^{68}Ga]FH-**16**-Ga and 98.6 ± 0.3% for [^{68}Ga]FH-**21**-Ga (where *n* = 3). **(B)** PD10-SEC traces with saline as eluent. RCPs were found to be 95.2% for [^{68}Ga]FH-**16**-Ga and 94.3% for [^{68}Ga]FH-**21**-Ga.

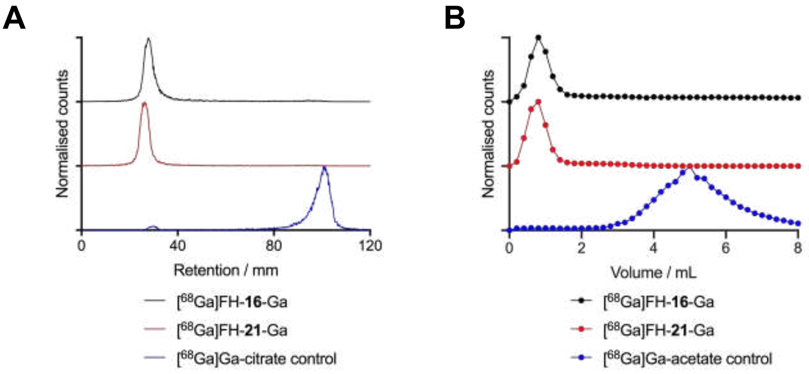

Figure 3.10. RCP over time of [^{68}Ga]FH-**16**-Ga and [^{68}Ga]FH-**21**-Ga when incubated with **(A)** PBS, **(B)** saline, **(C)** and 40 mM EDTA solution for 2 h at 37 °C and pH7.1.

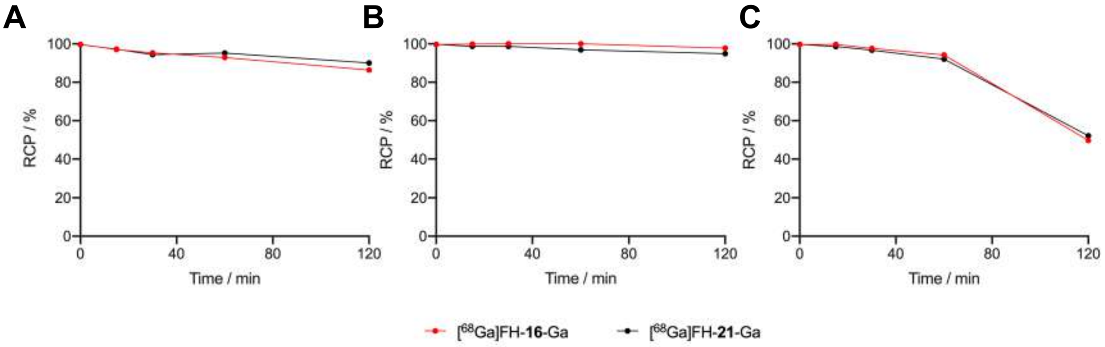

Cellular assays

Following successful radiochemical stability studies, cellular assays were performed to evaluate the specific uptake of the nanoparticle constructs. **Figure 3.11A** shows the cellular binding of constructs [^{68}Ga]FH-**16**-Ga and [^{68}Ga]FH-**21**-Ga to LNCaP (PSMA +ve) cells. When no azide is present, no significant difference was observed between the binding of [^{68}Ga]FH-**16**-Ga and [^{68}Ga]FH-**21**-Ga on LNCaP cells. Whilst the mean cell associated activity is in favour of increased [^{68}Ga]FH-**16**-Ga uptake, it would appear that non-specific internalisation is causing a large error associated with the result. When cells are exposed to azide during the cellular binding assay, a significant difference in cell uptake was observed between [^{68}Ga]FH-**16**-Ga *versus* [^{68}Ga]FH-**21**-Ga. Here, internalisation is prevented and results reflect the PSMA binding on the surface of the cell. To confirm this specific uptake, a blocking assay was performed (**Figure 11B**). In contrast to other PSMA blocking assays performed during this thesis, here, 2-PMPA was used as opposed to the free Glu-NH-CO-NH-Lys ligand (**10**). 2-PMPA is a well-known PSMA binder, introduced in **Chapter 1** (**Section 1.2.3**).[25] When cells are treated with 2-PMPA prior to the addition of [^{68}Ga]FH-**16**-Ga, a significant decrease in the uptake of the radiotracer was observed.

Figure 3.11. **(A)** Cellular binding assay of [^{68}Ga]FH-**16**-Ga and [^{68}Ga]FH-**21**-Ga with the LNCaP (PSMA +ve) cell line. Data given as the percentage of activity bound normalised per 1 mg mL^{-1} of total protein. When stated cell media contained 0.1% azide, and protein content was measured using a BCA assay. [^{68}Ga]FH-**16**-Ga *vs.* [^{68}Ga]FH-**21**-Ga (with azide), $p \leq 0.001$; [^{68}Ga]FH-**16**-Ga *vs.* [^{68}Ga]FH-**21**-Ga (no azide), ns. **(B)** Blocking assay with the LNCaP (PSMA *+ve*) cell line pre-treated with 2-PMPA (5 µM) before addition of [^{68}Ga]FH-**16**-Ga. Blocked [^{68}Ga]FH-**16**-Ga: with azide, $p \leq 0.05$; without azide, $p \leq 0.001$. Note: Student's *t*-test analysis: ns = not significant, * = *P*-value < 0.05, ** = *P*-value < 0.01, *** = *P*-value < 0.001.

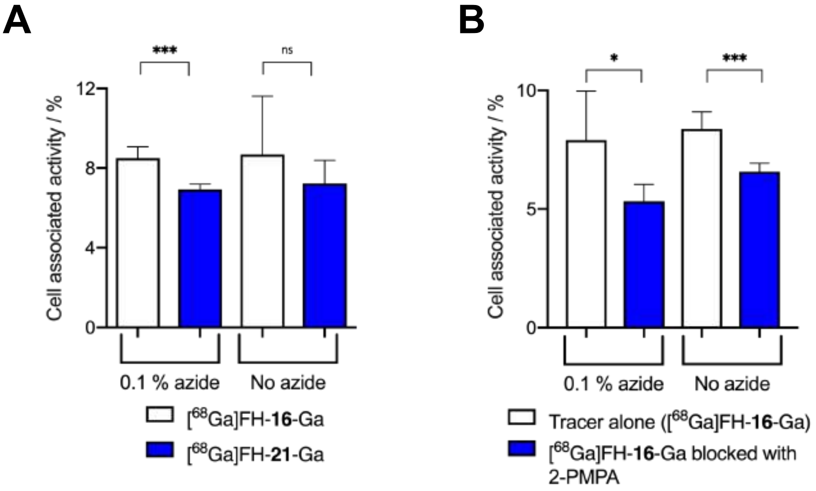

***In vivo* studies**

Small-animal PET images were acquired by using athymic nude mice bearing subcutaneous LNCaP tumours (*n* = 3). By 30 min post-administration, the majority of the activity associated with [^{68}Ga]FH-**16**-Ga accumulated in the liver and no significant tumour uptake was observed (**Figure 3.12A**). At *t* = 2 h post-injection, mice were euthanised and biodistribution studies performed. *Ex vivo* analysis confirmed that the majority of the activity remained in the liver and spleen with very little tumour uptake. Due to the lack of success of the initial imaging study with [^{68}Ga]FH-**16**-Ga, no further control studies were carried out in order to minimise the number of animals used. Despite the poor pharmacokinetic profiles and negligible tumour uptake, minimal activity was observed in the bladder and in the kidney following the biodistribution. The larger size of the nanoparticle constructs means that uptake into the liver is expected, whilst any dissociated activity would likely be excreted *via* the renal system. It is, therefore, logical to conclude that the activity remained bound to the nanoparticles demonstrating the stability of the constructs *in vivo*. This highlights the potential of using chelate-free, intrinsic radiolabelling in the radiosynthesis of metal oxide-based radiotracers.

Figure 3.12. (A) PET image of a mouse bearing a LNCaP tumour, T = tumour. 30 min coronal PET image recorded following injection with [^{68}Ga]FH-**16**-Ga. **(B)** Biodistribution data showing the accumulation of [^{68}Ga]FH-**16**-Ga radioactivity in different tissues at 2 h post-administration in mice bearing LNCaP tumours.

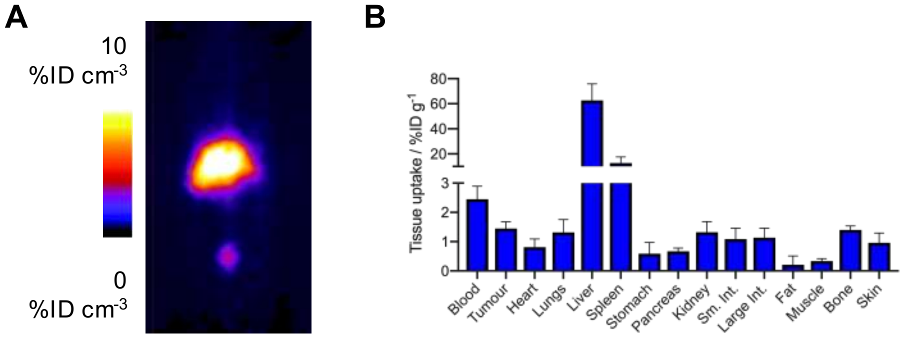

3.5 Conclusion

FH nanoparticles have been modified with a Glu-NH-CO-NH-Lys bisphosphonate derivative (**16**) to create a PET/MR agent targeted towards PSMA (FH-**16**). The radiolabelling of FH-**16** provided specific activities of 1.15 MBq μg^{-1}. This is 100-fold greater than the specific activities achieved with the chelate based methods in the radiolabelling of Fe_2O_3@Au nanoparticles (12.1 kBq μg^{-1}). Although cellular studies proved promising, *in vivo* studies showed no significant tumour uptake. Again, following modification and purification procedures, the

ζ-potential of the nanoparticles was not sufficiently negative to avoid macrophage uptake. Future work should concentrate on modifying the coating which could provide a particle size and surface charge sufficient to avoid accumulation in the liver. On a positive note, our experiments provide strong support that chelate-free intrinsic radiolabelling can be used to radiolabel nanoparticles, with advantages of simplicity and superior specific activities over conventional chelate-based methods.

Chapter 4: Multi-functionalised graphene nanoflakes as tumour-targeting theranostic drug-delivery vehicles

Adapted from
J. Lamb *et al*., *Chem. Sci.*, 2019, **10**, 8880-8888

4.1 Aims of chapter

In this chapter, we present a theranostic agent synthesised using graphene nanoflakes (GNFs). GNFs consist of a graphene sheet approximately 30 nm in diameter with a pristine aromatic system and an edge terminated with carboxylic acid groups. Their high water solubility and relative ease of functionalisation using carboxylate chemistry means that GNFs are potential scaffolds for the synthesis of theranostic agents. In this work, GNFs were multi-functionalised with derivatives of (*i*) a peptide-based Glu-NH-C(O)-NH-Lys ligand that binds prostate-specific membrane antigen (PSMA), (*ii*) a potent anti-mitotic drug (*R*)-ispinesib, (*iii*) the chelate desferrioxamine B (DFO), and (*iv*) an albumin-binding tag reported to extend pharmacokinetic half-life *in vivo*. Subsequent ^{68}Ga radiochemistry and experiments *in vitro* and *in vivo* were used to evaluate the performance of GNFs in theranostic drug design.

4.2 Introduction

In recent years, graphene-based nanomaterials have been studied for potential use in various biological applications.[338] For instance, modified graphene nanomaterials and carbon nanotubes have potential for use in anti-cancer treatments, as drug delivery vehicles, and in diagnostic imaging.[255,339–341] If these different applications can be combined then graphene nanomaterials could be used in the synthesis of theranostic agents.[342] The covalent modification of graphene sheets and carbon nanotubes is chemically challenging. Disrupting the delocalised π-bonding network of the graphene sheet is thermodynamically unfavourable, due to steric and electronic factors.[343] Most reactions that lead to graphene or nanotube functionalisation overcome these issues by exposing the material to harsh reagents and conditions.[344] As a result, the activation chemistry often forms a heterogeneous surface consisting of different graphene oxide (GO) and reduced graphene oxide (rGO) groups.[345–347] Modification of the oxygen-containing functional groups on GO and rGOs is relatively simple and the increased polarity improves water solubility of the sheets.

While GO and rGO are promising scaffolds for drug design, the heterogenous chemical nature of graphene materials is an issue. Specifically, standard GO and rGO materials contain varying amounts of oxide, hydroxide and epoxide groups scattered throughout their structure. This makes it challenging to control the chemo- and regioselectivity of functionalisation reactions. In addition, heterogeneity in the starting materials hinders batch-to-batch reproducibility by increasing variability in the product.

In an effort to circumvent some of these issues, the group of Prof. Dr Christoph Salzmann (University College London, United Kingdom) synthesised edge-carboxylated graphene nanoflakes (GNFs) *via* the acidic breakdown of chemical vapour deposition (CVD) of multi-walled carbon nanotubes.[348,349] Unlike GO and rGO materials, GNFs consist of a single graphene sheet approximately 30 nm in diameter with a pristine aromatic system. The GNF edge is terminated with carboxylic acid groups that can form carboxylic anhydrides (**Figure 4.1A**).[349] The high water-solubility, negative ζ-potential (-37 ± 10.2 mV), and relative ease of functionalisation using carboxylate chemistry means that GNFs are potentially suitable platforms for the design of theranostic agents, whereby derivatisation reactions take place regioselectively at the carboxylated edge. An atomic force microscopy image of GNFs spin-coated from an aqueous dispersion onto highly oriented pyrolytic graphite is shown in **Figure 4.1B**.

Figure 4.1. (A) Schematic chemical structure of a small per-carboxylate edge-terminated GNF (not to scale). **(B)** Atomic force microscopy image of GNFs spin-coated onto highly oriented pyrolytic graphite (Figure reproduced with permission from Prof. C. Salzmann, UCL).

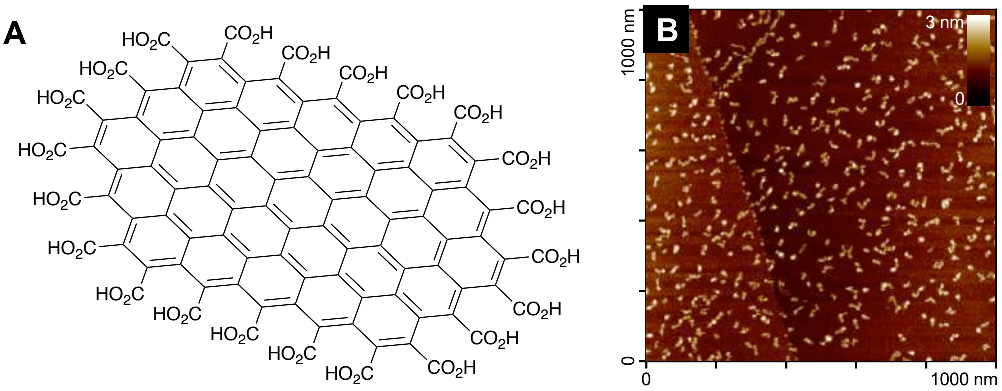

In this chapter, we used pristine GNFs (provided through collaboration with Prof. C. Salzmann) to synthesise a series of theranostic agents for targeted drug delivery and PET imaging. With this in mind, the GNFs were decorated with several different components. DFO is a well-known chelator for Fe^{3+}, Zr^{4+} and Al^{3+} ions (among others) but also binds gallium with high affinity (formation constant, $\log\beta$ = 28.2).[350] (*R*)-Ispinesib is an extremely potent anti-mitotic, anti-cancer drug which targets the kinesin spindle protein (KSP); a motor protein that plays a critical role in mitosis by mediating centrosome separation and bipolar spindle formation.[351] Inhibiting KSP causes cell cycle arrest at the mitotic phase, eventually leading to apoptosis.[352] Alongside its potency and selectivity, (*R*)-ispinesib is a convenient choice of drug for GNF modification as it bears a free primary amine which lies outside of the KSP binding pocket and is available for chemical modification.[351] Next, we sought to deliver the theranostic constructs to a tumour by incorporating a biologically active vector that targets a biomarker on cancer cells. For this purpose, we selected the previously introduced urea-based, PSMA binding, Glu-NH-C(O)-NH-Lys group. Finally, due to the small size of the GNFs, we hypothesised that they would exhibit rapid excretion *in vivo*. Therefore, we also decorated the GNFs using a pharmacokinetic modifying group (albumin binding tag) that can alter protein interactions with serum proteins. Selection of the pharmacokinetic modifying group was based on a report from Trüssel *et al.* who used lipophilic compounds which interact with albumin to extend the blood-pool half-life of antibody fragments.[353] In summary, the synthesis, *in vitro* and *in vivo* evaluation of a theranostic GNF vehicles with up to four different functionalities was explored.

4.3 Results and discussion

4.3.1 Functionalisation of GNFs

Four different GNF constructs (**GNF-1**, **-2**, **-3** and **-4**, **Figure 4.2**) were synthesised to evaluate the use of GNFs as a platform for the construction of theranostic agents. **GNF-1** was produced by pre-activating the carboxylate edge with HATU and conjugating to DFO *via* amide bond formation. The DFO chelate can be radiolabelled readily with $^{68}Ga^{3+}$ ions using established methods, allowing the use of radiochemistry to determine the success of the chemical reaction.[354] Radiolabelling (see below) confirmed that the DFO functionalisation reaction and purification was successful, indicating that the chemistry performed at the carboxylated edge was effective. With this information, we then used the same conjugation chemistry to functionalise the GNF nanoparticles with Glu-NH-C(O)-NH-Lys and (*R*)-ispinesib producing **GNF-2**. The free amine on all components allowed functionalisation *via* a one-pot, multi-component reaction. Purification was achieved on silica gel; interestingly, when 100% water was used as the mobile phase, the modified GNFs moved to the solvent front, allowing efficient separation from the other compounds in the reaction mixture which were retained (**Experimental**; **Figure 6.63**).

Figure 4.2. Schematic structures of [^{68}Ga]**GNF-1**, **-2**, **-3**, and **-4**. In each case, the GNFs are functionalised with multiple copies of each component. **(A) GNF-1** with the chelate DFO. **(B) GNF-2** with (*R*)-ispinesib, DFO, and the PSMA binding motif. **(C) GNF-3** with (*R*)-ispinesib, and the PEG$_4$-PSMA binding motif. **(D) GNF-4** with (*R*)-ispinesib, DFO, PEG$_4$-PSMA, and an albumin binding motif.

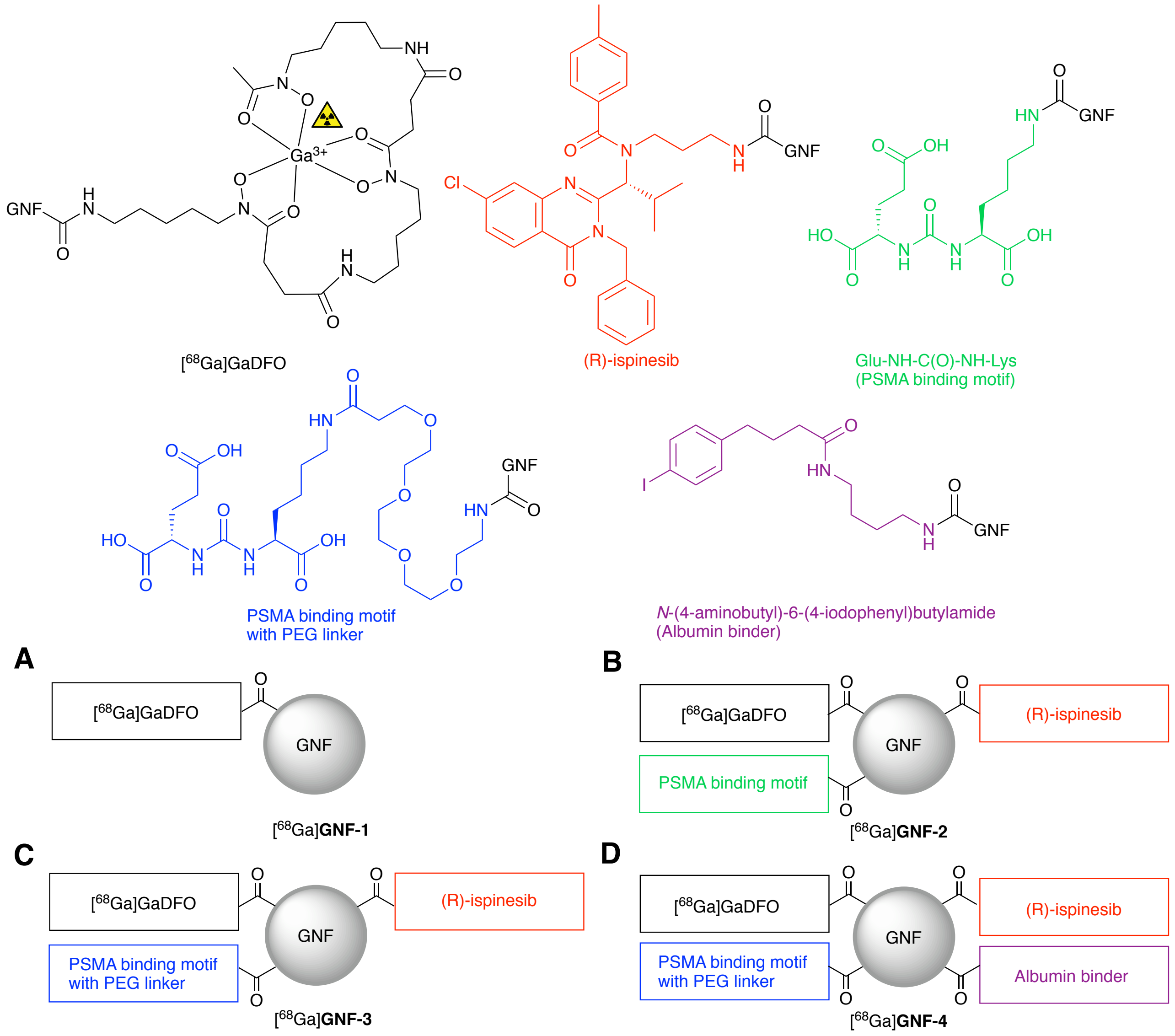

GNF-3 and **GNF-4** were then synthesised by using the same components and chemistry with added modifications. We hypothesised that by creating some distance between the GNF and Glu-NH-C(O)-NH-Lys, PSMA binding would be improved, and hence, increasing the specific uptake in target cells (LNCaP [PSMA +ve]). **GNF-3** included a short polyethylene glycol (PEG)$_4$ linker between the GNF and the PSMA ligand. The synthesis of Glu-NH-C(O)-NH-Lys-NH-C(O)-PEG$_4$-NH$_2$ (**Experimental**; **Scheme 6.12**) allowed the free amine to be used in the equivalent amide bond formation as before. Next, it was also speculated that the relatively small size and low lipophilicity of the GNFs would cause fast excretion of the compounds *in vivo*. This hypothesis was based on previous works, which demonstrate the rapid excretion of carbon nanotubes *via* the renal system.[355] Therefore, **GNF-4** sees the further addition of *N*-(4-aminobutyl)-6-(4-iodophenyl)butylamide – a recognised affinity tag for albumin – in an attempt to increase circulation times. Anti-body fragments with similar derivatisation have been reported to bind albumin, and in turn, showed increased circulation half-life *in vivo*.[353,356]

Following the synthesis of the four GNF constructs, the ζ-potentials were measured. **GNF-1** and **-2** exhibited similar ζ-potentials (-36.0 ± 4.87 and -39.5 ± 8.12 mV, respectively) compared to the native, non-functionalised GNFs (-37.0 ± 10.2 mV, consistent with previous reports[349]). **GNF-3** displayed a decrease in ζ-potential (-60.7 ± 10.3 mV) consistent with the additional PEG_4 ether groups causing an increase in negative charge at the slipping plane. Despite also containing the PEG_4 linker, **GNF-4** displayed a less negative ζ-potential (-42.3 ± 7.80 mV) arising from the addition of the lipophilic *N*-(4-aminobutyl)-6-(4-iodophenyl)butylamide group.

4.3.2 Radiochemistry

Radiochemical synthesis

DFO modification allowed for the efficient radiolabelling of **GNF-1, -2, -3** and **-4**, using the same general procedure for each construct. $[^{68}Ga][Ga(H_2O)_6]Cl_3(aq.)$ (~40 MBq) was added to an aqueous solution of the functionalised GNFs (25 µg) buffered with NaOAc (0.2 M, pH4.4) and incubated for 10 min at 21 °C (*n* = 3, independent reactions per compound). Radiochemical reactions were monitored by using radio-instant thin-layer chromatography (radio-iTLC) and size-exclusion chromatography (SEC) (**Figure 4.3**). Radiochemical conversions (RCCs) for the synthesis of ^{68}Ga-labelled **GNF-1, -2, -3** and **-4** were typically >97% (measured by radio-iTLC), with specific activities ranging from 8.7±2.4 to 10.4 ± 3.0 GBq mg^{-1} (activity per mass of GNF)(**Table 4.1**). Extending reaction times and heating the mixtures to 70 °C did not improve the percentage of radiochemical conversion. Chelate-free radiolabelling of rGO with $^{64}Cu^{2+}$ has been reported.[219] A chelate-free approach can be beneficial as the addition of chelates to a nanoparticle (or other biological vector) can often alter the properties of the graphene, hence changing results *in vivo*.[192] The intrinsic radiolabelling of the GNFs with ^{68}Ga was attempted, but no labelling was observed, which provided further confirmation that the DFO functionalisation was successful.

Figure 4.3. Radiochemical data on the ^{68}Ga-radiolabelling of **GNF-1, -2, -3** and **-4**. **(A)** Radio-iTLC with silica gel as stationary phase and H_2O as mobile phase. **(B)** Radio-SEC-HPLC with 200 mM arginine in PBS as mobile phase.

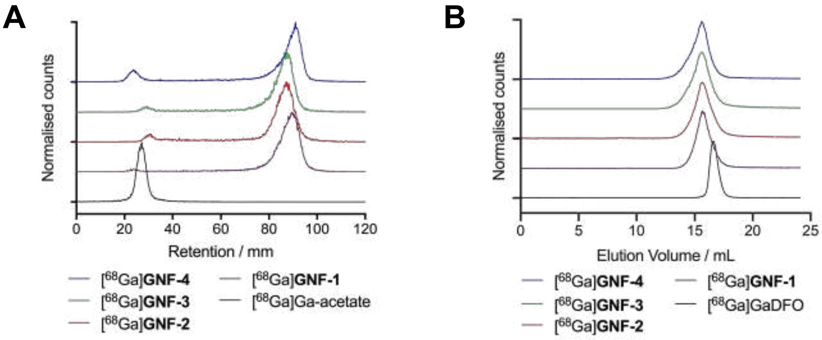

By using the experimentally measured molar activity of the [^{68}Ga][Ga(H_2O)$_6$]Cl_3(aq.) stock solutions, radioactive titrations allowed the quantification of the amount of DFO loaded per unit mass of GNF. Titration experiments showed that the functionalised compounds **GNF-1, -2, -3,** and **-4** contained similar amounts of DFO (ranging from ~44 – 53 nmol DFO per mg GNF), indicating that the conjugation reactions proceeded with similar efficiency for each compound (**Figure 4** and **Table 1**).

Figure 4.4. Plots showing percentage RCC when a standard aliquot of ^{68}Ga was titrated with varying concentrations of **(A) GNF-1**, **(B) GNF-2**, **(C) GNF-3**, and **(D) GNF-4**.

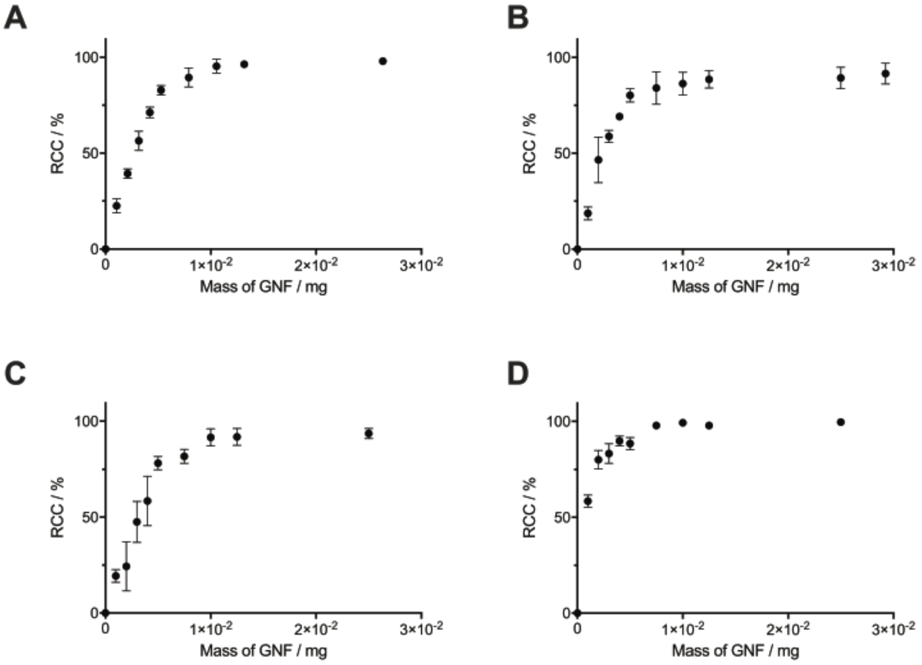

Table 4.1. Characterisation data associated with [^{68}Ga]**GNF-1, -2, -3** and **-4**.

	[^{68}Ga]**GNF-1**	[^{68}Ga]**GNF-2**	[^{68}Ga]**GNF-3**	[^{68}Ga]**GNF-4**
RCC /%	99.1±0.7	98.6±0.2	97.4±0.6	97.3±0.4
Specific Activity /GBq mg^{-1}	9.08±2.59	8.79±0.40	10.41±2.98	8.7±2.44
Mole of DFO per mass of GNF / nmol mg^{-1}	46.1±13.1	44.6±2.26	52.8±15.1	44.4±12.4
logD value	-3.34±0.02	-2.48±0.01	-3.14±0.06	-1.75±0.07
ζ-potential / mV	-36.0±4.87	-39.5±8.12	-60.7±10.3	-42.3±7.80

Lipophilicity measurements

Estimates of the lipophilicity of the samples were obtained by measuring distribution coefficients (log*D*) using standard *n*-octanol / PBS (pH7.4) partition experiments (**Table 4.1**). As expected, radiolabelled compounds [^{68}Ga]**GNF-1**, **-2**, **-3** and **-4**, were found to have negative log*D* values in the range -1.75 to -3.34. Functionalisation of the GNF-DFO flakes with Glu-NH-C(O)-NH-Lys and (*R*)-ispinesib (**GNF-2**) reduced the hydrophilicity (log*D* value of -2.48 ± 0.01, *n* = 3), which suggested that the lipophilic quinazolinone drug was loaded onto the particles. For **GNF-3**, the presence of the PEG$_4$-spacer between the nanoparticle and the Glu-NH-C(O)-NH-Lys group increased the hydrophilicity (log*D* = -3.14 ± 0.06, *n* = 3). Also, as anticipated, loading the nanoflakes with the *N*-(4-aminobutyl)-6-(4-iodophenyl)butylamide tag made construct **GNF-4** less hydrophilic (log*D* = -1.75 ± 0.07, *n* = 3). Overall, the changes in measured lipophilicity values map to the anticipated changes associated with functionalisation of GNFs with the different components.

Stability studies

Stability studies *in vitro* confirmed that the ^{68}Ga-radioactivity remained bound to the particles when incubated in solutions of saline (2 h), PBS (2 h) or human serum (2.5 h) at 37 °C (**Figure 4.5**).

Figure 4.5. Percentage radiochemical purity (RCP) of [^{68}Ga]**GNF-1, -2, -3** and **-4** determined from **(A)** radio-iTLC following incubation with PBS up to 2 h at 37 °C, **(B)** radio-iTLC following incubation with saline up to 2 h at 37 °C, **(C)** radio-SEC following incubation at 37 °C with human serum albumin for 2.5 h.

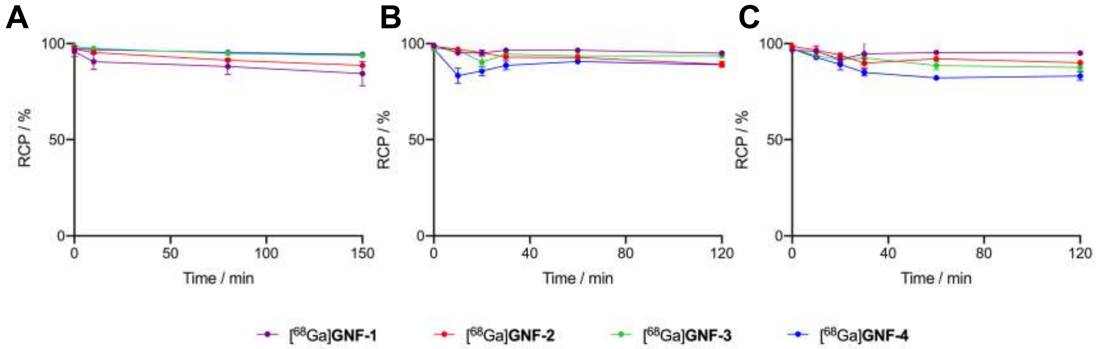

4.3.3 Cellular studies

To determine the presence and activity of the (*R*)-ispinesib and Glu-NH-C(O)-NH-Lys on **GNF-2**, **-3**, and **-4**, a range of different cellular assays were performed. The PSMA positive and overexpressing cell line LNCaP was used in all cell assays, with PC-3 (PSMA -ve) cells used in selected control experiments.[357]

Anti-proliferation assays

Cellular anti-proliferation (MTT) assays *in vitro* were used to measure growth inhibition induced by incubation of LNCaP cells with varying concentrations of the different GNF constructs. In positive control experiments, a classic biphasic profile was observed after incubating cells for 48 h with (*R*)-ispinesib (**Figure 4.6**).[351] Analysis of the growth curves gave two distinct values for the growth-inhibition (GI_{50}) values with a $GI_{50}(1)$ of 3.3 ± 2.3 μM and a second $GI_{50}(2)$ value of 0.7 ± 26.7 nM. At high concentrations, the compound is cytotoxic to cells which corresponds to the first $GI_{50}(1)$ value. At lower concentrations between the values of $GI_{50}(1)$ and $GI_{50}(2)$, a plateau region is observed in which the cells are cytostatic with cell cycle arrest occurring in the G_2/M phase. As the drug concentration decreases into the nanomolar range, a second step is observed corresponding to the $GI_{50}(2)$ value, followed by recovery of cellular proliferation to control levels.

Figure 4.6. Cellular anti-proliferation (MTT) curves showing the response of LNCaP (PSMA +ve) cells to treatment with (*R*)-ispinesib.

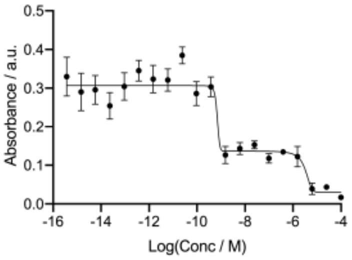

To determine the success of the functionalisation of the GNF with (*R*)-ispinesib, cells were exposed to **GNF-2** to observe the effect on proliferation. **GNF-2** exhibited a similar biphasic profile to the drug alone (**Figure 4.6**), indicating that the nanoflake was successfully modified with (*R*)-ispinesib and was also a potent inhibitor of cellular growth and proliferation (**Figure 4.7A**). To determine if further functionalisation of a graphene nanoflake with PEG_4 linkers and additional pharmacokinetic modifying groups (the albumin binder) had an impact on the anti-proliferative activity, equivalent MTT assays were conducted using **GNF-3** and **GNF-4** (**Figures 4.7B** and **4.7C**). Again, a biphasic profile was observed for both compounds which suggested more extensive derivatisation of a nanoflake did not alter the drug loading capacity. Similar to (*R*)-ispinesib, two separate growth inhibition values could be extracted from the biphasic curves giving values centred in the micro- ($GI_{50}(1)$ / μg mL^{-1}) and nano- ($GI_{50}(2)$ / ng mL^{-1}) mass concentration ranges for **GNF-2**, **GNF-3** and **GNF-**

4 (**Table 4.2**). It is worth noting that anti-proliferation assays with (*R*)-ispinesib alone requires the use of DMSO to solubilise the compound. The high water-solubility of the GNFs means that the use of DMSO was unnecessary when using the GNF constructs. This simplified formulation provides additional support for development of nanoflakes as potential drug-delivery vehicles.

Figure 4.7. Cellular anti-proliferation (MTT) curves showing the response of LNCaP (PSMA +ve) cells to treatment with **(A) GNF-2, (B) GNF-3** and **(C) GNF-4**. In each plot, the black data points correspond to treatment of the LNCaP cells with the native (non-functionalised) GNF in the same formulation as the active compounds.

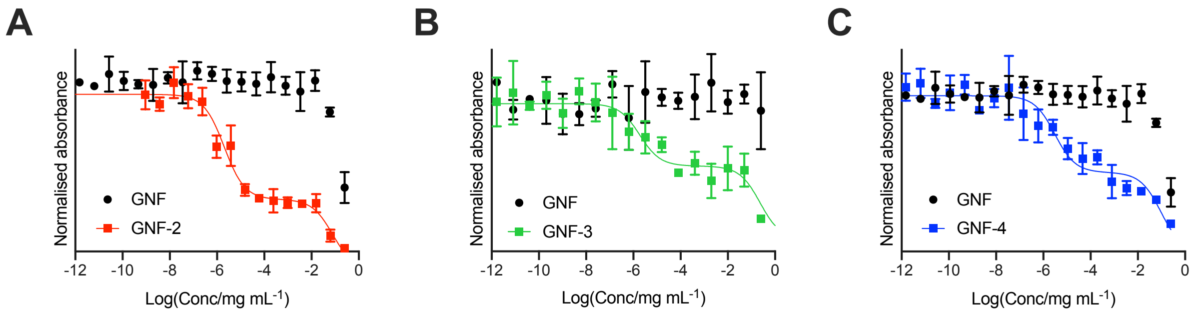

Table 4.2. GI$_{50}$ values of **GNF-2**, **-3** and **-4** extracted from the biphasic profiles observed in the anti-proliferation assays.

	GNF-2	GNF-3	GNF-4
Log(GI$_{50}$(1)/mg mL^{-1})	-5.70±0.11	-5.73±0.73	-5.52±0.18
Log(GI$_{50}$(2)/mg mL^{-1})	-1.11±0.41	-0.63±0.50	-1.02±0.18

Cell cycle analysis

Although the biphasic profile in MTT assays is a characteristic feature of KSP inhibition using (*R*)-ispinesib, as additional confirmation, the mechanism of cell cycle inhibition was evaluated by using fluorescence-assisted cellular sorting (FACS). After treatment of LNCaP cells for 36 h with two different concentrations of GNF constructs, (12 ng mL^{-1} and 120 ng mL^{-1} of **GNF**, **GNF-2**, **-3** and **-4**) the DNA content was measured by staining cells with propidium iodide (PI). Fluorescence-activated cell sorting (FACS) analysis showed that samples treated with **GNF-2**, **-3** or **-4** exhibited a dramatic and statistically significant increase in the proportion of cells in the G$_2$/M phase compared with vehicle-treated cells or cells treated with GNF alone (**Figure 4.8**, and **Table 4.3**). For example, cells treated with 120 ng mL^{-1} **GNF-2** showed an increased number of cells in the G$_2$/M phase (~87%) in comparison with control samples which gave relative G$_2$/M phase populations of 9% in untreated samples, and 7% in GNF treated samples. Interestingly, the proportion of cells in the G$_2$/M phase was also seen by FACS to be concentration dependent. For LNCaP cells treated with a lower concentration of **GNF-2** (12 ng mL^{-1}), the percentage of cells in G_2/M phase reduced to 29%. This observation is consistent with the biphasic curve seen in the anti-proliferation assay. Collectively, the anti-proliferation assays and FACS data support the conclusion that **GNF-2, -3** and **-4** were successfully functionalised with (*R*)-ispinesib and that the drug remained active toward KSP inhibition.

Figure 4.8. Cell cycle profiles derived from FACS analysis with concentrations **(A)** 120 ng mL^{-1} and **(B)** 12 ng mL^{-1} of GNF compounds. 2N (diploidy) refers to the G_0/G_1 phase whilst 4N (tetraploidy) refers to G_2/M phase.

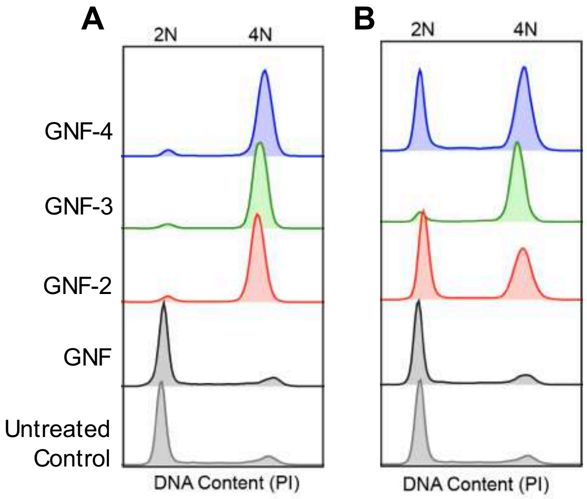

Table 4.3. Percentage of cells in the G_0/G_1, S and G_2/M phase. Data extracted from cell cycle analysis using the FlowJo software (Watson model).

		Cells associated with each cell cycle phase / %		
Sample	Concentration / ng mL^{-1}	G_0/G_1	S	G_2/M
Untreated	N/A	74.1	15.8	8.97
GNF	120	71.2	10.6	7.24
	12	69.2	11.6	10.2
GNF-2	120	4.92	5.21	87.3
	12	38.2	9.51	29.3
GNF-3	120	4.15	4.06	89.6
	12	4.43	10.8	78.7
GNF-4	120	5.79	6.49	77.6
	12	36.4	12.5	36.7

Confocal Microscopy

As a final confirmation that the mechanism of G_2/M phase arrest was associated with KSP inhibition, confocal microscopy images of cells that were incubated with **GNF**, **GNF-2**, **-3** or **-4** (and controls) were obtained (**Figure 4.9**). Untreated samples and slides treated with the control **GNF** sample showed predominantly cells in interphase region of the cell cycle with DNA (stained with Hoechst 33342) concentrated in a well-defined nucleus. These control experiments showed no evidence of G_2/M phase arrest and confirmed that the native GNFs do not interfere with the cell cycle which provided further corroboration of the FACS data (see above). In comparison, cells treated with **GNF-2**, **-3** or **-4** exhibited a characteristic punctate pattern of DNA distributed throughout the cell with no defined nucleus. The phenotype observed in these confocal cellular fluorescence microscopy data is consistent with previous reports on the mechanism of action of (*R*)-ispinesib in various cancer cells.[351,358,359]

Figure 4.9. Confocal microscopy images showing the effects of treatment of LNCaP cells with **GNF**, **GNF-2**, **GNF-3** and **GNF-4**. Microtubules stained with Alexa Flour 568 (red) and DNA stained with Hoechst 33342 (blue). (Inset) White scale bars correspond to 10 μm.

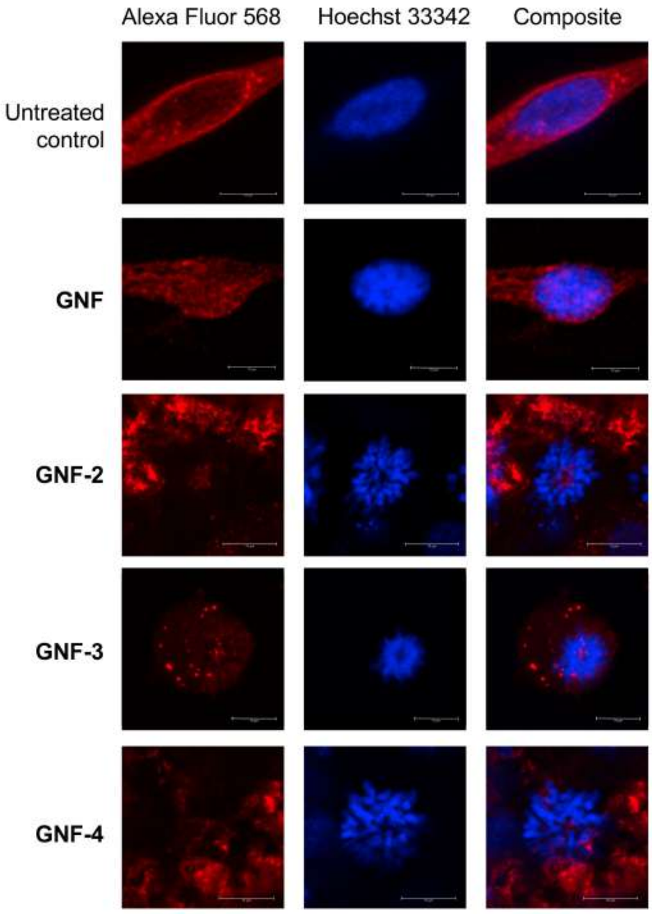

Cellular association assays

As previously discussed (**Chapter 1**; **Section 1.2.3**) PSMA is a membrane-bound zinc metalloenzyme which is upregulated in many prostate cancer cells. The Glu-NH-C(O)-NH-Lys group is a well-documented inhibitor of PSMA and many urea-based, small-molecule radiotracers have been tested *in vivo* and in human trials.[354,324,360–362] To determine if **GNF-2**, **-3** and **-4** were successfully functionalised with the PSMA binding motif, radioactive cellular binding and blocking assays were conducted using LNCaP cells (PSMA +ve; **Figure 10A**). [^{68}Ga]**GNF-2**, [^{68}Ga]**GNF-3** and [^{68}Ga]**GNF-4** showed an increased uptake in LNCaP cells compared with [^{68}Ga]**GNF-1**. PC-3 cells (PMSA –ve) were used as a negative control cell line. A statistically significant decrease in cellular uptake was observed in PC-3 cells compared with the activity accumulation in the LNCaP cells for [^{68}Ga]**GNF-2** (P-value < 0.01), [^{68}Ga]**GNF-3** (P-value < 0.001) and [^{68}Ga]**GNF-4** (P-value < 0.0001). These results were encouraging and suggested that the functionalisation of GNFs with tumour-targeting groups was successful. However, in both the PC-3 and LNCaP cell lines, absolute uptake of the radioactivity was relatively low and non-specific binding accounted for up to ~50% of the cell-associated activity. For instance, this non-specific binding component can be seen in the relative amount of [^{68}Ga]**GNF-1** *versus* the 'targeted' GNF constructs ([^{68}Ga]**GNF-2, -3** and **-4**). Non-specific binding is difficult to circumvent and is likely due to the non-specific interactions of the GNFs with cellular proteins. Protein interactions have been observed for other nanographene materials.[363,364]

We hypothesised that increasing the distance between the GNFs and the Glu-NH-C(O)-NH-Lys targeting vector using a PEG$_4$ linker could potentially increase the cellular uptake and specificity for LNCaP cells. However, no difference was observed between the cell-associated uptake of [^{68}Ga]**GNF-2** and [^{68}Ga]**GNF-3** (**Figure 4.10A**). It is possible that the short PEG$_4$ chain is insufficient to shift the uptake mechanism away from non-specific accumulation and toward specific PSMA-mediated binding. Also of note, the slightly higher cell-associated activity observed for [^{68}Ga]**GNF-4** in LNCaP cells was simply attributed to an increased non-specific uptake which was seen in the data using PC-3 cells.

Cellular blocking assay

The cellular association assays suggested that a two-state mechanism of cellular binding, involving both specific and non-specific accumulation, was operating for the targeted constructs **GNF-2**, **-3**, and **-4**. Therefore, to provide further confirmation of the presence of the Glu-NH-C(O)-NH-Lys group on **GNF-2**, **-3**, and **-4**, and to evaluate the fraction of specific binding observed using the LNCaP cells, blocking studies were performed. LNCaP cells were first incubated with ~1000-fold excess of the free Glu-NH-C(O)-NH-Lys ligand (5 μM) for 1 h prior to the addition of radiotracers (**Figure 4.10B**). The blocking studies confirmed that the radioactivity associated with the LNCaP cells could be reduced by 32 ± 9% for [^{68}Ga]**GNF-2**, 76 ± 36% for [^{68}Ga]**GNF-3** and

37 ± 10% for [^{68}Ga]**GNF-4**. Whilst a low percentage of cellular association and the relatively high fraction of non-specific binding indicate that more work is required to optimise these constructs, the blocking experiments confirmed that GNFs can be targeted toward specific biomarkers on cancer cells.

Figure 4.10 (A) Cellular binding assay of [^{68}Ga]**GNF-1, -2, -3** and **-4** with the LNCaP (PSMA +ve) and PC-3 (PSMA –ve) cell lines. Data given as activity bound per 1 mg mL^{-1} of protein. All cell media contained 0.1% azide and protein content was measured by using a BCA assay. For the LNCaP cell line: [^{68}Ga]**GNF-1** *vs.* [^{68}Ga]**GNF-2**, *P*-value<0.01; [^{68}Ga]**GNF-1** *vs.* [^{68}Ga]**GNF-3** *P*-value < 0.001; [^{68}Ga]**GNF-1** *vs.* [^{68}Ga]**GNF-4**, *P*-value < 0.0001. Comparison of cell lines: PC-3 *vs.* LNCaP [^{68}Ga]**GNF-2**, *P*-value < 0.01; [^{68}Ga]**GNF-3**, *P*-value < 0.001; and [^{68}Ga]**GNF-4**, *P*-value < 0.0001 **(B)** Blocking assay with the LNCaP (PSMA +ve) cell line pre-treated with free Glu-NH-C(O)-NH-Lys ligand (5 μM) before addition of radiotracers. Note: Student's *t*-test analysis: ns = not significant, * = *P*-value < 0.05, ** = *P*-value < 0.01, *** = *P*-value < 0.001.

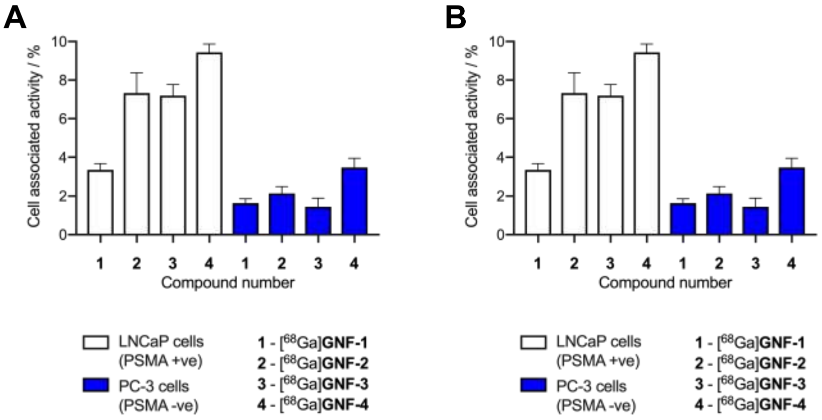

4.3.4 *In vivo* studies

Next, to gauge the potential of using nanoflakes *in vivo*, we performed dynamic PET imaging to measure the pharmacokinetic (PK) distribution and excretion profiles of [^{68}Ga]**GNF-3** and [^{68}Ga]**GNF-4** in athymic nude mice bearing subcutaneous LNCaP tumours (*n* = 3 mice / compound). The main goal was to measure time-activity curves to obtain a baseline PK profile of GNFs, and to evaluate if functionalisation of the GNF constructs with an albumin binding tag could modulate blood pool concentrations, circulation times and excretion pathways.

Pilot PET imaging experiments indicated that the small size and high hydrophilicity of the [^{68}Ga]**GNF-3** and [^{68}Ga]**GNF-4** facilitated rapid extraction from the blood pool by a renal excretion pathway and elimination through the bladder (**Figure 4.11**). Renal clearance of [^{68}Ga]**GNF-3** and [^{68}Ga]**GNF-4** is an interesting observation that may help to minimise the radiation burden to background tissues and facilitate further optimisation of radiotracers based on GNFs. Time-activity curves (TACs) showed that [^{68}Ga]**GNF-3** was essentially first-pass extracted from the blood pool by the kidneys. Peak uptake in the kidney reached 38 ± 4 %ID cm^{-3} within in the first two minutes post-administration. Concordantly, accumulation of ^{68}Ga-radioactivity in the bladder was observed to increase immediately after injection confirming that the [^{68}Ga]**GNF-3** particles are not retained in the kidney (**Figure 4.11B**). In contrast, the peak in radioactivity in the kidneys for [^{68}Ga]**GNF-4** occurred between 4 – 6 minutes post-administration with a similar time delay observed before activity was seen to accumulate in the bladder (**Figures 4.11C**). For both [^{68}Ga]**GNF-3** and [^{68}Ga]**GNF-4**, blood pool activity (as measured by manually drawing volumes of interest [VOIs] over the left ventricle of the heart) showed a peak in the first frame after bolus injection of the radiotracer and a rapid decrease over the imaging time window. In comparison to [^{68}Ga]**GNF-3**, the slight delay in extraction of the [^{68}Ga]**GNF-4** activity from the blood pool by the kidney, gave a higher blood pool peak activity of 48 ± 5 %ID cm^{-3}. Kinetic analysis of the TACs found that the effective half-life of [^{68}Ga]**GNF-3** in the blood pool (heart) was 3.85 ± 0.35 min. whereas for [^{68}Ga]**GNF-4** the half-life increased to 5.22 ± 0.61 min ($p < 0.05$). These TAC data indicate that modification of the GNF particles with the albumin binding tag has a small but significant effect on prolonging the circulation time and reducing the elimination rate of [^{68}Ga]**GNF-4**.

Figure 4.11. PET images recorded in mice bearing LNCaP tumours, T = tumour. **(A)** 2 h coronal PET image recorded following injection with [^{68}Ga]**GNF-4**. TACs plotted with data extracted from 30 min dynamic PET analysis (15 × 2 min scans) with injection of **(B)** [^{68}Ga]**GNF-3** (n = 3) and **(C)** [^{68}Ga]**GNF-4** (n = 4) at t = 2 min. VOI were defined and data extracted using the VivoQuant™ software.

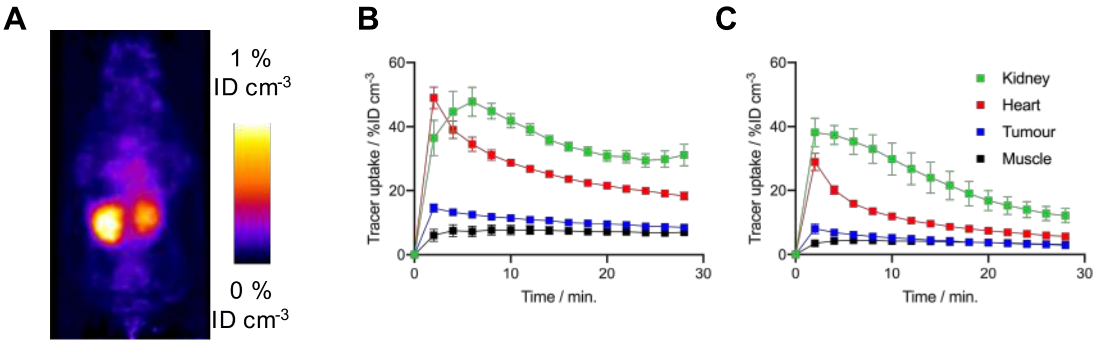

For both [^{68}Ga]**GNF-3** and [^{68}Ga]**GNF-4**, tumour-associated radioactivity was found to be low and non-specific. The TAC profiles of VOIs drawn over the tumours showed that the PK profile followed the same trend as the blood pool associated activity, indicating that the constructs do not show specific accumulation in the tumours. This result is partially consistent with the cellular data which also showed low absolute accumulation in tumour cells. Factors leading to this lack of specific tumour uptake include the relatively high component of non-specific binding found for GNFs on LNCaP cells, the rapid excretion profile, and potentially, a reduced access or affinity of the Glu-NH-C(O)-NH-Lys binding ligand for the PSMA target when bound to the GNF particles. In spite of the absence of tumour uptake, the PET imaging data provided valuable information, which will facilitate further optimisation of the GNFs as potential drug delivery vehicles and theranostic agents. The following chapter of this thesis addresses issues of rapid excretion and low tumour uptake by conjugating GNFs to mAbs.

4.4 Conclusions

GNFs were used as scaffolds for the synthesis of targeted theranostic agents. Multi-functionalised GNFs can be prepared with a diverse range of components including metal-binding chelates, tumour-targeting ligands, cytotoxic drugs and pharmacokinetic modification groups. Derivatisation of GNFs with the potent drug molecule (*R*)-ispinesib gave constructs that remained pharmacologically active with the mode of action consistent with mitotic phase arrest induced by KSP motor protein inhibition. An additional advantage of using a nanoflake carrier is that binding (*R*)-ispinesib to the GNFs enabled the drug to be solubilised in water.[365] In addition, GNFs functionalised with the Glu-NH-C(O)-NH-Lys group exhibited enhanced cellular uptake. Although a significant fraction of cellular association was assigned to non-specific interactions, it was found that targeted GNFs showed specific binding toward PSMA expressing cells. Dynamic PET imaging found that functionalised GNFs have rapid blood pool clearance and renal excretion, but experiments also demonstrated that functionalising with an albumin-binding tag results in meaningful modulation of the pharmacokinetic profile. Further optimisation is required to enhance the uptake kinetics and distribution of functionalised GNFs *in vivo*. In summary, experimental data has supported our conclusion that GNFs are a highly versatile platform for theranostic drug development.

Chapter 5: Graphene nanoflake antibody conjugates as potential PET/MR imaging agents

5.1 Aims of Chapter

In **Chapter 4**, we demonstrated the potential of using GNFs as tumour-targeted drug delivery vehicles.[366] However, despite successful results *in vitro*, poor pharmacokinetics *in vivo* led to rapid excretion *via* the renal system and negligible tumour uptake. Modification of the GNFs with albumin binding groups led to a small, but significant increase in the blood half-life, confirming that transient binding to globular proteins in serum can alter the pharmacokinetic profile. Therefore, in **Chapter 5** we sought to develop a multi-modal GNF construct featuring a stable covalent conjugate bond to an antibody (mAb). The hypothesis was that attaching mAbs to GNF constructs would simultaneously increase blood pool circulation times, and facilitate target-specific binding and retention in tumours *via* binding of the mAb to various upregulated biomarkers on cancer cells.

5.2 Introduction

Graphene materials have been previously conjugated to larger biomolecules (e.g. mAbs) using a number of different techniques.[367–375] Li *et al.* modified rGO film with pyrene carboxylic acid *via* π-π interactions. EDC/sulfo-NHS was then used to activate the free carboxylic acids, facilitating conjugation to the protein using lysine residues.[368] Alternatively, McDevitt *et al.* conjugated rituximab to carbon nanotubes by using a maleimide coupling to the cysteine residues.[369] These conjugation methods were later used to modify carbon nanotubes with the E4G10 mAb indicating the versatility of the method.[375] Despite successful conjugation, the use of GO and rGO materials produces highly heterogeneous products reducing batch-to-batch reproducibility. GNFs consist of a single graphene sheet 30 ± 9 nm in diameter with a pristine aromatic system and an edge that is terminated with carboxylic acid groups.[348,349] As we demonstrated previously that selective modification of the carboxylated edge can be achieved by using simple amide bond forming reactions, by using GNFs as a scaffold we can remove a certain degree of heterogeneity in the obtained product when compared with other GO, rGO or nanotube constructs.

Due to the recent advent of combined PET/MR scanners, there is now a need for the development of imaging agents that combine both PET and MR imaging capabilities in a single construct (**Chapter 1**; **Section 1.3.2**). As GNFs can be multi-functionalised with a variety of compounds, the material is an ideal candidate to act as a platform for incorporating both MRI and PET agents in the same molecule. To create this multi-functional construct, we chose to decorate the GNFs with the GdDOTAGA complex and the DFO chelate. Here, the paramagnetic Gd^{3+} ions shorten the T_1 (longitudinal) relaxation times of nearby protons in water providing a positive contrast in T_1-weighted MR images. Meanwhile, the DFO chelate can form coordination complexes with both $^{68}Ga^{3+}$ and $^{89}Zr^{4+}$ ions allowing PET imaging.

To target the multi-modal GNFs toward cancer-specific biomarkers, both onartuzumab (MetMAb^{TM}; Genentech) and trastuzumab (Herceptin^{TM}; Genentech) were tested. Onartuzumab binds to the human hepatocyte growth-factor receptor (c-MET) whilst trastuzumab targets an epitope on the human epidermal growth-factor receptor 2 (HER2/*neu*). These target proteins are both over-expressed in a number of cancer cell lines and tumour types (**Chapter 1**; **Section 1.2.3**). Due to the complexity of forming a covalent GNF-antibody conjugation, a fluorescent GNF derivative was synthesised to facilitate characterisation and optimisation of the reaction conditions. The ease of tracking molecules with fluorescent tags allows for the efficient measurement of the conjugation success and determination of whether the attachment of the GNF alters the specific cellular binding and uptake by the antibody-antigen interaction. Therefore, in this work, initial conjugation and cellular studies were carried out by using a GNF decorated with a boron-dipyrromethene (BODIPY) derivative. BODIPY dyes are known to be highly fluorescent whilst offering thermal and photochemical stability under aqueous conditions.[376] Hence, BODIPY dyes provide a suitable basis from which to carry out the pilot studies; allowing us to design and optimise the conjugation methodology to produce GNF-mAb constructs. Furthermore, BODIPY derivatives are commonly used as optical imaging agents so the production of a fluorescent BODIPY-GNF-mAb could find further application in confocal microscopy, tissue staining, or fluorescence mediated tomography (FMT) *in vivo*.[377–381] This demonstrates the potential of the GNF constructs to also offer further imaging functions.

Overall, we report the synthesis and characterisation of several GNF-mAb derivatives for potential use in PET/MR imaging. Initial conjugation techniques were developed *via* the use of a GNF-BODIPY derivative, where tests are carried out using both trastuzumab and onartuzumab. The obtained products were evaluated *in vitro* by using FACS analysis. The methods developed were then used to conjugate GNF-GdDOTAGA-DFO to trastuzumab which was further radiolabelled with ^{89}Zr yielding [^{89}Zr]GNF-GdDOTAGA-ZrDFO-trastuzumab. Following characterisation of the radiolabelled product, the construct was evaluated *in vitro* and *in vivo* by using small-animal PET imaging and biodistribution studies.

5.3 Results and discussion

5.3.1 BODPIY-GNF antibody conjugates

Synthesis of GNF-BODIPY

The synthesis of the BODIPY-GNF was achieved *via* methods previously established by our group (see Chapter 4).[366] Briefly, a BODIPY aniline (compound **28**, see experimental for details) was synthesised in accordance with reported procedures.[382] The aniline derivative provided a free amine which was coupled to the carboxylated edge using standard amide coupling procedures (**Experimental**; **Section 6.5.1**). Once GNF-

BODIPY (**Figure 5.1**) was obtained the absorption/emission spectra was measured ($\lambda_{\text{abs max}}$ = 498 nm, $\lambda_{\text{ems max}}$ = 510 nm), and the maximum emission intensity was measured for solutions of different concentrations.

Figure 5.1. (A) Schematic structure of BODIPY-GNF. Note, the GNF is functionalised with multiple copies of the BODIPY aniline derivative. **(B)** Absorption/emission spectrum of BODIPY-GNF **(C)** Change in emission intensity at 520 nm with change in particle molality of BODIPY-GNF.

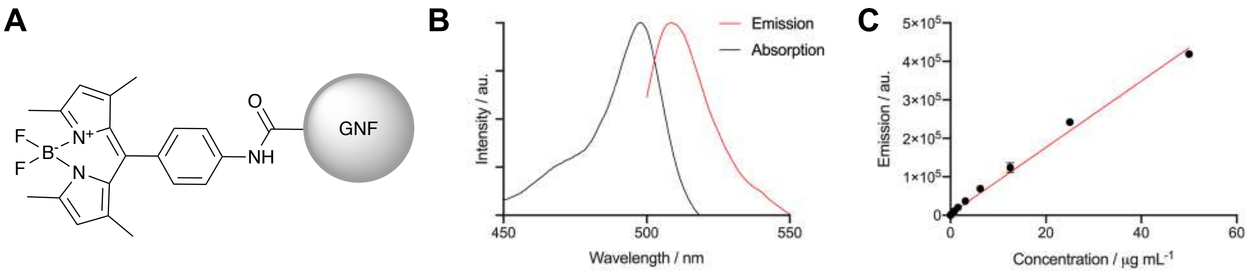

Conjugation of BODIPY-GNF to trastuzumab

Following the synthesis of BODIPY-GNF, conjugation to pre-purified trastuzumab was carried out by using EDC/NHS mediated coupling. The unique absorption maxima of the BODIPY-GNF (λ_{max} = 498 nm) construct allowed us to characterise reactions by monitoring SEC-HPLC at both 490 nm and 280 nm (for tracking the protein component). This spectroscopic monitoring facilitated optimisation of the reaction conditions. As the particle size and the precise number of free carboxylic acids on the BODIPY-GNF is unknown, this optimisation process required a certain amount of 'trial and error' to find the correct conditions. To avoid larger aggregates, it was necessary to limit the possibility of multiple antibodies conjugating to each GNF. It was also necessary to avoid larger mAb conjugates which may form due to polymerisation with excess EDC/NHS. Initial reaction conditions yielded a product that appeared to have a larger amount of aggregate (**Figure 5.2A**), especially when observing absorption at 490 nm. This is indicative of aggregate formation and multiple antibodies conjugating to each GNF. To avoid this, follow up reaction conditions involved lowering the amount of GNF and EDC/NHS in comparison to protein. This produced a structure that was analysed in **Figure 5.2B**. Here, little aggregate was present, yet it was apparent that the conjugation between the GNF and the mAb was successful; by following the BODIPY-GNF channel (λ = 490 nm) on the chromatogram, the primary peak observed corresponds to the correct elution time (18.1 min) associated with elution of the protein.

Scheme 5.1. EDC/NHS coupling of BODIPY-GNF to an antibody (trastuzumab).

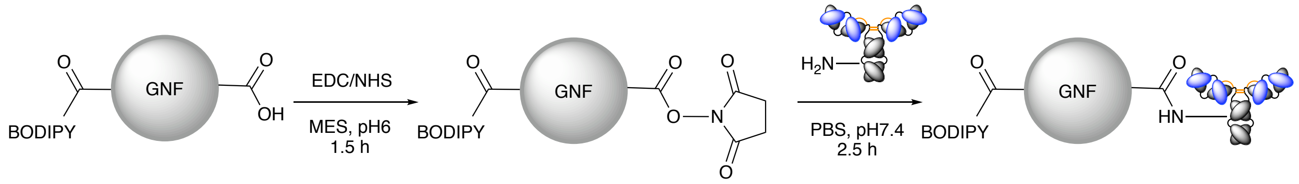

Figure 5.2. (A&B) SEC-HPLC chromatograms of trastuzumab, BODIPY-GNF and the BODIPY-GNF-trastuzumab conjugates. When more than one mAb is present on each GNF (mAb-to-GNF ratio, n ≥ 2) the construct elutes at 16.2 min. Elution at 18.3 min relates to either non-functionalised mAb or a GNF functionalised with 1 mAb (n = 1). Non-functionalised GNF and GNF-BODIPY (n = 0) elutes at 24.6 min and small molecules elute at 28.6 min. **(C)** Pictorial representation of constructs assigned on chromatograms.

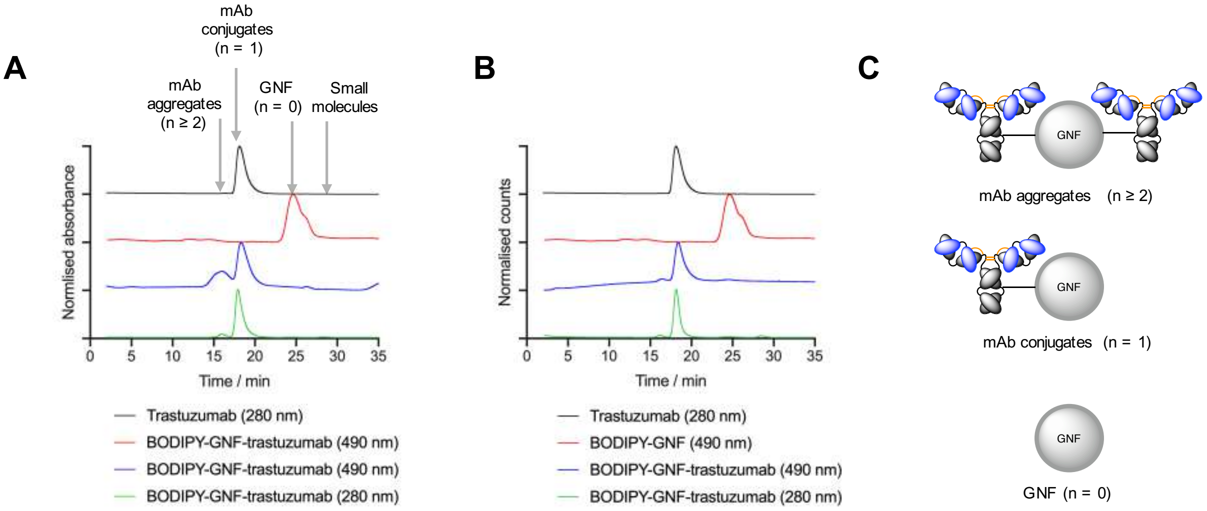

It is possible to determine the amount of GNF present in the mAb conjugate by measuring the emission of the obtained product and comparing this to the data seen in **Figure 5.1C**. Here, it should be noted that it was assumed that the emission of the construct did not change when conjugated to the mAb. However, the emission of the sample allowed us to approximate that the sample contained 12.3 ± 0.7 µg of GNF per 1 mg of protein. By observing previously obtained STM images, it can be seen that the GNF flakes have a length of approximately 30 nm and a width of approximately 10 nm.[348] From this size estimation, and previous data reported by Vorontsov *et al.*, we can approximate the molecular weight of a GNF to be 12,000 g mol^{-1} giving 1.02 nmol of GNF in the product.[383] Due to the large molecular weight of trastuzumab (145 kDa), 1 mg is equivalent to 6.87 nmol. From the estimated moles of GNF and the measured moles of protein we can determine that on average, the constructs contain ~7 mAbs per GNF. It should be noted that this calculation uses several approximations and assumptions, since accurate determination of the number of moles (or concentration) of nanoparticles remains challenging, but given the size of the GNFs, the estimated loading ratio seems feasible.

Cellular binding of BODIPY-GNF-trastuzumab

Following successful conjugation of the BODIPY-GNF to trastuzumab, our next goal was to establish whether the BODIPY-GNF-trastuzumab constructs retained affinity and specificity toward the target biomarker (HER2/*neu*). The SK-OV-3 ovarian cancer cell line is known to overexpress the HER2/*neu* antigen, and therefore, this line was used in cellular binding assays with BODIPY-GNF-trastuzumab. To establish the intensity of the emission associated with cells, FACS analysis was used (**Figure 5.3**). FACS experiments demonstrated that the fluorescence intensity is significantly higher (~2.7-fold) in cells that are treated with BODIPY-GNF-mAb compared with the vehicle-treated (*P*-value < 0.01). As a further measure of specificity, the binding of the control compound BODIPY-GNF was measured which showed a dramatic decrease (~2.2-fold) in fluorescence intensity compared with BODIPY-GNF-trastuzumab (*P*-value < 0.05). Finally, as additional proof of specific cellular binding, a blocking study was performed in which cells were pre-treated with an excess of trastuzumab (333-fold excess) before treatment with BODIPY-GNF-trastuzumab. Blocking resulted in a ~2.2-fold decrease in mean fluorescence intensity (*P*-value < 0.05), giving a signal intensity that was statistically identical to the vehicle-treated and BODIPY-GNF controls. Collectively, these cellular binding studies provide convincing experimental evidence that BODIPY-GNF-trastuzumab exhibited specific binding *via* the mAb-antigen interaction.

Figure 5.3. FACS analysis of cells treated with BODIPY-GNF-mAb and relevant controls. **(A)** Histogram of obtained data following appropriate gating using the Flowjo software. **(B)** The mean fluorescence intensity of each sample was extracted using Flowjo software and values were directly compared (*n* = 3). Note: Student's *t*-test analysis: ns = not significant, * = *P*-value < 0.05, ** = *P*-value < 0.01, *** = *P*-value < 0.001.

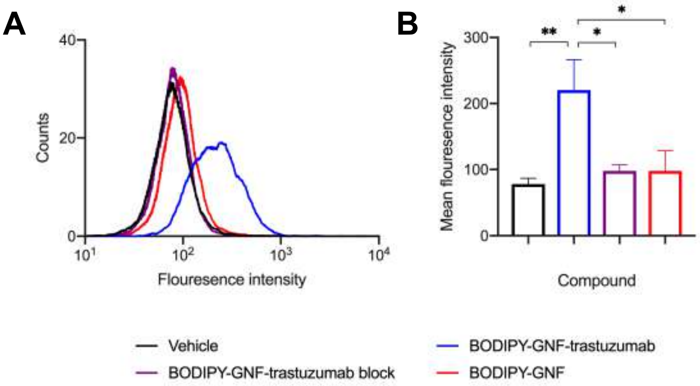

Conjugation of BODIPY-GNF to onartuzumab (MetMAb)

Whilst conjugation to trastuzumab was successful, we wanted to demonstrate the versatility of the constructs by also conjugating BODIPY-GNF to an alternative mAb, pre-purified onartuzumab. Conjugation was achieved by using our previously established methods (*vide supra*). SEC-HPLC (**Figure 5.4A**) allowed us to determine that the conjugation was successful by monitoring the co-elution of the BODIPY (490 nm) channel with that of the protein (280 nm). Due to the smaller size of onartuzumab (99.16 kDa), complete separation and removal of free BODIPY-GNF was not achieved and this can be observed from the peak in the SEC-HPLC (24 min.; **Figure 4A** blue trace). From the integrated absorption profile of the BODIPY channel the purity of the BODIPY-GNF-onartuzumab was estimated to be 84%. In spite of the difficulties in purifying the BODIPY-GNF-onartuzumab, FACS analysis was conducted with the same controls (including the impurity molecule BODIPY-GNF) as mentioned in the previous section (**Figure 5.4B&C**). In this case, MKN-45 gastric carcinoma cells (overexpressing the c-MET receptor) were treated with BODIPY-GNF-onartuzumab and an increased fluorescence intensity (~2.5-fold) was observed compared with the vehicle-treated control (*P*-value < 0.001). The onartuzumab blocking control and the BODIPY-GNF control samples both gave a significant decrease in fluorescence intensity (~1.5-fold; *P*-value < 0.001 and *P*-value < 0.01, respectively), confirming the specific binding of the BODIPY-GNF-onartuzumab. In contrast to the BODIPY-GNF-trastuzumab studies where a ~2.2-fold difference was observed between the experiments and the control studies, BODIPY-GNF-onartuzumab gave a slightly lower difference of ~1.5-fold. In part this may be explained by the fact that onartuzumab is a monovalent, one-armed engineered antibody whereas trastuzumab is bivalent and thus has a higher avidity and a reduced likelihood of compromising the immunoreactivity during the GNF conjugation reactions. This indicates the robustness of using the larger bivalent mAb, trastuzumab. For this reason, subsequent studies focused on the use of GNF-trastuzumab constructs.

Figure 5.4. (**A**) SEC-HPLC of BODIPY-GNF-onartuzumab with PBS as mobile phase. (**B**) FACS analysis of cells treated with BODIPY-GNF-onartuzumab and relevant controls. Histogram of obtained data following appropriate gating using the Flowjo software. (**C**) The mean fluorescence intensity of each sample was extracted and values were directly compared (*n* = 3). Note: Student's *t*-test analysis: ns = not significant, * = *P*-value < 0.05, ** = *P*-value < 0.01, *** = *P*-value < 0.001.

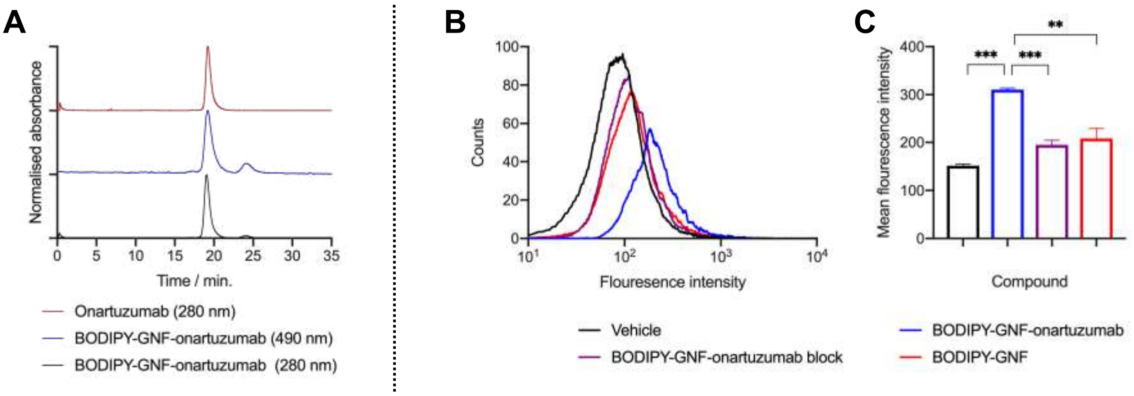

5.3.2 DFO-GNF antibody conjugates

Synthesis of DFO-GNF conjugates

With conjugation methods established, our next aim was to create radiolabelled GNF-mAb conjugates for PET imaging. To achieve this, the previously synthesised DFO-GNF was used (**Chapter 4**, **GNF-1**). Conjugation of DFO-GNF to trastuzumab was achieved by using conditions identical to those optimised during the BODIPY-GNF synthesis. SEC-HPLC analysis of both DFO-GNF and DFO-GNF-trastuzumab (**Figure 5.5**) indicated that conjugation was successful with absorption at 400 nm (following the GNF chromophore) for the DFO-GNF-trastuzumab (18.3 min).

Figure 5.5. (A) Schematic structure of DFO-GNF-trastuzumab. Note, the GNF is functionalised with multiple copies of DFO. **(B)** SEC-HPLC analysis of DFO-GNF and DFO-GNF-trastuzumab with PBS as mobile phase.

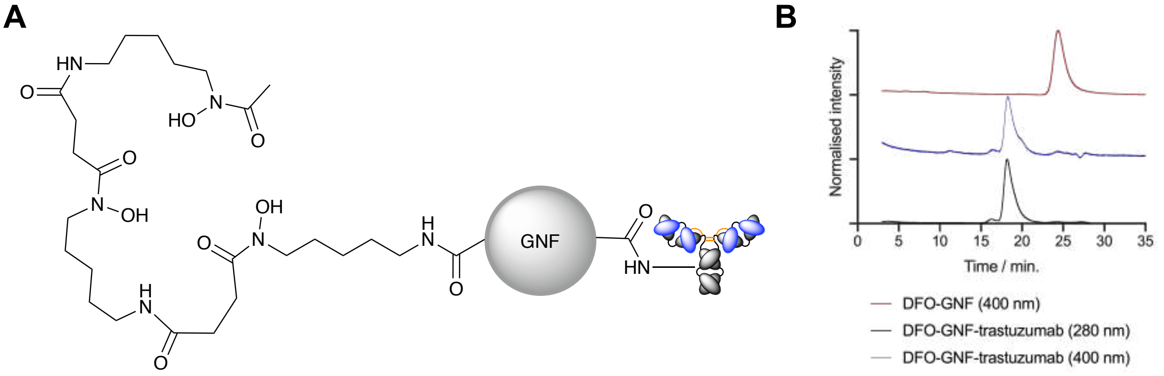

Radiolabelling DFO-GNF antibody conjugates

Due to the large size of trastuzumab and subsequent long circulation times *in vivo*, ^{89}Zr ($t_{1/2}$ = 78.41 h) was chosen to radiolabel the constructs due to the long half-life of the radionuclide. Radiolabelling was achieved in 45 min to synthesise [^{89}Zr]ZrDFO-GNF-trastuzumab with a decay-corrected RCY of 27.6%. Purification was achieved by using 100 kDa spin-centrifugation filters, but it was found that complete removal of the free radiolabelled [^{89}Zr]ZrDFO-GNF was challenging. For this reason a small peak associated with [^{89}Zr] ZrDFO-GNF was still observed in the radiotrace and the final [^{89}Zr]ZrDFO-GNF-trastuzumab formulation had a measured RCP of 82% (**Figure 5.6**). We note that previous studies (**Chapter 4**) established that radiolabelled GNFs which are not bound to protein are rapidly excreted via the kidney with no uptake in tumours, and negligible uptake was observed in cells. Therefore, the presence of this [^{89}Zr]ZrDFO-GNF was not anticipated to compete with the binding of [^{89}Zr]ZrDFO-GNF-trastuzumab *in vitro* or *in vivo*.

Figure 5.6. Radiochemical data for [^{89}Zr]ZrDFO-GNF-trastuzumab. **(A)** PD10-SEC with PBS as eluent **(B)** Radio-iTLC with silica gel as stationary phase and 50 mM DTPA as mobile phase. **(C)** Radio-SEC-HPLC with PBS as mobile phase.

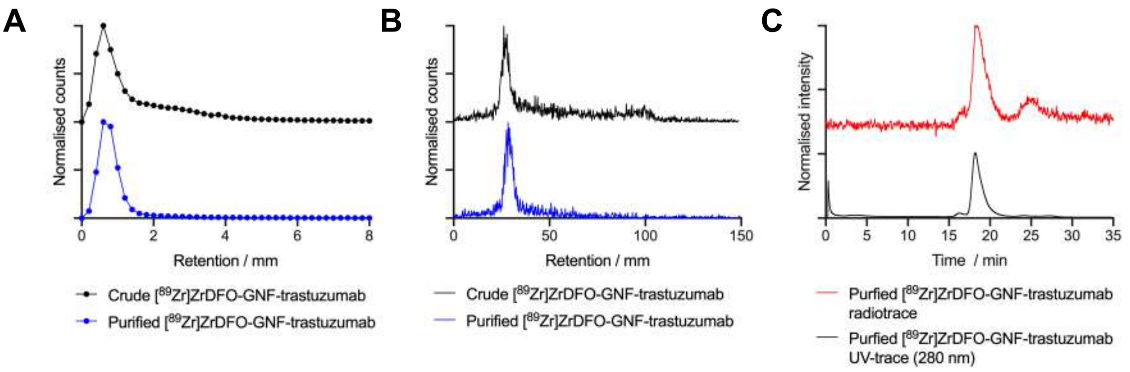

Cellular uptake of [^{89}Zr]ZrDFO-GNF-trastuzumab

FACS analysis with BODIPY-GNF-trastuzumab demonstrated specific binding to SK-OV-3 cells. This indicated that the trastuzumab remained immunoreactive and bound to HER2/*neu* despite functionalisation with the GNF. To further investigate the cell binding of these GNF-trastuzumab conjugates, a radiochemical cellular binding assay with [^{89}Zr]ZrDFO-GNF-trastuzumab was carried out. A standard Lindmo assay confirmed that [^{89}Zr]ZrDFO-GNF-trastuzumab remained immunoreactive with an IF value of 58.0 ± 2.3% (**Figure 5.7**).[384–389] Under the conditions employed, complete saturation was not fully reached, however, blocking studies further highlight the specific uptake of these constructs and the graphical analysis and linearisation allowed for estimation of the immunoreactive fraction of the product.

Figure 5.7. Lindmo cell binding assay **(A)** Saturation binding of [^{89}Zr]ZrDFO-GNF-trastuzumab to SK-OV-3 cells. **(B)** Lindmo straight line transformation of [^{89}Zr]ZrDFO-GNF-trastuzumab.

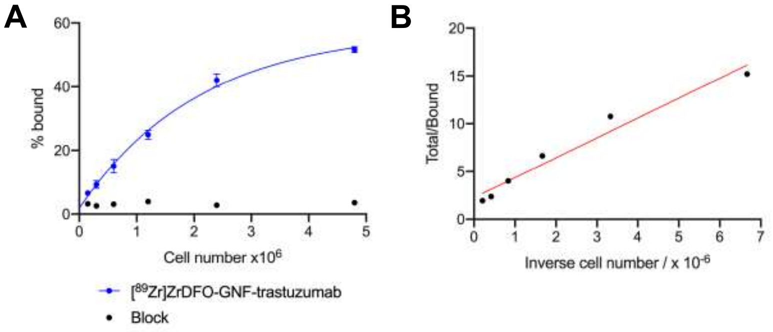

5.3.3 GdDOTAGA-DFO-GNF antibody conjugates

Functionalisation of GNFs with GdDOTAGA and DFO

As previous studies demonstrated the successful multi-functionalisation of the GNFs, the GNF-mAb conjugates became suitable candidates for creating a multi-modal PET/MR imaging agent. In pursuit of this aim, GNFs were functionalised with DFO (*vide supra*) for the conjugation of a PET isotope, and a GdDOTAGA derivative for MRI contrast. The DOTAGA chelate offers 8-donor atoms and is known to bind Gd^{3+} with a high thermodynamic stability (log*ß* = 25.6) and greater kinetic stability than DTPA complexes, thus making it a suitable candidate for further derivatisation.[390] Despite this, complex formation kinetics led to a slow reaction and heating was required to obtain the GdDOTAGA complex in a reasonable time scale.[391] Due to the thermal decomposition of the GNF constructs under elevated temperatures, the metallation must be performed prior to GNF linkage (**Scheme 5.2**). Compound **29** was isolated and characterised by using HR-MS and HPLC analysis and the r_1 relaxivity was measured by NMR to be 25.83 ± 2.71 mM^{-1} s^{-1}.

Scheme 5.2. Chemical synthesis of GdDOTAGA-PEG$_4$-NH$_2$ (**29**).

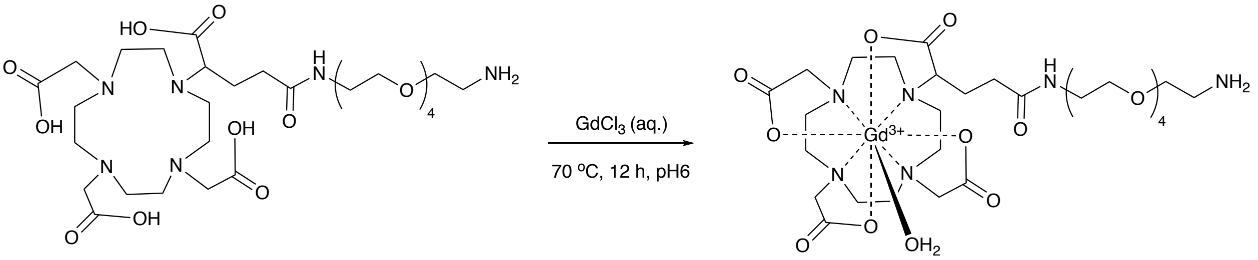

29

61%

Following complexation of the Gd^{3+}, compound **29** was conjugated to the carboxylated edge of the GNF by utilising the free amine on the GdDOTAGA-PEG$_4$-NH$_2$ in a standard amide coupling reaction. This reaction was carried out *in situ* with the DFO coupling, the conditions for which are detailed in **Chapter 4** (**Section 4.3.1**). As before, complete separation of starting materials *versus.* the functionalised GNF product on silica gel (R_f = 0.0-0.1 *vs*. R_f = 0.9-1.0, respectively; **Experimental**; **Figure 6.70**) allowed us to purify the GdDOTAGA-DFO-GNF product in high purity. Radiolabelling of the product with a known concentration of ^{68}Ga allowed us to determine that the product contained 13.4 ± 1.8 nmol of DFO per mg of GNF (n = 2). T$_1$ measurements allowed us to calculate the r_1 relaxivity of GdDOTAGA-DFO-GNF to be 0.88 ± 0.03 mL mg^{-1} s^{-1}, confirming that the paramagnetic Gd^{3+} ion was present on the material. By taking the T$_1$ relaxation time at a given concentration of GNF we are able to calculate that the GNF contains 45.0 ± 4.3 nmol of GdDOTAGA-PEG$_4$-NH$_2$ per mg of GNF giving a GdDOTAGA complex to DFO chelate ratio of approximately 3.4 : 1 on the GNF.

Radiochemical studies of GdDOTAGA-DFO-GNF

The synthesised GdDOTAGA-DFO-GNF was radiolabelled with ^{89}Zr^{4+} in 10 min at pH7.9 giving a RCC of 97% (determined *via* radio-iTLC). Due to range of sizes of the GNFs, PD10-SEC does not give adequate separation (**Figure 5.8A**). Therefore, radio-SEC-HPLC was used where the radiolabelled [^{89}Zr]GdDOTAGA-ZrDFO-GNF eluted at 24.1 min and small molecules eluted at 28.5 min (**Figure 5.8B**). This allowed us to determine a RCP of 98% for the purified [^{89}Zr]GdDOTAGA-ZrDFO-GNF. To assess the pharmacokinetic behaviour of the [^{89}Zr]GdDOTAGA-ZrDFO-GNF construct the radiotracer was administered *via* i.v. tail vein injection into an athymic nude mouse bearing a subcutaneous SK-OV-3 tumour (0.25 MBq, 40 µg GNF in 200 µL PBS). An initial PET image was acquired 5 min post-injection and showed that the majority of the activity was already cleared from the blood pool, extracted via kidneys, and was excreted though the bladder. This control study confirmed our previous observations and our hypothesis that radiolabelled GNF impurities that are not bound to protein are not retained *in vivo*. A subsequent PET image was recorded at 14 h post-injection which showed negligible amounts of radioactivity in the mouse and only a minor amount of activity retained in the kidneys and bone (~3 kBq in total; 1.2% of injected dose).

Figure 5.8. (A) Analytical PD-10-SEC elution profiles and **(B)** SEC-UHPLC chromatograms of [^{89}Zr]GdDOTAGA-ZrDFO-GNF.

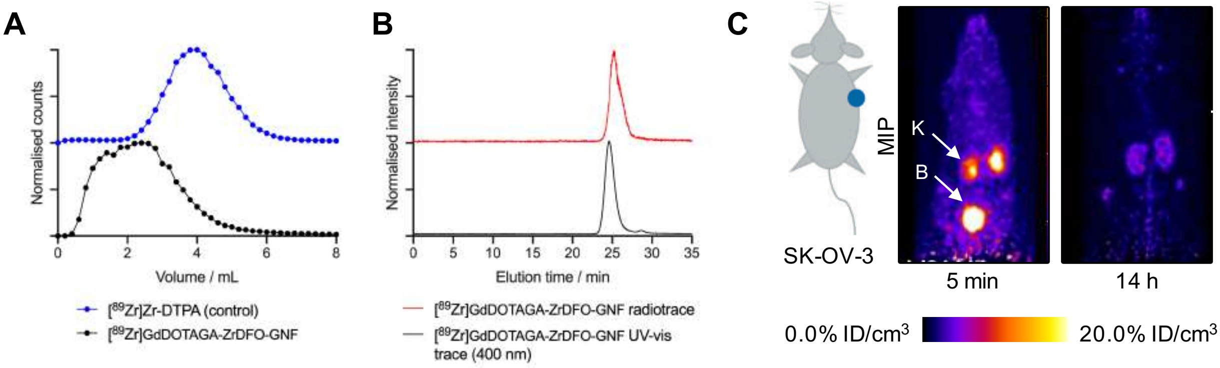

Conjugation of GdDOTAGA-DFO-GNF to trastuzumab

Once again, the methods established during the BODIPY-GNF conjugation were used to conjugate the GdDOTAGA-DFO-GNF to trastuzumab (**Figure 5.9**). Purification was carried out by using PD10 SEC and spin filtration (100 kDa) and product formation was confirmed by using SEC-HPLC. The r_1 relaxivity of GdDOTAGA-DFO-GNF-trastuzumab was measured by NMR to be 0.077 ± 0.001 mL mg^{-1} s^{-1} confirming that the Gd^{3+} ions remained present in the construct. By taking a known concentration of GdDOTAGA-DFO-GNF-trastuzumab we are able to determine a GdDOTAGA concentration of 0.99 ± 0.09 nmol per mg of protein. As we know the concentration of GdDOTAGA per unit mass of GNF, we are able to determine a GNF mass of 22.0 ± 0.1 µg per mg of protein. This corresponds to approximately 4 mAbs per GNF. It should be noted that due to the low concentrations of GdDOTAGA, these estimated numbers should be treated with caution. However, these approximations give us figures within the same order of magnitude as estimated obtained from the GNF-BODIPY experiments (*vide supra*).

Figure 5.9. Schematic structure of GdDOTAGA-DFO-GNF-trastuzumab. Note, the GNF is functionalised with multiple copies of [^{89}Zr]ZrDFO and GdDOTAGA and trastuzumab.

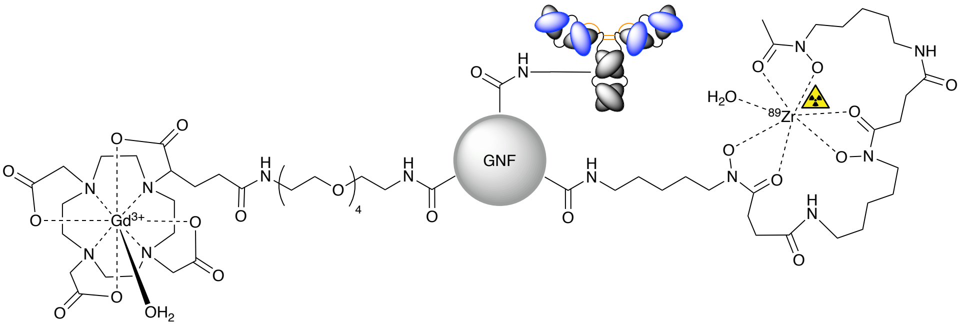

Radiolabelling of GdDOTAGA-DFO-GNF-trastuzumab with ^{89}Zr

Radiolabelling was achieved in 2 h to synthesise [^{89}Zr]GdDOTAGA-ZrDFO-GNF-trastuzumab with a RCY of 9.4 ± 4.5 % (*n* = 3). A lower RCY is reported here in comparison to [^{89}Zr]ZrDFO-GNF-trastuzumab as a large excess of radioactivity was added in order to push the radiolabelling reaction to completion and obtain sufficient product for use *in vivo*. PD10-SEC analysis of the crude product indicated a RCP of 6.3 ± 2.2 % (*n* = 3). Purification was achieved by using spin filtration (100 kDa) and PD10-SEC analysis of the purified [^{89}Zr]GdDOTAGA-ZrDFO-GNF-trastuzumab product gave a RCP of 91.4 ± 1.4 % (*n* = 3). The specific activity of the obtained product was found to be 1.72 ± 0.13 MBq mg^{-1} (*n* = 2; note: mass refers to protein mass only as determined experimentally from a BCA assay). Following characterisation, the stability of the [^{89}Zr]GdDOTAGA-ZrDFO-GNF-trastuzumab construct was tested by using a chelate challenge assay. The construct was incubated in DTPA (pH7.1, 50 mM) for 24 h, and by using PD10-SEC it was determined that 84% of the activity remained bound to [^{89}Zr]GdDOTAGA-ZrDFO-GNF-trastuzumab (**Experimental**; **Figure 6.72**).

Figure 5.10. Radiochemical data for [^{89}Zr]GdDOTAGA-ZrDFO-GNF-trastuzumab. **(A)** PD10-SEC with PBS as eluent **(B)** Radio-iTLC with silica gel as stationary phase and 50 mM DTPA as mobile phase. **(C)** Radio-SEC-HPLC with PBS as mobile phase.

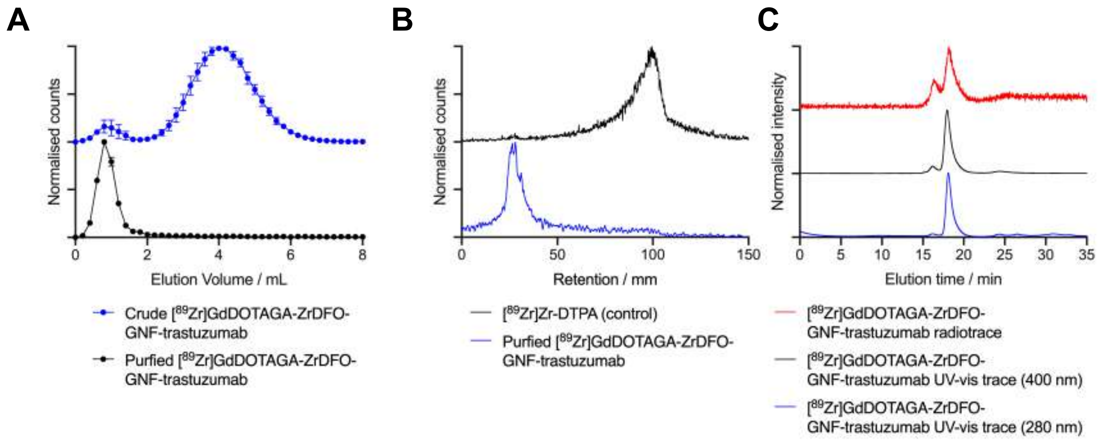

Cellular uptake of [^{89}Zr]GNF-GdDOTAGA-ZrDFO-trastuzumab

To investigate the specificity of [^{89}Zr]GdDOTAGA-ZrDFO-GNF-trastuzumab for HER2/*neu*, a radiochemical cellular binding assay was carried out by using SK-OV-3 cells. A standard Lindmo assay confirmed that [^{89}Zr]GdDOTAGA-ZrDFO-GNF-trastuzumab remained immunoreactive (IF = 62 ± 11%) (**Figure 5.11**). Blocking with a 1000-fold excess of free trastuzumab produced negligible binding of [^{89}Zr]GdDOTAGA-ZrDFO-GNF-trastuzumab confirming that the binding was facilitated *via* the antibody-antigen interaction.

Figure 5.11. Lindmo cell binding assay **(A)** Saturation binding of [^{89}Zr]GdDOTAGA-ZrDFO-GNF-trastuzumab to SK-OV-3 cells. **(B)** Lindmo straight line transformation of [^{89}Zr]GdDOTAGA-ZrDFO-GNF-trastuzumab .

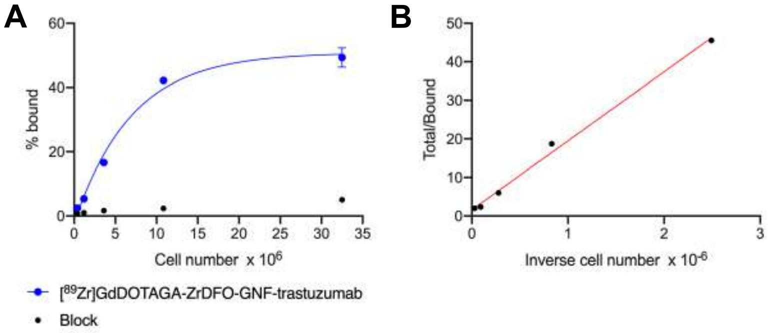

Small-animal PET imaging of [^{89}Zr]GdDOTAGA-ZrDFO-GNF-trastuzumab

Based on the successful results *in vitro*, the pharmacokinetic profile and tumour uptake of [^{89}Zr]GdDOTAGA-ZrDFO-GNF-trastuzumab was evaluated *in vivo* by using the PET imaging and biodistribution studies in athymic nude mice bearing subcutaneous SK-OV-3 tumours on the right flank. Mice were administered with [^{89}Zr]GdDOTAGA-ZrDFO-GNF-trastuzumab (0.11-0.14 MBq, 65-82 µg of mAb in 200 µL PBS) *via* i.v. tail vein injection, with a blocking formulation containing an additional 15.4-fold (1 mg total protein) of mAb. PET images were recorded at 1, 14, 24, 48, 72 and 90 h post-administration for both the normal and blocking groups (*n* = 4 mice / group). Visual inspection of images showed uptake of the [^{89}Zr]GdDOTAGA-ZrDFO-GNF-trastuzumab radiotracer into tumour tissue from 14 h onwards in the normal group (**Figure 5.12**). This uptake was not observed at the equivalent time points in the blocking group (**Experimental**; **Figure 6.73**). A large fraction of the injected radiotracer accumulated and was retained in the liver. Given the large size of the [^{89}Zr]GdDOTAGA-ZrDFO-GNF-trastuzumab construct, liver uptake was expected and is likely unavoidable unless the GNF-mAb constructs are redesigned to include coatings that could mask recognition by the reticuloendothelial system. Furthermore, significant bone uptake was also observed from 14 h onwards. ^{89}Zr^{4+} is known to accumulate in the bone of mice, and this observation is indicative of radiotracer metabolism leading to dissociation and release of an osseophilic ^{89}Zr^{4+} species of uncertain composition.[392]

Figure 5.12. [^{89}Zr]GdDOTAGA-ZrDFO-GNF-trastuzumab PET images recorded in mice bearing SK-OV-3 tumours on the right flank. T = tumour, H = heart, L = liver, S = spleen, B = bladder, Bo = Bone. "Block" = co-injected with non-radiolabelled trastuzumab.

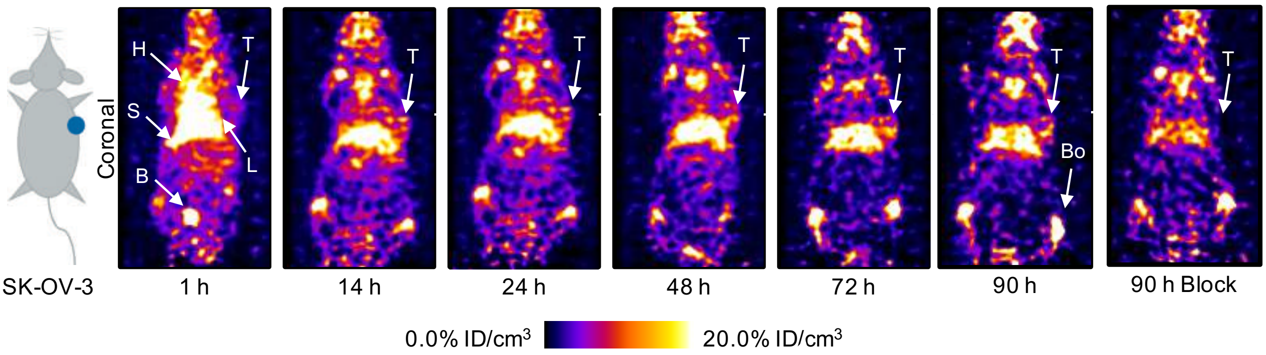

Volume of interest (VOI) analysis was used to quantify radiotracer distribution in different tissues based on the calibrated PET images (**Figure 5.13A**). Tumour uptake was higher for the normal group (Tumour VOI = 4.41 ± 0.83 %ID g^{-1}, 90 h, normal, *n* = 4;) when compared to mice that received the blocking formulation (Tumour VOI = 2.12 ± 0.48 %ID g^{-1}, 90 h, normal, *n* = 4). These data indicate that [^{89}Zr]GdDOTAGA-ZrDFO-GNF-trastuzumab displayed specific uptake in the tumour. VOI analysis of the heart is representative of activity circulating in the blood pool. From this we extracted a blood pool half-life ($t_{1/2}$) for the two groups where $t_{1/2}$(normal) = 7.05 ± 1.03 h (*n* = 4) and $t_{1/2}$(block) = 8.14 ± 0.58 h (*n* = 4) (**Figure 5.13B**). In comparison to our previous work with ^{68}Ga-radiolabelled GNFs (Chapter 4) and to [^{89}Zr]GNF-ZrDFO control described above (**Figure 5.8C**), the blood pool circulation time of [^{89}Zr]GdDOTAGA-ZrDFO-GNF-trastuzumab was greatly extended (c.f. Chapter 4: **GNF-4** $t_{1/2}$ = 5.22 ± 0.61 min). This extended blood pool half-life is strong evidence that the GNFs were successfully, and stably, conjugated to the mAb. At the 1 h time point, activity was found in the bladder for both groups of animals (Bladder VOI = 19.2 ± 7.2 %ID g^{-1}, 1 h, normal, [*n* = 4]; Bladder VOI = 21.5 ± 6.3 %ID g^{-1}, 1 h, block, [*n* = 4]). However, this activity was quickly excreted. The fraction of activity that displayed rapid renal elimination from the animals was is indicative of ^{89}Zr-radiolabelled GNFs not bound to protein or small molecule contaminants in the formulation of [^{89}Zr]GdDOTAGA-ZrDFO-GNF-trastuzumab. This initial excretion is also observed in the dose calibrator measurements of the whole-body activity in the mice (**Figure 5.14**). From 0-1 h there was a decrease (normal, 16.3 ± 5.4%; block, 7.2 ± 1.5%) in the retained activity. However, from 1-90 h this decrease followed the physical decay profile of ^{89}Zr. For comparison, when no mAb is conjugated to the GNF construct ([^{89}Zr]GNF-GdDOTAGA-ZrDFO), the majority of activity (76%, *n* = 1) is excreted within one hour (0-1 h) of injection.

Figure 5.13. (A) Time-activity bar chart showing the activity associated with different tissues (VOI) *versus*. time from quantitative analysis of the PET images in units of %ID g^{-1}.

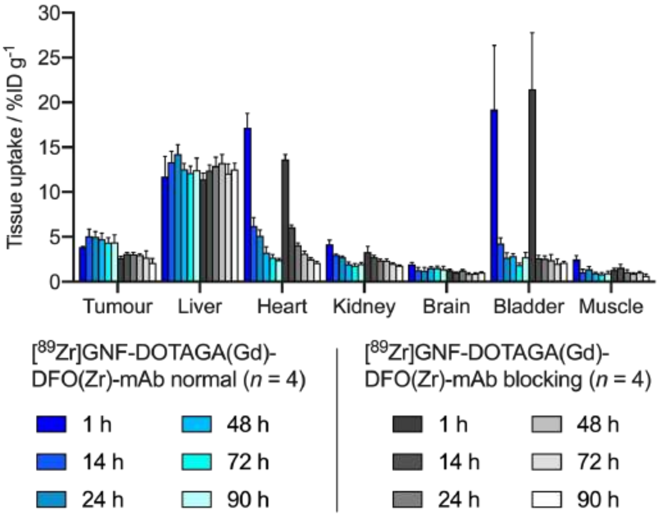

Figure 5.14. (A) Plot of the time-activity curves from the VOI analysis of the heart/blood pool measured by PET imaging. These data were used to extract the blood-pool half-life. **(B)** Plot of the measured whole-body activity retained in the normal (blue) and blocking (black) groups *versus* time after administration of [^{89}Zr]GdDOTAGA-ZrDFO-GNF-trastuzumab in SK-OV-3 tumour bearing mice. For reference the fast excretion of [^{89}Zr]GdDOTAGA-ZrDFO-GNF-trastuzumab is plotted (red), as well as the physical decay of ^{89}Zr (purple).

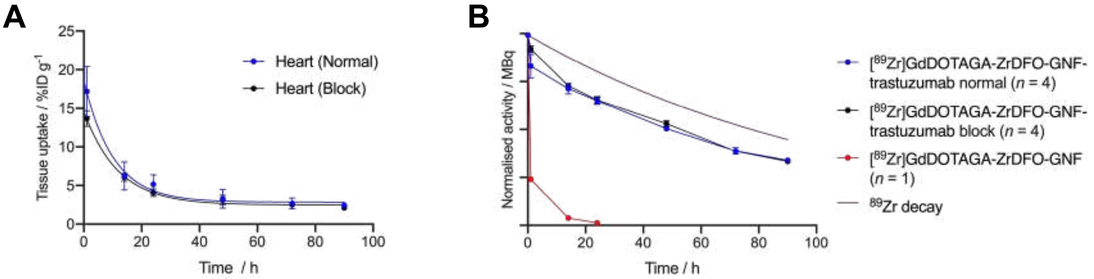

Biodistribution studies

Biodistribution studies were performed *ex vivo* after the final imaging time point at 90 h post-administration of [^{89}Zr]GdDOTAGA-ZrDFO-GNF-trastuzumab in SK-OV-3 tumour bearing mice (**Figure 5.15**). Following acquisition of the 90 h PET image, mice were euthanised by exsanguination under anaesthesia. Tissues were removed, washed, dried, weighed and the associated ^{89}Zr radioactivity was counted by using a gamma counter. **Experimental**; **Table 6.8** shows the full biodistribution data set. The data shows an increased accumulation of [^{89}Zr]GdDOTAGA-ZrDFO-GNF-trastuzumab in the normal group (7.53 ± 0.96 %ID g^{-1}, normal, *n* = 4) when compared to the block group (4.21 ± 1.05 %ID g^{-1}, block, *n* = 4). These data confirm that radiotracer uptake *in vivo* is facilitated *via* specific binding of the trastuzumab to the HER2/*neu*. In both groups, a large amount of activity was associated with the liver (20.87 ± 2.29 %ID g^{-1}, normal, *n* = 4; 22.95 ± 2.12 %ID g^{-1}, block, *n* = 4). This is to be expected given the large size of the constructs. In general, the biodistribution data are in excellent agreement with the quantitative analysis of the calibrated PET images.

Figure 5.15. Biodistribution data showing the accumulation of [^{89}Zr]GdDOTAGA-ZrDFO-GNF-trastuzumab radioactivity in different tissues at 90 h post-administration in mice bearing SK-OV-3 tumours.

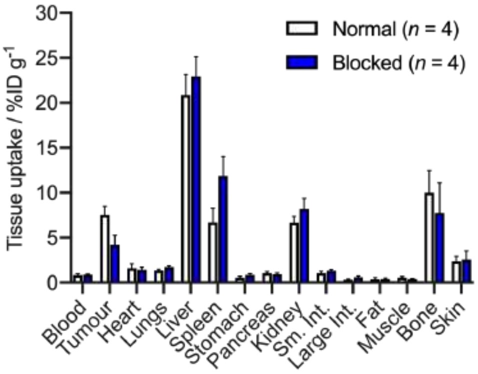

5.4 Conclusion

To conclude, we have successfully conjugated GNF constructs to both trastuzumab and onartuzumab, which allowed us to create multi-modal constructs for application in PET/MR imaging. GNF constructs were decorated with GdDOTAGA and DFO for subsequent ^{89}Zr radiolabelling. Following this, conjugation to trastuzumab allowed targeting of HER2/*neu* on SK-OV-3 cells and tumours which was demonstrated by using cellular binding assays. Finally, the pharmacokinetics and tumour-specific uptake of the [^{89}Zr]GdDOTAGA-ZrDFO-GNF-trastuzumab conjugate was evaluated *in vivo* by using small-animal PET imaging and biodistribution studies. Image analysis and biodistribution data indicated specific uptake in SK-OV-3 tumours, highlighting the potential of these constructs for use in the design of multi-modal imaging agents.

Thesis Conclusion

In this thesis, we have on focused the development of multi-modal imaging agents based on iron oxide nanoparticles and GNFs. We have explored various stages of radiotracer construction; from basic synthesis and radiochemistry, to cellular and animal studies.

Chapter 2 concentrated on the fundamental principles of nanoparticle synthesis and radiolabelling. Initially, we investigated two methods for the synthesis of iron oxide nanoparticles; co-precipitation and thermal decomposition. Both routes produced nanoparticles which were sufficiently small, accelerating the transverse relaxation of local water molecules to a range suitable for MR imaging. We also characterised and compared the commercially available nanoparticles, FH, as well as Fe_2O_3@Au nanoparticles obtained *via* a collaboration. The next section of Chapter 2 developed and investigated radiolabelling methods. Initially, classical, chelate-based methods were used to label nanoparticles with ^{68}Ga. The methods explored involved the use of traditional surface-based chemistries to label Fe_2O_3@Au with a ^{68}Ga, dithiolane chelate, as well as new method of conjugation using a photoactivatable chelate to derivatise the nanoparticle coating. We also studied intrinsic, chelate-free methods of radiolabelling nanoparticles which produced higher RCCs in shorter times timescales. To explore the mechanism of chelate-free radiolabelling further, the first kinetic studies were performed.

In Chapter 3 we built on the concepts developed in Chapter 2 to produce constructs for the potential use in PET/MRI. Both constructs were specifically targeted to cancer cells using the PSMA binding motif, and Fe_2O_3@Au nanoparticles were radiolabelled using a chelate method, whilst FH nanoparticles were radiolabelled using an intrinsic, chelate-free method. Following ^{68}Ga radiolabelling, constructs were tested *in vitro* using PSMA expressing, LNCaP cells which indicated specific uptake facilitated by the PSMA binding motif. Unfortunately, both constructs performed poorly when tested *in vivo* with small-animal PET imaging using athymic nude mice demonstrating rapid liver uptake and insignificant localisation in the tumour. Future work should involve altering the nanoparticles to improve the pharmacokinetic profile, and potentially enable the uptake of radiotracer into tumour tissue.

In Chapters 4 and 5, we have used GNFs to produce multi-modal imaging agents. Chapter 4 uses the GNFs as a scaffold to produce targeted theranostic agents. GNFs were loaded with derivatives of (*i*) a PSMA targeting vector, (*ii*) a potent anti-mitotic drug (*R*)-ispinesib, (*iii*) the chelate DFO for ^{68}Ga labelling, and (*iv*) an albumin-binding tag reported to extend pharmacokinetic half-life *in vivo*. Following synthesis and radiolabelling, *in vitro* experiments showed that constructs exhibited toxicity and specific uptake in LNCaP cells. Unfortunately, due to poor pharmacokinetics *in vivo*, GNFs were rapidly excreted and no significant tumour uptake was observed.

To address these issues, Chapter 5 conjugated an antibody to the GNF, improving specific uptake into target cells and increasing circulation times *in vivo*. The chemistries established in Chapter 4 were used to functionalise the GNFs with DFO for ^{89}Zr labelling and GdDOTAGA for MRI contrast, producing constructs with PET/MRI capabilities. The functionalised GNFs were then conjugated to the HER2/*neu* targeting mAb, trastuzumab, and subsequent *in vitro* assays demonstrated uptake in SK-OV-3 cells. Final small-animal PET imaging firstly demonstrated a longer circulation *in vivo*, as well as specific uptake in tumour tissue.

Chapter 6: Experimental

6.1 Standard Methods

6.1.1 Synthesis and Characterisation

NMR Spectroscopy

^{1}H, ^{13}C, ^{31}P and ^{19}F NMR spectra were measured in deuterated solvents on a Bruker AV-300, a Bruker AV-400, or a Bruker AV-500 spectrometer. Chemical shifts (δ) are expressed in parts per million (ppm) relative to the resonance of the residual solvent peaks or internal reference, for example, with DMSO δ_H = 2.50 ppm and δ_C = 39.5 ppm with respect tetramethylsilane (TMS, δ_H and δ_C = 0.00 ppm). Coupling constants (J) are reported in Hz. Peak multiplicities are abbreviated as follows: s (singlet), d (doublet), dd (doublet of doublets), t (triplet), q (quartet), m (multiplet), and br (broad).

Mass Spectrometry

High-resolution electrospray ionisation mass spectra (HR-ESI-MS) were measured by the mass spectrometry service at the Department of Chemistry, University of Zurich.

UV-Visible Spectroscopy

Electronic absorption spectra were recorded using a Nanodrop$^{\text{TM}}$ One$^{\text{C}}$ Microvolume UV-Vis Spectrophotometer (ThermoFisher Scientific, supplied by Witec AG, Sursee, Switzerland).

Sourcing of chemicals

Unless otherwise stated, all other chemicals were of reagent grade and purchased from SigmaAldrich (St. Louis, MO), Merck (Darmstadt, Germany), Tokyo Chemical Industry (Eschborn, Germany), abcr (Karlsruhe, Germany) or CheMatech (Dijon, France). Water (>18.2 MΩ·cm at 25 ºC, Puranity TU 3 UV/UF, VWR International, Leuven, Belgium) was used without further purification. Solvents for reactions were of reagent grade, and where necessary, were dried over molecular sieves.

Chromatography

Column chromatography was performed by using Merck silica gel *60* (63 – 200 µm) with eluents indicated in the experimental section. Standard thin-layer chromatography (TLC) for synthesis employed Merck TLC plates silica gel *60* on an aluminium base with the indicated solvent system. The spots on TLC were visualised either by UV/visible light (254 nm) or by staining with potassium permanganate or ninhydrin.

Transmission Electron Microscopy (TEM)

Samples (1 uL) were loaded onto 3 mm grids. TEM images were then measured on a Philips CM100 100 kV transmission electron microscope equipped with a digital CCD camera.

Dynamic Light Scattering (DLS)

Hydrodynamic size was measured with a Zetasizer Nano ZS90 (ZEN3690, Malvern Instruments Ltd, Malvern, UK) using polystyrene disposable cuvettes (Sarstedt AG &Co, Germany).

Zeta Potential measurements

ζ-potentials were measured with a Zetasizer Nano ZS90 (ZEN3690, Malvern Instruments Ltd, Malvern, UK) using Malvern disposable folded capillary cells. ζ-potential measurements consist of 20 runs (*n=3*).

XRD

Powder X-ray diffraction patterns (PXRD) were measured on an STOE STADI P diffractometer in transmission mode using Mo Kα1 radiation in a flat-plate sample holder with Ge monochromator and a position-sensitive microstrip solid-state detector (MYTHEN 1K).

IR measurements

Fourier transform infrared spectroscopy (FT-IR) was performed using a Bruker-Vertex 70 spectrometer.

Iron content calibration curve

A dilution series of iron(III) chloride (24-480 μM) was made in 2 M HCl. To 1 mL of each solution, 1.5 M ammonium thiocyanate solution (200 μL) was added. The solutions were mixed for 5 min and the absorbance measured.

Figure 6.1. Calibration plots for the determination of iron content in nanoparticles. **(A)** UV-vis spectrum (350-650 nm) for a variety of $[Fe(SCN)_6]^{3-}$ solutions with the λ_{max} = 466 nm. **(B)** $[Fe(SCN)_6]^{3-}$ concentration *vs.* absorbance at λ_{max} = 466 nm.

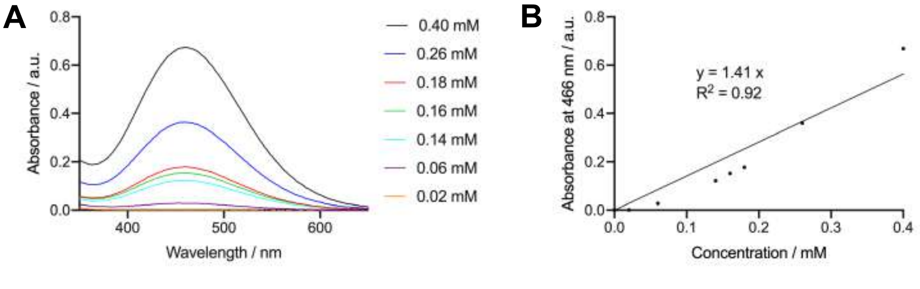

Amine content calibration (Kaiser assay)

Kaiser assay reagents

Reagent A – Potassium cyanide (1.65 mg, 25 μmol) was dissolved in water (2.5 mL). 100 μL of this solution was then added to pyridine (4.9 mL).

Reagent B – Ninhydrin (0.1 g, 0.56 mmol) dissolved in n-butanol (2 mL).

Reagent C – Phenol (4 g, 42.5 mmol) in *n*-butanol (2 mL).

Calibration curve

A dilution series of glutamic acid (0.3-4.6 mM) was made in water. To a 1 mL aliquot of sample reagent A (20 μL), reagent B (20 μL), and reagent C (20 μL) were added. The solution was heated to 100°C for 5 min and the absorbance measured.

Figure 6.2. Calibration plots for the determination of amine content. (A) UV-vis spectrum (500-650 nm) for a variety of amine concentrations with the λ_{max} = 568 nm. (B) Amine concentration vs. absorbance at λ_{max} = 568 nm.

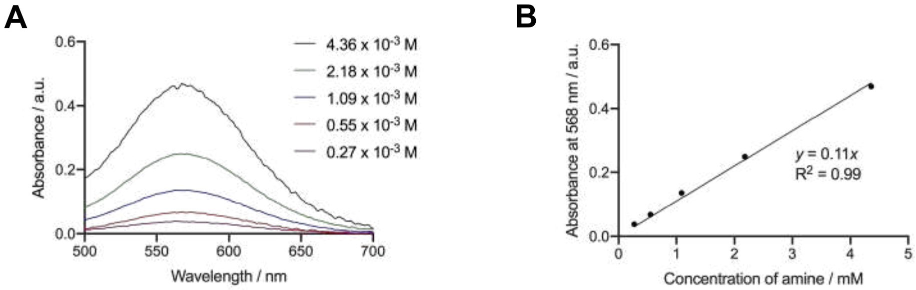

6.1.2 Cell culture

LNCaP

The human prostate cancer cell line LNCaP clone FCG (PSMA/positive, American Type Culture Collection (ATCC® CRL-1740™), Manassas, VA) was used. Cells were cultured at 37 °C in a humidified 5% CO_2 atmosphere in RPMI Medium 1640 containing [+]-L-glutamine (2.5 mM), supplemented with fetal bovine serum (FBS, 10% (v/v), ThermoFisher Scientific) and penicillin/streptomycin (P/S, 1% (v/v) of penicillin 10000 U/mL and streptomycin 10 mg/mL). Cells were grown by serial passage and were harvested by using trypsin (0.1%).

PC-3

The human prostate cancer cell line PC-3 (American Type Culture Collection (ATCC® CRL-1435™), Manassas, VA) was used. Cells were cultured at 37 °C in a humidified 5% CO_2 atmosphere in DMEM/F12 (1:1) (Dulbecco's Modified Eagle Medium, F-12 Nutrient mixture (Ham), ThermoFisher Scientific, Schlieren, Switzerland) medium containing [+]-L-glutamine (2.5 mM), supplemented with fetal bovine serum (FBS, 10% (v/v), ThermoFisher Scientific) and penicillin/streptomycin (P/S, 1% (v/v) of penicillin 10000 U/mL and streptomycin 10 mg/mL). Cells were grown by serial passage and were harvested by using trypsin (0.5%).

SK-OV-3

The human ovarian cancer cell line SK-OV-3 (HER2/neu-positive, American Type Culture Collection (ATCC- HTB-77), Manassas, VA) was used. Cells were cultured at 37 °C in a humidified 5% CO_2 atmosphere in DMEM/F12

(1:1) (Dulbecco's Modified Eagle Medium, F-12 Nutrient mixture (Ham), ThermoFisher Scientific, Schlieren, Switzerland) medium containing [+]-L- glutamine (2.5 mM), supplemented with fetal bovine serum (FBS, 10% (v/v), ThermoFisher Scientific) and penicillin/streptomycin (P/S, 1% (v/v) of penicillin 10000 U/mL and streptomycin 10 mg/mL). Cells were grown by serial passage and were harvested by using trypsin (0.5%).

MKN-45

The human gastric cancer cell line MKN-45 (Leibniz Institute DSMZ- German collection of Microorganisms and Cell cultures (ACC 409) was used. Cells were cultured at 37 °C in a humidified 5% CO_2 atmosphere in RPMI Medium 1640 containing [+]-L-glutamine (2.5 mM), supplemented with fetal bovine serum (FBS, 10% (v/v), ThermoFisher Scientific) and penicillin/streptomycin (P/S, 1% (v/v) of penicillin 10000 U/mL and streptomycin 10 mg/mL). Cells were grown by serial passage and were harvested by using trypsin (0.25%).

BCA Assay

Working reaction buffer was freshly prepared by adding $Cu(SO_4)_2$ (4%) to Pierce BCA Protein Assay Reagent A (ThermoFisher Scientific) in a 1:50 ratio. Cell lysate (5 µL) was added to the working reaction buffer (50 µL) in triplicate in a 96 well plate. The plate was incubated for 30 min at 37 °C. The absorbance was measured on Hidex-Sense Plate Reader using the BCA Assay programme. Absorbance was compared to a standard solution curve (using BSA protein). The protein concentrations of cell lysates were normalised by dilution in saline.

Xenograft models

All experiments involving mice were conducted in accordance with an animal experimentation licence approved by the Zurich Canton Veterinary Office, Switzerland (Jason P. Holland). Experimental procedures also complied with guidelines issued in the Guide for the Care and Use of Laboratory Animals. Athymic nude mice (Crl:NU(NCr)-Foxn1nu, 27 – 35 g, 6 – 8 weeks old) were obtained from Charles River Laboratories Inc. (Freiburg im Breisgau, Germany) and were allowed to acclimatise at the University of Zurich Laboratory Animal Services Center vivarium for at least 1 week prior to implanting tumour cells. Mice were provided with food and water ad libitum. Tumours were induced on the shoulders by sub-cutaneous (s.c.) injection of either LNCaP (2.5×10^6 cells) or SK-OV-3 (7×10^{6}) cells. The cells were injected in a 200 µL suspension of a 1:1 v/v mixture of PBS and reconstituted basement membrane (Corning® Matrigel® Basement Membrane Matrix, obtained from VWR International). Tumours developed after a period of between 3-8 weeks depending on cell line. Tumour volume (V / mm^3) was estimated by external Vernier caliper measurements of the longest axis, a / mm, and the axis perpendicular to the longest axis, b / mm. The tumours were assumed to be spheroidal and the volume was calculated in accordance with **Equation 6.1**. All mice injected with cancer cells developed tumours and the average volume of the LNCaP tumours was 325 ± 133 mm^3 ($n = 6$ mice).

Equation 6.1. Approximation of tumour volume.

$$V = \frac{4\pi}{3} \cdot \left(\frac{a}{2}\right)^2 \cdot \left(\frac{b}{2}\right)$$

6.1.3 Radiochemical Methods

All instruments for measuring radioactivity were calibrated and maintained in accordance with previously reported routine quality control procedures.[393]

Gallium-68

$[^{68}Ga][Ga(H_2O)_6]Cl_3(aq.)$ was obtained from $^{68}Ge/^{68}Ga$-generators (Eckert&Ziegler, Model IGG100 Gallium-68 Generator), eluted with 0.1 M HCl(aq.). The eluted ^{68}Ga activity was trapped and purified by using a strong cation exchange column (Strata-XC, [SCX], Eckert&Ziegler). $[^{68}Ga][Ga(H_2O)_6]Cl_3(aq.)$ was eluted from the SCX cartridge by using a solution containing 0.13 M HCl(aq.) and approx. 5 M NaCl(aq.) (SCX eluent). The generator gave varying molar activities. For radiolabelling experiments the ^{68}Ga stock solution was typically added as the limiting reagent to an aqueous reaction mixture buffered with NaOAc (approx. 0.2 M, pH4.4).

Zirconium-89

$[^{89}Zr][Zr(C_2O_4)_4]^{4-}$ (aq.) was obtained as a solution in ~1.0 M oxalic acid from PerkinElmer (Boston, MA, manufactured by the BV Cyclotron VU, Amsterdam, The Netherlands) and was used without further purification.

Indium-111

$[^{111}In]InCl_3(aq.)$ dissolved in HCl (~0.1 M) was obtained from a commercial source and used without further purification (B.e. imaging, Schwyz, Switzerland).

Copper-64

$[^{64}Cu]CuCl_2(aq.)$ dissolved in HCl (~0.5-3.0 M) was obtained from a commercial source and used without further purification (IPHC, Paris, France).

Radio-iTLC

Radioactive reactions were monitored by using instant thin-layer chromatography (iTLC). Glass-fibre iTLC plates impregnated with silica-gel (iTLC-SG, Agilent Technologies) were developed in water (>18.2 MΩ·cm) and analysed on a radio-TLC detector (SCAN-RAM, LabLogic Systems Ltd, Sheffield, United Kingdom). Radiochemical conversion (RCC) was determined by integrating the data obtained by the radio-TLC plate reader and determining both the percentage of radiolabelled product and 'free' ^{68}Ga, ^{89}Zr, ^{64}Cu or ^{111}In. Integration and data analysis were performed by using the software Laura version 5.0.4.29 (LabLogic).

Size Exclusion Chromatography

Samples were analysed by using two methods of SEC. The first was an automated size-exclusion column (Bio-Rad Laboratories, ENrich SEC 70, 10 ± 2 µm, 10 mm ID x 300 mm) connected to a HPLC device (Rigol L-3000, Contrec AG, Switzerland) equipped with a UV/visible detector (absorption measured at 400 nm) as well as a radioactivity detector (FlowStar2 LB 514, Berthold Technologies, Zug, Switzerland). Isocratic elution with phosphate buffered saline (PBS, pH7.4) with 200 mM arginine was used. The second method used a manual procedure involving size-exclusion column chromatography using a PD-10 desalting column (Sephadex G-25 resin, 85-260 µm, 14.5 mm ID x 50 mm, >30 kDa, GE Healthcare). For analytical procedures, PD-10 columns were eluted with sterile saline or PBS. A total of 40 x 200 µL fractions were collected up to a final elution volume of 8 mL. Note that the loading/dead-volume of the PD-10 columns is precisely 2.50 mL which was discarded prior to aliquot collection. For quantification of radioactivity, each fraction was measured on a gamma counter.

Quantification of radioactivity

For quantification of radioactivity, each fraction was measured on a gamma counter (HIDEX Automatic Gamma Counter, Hidex AMG, Turku, Finland) using a counting time of 30 s and an energy window between 480 – 558 keV for ^{68}Ga (511 keV emission), between 480 – 558 keV for ^{89}Zr (511 keV emission), 15 – 2047 keV for ^{111}In, and 480-558 keV for ^{64}Cu (511 keV emission). Appropriate background and decay corrections were applied throughout.

Calculation of the molar activities of radionuclides

The molar activities of radionuclides were determined *via* the titration of the nuclide with a known concentration of appropriate chelate (^{68}Ga-DFO, ^{89}Zr-DFO, ^{64}Cu-DTPA, ^{111}In-DTPA).

For example: The molar activity of ^{68}Ga is determined via titration with DFO. Briefly, DFO samples were prepared at a variety of concentrations and buffered with NaOAc (0.2 M, pH 4.4). Aliquots of [^{68}Ga][Ga(H$_2$O)$_6$]Cl$_3$(aq.) stock solution (ca. 16 MBq) were added to each sample and after 10 min radio-iTLC was used to gain a RCC. Data prior to saturation was fitted linearly (**Figure 3**). This was used to obtain a molar activity of 197 ± 4.8 MBq nmol^{-1}.

Figure 6.3. DFO titration to calculate the molar activity of the ^{68}Ga generator.

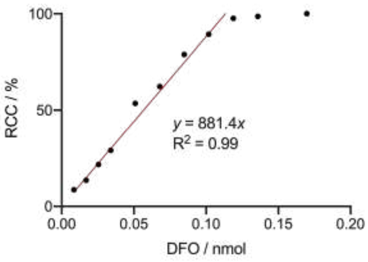

PET image acquisition

Mice were anesthetised by inhalation of between 2 – 4% isoflurane (Attane^{TM}, Piramal Enterprises Ltd, India, supplied by Provet AG, Lyssach, Switzerland)/oxygen gas mixture. PET imaging experiments were conducted on a Genesis G4 PET/X-ray scanner (Sofie Biosciences, Culver City, CA).[394] For each mouse the tail vein was warmed gently using a warm water bath, a catheter inserted in the tail vein and then placed on the scanner bed in the prone position. PET images were acquired using a γ-ray energy window of 150–650 keV, and a coincidence timing window of 20 ns. Images were reconstructed by iterative ordered subset maximum expectation (OSEM; 60 iterations) protocols. The reported reconstructed spatial resolution is 2.4 µL at the centre of the field-of-view (FOV). Image data were normalised to correct for non-uniformity of response of the PET, attenuation, random events, dead-time count losses, positron branching ratio, and physical decay to the time of injection, but no scatter or partial-volume averaging correction was applied. An empirically determined system calibration factor (in units of [Bq/voxel]/[MBq/g] or [Bq/cm^3]/[MBq/g]) for mice was used to convert voxel count rates to activity concentrations. The resulting image data were normalised to the administered activity to parameterise images in terms of %ID cm^{-3} (equivalent to units of %ID/g assuming a tissue density of unity). Images were analysed by using VivoQuant^{TM} 3.5 patch 2 software (InviCRO, Boston, MA). For image quantification and measurements of time-activity curves (TACs), 3-dimensional volumes-of-interest (VOIs) were drawn manually to determine the maximum and mean accumulation of radioactivity (in units of %ID cm^{-3} and decay corrected to the time of injection) in various tissues.

6.2. Experimental methods associated with Chapter 2

6.2.1 Synthesis and characterization of nanoparticles

Co-precipitation synthesis of Fe_3O_4 nanoparticles

Scheme 6.1. Reaction of iron(III) and iron (II) in basic conditions to form magnetite

$$2Fe^{3+} + Fe^{2+} + 8OH^{-} \longrightarrow Fe_3O_4 + H_2O$$

NB. All solutions used during this synthesis were degassed by the bubbling of nitrogen through the solutions for 5 h. As well as this, care was made to avoid oxygen reaching the reaction mixture during synthesis.

To a solution of iron(III) chloride hexahydrate (400 mg, 1.48 mmol) and iron(II) chloride (94 mg, 0.74 mmol) in water (13 mL), 30% ammonia (1.5 mL) solution was added. The resulting black precipitate was collected and transferred to a round bottom flask using water (15 mL) and sonication. 2M nitric acid (3.2 mL) and iron(II) nitrate nonahydrate (327 mg, 0.81 mmol) was added and the reaction was refluxed for 1.5 h. Following this, the reaction was allowed to cool to room temperature and then dialysed (dialysis tubing: MWCO = 14,000 g mol^{-1}) against 0.01M nitric acid for 3 days. Centrifugation (4000 rpm, 2 h) was used to remove aggregates and the dispersion was decanted to yield Fe_3O_4 as dark brown solution.

Iron content determination of Fe_3O_4 nanoparticles

Fe_3O_4 (1.0 mg) was dissolved in 10 M HCl (0.5 mL) and heated to 70 °C for 3 h. A portion of this solution (0.2 mL) was diluted into ammonium persulfate (1.5 M, 0.8 mL). Following this, ammonium thiocyanate solution (0.2 mL, 1.5 M) was added to all samples. After 5 min a dilution series was performed and the UV-vis spectra were recorded. Using previously determined extinction coefficients the particles were found to contain 12.72 ± 0.04 mmol iron per g of nanoparticle. This means nanoparticles are $70.9 \pm 0.2\%$ iron by mass.

Chemical synthesis of Fe_3O_4@OA nanoparticles

Reaction carried out under nitrogen. A solution of iron(III) acetylacetone (150 mg, 0.42 mmol) in diphenyl ether (2 mL) was prepared. Separately, in the reaction vessel a solution of oleic acid (0.21 mL, 0.67 mmol), oleylamine (0.22 mL, 0.67 mmol), and 1,2-hexandecanediol (290 mg, 1.12 mmol) in diphenyl ether (1.2 mL) was prepared. Simultaneously, both mixtures were heated to 120°C and then then 1 mL of the iron solution was injected into the reaction vessel. The reaction was then heated to 200°C for 30 min and then 265°C for a further 30 min. The reaction was allowed to cool to room temperature and ethanol (4 mL) was added. The resulting precipitate was collected and re-dispersed in a solution of oleic acid (5 μL) and oleylamine (5 μL) in hexane (4 mL). Solution was then centrifuged (4000 rpm, 5 min) and solution decanted. The addition of ethanol (6 mL) then caused precipitation which was collected and re-dispersed in hexane (4 mL) to yield Fe_3O_4@OA as a dark brown solution.IR: ν_{max}/cm^{-1} 2846 (CH), 2794 (CH), 985 (FeO), 480 (FeO).

Iron content determination of Fe_3O_4@OA

Fe_3O_4@OA (20.27 mg) was dissolved in 10 M HCl (1 mL) and heated to 70 °C for 3 h. A portion of this solution (0.2 mL) was diluted into ammonium persulfate (1.5 M, 0.8 mL). Following this, ammonium thiocyanate solution (0.2 mL, 1.5 M) was added to all samples. After 5 min a dilution series was performed and the UV-vis spectra were recorded. Using the previously obtained calibration plot the particles were found contain 5.14±0.48 mmol per g of nanoparticle. This equates to a 28.5±2.9% iron content by mass.

$Al(OH)_3$ functionalisation of Fe_3O_4@OA to synthesise Fe_3O_4@$Al(OH)_3$

To a solution of Fe_3O_4@OA in diethyl ether (1 mL, 2.25 mg mL^{-1}) a solution of $AlCl_3$ (0.36 mg, 2.70 μmol) in diethyl ether (0.5 mL) was added. The reaction was sonicated for 5 min and then acetone (400 μL) was added. The resulting precipitate was collected *via* centrifugation (16000 RPM, 20 min), dried and then re-dispersed into water (2 mL). IR: ν_{max}/cm^{-1} 3029 br (OH), 1553 (OH), 856 (FeO), 522 (Fe-O).

Iron content determination of Fe_3O_4@$Al(OH)_3$

Fe_3O_4@$Al(OH)_3$ (7.52 mg) was dissolved in 10 M HCl (1 mL) and heated to 70 °C for 3 h. A portion of this solution (0.2 mL) was diluted into ammonium persulfate (1.5 M, 0.8 mL). Following this, ammonium thiocyanate solution (0.2 mL, 1.5 M) was added to all samples. After 5 min a dilution series was performed and the UV-vis spectra were recorded. Using the previously obtained calibration plot the particles were found contain 2.04±0.14 mmol per g of nanoparticle. This equates to a 11.3±1.1% iron content by mass.

APTES functionalisation of Fe_3O_4@OA to synthesise Fe_3O_4@APTES

To a solution of Fe_3O_4@OA in hexane (10 mL, 1 mg mL^{-1}) a solution of APTES (30 μL, 28.3 μg, 0.13 μmol) in a 1:1 H_2O:EtOH (1 mL) was added. The reaction was shaken vigorously for 14 h. The resulting precipitate was washed with hexane (3 x 5 mL) and the particles were dispersed in dilute HCl (0.1 mM, 10 mL). IR: ν_{max}/cm^{-1} 2909 (CH), 2831 (CH), 1507 (NH), 1396 (Si-C), 1283 (Si-O), 1036 (Fe-O), 541 (FeO).

Iron content determination of Fe_3O_4@APTES

Fe_3O_4@APTES (3.12 mg) was dissolved in 10 M HCl (1 mL) and heated to 70 °C for 3 h. A portion of this solution (0.2 mL) was diluted into ammonium persulfate (1.5 M, 0.8 mL). Following this, ammonium thiocyanate solution (0.2 mL, 1.5 M) was added to all samples. After 5 min a dilution series was performed and the UV-vis spectra were recorded. Using the previously obtained calibration plot the particles were found contain 4.20±0.31 mmol per g of nanoparticle. This equates a 23.4±1.8% iron content by mass.

Amine content determination of Fe_3O_4@APTES

In a test tube, a solution of Fe_3O_4@APTES (1 mg mL^{-1}, 20 μL) and the Kaiser assay reagents (20 μL A, 20 μL B and 20 μL C) was prepared. As a comparison, a tube with Fe_3O_4@OA (20 μL) the Kaiser assay reagents (20 μL A, 20 μL B and 20 μL C) was prepared. Both test tubes were heated to 110 °C for 5 min, with a blue colour being observed in the Fe_3O_4@APTES test tube. The absorbance was recorded and using the amine content calibration curve (**Figure 2**) the amine content was found to be 1.3 mM.

Determination of Fe_2O_3@Au composition (ICP-MS)

Samples measured by UZH ICP-MS service. Samples were dissolved in nitric acid (3 mL, 2%) in a 1:1000 dilution before measurements were carried out on an Agilent 8800 ICP-MS. Data was then compared to iron and gold calibration plots. Samples were found to contain 24.8 ± 0.4 µg ml^{-1} iron and 106.0 ± 0.1 µg ml^{-1} gold.

T_2 relaxation times

T_2 relaxation times were measured for nanoparticles using a Bruker AV-III 11.74 T 500 MHz NMR. Nanoparticles were measured at a concentration of 1 mg mL^{-1} and then the relaxivity was calculated (**Chapter 1**; **Equation 1.3**) using the known iron concentration. T_2 relaxation of pure water was found to be 363.7 ms.

6.2.2 Radiolabeling of nanoparticles

Chelate based radiolabeling of Fe_2O_3@Au

*Synthesis of (R)-lipoic acid-$(PEG)_4$-DOTAGA (2) and chelation to gallium (^{nat}Ga-**2**)*

Synthesis of compound **1**

To a solution of (±)-α-Lipoic acid (400 mg, 1.92 mmol) in DCM (20 mL), EDC (423 mg, 2.21 mmol) and NHS (254 mg, 2.21 mmol) were added. After 3 h the reaction was washed with water (3 x 30 mL) and brine (1 x 30 mL), dried with anhydrous $MgSO_4$, and solvent removed under reduced pressure to isolate product as a yellow solid (438 mg, 1.44 mmol, 76%). ^{1}H NMR (400 MHz, $CDCl_3$) δ 3.61 (dq, *J* = 8.3, 6.4 Hz, 1H), 3.26 – 3.10 (m, 2H), 2.87 (s, 4H), 2.66 (t, *J* = 7.4 Hz, 2H), 2.56 – 2.44 (m, 1H), 1.96 (s, 1H), 1.82 (p, *J* = 7.4 Hz, 2H), 1.78 – 1.69 (m, 2H), 1.66 – 1.54 (m, 2H).^{13}C NMR (126 MHz, $CDCl_3$) δ 169.72, 169.02, 56.69, 40.76, 39.12, 35.02, 31.39, 28.93, 26.20, 24.97.

Figure 6.4. ^{1}H NMR spectrum ($CDCl_3$, 400 MHz) of compound **1**.

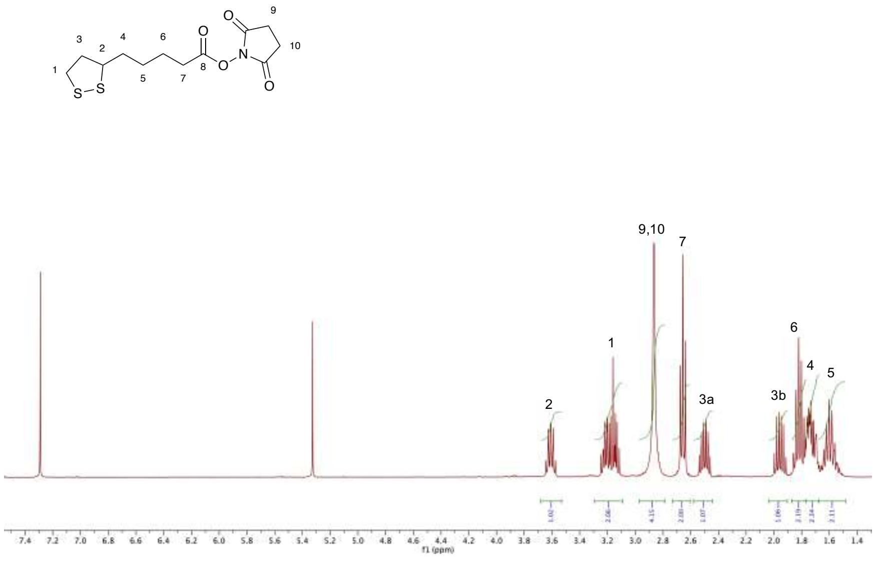

Figure 6.5. $^{13}C\{^1H\}$ NMR spectrum ($CDCl_3$, 126 MHz) of compound **1**.

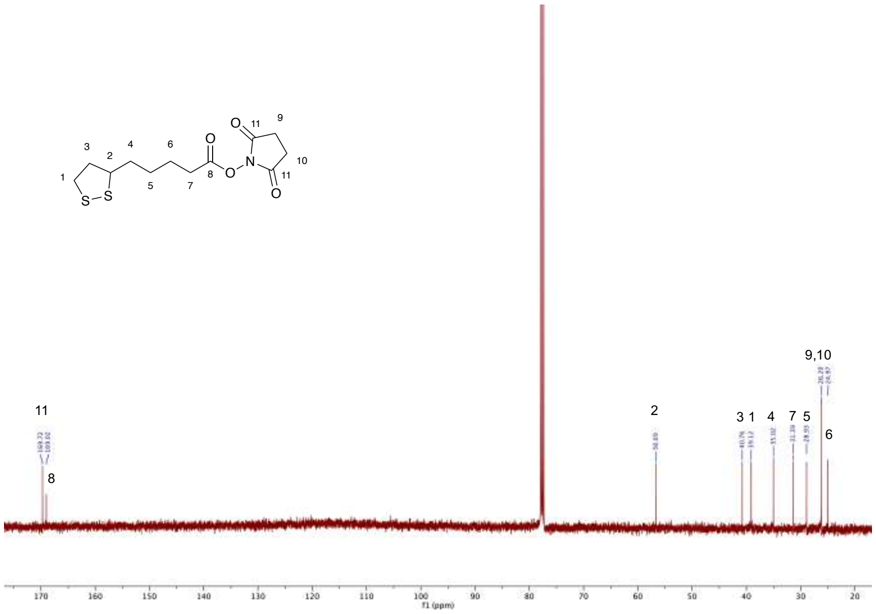

Synthesis of compound **2**

To a solution of compound **1** (13.1 mg, 43.2 μmol) in DMF (1 mL) and TEA (40 μL), NH_2-$(PEG)_4$-DOTAGA (30 mg, 43.2 μmol) was added. The solution was stirred for 24 h at room temperature before further addition of compound **1** (16.9 mg, 28.8 μmol). The reaction was then stirred for a further 24 h and then the solvent was removed under reduced pressure. The solid was washed with diethyl ether (1 x 5 mL) and DCM (3 x 5 mL) to yield **2** as an off-white solid (12.1 mg, 13.8 µmol, 32%). ^{1}H NMR (500 MHz, D_2O) δ 4.10 – 2.83 (m, 46H), 2.58 – 2.54 (m, 2H), 2.50 (dq, *J* = 12.3, 6.1 Hz, 1H), 2.27 (t, *J* = 7.3 Hz, 2H), 2.00 (d, *J* = 13.7, 6.7 Hz, 3H), 1.76 (dtd, *J* = 13.6, 7.9, 5.5 Hz, 1H), 1.69 – 1.56 (m, 3H), 1.42 (p, *J* = 7.4 Hz, 2H). ^{13}C NMR (126 MHz, D_2O) δ 176.99, 176.98, 176.95, 69.64, 69.59, 69.42, 69.40, 68.88, 68.76, 56.52, 40.26, 38.93, 38.88, 38.06, 35.46, 33.70, 27.81, 25.01. HRMS (ESI+) (m/z): calculated for $C_{37}H_{68}N_6O_{14}S_2^{2+}$ ($[M+2H]^{2+}$): 442.2112; found: 442.2118) (100%).

Figure 6.6. ^{1}H NMR spectrum (D_2O, 500 MHz) of compound **2**.

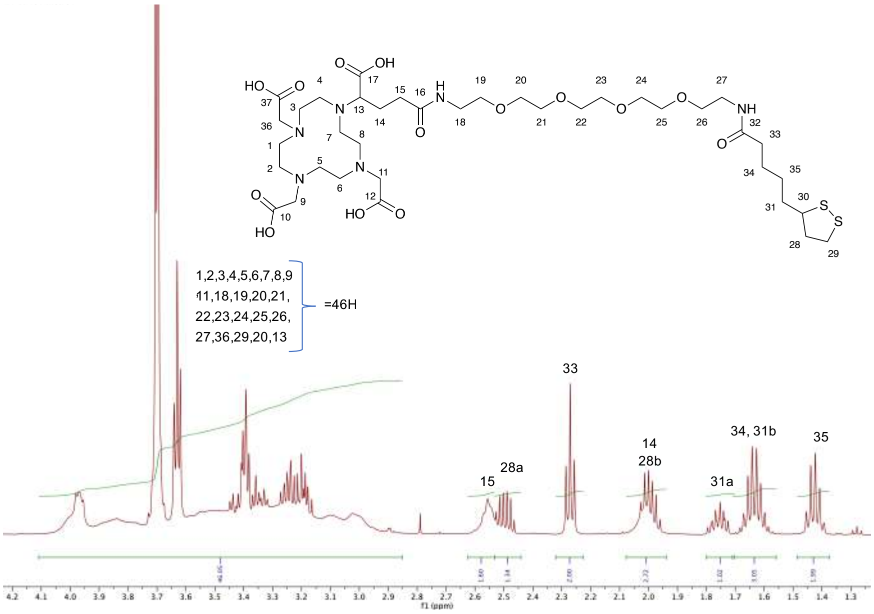

Figure 6.7. 2D-COSY spectrum (D_2O) of compound **2** (region between δ_H = 1.0 – 4.4 ppm).

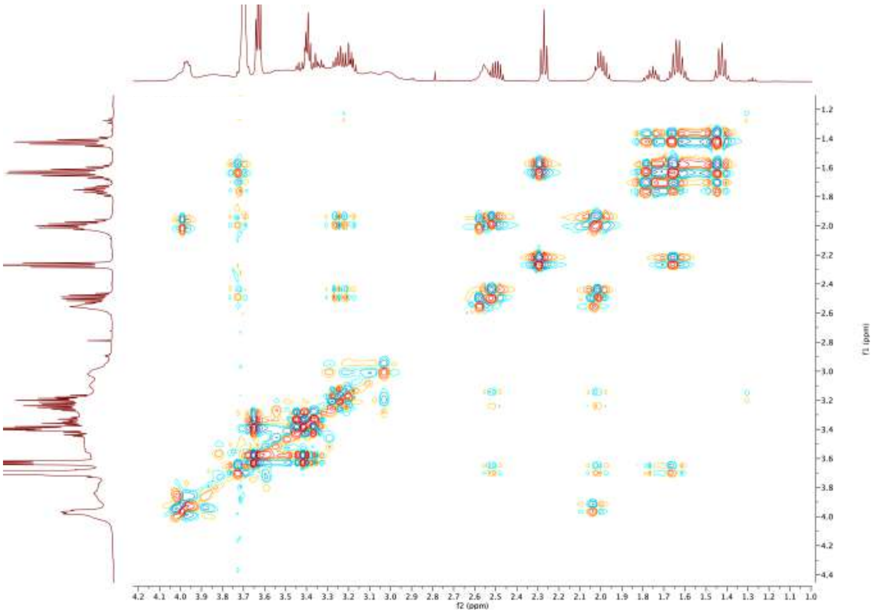

Figure 6.8. $^{13}C\{^1H\}$ NMR spectrum (D_2O, 126 MHz) of compound **2**.

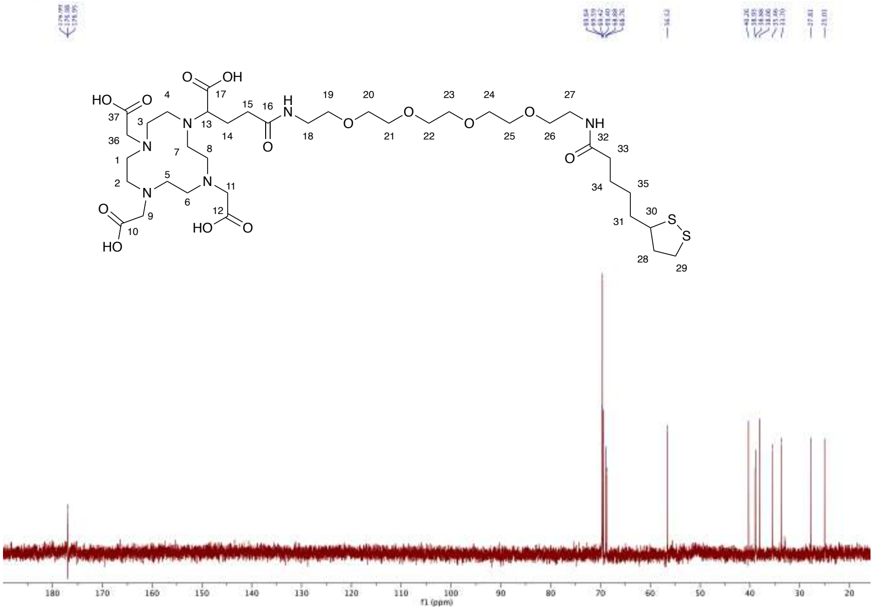

Figure 6.9. 2D-HSQC spectrum (D_2O) of compound **2**.

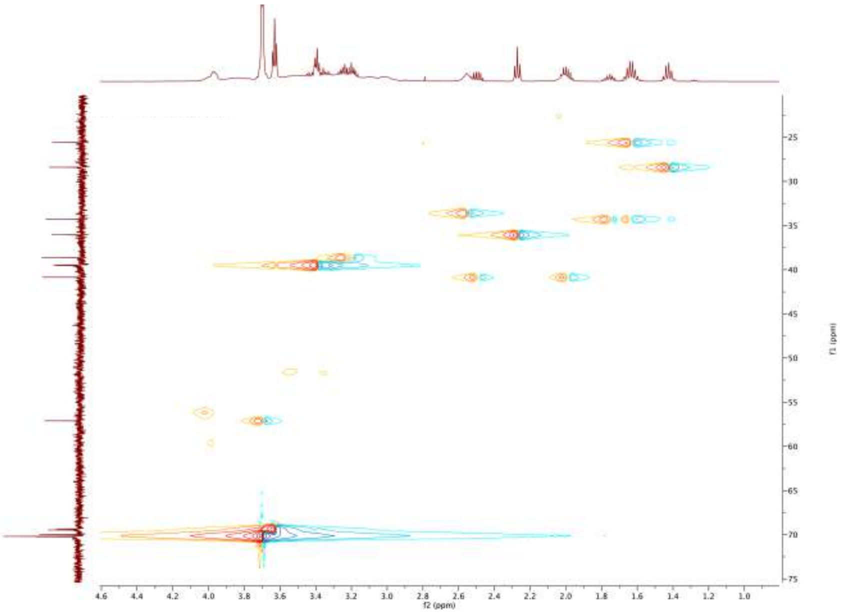

Synthesis of compound ^{nat}Ga-**2**

To a solution of compound **2** (3 mg, 3.4 µmol) in water (100 µL) gallium nitrate (0.93 mg, 3.4 µmol) was added. The solution was heated at 70 °C for 10 min and to yield ^{nat}Ga-**2** in a quantitative yield. t_R (RP-HPLC) = 6.24 min (detection at λ = 254 nm). RP-HPLC method: A flow rate of 1.0 mL min^{-1} with a linear gradient of A (distilled H_2O containing 0.1% TFA) and B (acetonitrile): t = 0 min, 95% A; t = 12 min, 5% A; t = 15 min, 5% A. HRMS (ESI+) (m/z): calculated for $C_{37}H_{65}GaN_6O_{14}S_2^{2+}$ ($[M+H]^{2+}$): 475.1623; found: 442.2118) (100%).

Figure 6.10. HR-ESI-MS data for compound ^{nat}Ga-**2**.

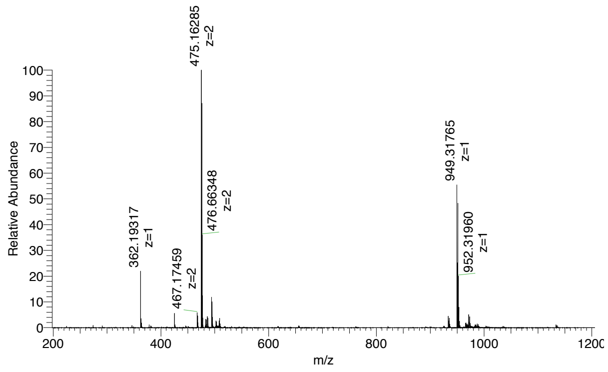

Radiolabelling of compound ***2*** *- Synthesis of [^{68}Ga]Ga-**2***

Radiolabelling reactions to prepare [^{68}Ga]LA-(PEG)$_4$-DOTAGA-Ga ([^{68}Ga]Ga-**2**) were accomplished by addition of an aliquot of [^{68}Ga][Ga(H_2O)$_6$]Cl_3(aq.) stock solution (ca. 12.8 MBq) to an aqueous solution of **2** (5 µL, 11.3 µg, 12.8 nmol) buffered with NaOAc (0.2 M, pH 4.4). The reaction was monitored by using radio-iTLC and was found to be complete after 10 min. at 70 °C giving a radiochemical conversion (RCC) >99% (n = 5, R_f = 0.00 – 0.20, eluent: 0.2 M citrate buffer). The product was characterised by analytical HPLC (Nucleodur EC 250/4, 4 mm ID x 250 mm (C18 HTec, 5 µm) at a flow rate of 1.0 mL min^{-1} with a linear gradient of A (distilled H_2O containing 0.1% TFA) and B (acetonitrile): t = 0 min, 95% A; t = 12 min, 5% A; t = 15 min. Note that the UV/vis detector and radioactivity detector were arranged serially with an offset time of approximately 0.10 min. The identity of the radiolabelled compound ^{68}Ga-**2** was confirmed with an authenticated sample of ^{nat}Ga-**2**.

*Chemical synthesis of [^{68}Ga]Fe_2O_3@Au-(Ga-**2**)*

[^{68}Ga]Ga-**2** was prepared as described above and then neutralised with NaOH (1M, approx. 25 µL). An aliquot of [^{68}Ga]Ga-**2** (3.5 µL, 0.17 nmol) was added to Fe_2O_3@Au (190 µL, 24.8 µg, 102.03 nmol of Au) and reaction vortexed. After 5 mins radio-iTLC (stationary phase: silica gel, mobile phase: MeOH/H_2O 1:1 with 0.5% HCl) indicated a RCC>97% (n = 3, R_f = 0.0 – 0.23). PD10-SEC (eluent: water) indicated a RCP of 94%.

*Loading capacity of Fe_2O_3@Au with ^{68}Ga-**2***

[^{68}Ga]Ga-**2** was prepared as described above and then neutralised with NaOH (1M, approx. 25 µL). A dilution series was then performed (0.6-23.3 µM) and 20 µL of each ^{68}Ga-**2** sample was added to 20 µL Fe_2O_3@Au (0.54 mM). Radio-iTLC was then used to determine the RCC. It was found that concentrations of [^{68}Ga]Ga-**2** > 2.33 µM saturated the nanoparticle surface and led to free [^{68}Ga]Ga-**2** in solution.

*Kinetic study of the functionalisation of nanoparticles with ^{68}Ga-**2***

[^{68}Ga]Fe_2O_3@Au-(Ga-**2**) reactions were prepared as described above by using the maximum concentration of chelate (2.33 µM) and cooled to 4 °C. On addition of [^{68}Ga]Ga-**2**, aliquots were taken at time intervals (5-90 s) and the RCC determined. The rate constant was determined by fitting the data to second-order rate kinetics.

Control studies

Scheme 6.2. Chemical synthesis of [^{68}Ga]Ga-DOTAGA-PEG$_4$-NH$_2$ ([^{68}Ga]Ga-**3**) and the control reaction with Fe_2O_3@Au.

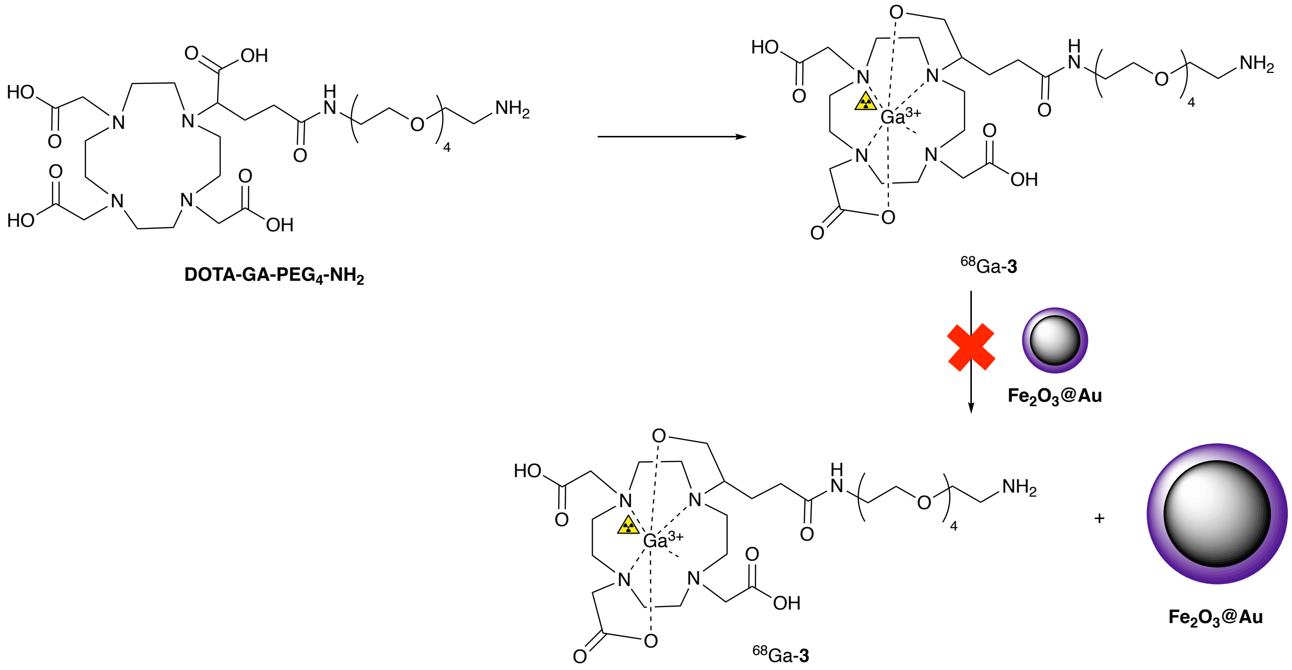

Preparation of ^{68}Ga-**3**

Radiolabeling reactions to prepare [^{68}Ga]DOTAGA-Ga-(PEG)$_4$-NH$_2$ ([^{68}Ga]Ga-**3**) were accomplished by addition of an aliquot of [^{68}Ga][Ga(H_2O)$_6$]Cl_3(aq.) stock solution (10.7 MBq) to an aqueous solution of **3** (8.90 µg, 12.8 nmol) buffered with NaOAc (0.2 M, pH 4.4). The reaction was monitored by using radio-iTLC and was found to be complete after 10 min. at 70 °C giving a radiochemical conversion (RCC) = 98% (R_f = 0.00 – 0.32, eluent: 0.2 M citrate buffer, pH4.5).

Incubation of ^{68}Ga-**3** with NP

^{68}Ga-**3** was prepared as described above and then neutralised with NaOH (1M, approx. 25 µL). An aliquot of ^{68}Ga-**3** (10 µL, 0.47 nmol) was added to Fe_2O_3@Au (190 µL, 102.03 nmol of Au) and reaction vortexed. After 5 mins PD10 size exclusion chromatography (eluent: 100% water) indicated the absence of radiolabeled NP.

Figure 6.11. (A) Radio-iTLC data irradiated for [^{68}Ga]Ga-**3** with silica as stationary phase and 0.2 M citrate buffer (pH4.5) as eluent. **(B)** PD10-SEC (water as eluent) following incubation of [^{68}Ga]Ga-**3** with Fe_2O_3@Au.

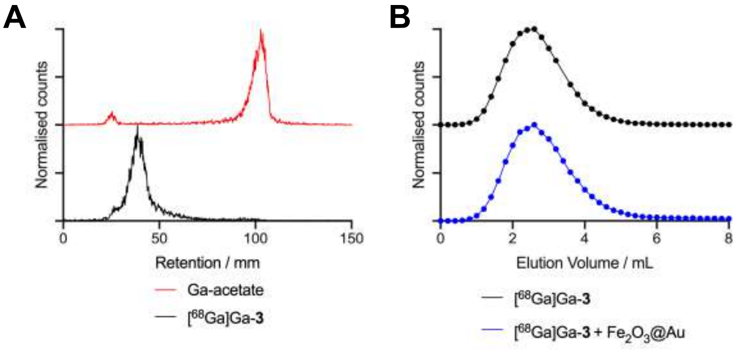

Photoconjugation of radiolabelled photo-activatable chelate to nanoparticle surface

Radiolabelling of photoactivatable chelate

Scheme 6.3. Synthesis of [^{68}Ga]GaDOTA-PEG$_4$-ArN$_3$ ([^{68}Ga]Ga-**4**)

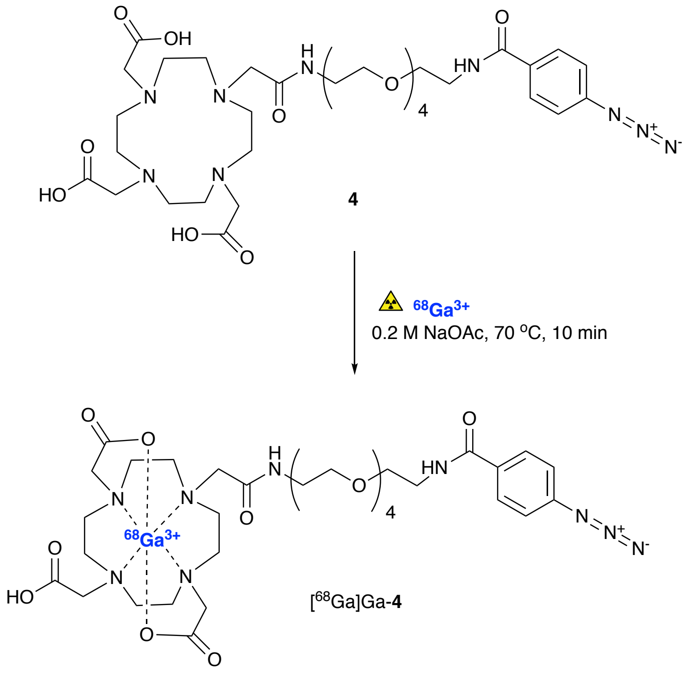

High chelate concentration synthesis of [^{68}Ga]Ga-**4**

Radiolabelling reaction to prepare [^{68}Ga]GaDOTA-PEG$_4$-ArN$_3$ ([^{68}Ga]Ga-**4**) was accomplished by addition of an aliquot of [^{68}Ga][Ga(H$_2$O)$_6$]Cl$_3$(aq.) stock solution (54.38 MBq) to an aqueous solution of DOTA-PEG$_4$-ArN$_3$ (50 mM, 20 µL, 10 nmol) buffered with NaOAc (0.2 M, pH 4.4). The reaction was monitored by using radio-iTLC and was found to be complete after 10 min. at 70 °C. Characterisation data analogous to that of the chelate at lower concentration below.

Low chelate concentration synthesis of [^{68}Ga]Ga-**4**

Radiolabelling reaction to prepare [^{68}Ga]GaDOTA-PEG$_4$-ArN$_3$ was accomplished by addition of an aliquot of [^{68}Ga][Ga(H$_2$O)$_6$]Cl$_3$(aq.) stock solution (28.4 MBq) to an aqueous solution of DOTA-PEG$_4$-ArN$_3$ (0.5 mM, 20 μL, 10 nmol) buffered with NaOAc (0.2 M, pH 4.4). The reaction was monitored by using radio-iTLC and was found to be complete after 10 min. at 70 °C giving a radiochemical conversion (RCC) >99% (R_f = 0.08 – 0.21). RP-UHPLC: t_R(radioactive trace) = 8.60 min (RCP 98%). RP-UHPLC method: Nucleodur EC 250/4, 4 mm ID x 250 mm (C18 HTec, 5 μm) at a flow rate of 1 mL min^{-1} with a linear gradient of A (H$_2$O containing 0.1% TFA) and B (MeOH): t = 0-2 min., 80% A; t = 12 min., 5% A; t = 14 min., 5% A; t = 16 min., 80% A; t = 18 min., 80% A.

Control - Irradiation of chelate

Following the synthesis of [^{68}Ga]GaDOTA-PEG$_4$-ArN$_3$, an aliquot (100 μL) of the reaction was placed in a glass vial and the pH adjusted to pH8 with the addition of NaHCO$_3$ (1 M, 20 μL). The sample was then irradiated for 10 min at 365 nm and analysed via radio-iTLC and PD10-SEC where the 'RCC' was found to be 0.8%.

Figure 6.12. Characterisation data for irradiated [^{68}Ga]Ga-**4** **(A)** Radio-iTLC data with silica as stationary phase and 0.2 M citrate buffer (pH4.5) as eluent. **(B)** PD10-SEC with PBS as eluent

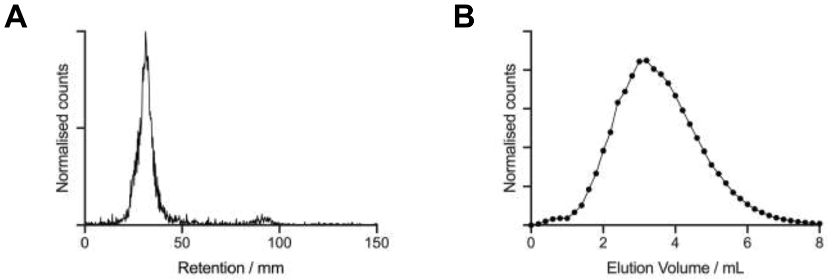

Functionalisation of FH with APTES

Scheme 6.4. Functionalisation of FH with APTES

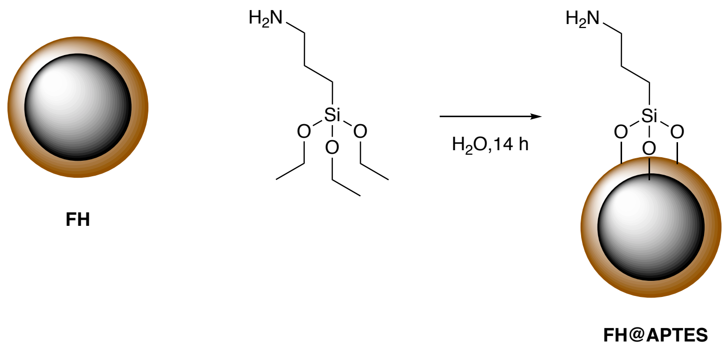

To a solution of FH nanoparticles (1 mL, 3 mg mL^{-1}), APTES (30 μL, 28.38 μg, 128.1 μmol) was added and the reaction was vortexed for 14 h. Purification was then carried out by using preparative PD10 with saline as the eluent and collecting the first 1.8 mL. Amine concentration was then determined by using the Kaiser assay and was found to be 31.47 μmol mg^{-1}. Samples were diluted to 1 mg mL^{-1} (31.47 mM amine).

Light mediated conjugation of [^{68}Ga]GaDOTA-PEG$_4$-ArN$_3$ to FH-APTES – High concentration of chelate

Following the synthesis of [^{68}Ga]Ga-**4**, an aliquot (100 μL) of the reaction (high chelate concentration synthesis) was placed in a glass vial and the pH adjusted to pH8 with the addition of $NaHCO_3$ (1 M, 20 μL). Following this an aliquot of FH-APTES (100 μL, 1 mg mL^{-1}) was added and the sample was irradiated at 365 nm for 10 min. The crude product was then analysed by using PD10-SEC (saline as eluent) and the RCC was found to be 1.4%.

Light mediated conjugation of [^{68}Ga]GaDOTA-PEG$_4$-ArN$_3$ to FH-APTES – Low concentration of chelate

Following the synthesis of [^{68}Ga]Ga-**4**, an aliquot (100 μL) of the reaction was placed in a glass vial and the pH adjusted to pH8 with the addition of $NaHCO_3$ (1 M, 20 μL). Following this an aliquot of FH-APTES (100 μL, 1 mg mL^{-1}) was added and the sample was irradiated at 365 nm for 10 min. The crude product was then analysed using PD10-SEC (saline as eluent) and the RCC was found to be 4.1%. Purification of the sample could then be carried out using preparative PD10-SEC (saline as eluent) by collecting the first 1 mL eluted giving a RCY of 3.3 %. A second analytical PD10-SEC (saline as eluent) determined the RCP to be 97%.

Conjugation of [^{68}Ga]GaDOTA-PEG$_4$-ArN$_3$ to FH-APTES – control studies

No irradiation control

Following the synthesis of [^{68}Ga]Ga-**4**, an aliquot (100 μL) of the reaction was placed in a glass vial and the pH adjusted to pH8 with the addition of $NaHCO_3$ (1 M, 20 μL). Following this an aliquot of FH-APTES (100 μL, 1 mg mL^{-1}) was added and the sample was left in the dark for 10 min. The crude product was then analysed using SEC-PD10 (saline as eluent) and the 'RCC' was found to be 0.7%.

No amine control

Following the synthesis of [^{68}Ga]Ga-**4**, an aliquot (100 μL) of the reaction was placed in a glass vial and the pH adjusted to pH8 with the addition of $NaHCO_3$ (1 M, 20 μL). Following this an aliquot of FH (100 μL, 1 mg mL^{-1}) was added and the sample was irradiated at 365 nm for 10 min. The crude product was then analysed by using SEC-PD10 (saline as eluent) and the 'RCC' was found to be 1.3%.

Functionalisation of Fe_3O_4 with alendronate

Scheme 6.5. Functionalisation of Fe_3O_4 with alendronate

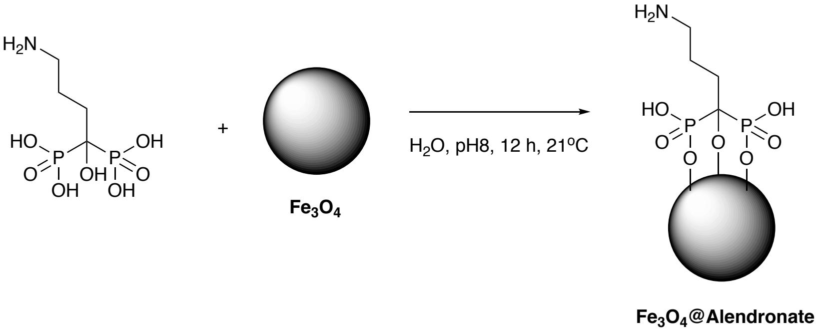

A solution of sodium alendronate (3 mg, 9.22 μmol) in water (200 μL) was prepared and the pH was adjusted to pH8 by the addition of NaOH (2M, 4 μL). This was then added to a dispersion of Fe_3O_4 (200 μL, 18.76 mg mL^{-1}) in water (2 mL). The reaction was mixed overnight by heavy agitation and then purified using PD10-SEC using water as the eluent and collecting the first 1.8 mL eluted. The amine content was then determined using the Kaiser assay and found to be 4.93 μmol mg^{-1} (7.05 mM). Samples were diluted to 1 mg mL^{-1} (4.93 mM amine).

Photoconjugation of [^{68}Ga]GaDOTA-PEG$_4$-ArN$_3$ to Fe_3O_4@Alendronate

Following the synthesis of [^{68}Ga]Ga-**4** the pH was adjusted to pH8 with the addition of $NaHCO_3$ (1 M, 35 μL). An aliquot (10 μL) was then added to Fe_3O_4@Alendronate (100 μL, 1 mg mL^{-1}) was added and the sample was irradiated at 365 nm for 10 min. The crude product was then analysed using PD10-SEC (water as eluent) and the RCC was found to be 7.4 ± 0.3% (*n* = 3). Purification of the sample could then be carried out using preparative PD10-SEC (water as eluent) by collecting the first 1 mL eluted giving a RCY of 6.0 ± 0.2% (*n* = 3). A second analytical PD10-SEC (water as eluent) determined the RCP to be 91%.

Photoconjugation of [^{68}Ga]GaDOTA-PEG$_4$-ArN$_3$ to Fe_3O_4@Alendronate - Control Studies

No irradiation control

Following the synthesis of [^{68}Ga]Ga-**4** the pH was adjusted to pH8 with the addition of $NaHCO_3$ (1 M, 35 μL). An aliquot (10 μL) was then added to Fe_3O_4@Alendronate (100 μL, 1 mg mL^{-1}) was added and the sample was incubated in the dark for 10 min. The crude product was then analysed by using PD10-SEC (water as eluent) and the 'RCC' was found to be 1.7%.

No amine control

Following the synthesis of [^{68}Ga]GaDOTA-PEG$_4$-ArN$_3$ the pH was adjusted to pH8 with the addition of $NaHCO_3$ (1 M, 35 μL). An aliquot (10 μL) was then added to Fe_3O_4 (100 μL, 1 mg mL^{-1}) was added and the sample was irradiated at 365 nm for 10 min. The crude product was then analysed by using PD10-SEC (water as eluent) and the 'RCC' was found to be 1.6%.

Chelate-free radiolabelling of iron oxide nanoparticles

Chelate free radiolabeling of Fe_3O_4@$Al(OH)_3$

To Fe_3O_4@$Al(OH)_3$ solutions (750 μL, 750 μg) buffered with NaOAc (0.2 M, pH 4.4) aliquots of [^{68}Ga][Ga(H_2O)$_6$]Cl_3(aq.) stock solution (~25.0 MBq) were added. Reactions were incubated at 21 °C and 70 °C for 10 min. The RCC was determined by radio-iTLC (stationary phase: silica gel, mobile phase: 1 M citrate buffer, pH 4.5) to be 37.2% (@21 °C) and 96.1% (@70 °C).

Chelate free radiolabeling of Fe_3O_4@ATPES

To Fe_3O_4@ATPES solutions (750 μL, 750 μg) buffered with NaOAc (0.2 M, pH 4.4) aliquots of [^{68}Ga][Ga(H_2O)$_6$]Cl_3(aq.) stock solution (~25.0 MBq) were added. Reactions were incubated at 21 °C and 70 °C for 10 min. The RCC was determined by radio-iTLC (stationary phase: silica gel, mobile phase: 1 M citrate buffer, pH 4.5) to be 98.2% (@21 °C) and 99.2% (@70 °C).

Kinetic study of ^{68}Ga radiolabeling of Fe_3O_4

To Fe_3O_4 solutions (100 μL, 100 μg) aliquots of [^{68}Ga][Ga(H_2O)$_6$]Cl_3(aq.) stock solution (~0.40 MBq) were added. Reactions were incubated at 21 °C, 37 °C, 50 °C and 70 °C at pH2. Aliquots of the reactions were taken at various time point and the RCC was determined by radio-iTLC (stationary phase: silica gel, mobile phase: 1:1 MeOH:H_2O with 1% HCl). Reactions were performed in triplicate and obtained RCCs are summarised in **Table 6.1**.

Table 6.1. Mean RCC and associated SEM for the ^{68}Ga radiolabeling of Fe_3O_4

	21 °C		37 °C		50 °C		70 °C	
Time / min.	Mean RCC / %	SEM / %	Mean RCC / %	SEM / %	Mean RCC / %	SEM / %	Mean RCC / %	SEM / %
0.25	-	-	-	-	14.8	2.8	60.2	3.0
0.5	3.4	-	5.0	1.2	22.4	4.9	79.7	1.8
1	5.9	0.1	5.8	0.1	35.9	4.3	87.3	2.2
2	-	-	-	-	58.8	8.0	93.9	0.6
3	6.2	0.1	12.8	0.8	76.1	6.2	96.7	0.2
5	-	0.4	-	-	84.0	3.8	98.3	0.8
6	8.9	0.5	14.1	0.1	-	-	-	-
10	-	-	-	-	92.3	1.2	97.5	0.4
12	13.7	0.5	30.7	4.5	-	-	-	-
15	-	3.7	-	-	92.8	0.3	97.8	0.1
20	20.2	0.6	55.2	3.3	-	-	-	-
-30	25.6	2.2	73.2	2.8	-	-	-	-
60	36.1	-	86.8	1.3	-	-	-	-
120	46.1	-	87.9	0.5	-	-	-	-

Kinetic study of ^{68}Ga radiolabeling of FH

To FH solutions (100 μL, 100 μg) aliquots of [^{68}Ga][Ga(H_2O)$_6$]Cl_3(aq.) stock solution (~0.40 MBq) were added. Reactions were incubated at 37 °C, 50 °C, 70 °C and 90 °C at pH3. Aliquots of the reactions were taken at various time point and the RCC was determined by radio-iTLC (stationary phase: silica gel, mobile phase: 100% H_2O). Reactions were performed in triplicate and obtained RCCs are summarised in **Table 6.2**.

Table 6.2. Mean RCC and associated SEM for the ^{68}Ga radiolabeling of FH

	37 °C		50 °C		70 °C		90 °C	
Time / min.	Mean RCC / %	SEM / %	Mean RCC / %	SEM / %	Mean RCC / %	SEM / %	Mean RCC / %	SEM / %
0.25	-	-	1.8	0.5	14.6	2.3	44.5	7.6
0.5	-	-	4.9	0.8	34.0	2.1	73.9	3.4
1	0.5	0.1	10.2	1.5	57.5	4.2	86.8	2.0
2	-	-	21.6	3.3	76.7	3.9	94.0	0.4
3	1.5	0.1	30.6	4.3	82.3	3.4	93.5	1.2
5	2.4	0.4	45.7	6.2	89.7	1.8	96.0	1.1
10	6.7	0.5	59.1	4.6	92.0	1.8	97.4	0.4
15	-	-	67.8	4.9	95.4	2.2	96.8	0.5
20	13.0	0.5	75.9	3.3	96.1	0.4	-	-
30	20.2	3.7	83.1	2.4	97.0	0.3	-	-
60	44.4	0.6	87.8	1.7	-	-	-	-
120	64.1	2.2	-	-	-	-	-	-

Kinetic study of ^{111}*In radiolabeling of* Fe_3O_4

To a portion of [^{111}In]InCl$_3$(aq.) (6.08 MBq) 1 M acetate buffer (20 μL, pH4.4) was added. This [^{111}In]In(OAc)$_3$ stock was then used for the following reactions. To Fe_3O_4 solutions (50 μL, 50 μg) aliquots of [^{111}In]In(OAc)$_3$(aq.) stock solution (~0.21 MBq) were added. Reactions were incubated at 37 °C, 50 °C, 70 °C and 90 °C at pH3. Aliquots of the reactions were taken at various time point and the RCC was determined by radio-iTLC (stationary phase: silica gel, mobile phase: 50 mM DTPA, pH7.1). N.B. TLC were quantified by dividing the TLC in two and measuring the associated activity using the Hidex Gamma counter (as opposed to using the TLC plate reader). Reactions were performed in triplicate and obtained RCCs are summarised in **Table 6.3**.

Table 6.3. Mean RCC and associated SEM for the ^{111}In radiolabeling of Fe_3O_4

	37 °C		50 °C		70 °C		90 °C	
Time / min.	Mean RCC / %	SEM / %	Mean RCC / %	SEM / %	Mean RCC / %	SEM / %	Mean RCC / %	SEM / %
0.25	-	-	-	-	8.7	0.8	21.0	0.3
0.5	-	-	-	-	16.9	1.2	26.2	0.7
1	-	-	19.7	0.7	23.7	1.9	33.5	1.4
2	6.4	1.0	22.8	2.2	26.4	1.5	36.8	1.0
3	-	-	-		32.6	5.4	55.2	9.2
5	11.7	0.5	28.8	5.5	46.0	6.3	66.3	7.7
10	14.9	3.0	47.9	1.4	56.7	3.1	80.5	4.8
15	-	-	50.5	4.1	69.3	1.6	86.4	4.2
20	24.7	4.1	54.7	4.9	71.3	3.7	89.9	5.0
30	30.6	1.1	61.1	9.2	75.6	2.5	-	-
60	39.0	1.5	77.0	6.2	-	-	-	-

Kinetic study of ^{111}In radiolabeling of FH

To a portion of [^{111}In]$InCl_3$(aq.) (6.08 MBq) 1 M acetate buffer (20 μL, pH 4.4) was added. This [^{111}In]$In(OAc)_3$ stock was then used for the following reactions. To FH solutions (50 μL, 50 μg) aliquots of [^{111}In]$In(OAc)_3$(aq.) stock solution (~0.21 MBq) were added and reactions were buffered with 0.2M NaOAc (pH 4.4). Reactions were incubated at 37 °C, 43 °C, 50 °C and 70 °C at pH4.4. Aliquots of the reactions were taken at various time point and the RCC was determined by radio-iTLC (stationary phase: silica gel, mobile phase: 100% H_2O). N.B. TLC were quantified by dividing the TLC in two and measuring the associated activity using the Hidex Gamma counter (as opposed to using the TLC plate reader). Reactions were performed in triplicate and obtained RCCs are summarised in **Table 6.4**.

Table 6.4. Mean RCC and associated SEM for the ^{111}In radiolabeling of FH

	37 °C		43 °C		50 °C		70 °C	
Time / min.	Mean RCC / %	SEM / %	Mean RCC / %	SEM / %	Mean RCC / %	SEM / %	Mean RCC / %	SEM / %
0.25	-	-	-	-	-	-	47.0	4.3
0.5	-	-	-	-	-	-	61.8	2.9
1	-	-	14.5	2.3	35.3	2.1	76.7	0.7
2	-	-	38.2	1.7	50.4	2.5	88.6	0.4
3	-	-	-	-	-	-	90.2	0.2
5	19.2	1.8	64.4	6.5	81.3	1.2	90.2	0.3
10	28.6	0.8	74.7	2.8	90.2	0.2	89.7	0.3
15	-	-	76.9	6.1	90.4	0.3	-	-
20	41.3	3.5	82.5	3.3	90.2	0.2	89.6	0.3
30	44.9	1.1	85.2	0.5	90.3	0.3	88.7	0.5
60	52.6	2.1	88.6	1.1	-	-	47.0	4.3

Thiol mediated radiolabelling of Fe_2O_3@Au

Neutralisation of ^{64}Cu stock

The pH of a portion of the ^{64}Cu stock solution (50 μL, 2.85 MBq) was adjusted to pH7 *via* the addition of NH_4OAc (1 M, 7 μL) and Na_2CO_3 (1 M, 35 μL).

Functionalisation of Fe_2O_3@Au with CH_3-PEG_n-SH to produce Fe_2O_3@Au(-S-PEG_n-CH_3)$_x$

CH_3-PEG_n-SH - Average $M_n = 800$ - Estimated Mw ≈ 35310 g mol^{-1}

Using the approximate molecular weight a stock solution of CH_3-PEG_n-SH was prepared in H_2O with the concentration of ~ 1 mM. This was then diluted to ~ 46.54 μM. An aliquot of CH_3-PEG_n-SH (~ 46.54 μM, 10.5 μL) was added to Au@Fe_2O_3 NP (490 μL). The sample was incubated for 1 h at 21 °C and then used without further purification.

Radiolabelling of Au@Fe_2O_3(-S-PEG_n-CH_3)$_x$

To test varying temperatures parallel reactions were prepared. To a Au@Fe_2O_3(-S-PEG_n-CH_3)$_x$ solution (48 μL) an aliquot of neutralised ^{64}Cu stock (2 μL, ~0.2 MBq) was added. The reaction was left at 4 °C, 21 °C, 37 °C or 50 °C. Aliquots of the reaction were taken for TLC analysis at time points between 0-60 min.

Reaction conditions - 20 min at 50 °C

To a Au@Fe_2O_3(-S-PEG_n-CH_3)$_x$ solution (48 μL) an aliquot of neutralised ^{64}Cu stock (3.5 μL, ~0.2 MBq) was added. The reaction was incubated at 50 °C for 20 min. The RCC was determined to be 88.1 ± 1.6% (*n* = 2) using radio-iTLC. The RCP was determined to be 93.3 ± 1.2 % (*n* = 2) using PD-10 SEC with water as the eluent. The reaction was purified by PD10-SEC taking the first 1.8 mL to give a RCY of 74.8% and RCP of 99.6%.

Reaction conditions - 1 h at 37 °C

To a Au@Fe_2O_3(-S-PEG_n-CH_3)$_x$ solution (48 μL) an aliquot of neutralised ^{64}Cu stock (3.5 μL, ~0.2 MBq) was added. The reaction was incubated at 37 °C for 1 h. The RCC was determined to be 91.1 ± 1.8% (*n* = 3) using radio-iTLC. The RCP was determined to be 85.3 ± 8.6% (*n* = 2) using PD-10 SEC with water as the eluent.

Control studies

Control 1 – radiolabelling of non-functionalised nanoparticles (bare Fe_2O_3@Au NP)

To test varying temperatures three reactions were prepared. To a NP solution (190 μL) an aliquot of neutralised ^{64}Cu stock (3.5 μL, ~95 kBq) was added. The reaction was left at 21 °C, 37 °C or 70 °C. Aliquots of the reaction for were taken for TLC analysis after 1 h.

Control 2 – radiolabelling of CH_3-PEG_n-SH

Preparation of CH_3-PEG_n-SH solution**.** An aliquot of CH_3-PEG_n-SH (~ 46.54 μM, 10.5 μL) was added to H_2O (490 μL). The sample was incubated for 1 h at 21 °C and then used without further purification. To test varying temperatures three reactions were prepared. To the CH_3-PEG_n-SH solution (48 μL) an aliquot of neutralised ^{64}Cu stock (2 μL, ~0.2 MBq) was added. The reaction was left at room temperature, 37 °C or 70 °C. Aliquots of the reaction were taken for TLC analysis at 60 min.

6.3 Experimental methods associated with Chapter 3

6.3.1 PSMA targeting

Synthesis and characterisation

Scheme 6.6. Chemical synthesis of Glu- NH-CO-NH-Lys, **9**

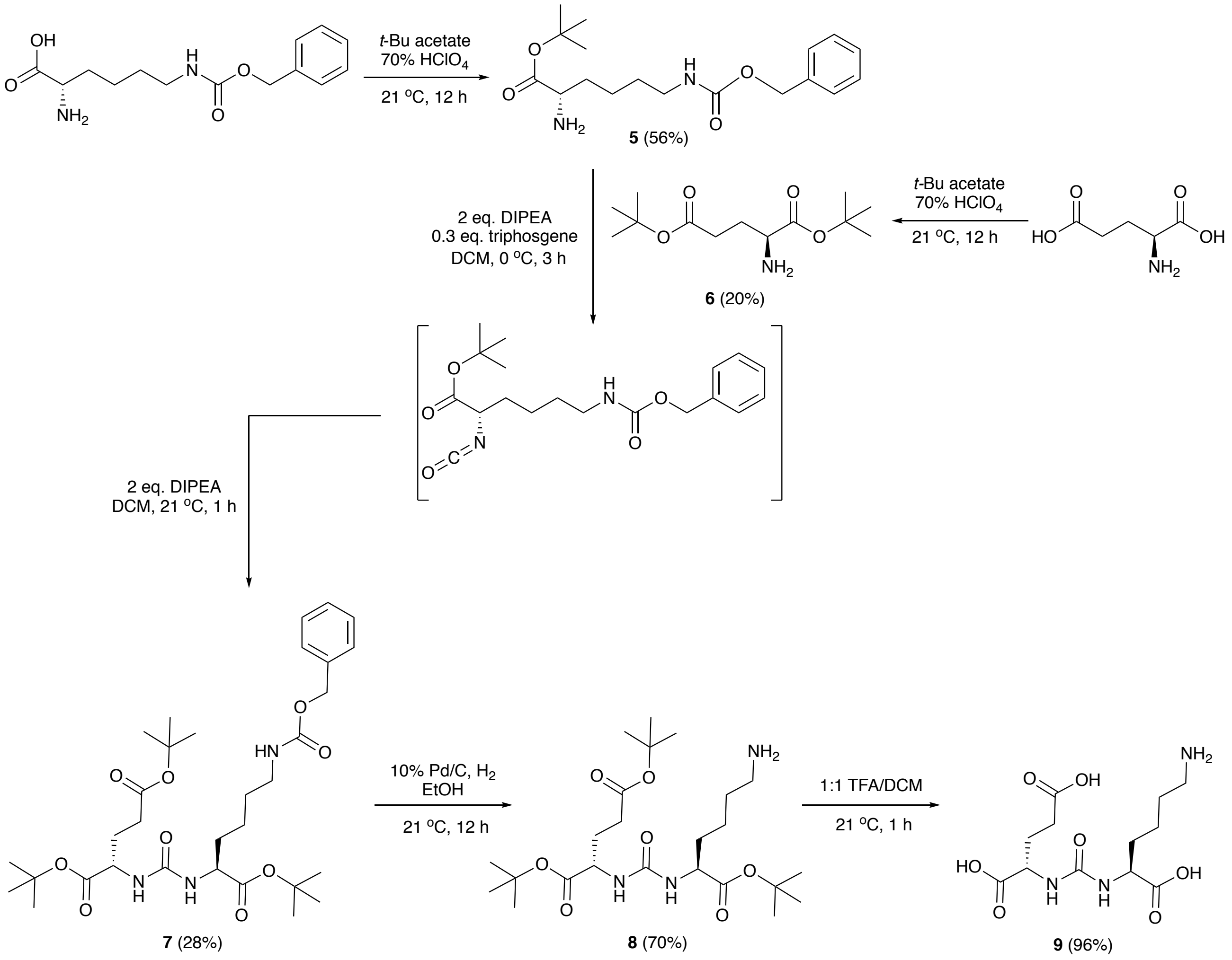

Synthesis of compound **5**

To a solution of *N*-CBz-L-Lysin (2.0 g, 7.1 mmol) in *t*-butyl acetate (20 mL), 70% perchloric acid (1.0 mL) was added and the mixture stirred at 21 °C for 20 h. Ethyl acetate (50 mL) was added and mixture extracted with water (50 mL), 0.5 M HCl (50 mL), then water (50 mL). Aqueous layers were combined followed by addition of 30% NaOH (aq.) until pH11. Product was extracted with ethyl acetate (3 x 100 mL), organic layer washed with brine, dried over anhydrous $MgSO_4$, and solvent removed under reduced pressure. The crude product was purified on silica gel (50-75% EtOAC/Hexane) to isolate compound **5** as a clear oil (1.3 g, 4.0 mmol, 56%). ^{1}H NMR (400 MHz, $CDCl_3$) δ (ppm) 7.37 – 7.27 (m, 5H), 5.09 (s, 2H), 4.83 (s, 1H), 3.31 (dd, J = 7.3, 5.5 Hz, 1H), 3.20 (dd, J = 13.1, 6.6 Hz, 2H), 1.91 (s, 2H), 1.81 – 1.64 (m, 1H), 1.62 – 1.48 (m, 3H), 1.45 (s, 9H), 1.36-1.44 (m, 2H).

$^{13}C\{^{1}H\}$ NMR (101 MHz, $CDCl_3$) δ (ppm) 175.35, 156.47, 136.70, 128.51, 128.10, 80.99, 66.55, 54.84, 40.85, 34.50, 29.71, 28.07, 22.81. R_f (silica gel, EtOAc:Hexane 3:1) = 0.43. HRMS (ESI+) (m/z): calculated for $C_{18}H_{29}N_2O_4^+$ ($[M+H]^+$): 337.4395; found: 337.2120 (100%).

Figure 6.13. ^{1}H NMR spectrum ($CDCl_3$, 400 MHz) of compound **5**.

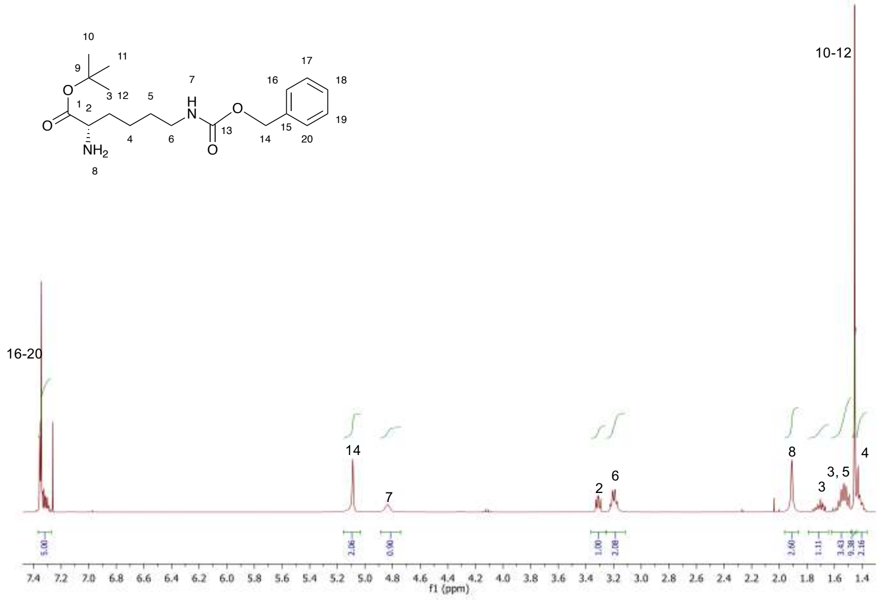

Figure 6.14. $^{13}C\{^{1}H\}$ NMR spectrum ($CDCl_3$, 400 MHz) of compound **5**.

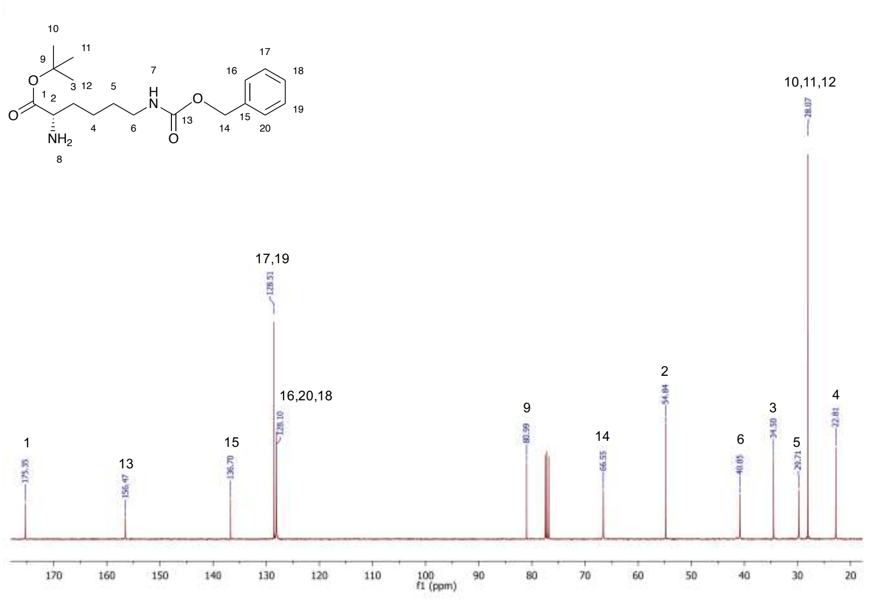

Synthesis of compound **6**

To a solution of L-glutamic acid (1.0 g, 7 mmol) in t-butyl acetate (20 mL), 70% perchloric acid (1.0 mL) was added and the mixture stirred at 21 °C for 20 h. Ethyl acetate (50 mL) was added and mixture extracted with water (50 mL), 0.5 M HCl (50 mL), then water (50 mL). Aqueous layers were combined, neutralised with saturated $NaHCO_3$ (aq.) and extracted with ethyl acetate (3 x 100 mL). The organic layer was washed with brine, dried over anhydrous $MgSO_4$, and solvent removed under reduced pressure. The crude product was purified on silica gel (20-50% EtOAC/Hexane) to isolate compound **6** as a clear oil (350 mg, 2.3 mmol, 20%). ^1H NMR (400 MHz, $CDCl_3$) δ (ppm) 3.36 (dd, J = 8.2, 5.2 Hz, 1H), 2.35 (t, J = 7.6 Hz, 2H), 2.05 – 1.94 (m, 1H), 1.82 (s, 2H), 1.80 – 1.71 (m, 1H), 1.46 (s, 9H), 1.44 (s, 9H). $^{13}C\{^1H\}$ NMR (101 MHz, CDCl3) δ (ppm) 174.84, 172.71, 81.44, 80.55, 54.43, 32.06, 30.07, 28.24, 28.19. R_f (silica gel, EtOAc:Hexane 1:1) = 0.40. HRMS (ESI+) (m/z): calculated for $C_{13}H_{26}NO_4^+$ ($[M+H]^+$): 260.1817; found: 260.1854 (100%).

Figure 6.15. ^1H NMR spectrum ($CDCl_3$, 400 MHz) of compound **6**.

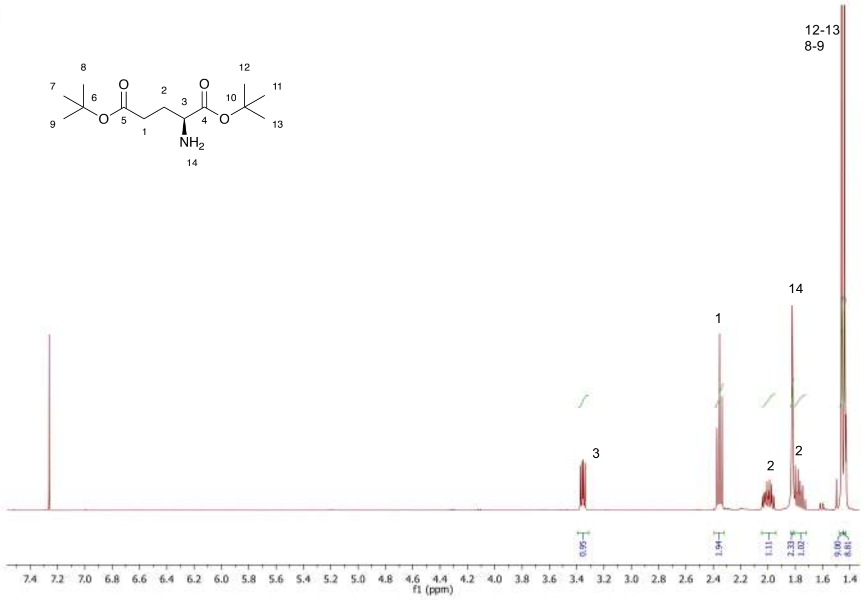

Figure 6.16. $^{13}C\{^1H\}$ NMR spectrum ($CDCl_3$, 400 MHz) of compound **6**.

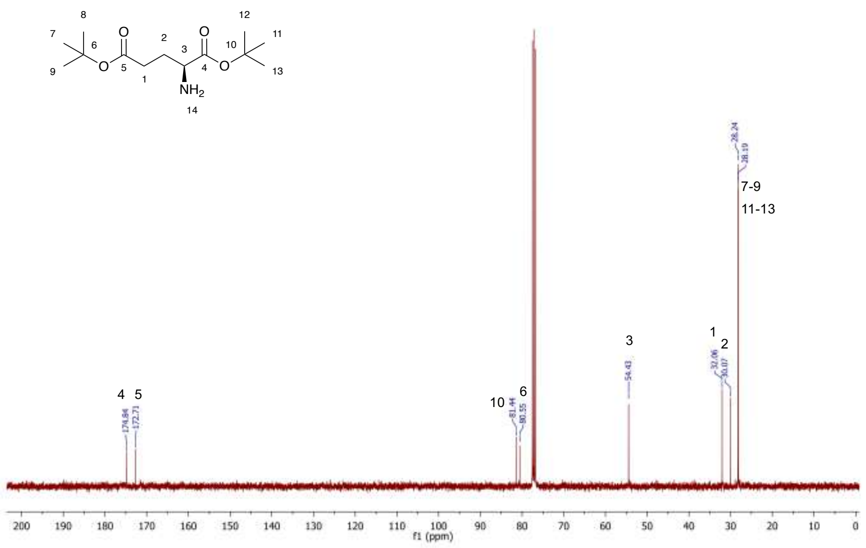

Synthesis of compound **7**

Under an N_2 atmosphere, a solution of triphosgene (0.2 g, 0.7 mmol) in DCM (20 mL) was cooled to 0 °C and a solution of **6** (0.7 g, 2.0 mmol) in DCM (1 mL) and DIPEA (1 mL) was added dropwise over 2 h. The reaction reached room temperature and a solution of **5** (0.5 g, 2.0 mmol) in DCM (1 mL) and DIPEA (1 mL) was added in one portion then stirred for 1 h. The mixture was concentrated to dryness, dissolved in EtOAc (50 mL) then washed with 2 M $NaHSO_4$ (2 x 40 mL) and sat. NaCl (aq.). Organic phase was dried over anhydrous $MgSO_4$ and solvent removed under reduced pressure. The crude product was purified on silica gel (20-50% EtOAC/Hexane) to isolate compound **7** as a clear oil (0.2 g, 0.3 mmol, 28%). ^1H NMR (ppm) (400 MHz, $CDCl_3$) ^1H NMR (400 MHz, $CDCl_3$) δ 7.44 – 7.29 (m, 5H), 5.26 – 4.92 (m, 5H), 4.32 (m, 2H), 3.25 – 3.11 (m, 2H), 2.41 – 2.19 (m, 2H), 2.16 – 1.96 (m, 1H), 1.91 – 1.71 (m, 2H), 1.60-1.71 (m, 3H), 1.51-1.59 (m, 3H), 1.45 – 1.43 (m, 27H), 1.40 – 1.24 (m, 2H). $^{13}C\{^1H\}$ NMR (101 MHz, $CDCl_3$) δ (ppm) 172.56, 172.19, 171.97, 156.98, 156.57, 136.66, 128.47, 128.05, 128.02, 82.25, 81.88, 80.66, 66.58, 53.38, 53.08, 40.61, 32.54, 31.53, 29.35, 28.29, 28.07, 28.01, 27.99, 22.21. R_f (silica gel, EtOAc:Hexane 1:1) = 0.58. HRMS (ESI+) (m/z): calculated for $C_{32}H_{52}N_3O_9^+$ ($[M+H]^+$): 622.2698; found: 622.3704 (100%).

Figure 6.17. ^1H NMR spectrum ($CDCl_3$, 400 MHz) of compound **7**.

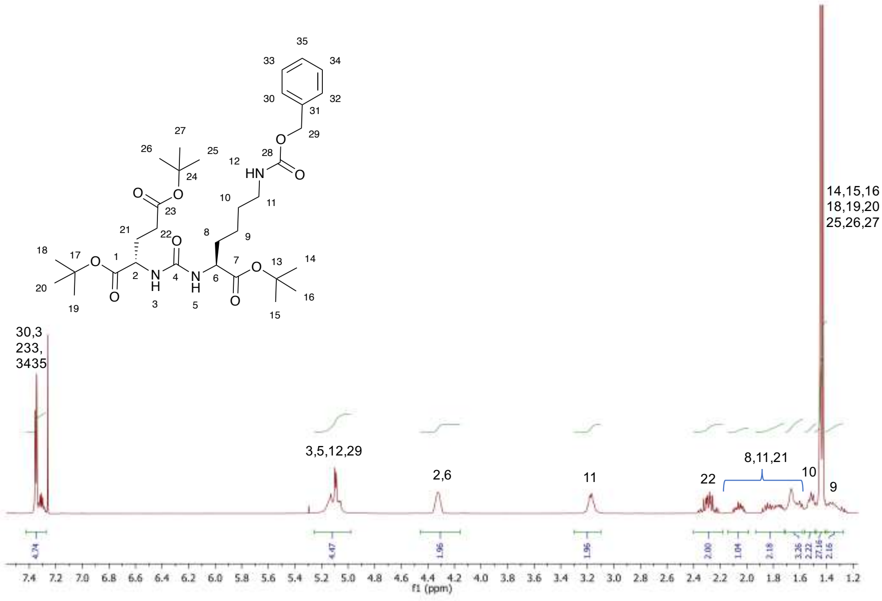

Figure 6.18. $^{13}C\{^{1}H\}$ NMR spectrum ($CDCl_3$, 400 MHz) of compound **7**.

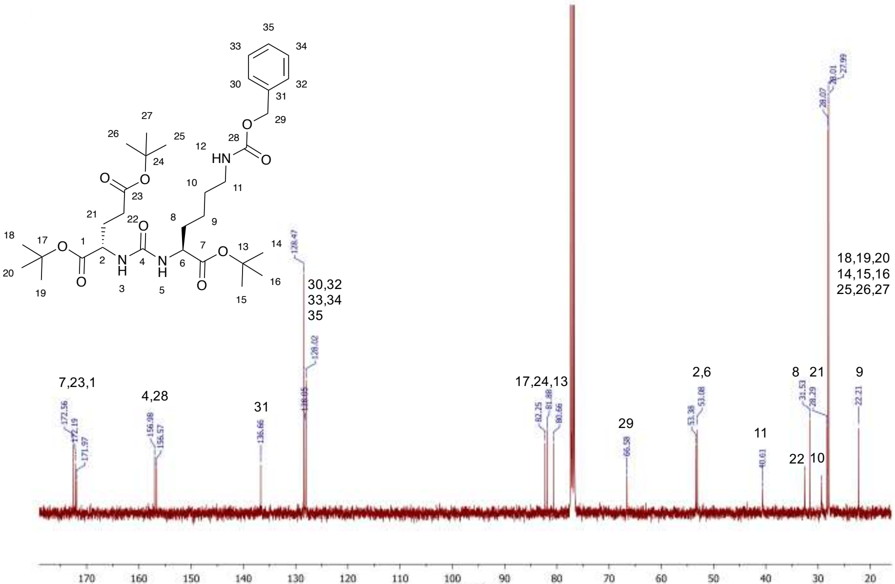

Synthesis of compound **8**

To a solution of **7** (190 mg, 0.30 mmol) in EtOH (10 mL) and Pd/C (20 mg) was added. The mixture was degassed with N_2, system flushed with H_2, and then reaction stirred for 20 h under an H_2 atmosphere. The mixture was passed through Celite® using EtOH (20 mL) and the solvent was removed under reduced pressure to yield compound **8** as a yellow oil (100 mg, 0.21 mmol, 70%). ^{1}H NMR (400 MHz, $CDCl_3$): δ 5.36 (s, 1H), 5.34 (s, 1H), 4.36 – 4.27 (m, 2H), 2.71 (t, *J* = 6.7 Hz, 2H), 2.51 (s, 2H), 2.39 – 2.19 (m, 2H), 2.11–2.00 (m, 1H), 1.91 – 1.69 (m, 2H), 1.66 – 1.53 (m, 1H), 1.53 – 1.45 (m, 2H), 1.45–1.38 (m, 27H), 1.38 – 1.26 (m, 2H). $^{13}C\{^{1}H\}$ NMR (101 MHz, $CDCl_3$) δ 172.76, 172.58, 157.12, 82.14, 81.78, 80.63, 53.56, 53.13, 41.56, 32.78, 32.37, 31.76, 28.45, 28.20, 28.14, 28.13, 22.44. HRMS (ESI+) (m/z): calculated for $C_{24}H_{46}N_3O_7^+$ ($[M+H]^+$): 488.33303; found: 488.3331 (100%).

Figure 6.19. ^{1}H NMR spectrum (CDCl$_3$, 400 MHz) of compound **8**.

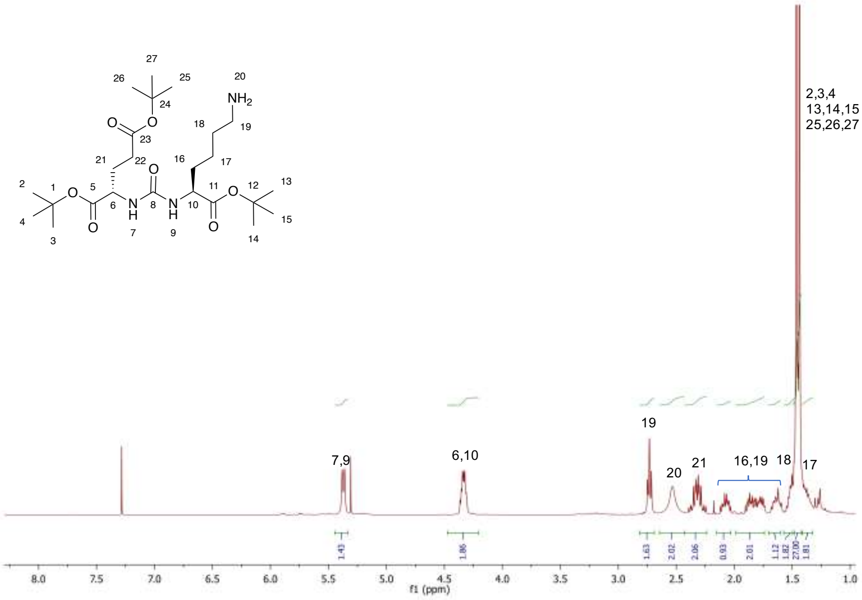

Figure 6.20. ^{13}C{^{1}H} NMR spectrum (CDCl$_3$, 400 MHz) of compound **8**.

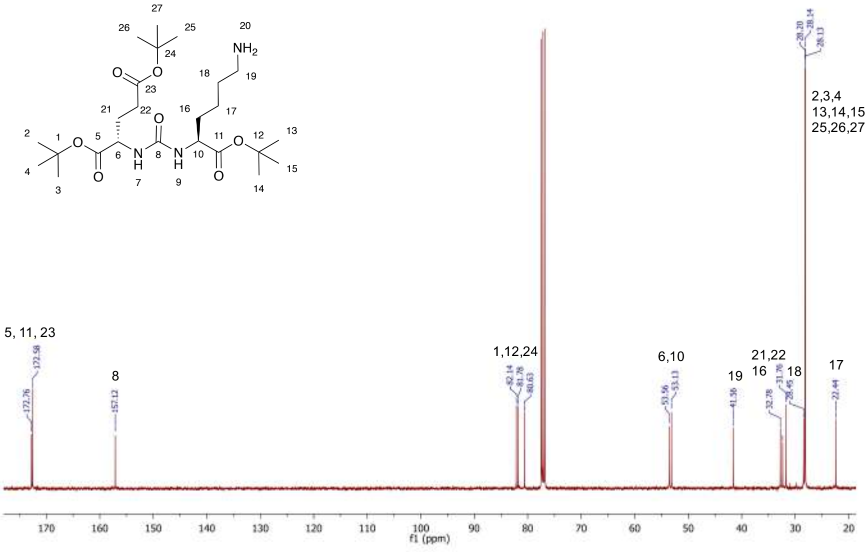

Synthesis of compound **9**

Compound **8** (200 mg, 0.41 mmol) was stirred in 1:1 TFA/DCM (2 mL) for 1 h. Cold diethyl ether (15 mL) was added, the formed precipitate was collected, washed with cold ether (3 x 5 mL) and dried under reduced pressure. HCl (0.5 M, 1 mL) was added and then lyophilised to yield **9** as a white solid (128 mg, 0.40 mmol, 98%). ^{1}H NMR (400 MHz, MeOD) δ 4.36 – 4.25 (m, 2H), 2.98 – 2.85 (m, 2H), 2.51 – 2.34 (m, 2H), 2.22 – 2.09 (m, 1H), 1.99 – 1.81 (m, 2H), 1.79 – 1.61 (m, 3H), 1.57 – 1.40 (m, 2H). ^{13}C NMR (101 MHz, D$_2$O) δ 177.27, 176.91, 176.35, 159.35, 52.89, 52.57, 39.21, 30.40, 30.05, 26.12, 21.96. HRMS (ESI+) (m/z): calculated for $C_{12}H_{22}N_3O_7^+$ ([M+H]$^+$): 320.1452; found: 320.1454) (100%).

Figure 6.21. ^{1}H NMR spectrum (MeOD, 400 MHz) of compound **9**.

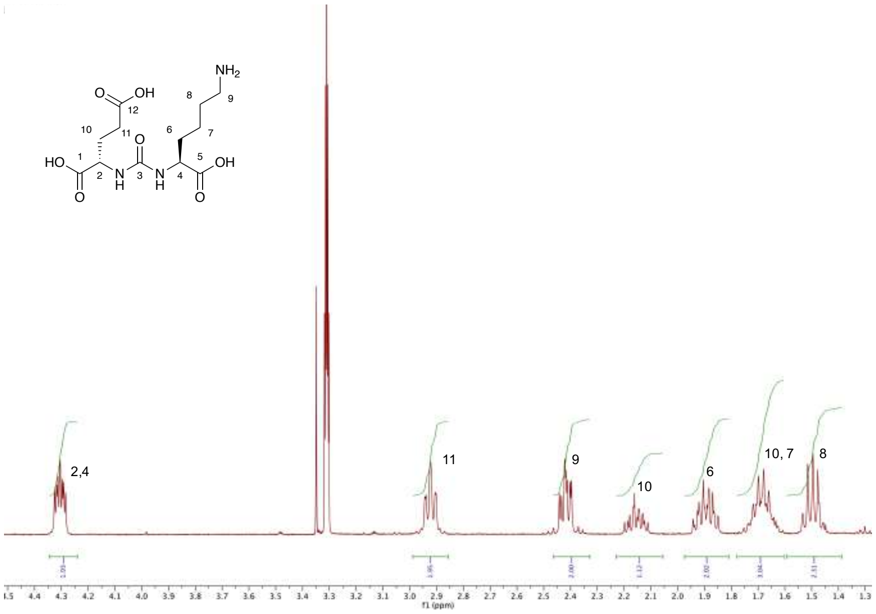

Figure 6.22. ^{13}C {^{1}H} NMR spectrum (D$_2$O, 400 MHz) of compound **9**.

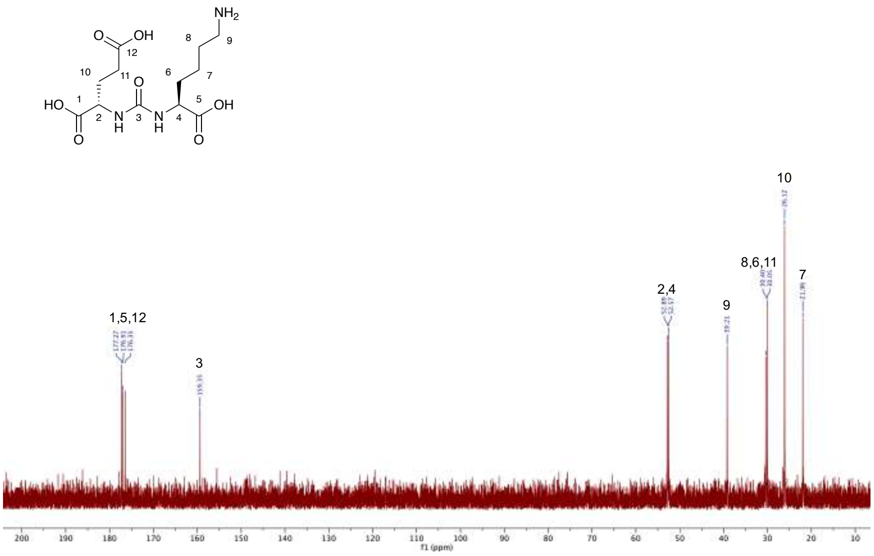

6.3.2 Chelate conjugated, ^{68}Ga radiolabeled, PSMA targeted gold coated iron oxide nanoparticles for PET/MR imaging

Synthesis and characterisation

Scheme 6.7. Chemical synthesis of the Glu-NH-CO-NH-Lys lipoic acid derivative (Glu-NH-CO-NH-Lys-LA, **10**)

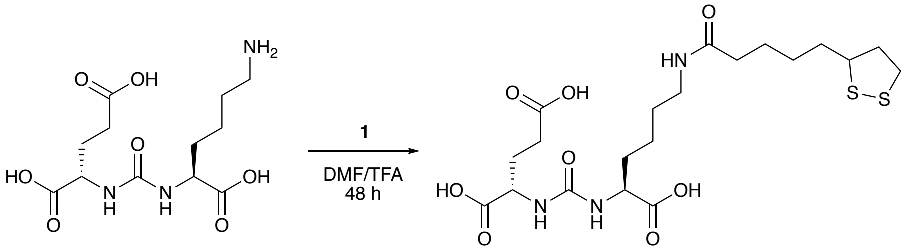

9

96%

10

18%

Synthesis of compound **10**

To a solution of compound **1** (42.2 mg, 0.14 mmol) in DMF (1 mL) and TEA (40 μL), compound **9** (44.3 mg, 0.14 mmol) was added. The solution was stirred for 24 h at 21 °C before further addition of compound **9** (17.9 mg, 59 μmol). The reaction was then stirred for a further 24 h and then the solvent was removed under reduced under reduced pressure. The solid was washed with DCM (3 x 5 mL) and cold water (1 x 5 mL) to yield **10** as a white solid (12.7 mg, 25 μmol, 18%). ^{1}H NMR (400 MHz, D_2O/MeCN-d_3) δ 4.74 (dd, J = 8.8, 5.3 Hz, 1H), 4.68 (dd, J = 8.5, 5.0 Hz, 1H), 4.21 – 4.12 (m, 1H), 3.78 – 3.69 (m, 2H), 3.66 (t, J = 6.8 Hz, 2H), 3.05 – 2.98 (m, 1H), 2.96 (t, J = 7.6 Hz, 2H), 2.70 (t, J = 7.4 Hz, 2H), 2.67 – 2.58 (m, 1H), 2.51 – 2.39 (m, 2H), 2.36 – 2.07 (m, 6H), 2.07 – 1.86 (m, 6H). ^{13}C NMR (126 MHz, D_2O/MeCN-d_3) δ 179.09, 178.36, 178.08, 161.38, 59.27, 55.91, 55.34, 42.92, 41.58, 41.01, 38.42, 36.83, 33.93, 32.86, 31.02, 29.69, 28.05, 25.27. HRMS (ESI+) (m/z): calculated for $C_{20}H_{34}N_3O_8S_2^+$ ([M+H]$^+$): 508.1782; found: 508.1784) (100%).

Figure 6.23. ^{1}H NMR spectrum (D_2O/MeCN-d_3, 400 MHz) of compound **10**.

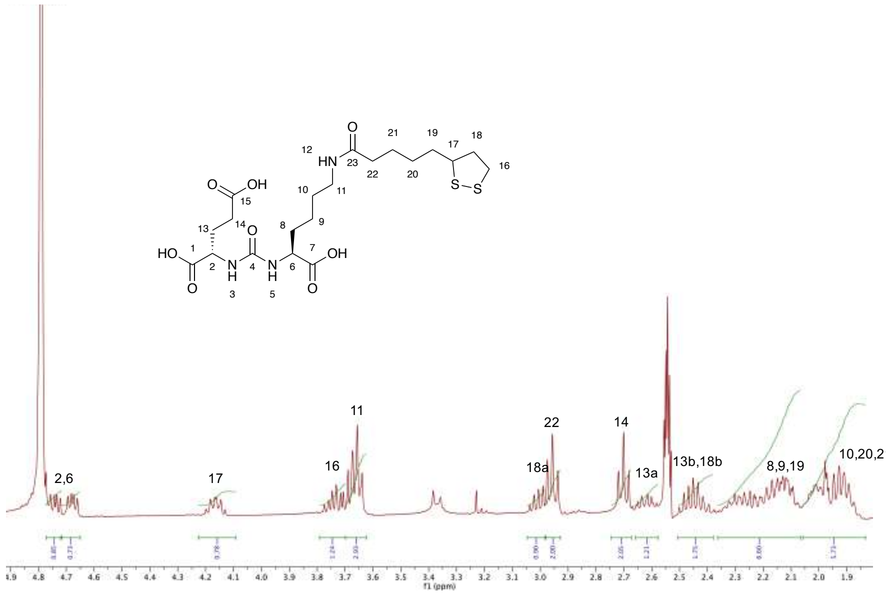

Figure 6.24. 2D-COSY spectrum (D_2O/MeCN-d_3) of compound **10** (region between d_H = 1.8 – 4.2 ppm).

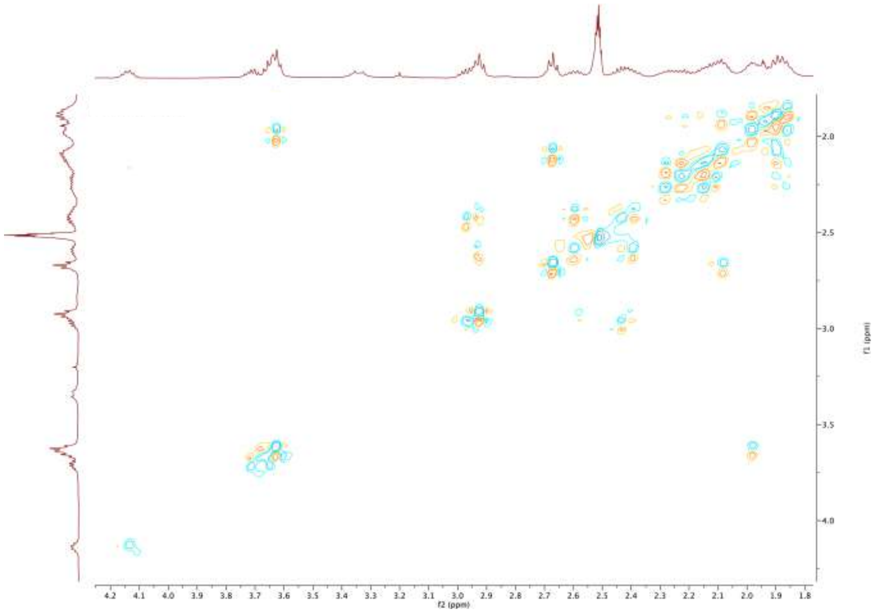

Figure 6.25. $^{13}C\{^1H\}$ NMRspectrum (D_2O/MeCN-d_3, 126 MHz) of compound **10**.

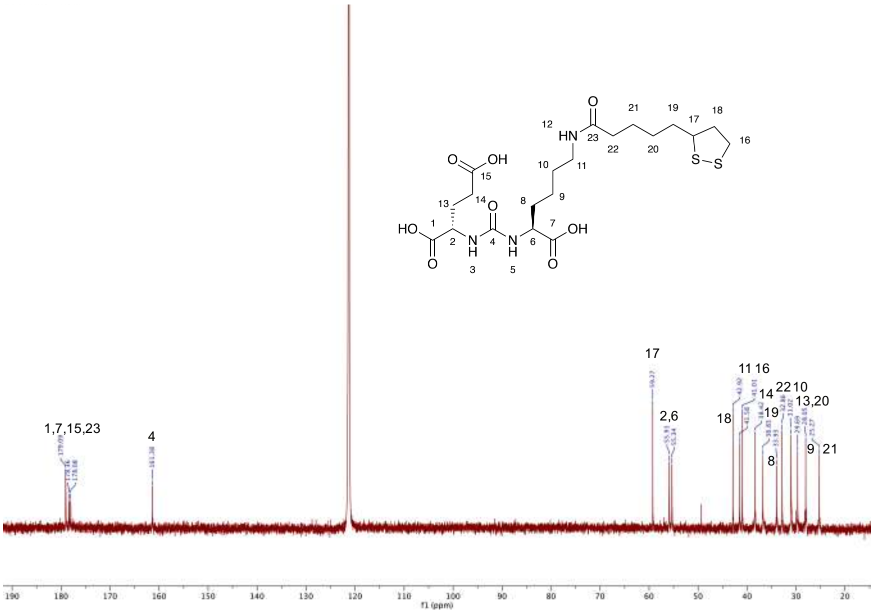

Figure 6.26. 2D-HSQC spectrum (D_2O/MeCN-d_3) of compound **10**.

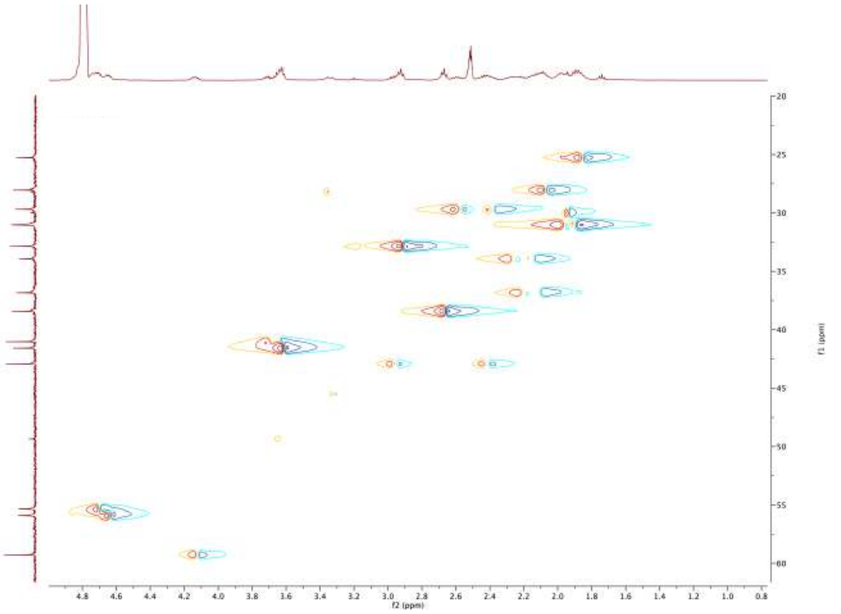

Radiochemistry

*Synthesis of [^{68}Ga]Fe_2O_3@Au-(Ga-**2**)-**10***

A solution of **10** was prepared in 1:4 MeCN:H_2O (3.81 mM), this was then further diluted in H_2O (48.6 µM). ^{68}Ga-**2** was prepared as described above and then neutralised with NaOH (1M, approx. 25 µL). An aliquot of

^{68}Ga-**2** (3.5 µL, 0.17 nmol) and compound **10** (3.5 µL, 48.6 µM, 0.17 nmol) was added to Fe_2O_3@Au (190 µL, 102.03 nmol of Au) and reaction vortexed. After 5 mins radio-iTLC (stationary phase: silica gel, mobile phase: MeOH/H_2O 1:1 with 0.5% HCl) gave a RCC>94% (*n* = 3, R_f = 0.0 – 0.23). PD10-SEC (eluent: saline) gave a RCP of 95%.

Stability studies

[^{68}Ga]Fe_2O_3@Au-(Ga-**2**)-**10** and [^{68}Ga]Fe_2O_3@Au-(Ga-**2**) were prepared as previously described. To 100 µL of the reaction, 100 µL of either saline +1% FBS, 50 mM EDTA, PBS 1% FBS or 50 mM cysteine was added. The samples were incubated at 37 °C. RCP was monitored *via* radio-TLC at time points up to 2 h.

Cellular studies

Cells were harvested and distributed in Eppendorf tubes (3 x 10^6 / vial) in media (270 µL) or media with sodium azide (270 µL, 0.1%), or in media containing free PSMA ligand (20 µM). Reactions were prepared as previously described and diluted (3-fold) in cell media and then added (30 µl, 8 kBq) to the prepared cells. After mixing for 1.5 h at 37 °C, the samples were centrifuged (2000 rpm, 3 min) and the cell pellet washed with ice-cold PBS (2 x 1 mL) keeping the samples on ice between washes. The radioactivity associated with each sample was quantified using the gamma counter. A BCA assay was then used to quantify the protein content of cell samples and this was used to normalise data. Experiments were performed in triplicate.

Small-animal PET imaging

[^{68}Ga]Fe_2O_3@Au-(Ga-**2**)-**10** was prepared as stated above and diluted 2-fold with PBS+1% FBS. 200 µL (0.4 MBq) was injected i.v. *via* the tail vein of a mouse (*n*=1) bearing an LNCaP tumour. Images were then acquired at 10 mins, 30 mins, 1 h and 3 h (10 min scan). Prior to image acquisition the mouse anaesthetised using an isoflurane dose between 3.0 – 4.0%. During image acquisition, the respiration rate of the animal was monitored via live video feed and anaesthesia was maintained by an experience animal experimenter by controlling the isoflurane dose between 1.5 – 2.0%. Images were reconstructed and analysed using VivoQuant^{TM} 3.5 patch 2 software (InviCRO, Boston, MA).

6.3.3 Chelate free, ^{68}Ga radiolabelled, PSMA targeted Feraheme® nanoparticles for PET/MR imaging

Synthesis of small molecules

Scheme 6.8. Chemical synthesis of **11**, NH_2-CH_2-CH_2-PEG4-C(O)NH-C(PO(OEt)$_2$)$_2$

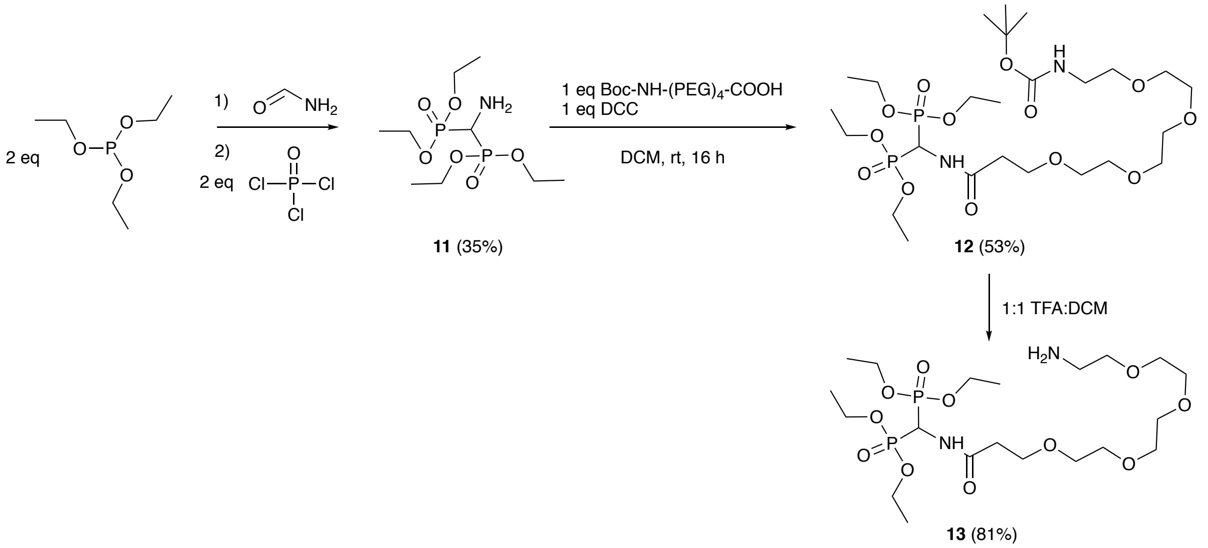

Synthesis of compound **11**

Synthesis of compound **11** uses modified literature procedures.[337]

To a solution of formamide (192 µL, 4.82 mmol) and triethyphosphite (1.67 mL, 9.64 mmol) cooled to -7.5 °C, phosphorus oxychloride (896 µL, 9.64 mmol) was added dropwise over 1 h. Reaction the allowed to come to 21 °C and stirred for 1 h. Reaction mixture was poured over 30% ammonia solution (9 mL) on ice (30 g), and extracted with DCM (3 x 40 mL). The solvent was removed under reduced pressure and crude product re-dissolved in DCM (60 mL). Product was extracted with 0.5 M HCl (60 mL), and then the aqueous phase was washed with DCM (3 x 40 mL). 1 M NaOH was added to aqueous phase until pH10 reached, and product extracted with DCM (5 x 40 mL), dried over anhydrous Na_2SO_4, and the solvent was removed under reduced pressure to isolate **11** as a clear oil (518 mg, 1.71 mmol, 35%) ^{1}H NMR (400 MHz, $CDCl_3$) δ 4.33 – 4.10 (m, 8H), 3.44 (t, J = 20.6 Hz, 1H), 2.15 (d, J = 1.8 Hz, 2H, -NH2), 1.34 (t, J = 7.1 Hz, 12H). ^{13}C{^{1}H} NMR (101 MHz, $CDCl_3$) δ 63.35 (dd, J = 7.8, 3.3 Hz), 47.76 (t, J = 144.6 Hz), 16.56 (t, J = 2.8 Hz). ^{31}P{^{1}H} NMR (162 MHz, $CDCl_3$) δ 19.85 (s). HRMS (ESI+) (m/z): calculated for $C_9H_{24}NO_6P_2^+$ ([M+H]$^+$): 304.1073; found: 304.1076) (100%).

Figure 6.27. ^{1}H NMR spectrum (CDCl$_3$, 400 MHz) of compound **11**.

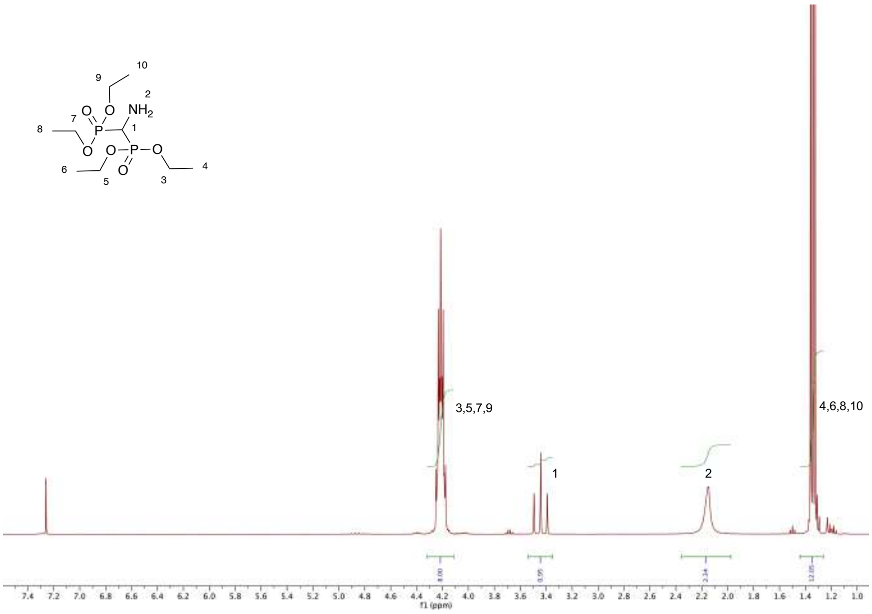

Figure 6.28. ^{13}C{^{1}H} NMR spectrum (CDCl$_3$, 400 MHz) of compound **11**.

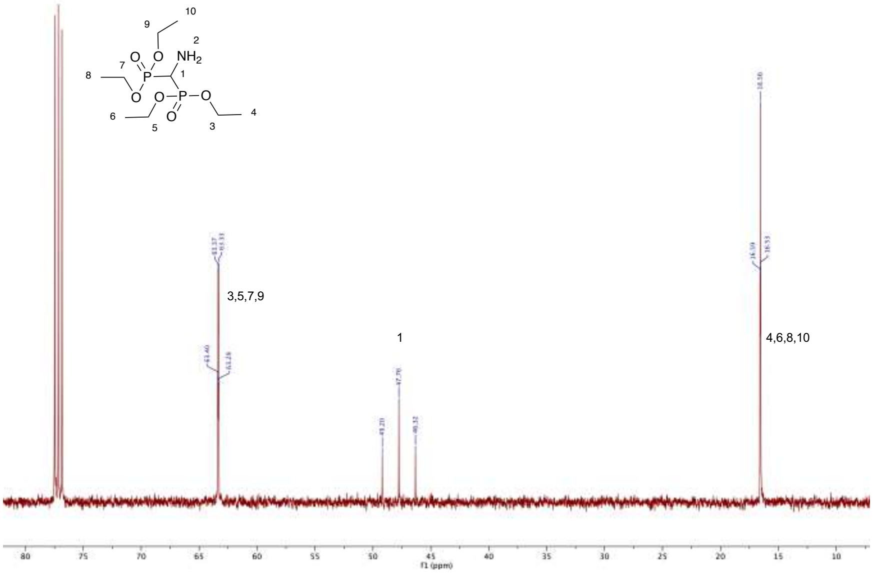

Figure 6.29. $^{31}P\{^1H\}$ NMR spectrum ($CDCl_3$, 162 MHz) of compound **11**.

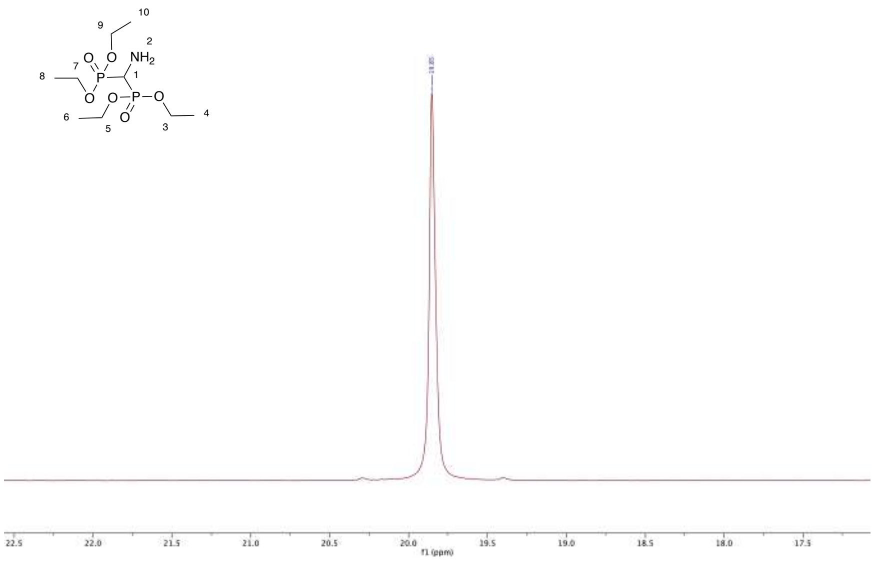

Synthesis of compound **12**

To a solution of Boc-NH-(PEG)$_4$-COOH (100 mg, 0.27 mmol) and dicyclohexylcarbodiimide (54 mg, 0.27 mmol) in DCM (5 mL), compound **11** (83 mg, 0.27 mmol) was added. The reaction was stirred for 16 h before being chilled at -18 °C and filtered. Solvent from the filtrate was removed under reduced pressure to yield the crude product which was purified on silica gel (4-10% MeOH/DCM) to isolate compound **12** as a clear oil (98 mg, 0.15 mmol, 53%). ^{1}H NMR (400 MHz, CDCl3) δ 7.01 (d, J = 9.1 Hz, 1H), 5.09 – 4.95 (m, 2H), 4.23 – 4.07 (m, 8H), 3.71 (t, J = 5.9 Hz, 2H), 3.65 – 3.54 (m, 12H), 3.49 (t, J = 5.2 Hz, 2H), 3.26 (q, J = 4.9 Hz, 2H), 2.53 (t, J = 5.9 Hz, 2H), 1.40 (s, 9H), 1.29 (td, J = 7.1, 3.4 Hz, 12H). $^{13}C\{^1H\}$ NMR (101 MHz, CDCl3) δ 170.67 (t, J = 4.1 Hz), 156.05, 79.17, 70.65, 70.61, 70.55, 70.53, 70.47, 70.28, 67.07, 63.60 (q, J = 2.9 Hz), 43.46 (t, J = 147.1 Hz), 40.40, 36.65, 29.73, 28.47, 16.43 (dt, J = 9.5, 2.9 Hz). ^{31}P NMR (162 MHz, CDCl3) δ 16.41 (d, J = 20.9 Hz, 2P). $^{31}P\ \{^1H\}$ NMR (162 MHz, CDCl3) δ 16.41 (s, 2P). R_f (silica gel, MeOH:DCM 1:9) = 0.53. HRMS (ESI+) (m/z): calculated for $C_{25}H_{52}N_2O_{13}P_2Na$ ($[M+Na]^+$): 673.2842; found: 673.2838) (100%).

Figure 6.30. ^1H NMR spectrum ($CDCl_3$, 400 MHz) of compound **12**.

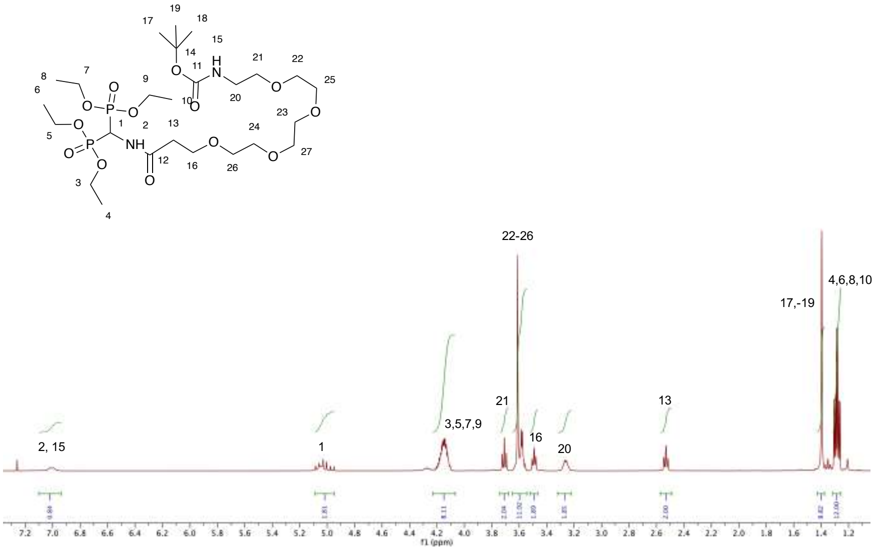

Figure 6.31. $^{13}C\{^1H\}$ NMR spectrum ($CDCl_3$, 400 MHz) of compound **12**.

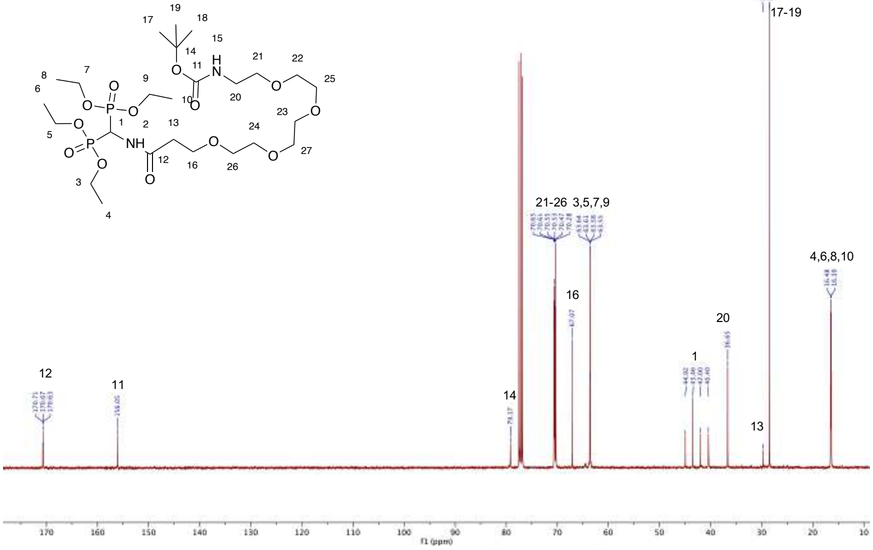

Figure 6.32. $^{31}P\{^1H\}$ NMR spectrum ($CDCl_3$, 162 MHz) of compound **12**.

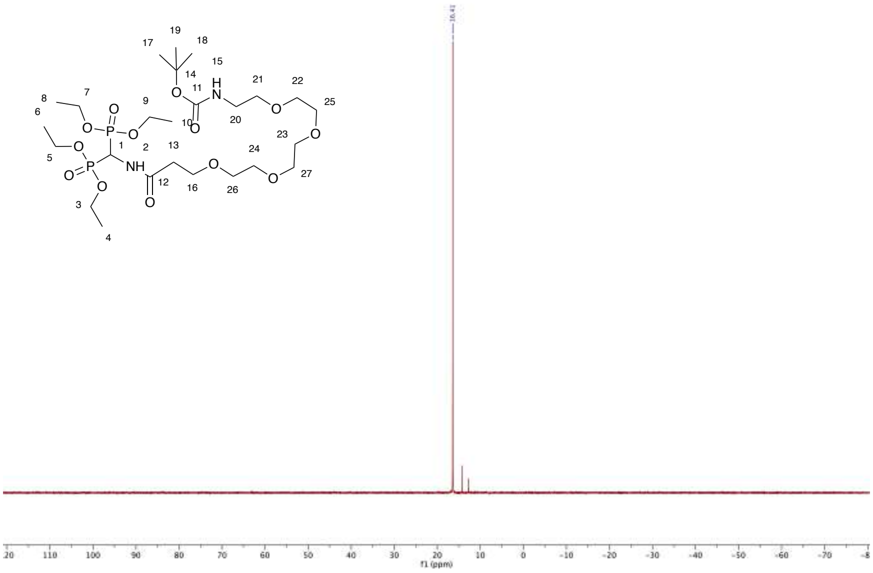

Synthesis of compound **13**

A solution of compound **12** (80 mg, 0.12 mmol) in DCM (0.5 mL) was cooled to cooled to 0 °C. TFA (0.5 mL) was added and reaction stirred at room temperature for 2 h. Toluene (10 mL) was added and the solvent was removed under reduced pressure. This last step was repeated three times to obtain the crude product which was purified on silica gel (5-10% MeOH/DCM with 1% TEA) to yield compound **13** as a yellow oil (56 mg, 0.10 mmol, 81%). ^1H NMR (400 MHz, $CDCl_3$) δ 5.68 (br s, 1H), 5.05 (td, *J* = 22.3, 9.9 Hz, 1H), 4.18 – 4.05 (m, 8H), 3.73 (m, *J* = 7.8, 5.0 Hz, 4H), 3.68 – 3.50 (m, 12H), 3.13 (br, 2H), 3.06 (m, 2H), 2.62 (t, *J* = 5.5 Hz, 2H), 1.26 (m, 12H). ^{13}C NMR (101 MHz, $CDCl_3$) δ 171.29, 70.10, 70.05, 70.01, 69.98, 69.94, 67.19, 67.07, 63.81 (dt, *J* = 24.4, 3.3 Hz), 43.46 (t, *J* = 148.1 Hz), 39.65, 35.68, 16.29 (dt, *J* = 6.1, 3.0 Hz). $^{31}P\ \{^1H\}$ NMR (162 MHz, $CDCl_3$) δ 16.59. R_f (silica gel, MeOH:DCM 1:9) = 0.53. HRMS (ESI+) (m/z): calculated for $C_{20}H_{45}N_2O_{11}P_2^+$ ($[M+H]^+$): 551.2493; found: 551.2944) (100%).

Figure 6.33. ^{1}H NMR spectrum (CDCl$_3$, 400 MHz) of compound **13**.

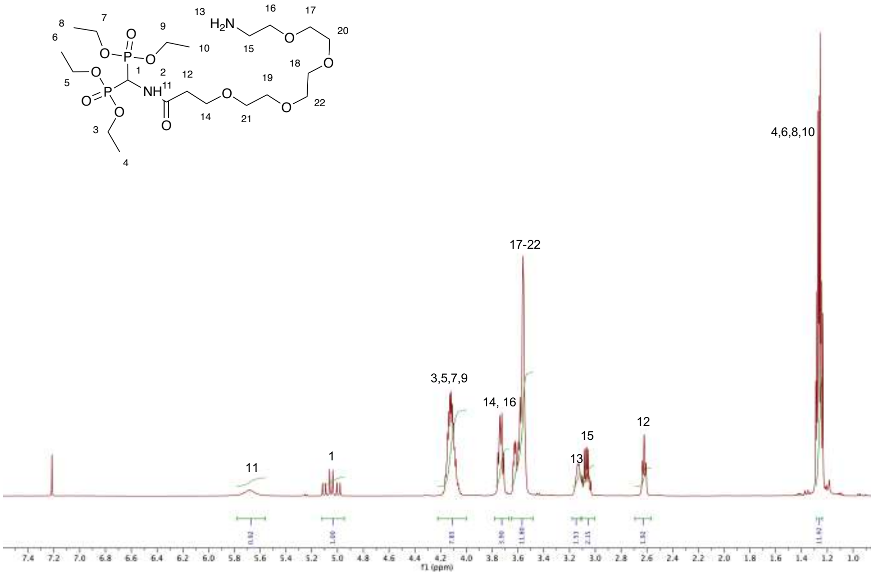

Figure 6.34. ^{13}C{^{1}H} NMR spectrum (CDCl$_3$, 101 MHz) of compound **13**.

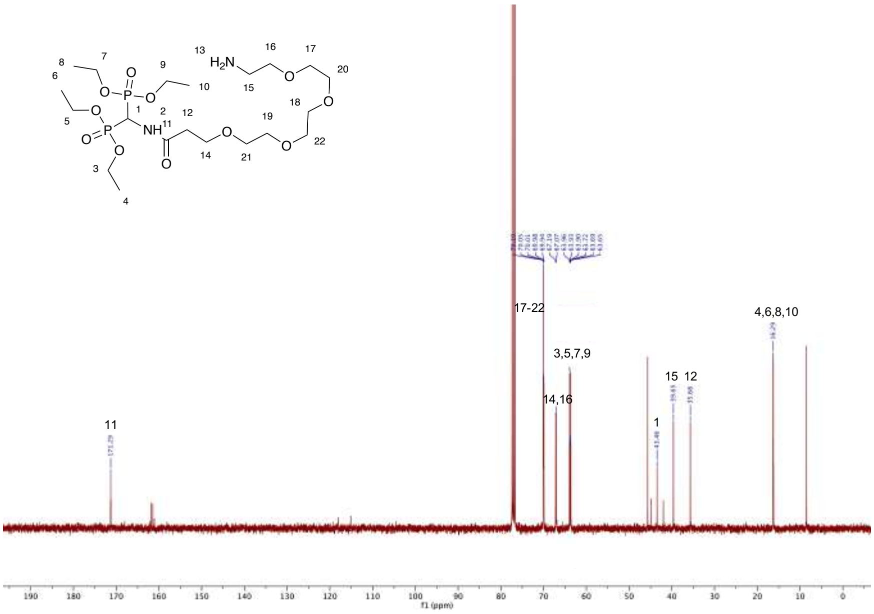

Figure 6.35. $^{31}P\{^1H\}$ NMR spectrum ($CDCl_3$, 162 MHz) of compound **13**.

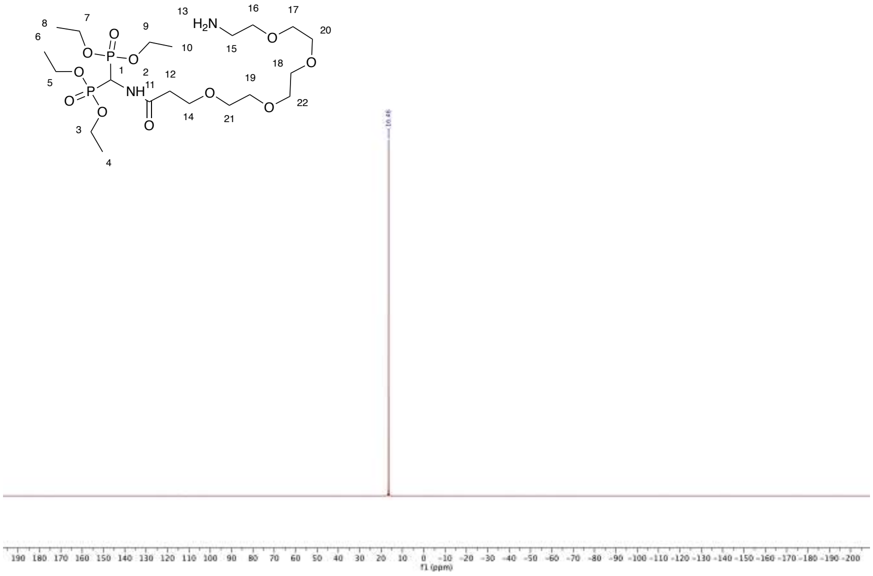

Scheme 6.9. Chemical synthesis of the functionalization of the PEGylated bisphosphonate with the PSMA binding motif (BP-(PEG)$_4$-NH-CO-Glu-NH-C(O)-NH-Lys).

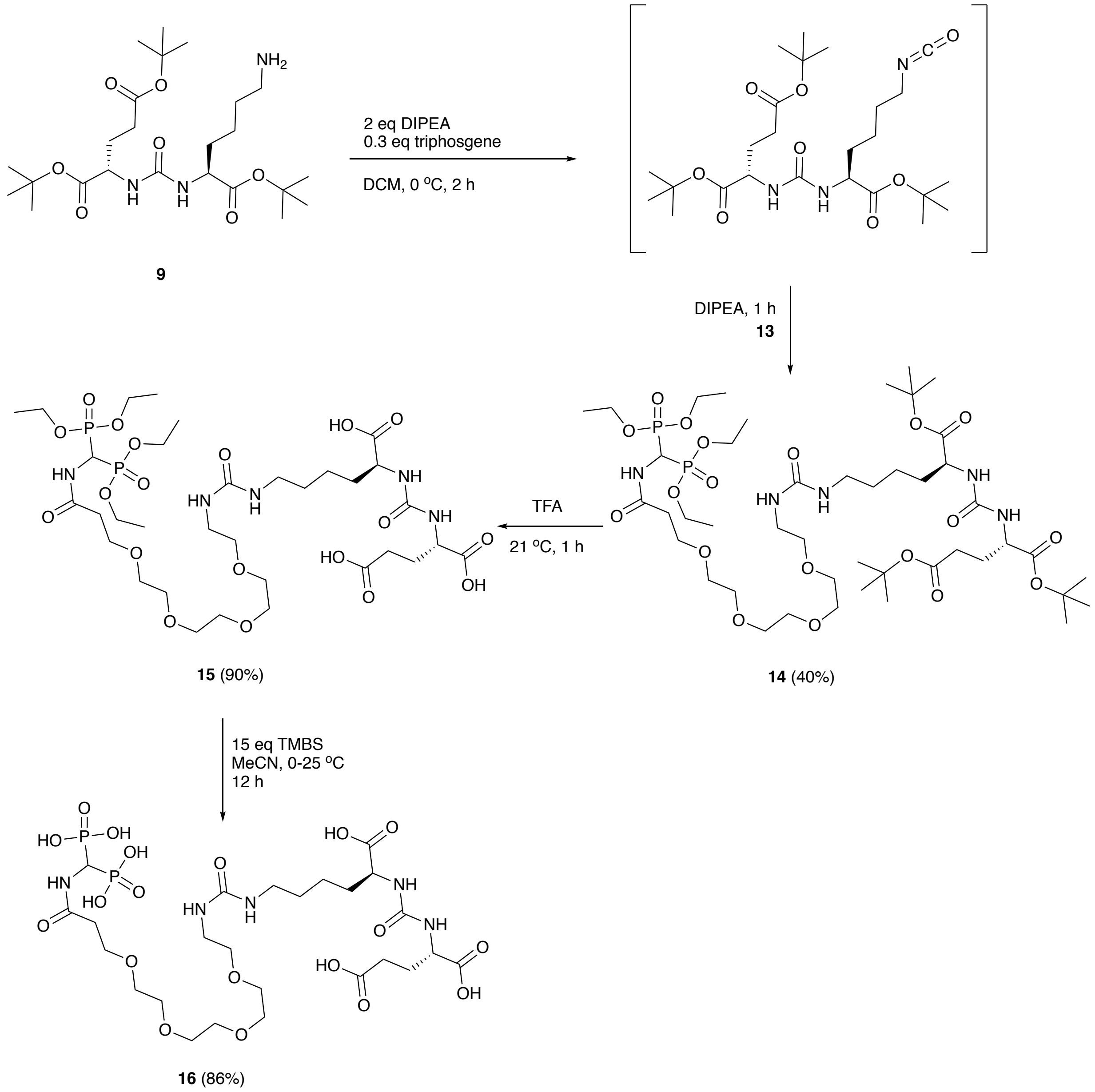

Synthesis of compound **14**

A solution of triphosgene (16 mg, 0.05 mmol) in dry DCM (2 mL) was cooled to 0 °C. A solution of **9** (80 mg, 0.16 mmol) in dry DCM (0.5 mL) and DIPEA (70 µL) was added dropwise over 2 h. Compound **13** in DCM (2 mL) and DIPEA (70 µL) then added in one portion and stirred for 1 h at room temperature. Reaction was then washed with water (2 x 5 mL) and brine (5 mL), dried with anhydrous MgSO$_4$ and solvent removed under reduced pressure. The crude product was purified on silica gel (5-10% MeOH/DCM) to isolate compound **14** as a yellow oil (70 mg, 0.07 mmol, 40%). ^{1}H NMR (400 MHz, CDCl$_3$) δ 7.26 (s, 1H), 5.93 (s, 4H), 5.05 (td, J = 21.9, 10.1 Hz, 1H), 4.35 – 4.20 (m, 2H), 4.18 – 4.07 (m, 8H), 3.69 (t, *J* = 6.0 Hz, 2H), 3.61 – 3.54 (m, 12H), 3.53 – 3.46 (m, 2H), 3.33 – 3.27 (m, 2H), 3.19 – 3.00 (m, 2H), 2.51 (t, *J* = 6.0 Hz, 2H), 2.34 – 2.16 (m, 2H), 1.81 – 1.49 (m, 4H), 1.50 – 1.40 (m, 4H), 1.40 – 1.34 (m, 27H), 1.26 (dt, *J* = 8.0, 6.4 Hz, 12H). ^{13}C NMR (101 MHz, $CDCl_3$) δ 172.89, 172.67, 172.34, 170.77 (t, *J* = 4.2 Hz), 159.19, 157.51, 81.75, 81.24, 80.34, 70.71, 70.61, 70.40, 70.34, 70.31, 70.24, 70.12, 67.00, 63.72 – 63.54 (m), 53.40, 52.78, 43.36 (t, *J* = 147.4 Hz), 40.29, 39.58, 36.46, 32.26, 31.66, 29.64, 28.50, 28.07, 28.01, 22.34, 16.36 (dt, *J* = 6.4, 3.0 Hz).^{31}P NMR (162 MHz, $CDCl_3$) δ 16.49 (d, *J* = 21.8 Hz). HRMS (ESI+) (m/z): calculated for $C_{45}H_{88}N_5O_{19}P_2^+$ ($[M+H]^+$): 1064.5543; found: 1064.5540) (100%).

Figure 6.36. ^{1}H NMR spectrum ($CDCl_3$, 400 MHz) of compound **14**.

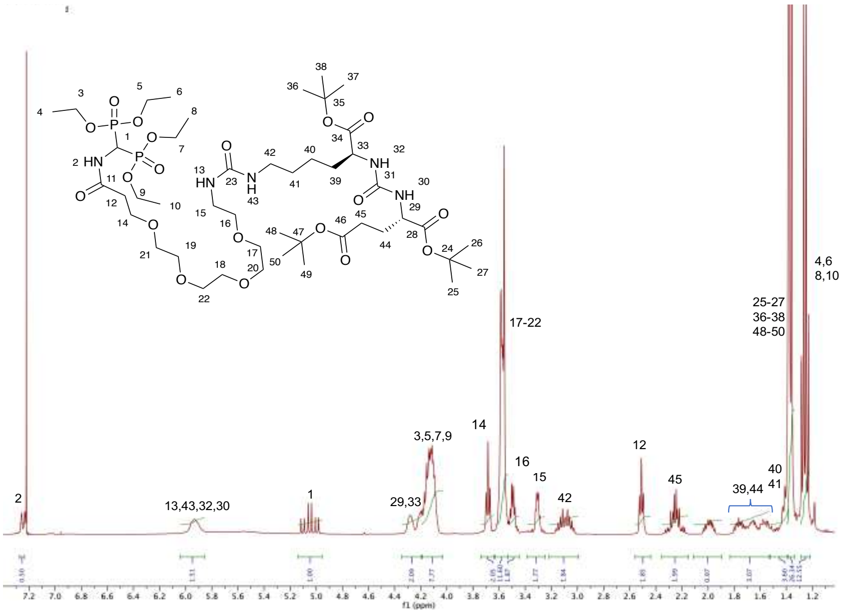

Figure 6.37. $^{13}C\{^1H\}$ NMR spectrum ($CDCl_3$, 400 MHz) of compound **14**.

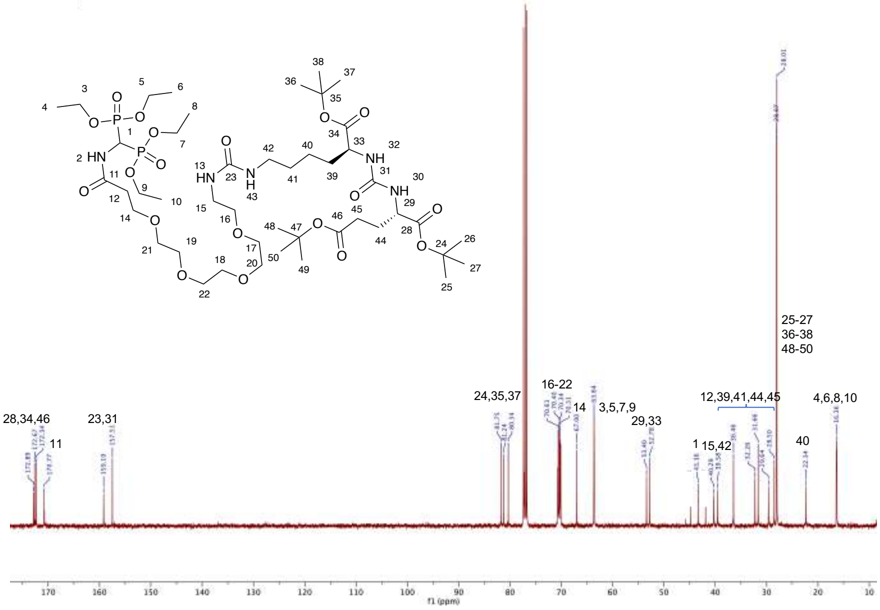

Figure 6.38. ^{31}P NMR spectrum ($CDCl_3$, 162 MHz) of compound **14**.

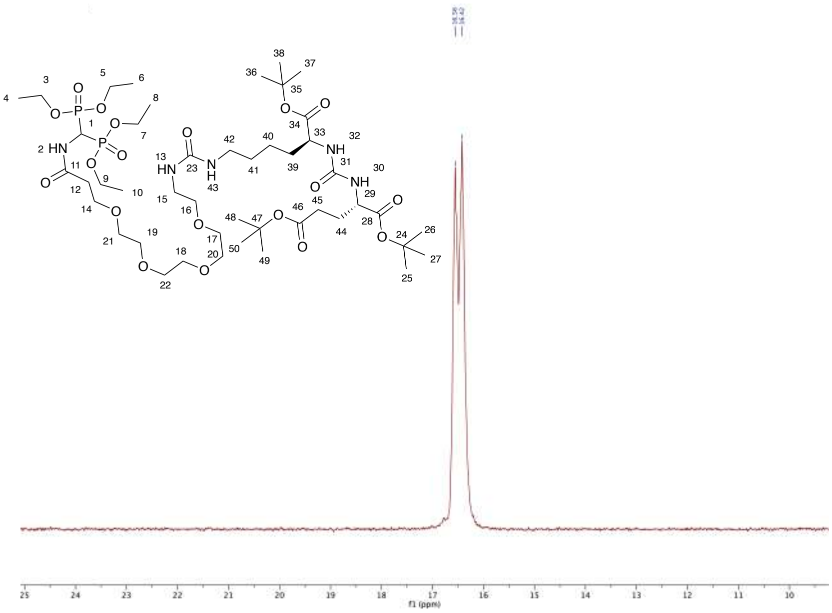

Synthesis of compound **15**

Compound **14** (70 mg, 0.07 mmol) was stirred in TFA (0.5 mL) for 60 min. Et_2O was added (6 mL) and precipitate collected and washed with ice cold Et_2O (3 x 5 mL) to yield **15** as a white solid (53 mg, 0.06 mmol, 90 %). ^{1}H NMR (400 MHz, MeOH) δ 5.12 (t, *J* = 22.9 Hz, 1H), 4.38 – 4.26 (m, 2H), 4.27 – 4.16 (m, 8H), 3.78 (t, *J* = 6.1 Hz, 2H), 3.69 – 3.59 (m, 12H), 3.54 (t, *J* = 5.3 Hz, 2H), 3.14 (s, 4H), 2.61 (t, *J* = 6.1 Hz, 2H), 2.49 – 2.39 (m, 2H), 2.24 – 2.09 (m, 1H), 1.99 – 1.80 (m, 2H), 1.75 – 1.63 (m, 1H), 1.59 – 1.49 (m, 2H), 1.47 – 1.42 (m, 2H), 1.36 (td, *J* = 7.1, 2.7 Hz, 12H). ^{31}P NMR (162 MHz, MeOD) δ 16.41. HRMS (ESI+) (m/z): calculated for $C_{33}H_{64}N_5O_{19}P_2^+$ ($[M+H]^+$): 896.3665; found: 896.3663) (75%).

Figure 6.39. ^{1}H NMR spectrum (MeOD, 400 MHz) of compound **15**.

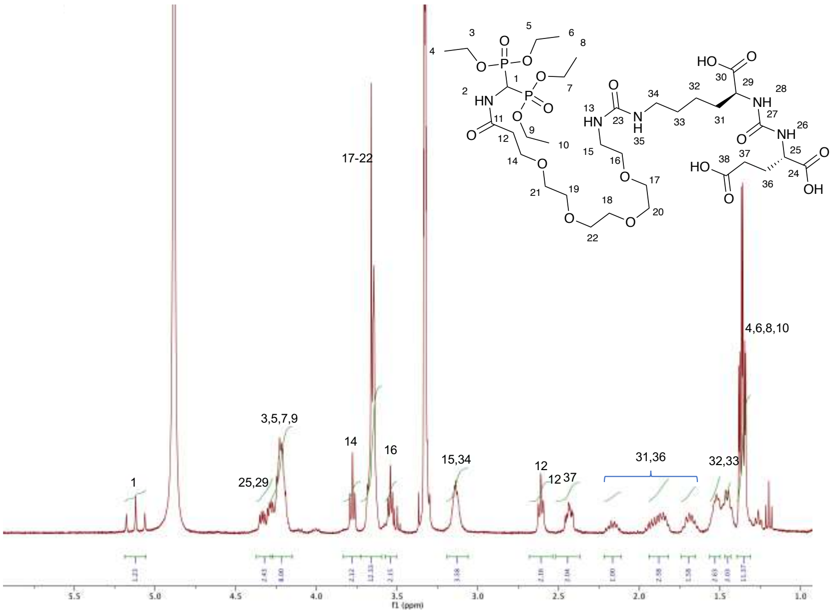

Figure 6.40.^{31}P{^{1}H} NMR spectrum (MeOD, 162 MHz) of compound **15**.

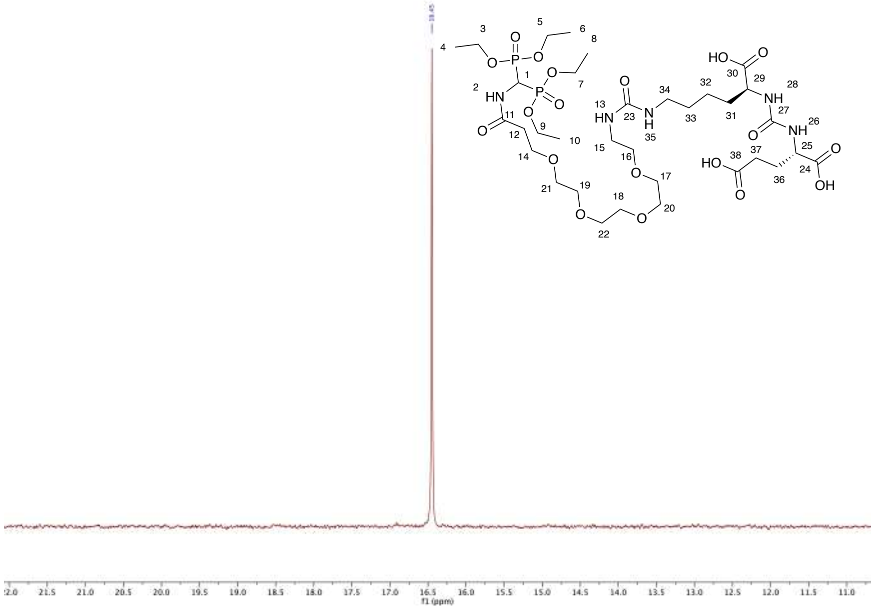

Synthesis of compound **16**

Under an N_2 atmosphere, compound **15** was dissolved in dry MeCN (4 mL) and cooled to 0 °C. Trimethylsiylbromide (0.67 mmol, 89 µL) was added dropwise then the reaction was allowed to reach room temperature and stirred for 12 h. Water (3 mL) was added and reaction and stirred for a further 1 h. The reaction was then filtered, wash with DCM (2 x 4 mL) and lyophilised to yield product as a white solid (30 mg, 38.3 µmol, 86%). ^{1}H NMR (400 MHz, D_2O) δ 4.53 (t, *J* = 21.1 Hz, 1H), 4.19 (dd, *J* = 9.1, 5.1 Hz, 1H), 4.12 (dd, *J* = 8.7, 4.9 Hz, 1H), 3.75 (t, *J* = 6.1 Hz, 2H), 3.67 – 3.56 (m, *J* = 2.3 Hz, 12H), 3.51 (t, *J* = 5.3 Hz, 2H), 3.22 (t, *J* = 5.2

Hz, 2H), 3.03 (t, $J = 5.1$ Hz, 2H), 2.58 (t, $J = 5.8$ Hz, 2H), 2.44 (t, $J = 7.3$ Hz, 2H), 2.20 – 2.05 (m, 1H), 1.97 – 1.83 (m, 1H), 1.83 – 1.71 (m, 1H), 1.71 – 1.60 (m, 1H), 1.50 – 1.37 (m, 2H), 1.38 – 1.28 (m, 2H). ^{13}C NMR (126 MHz, D_2O) δ 177.23, 177.16, 176.24, 172.94, 160.56, 159.32, 69.78, 69.57, 69.54, 69.49, 69.46, 69.41, 66.53, 58.48, 53.19, 52.53, 39.50, 39.46, 35.71, 30.57, 30.02, 28.63, 26.17, 22.19. ^{31}P NMR (203 MHz, D_2O) δ 13.30.

Figure 6.41. ^{1}H NMR spectrum (D_2O, 400 MHz) of compound **16**.

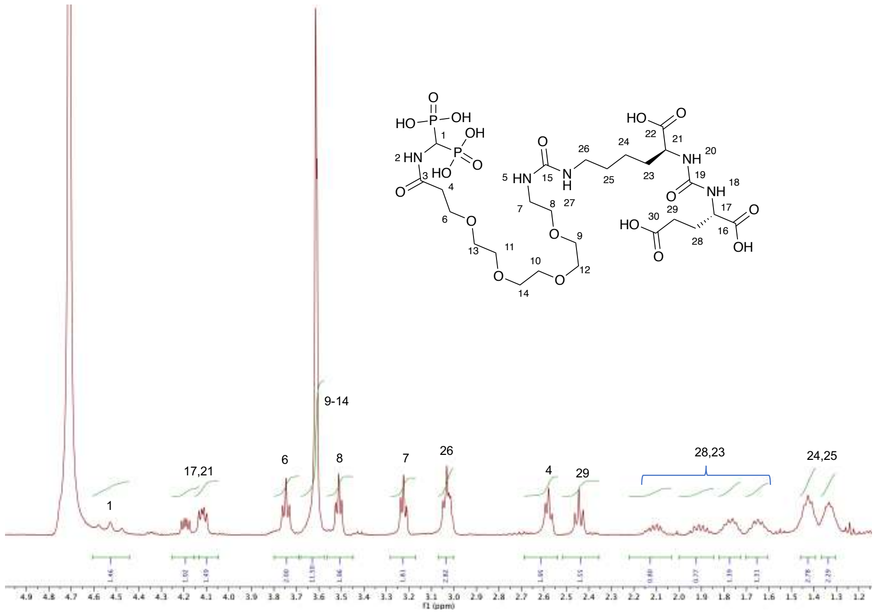

Figure 6.42. 2D-COSY spectrum (D_2O) of compound **16** (region between $\delta_H = 1.4 – 4.3$ ppm).

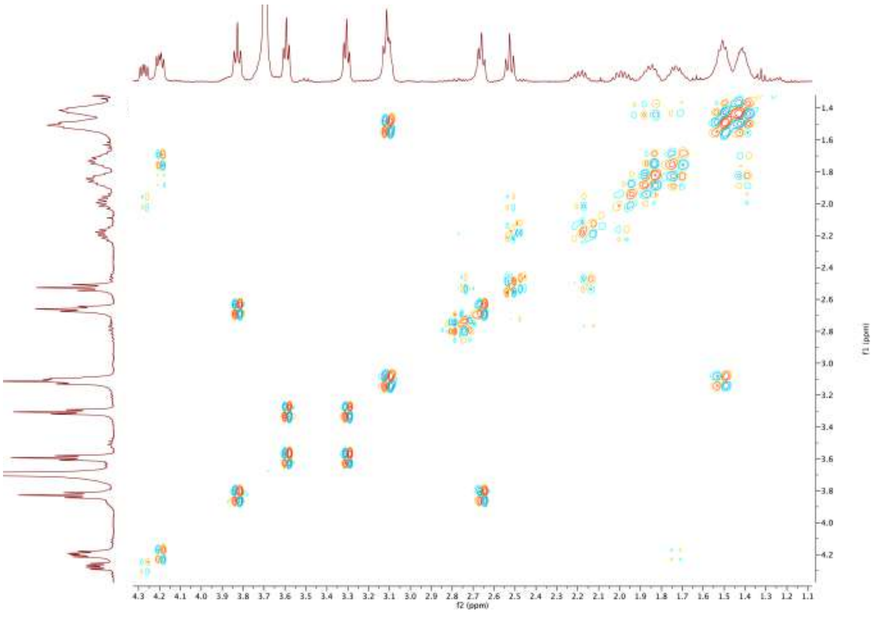

Figure 6.43. $^{13}C\{^{1}H\}$ NMR spectrum (D_2O, 400 MHz) of compound **16**.

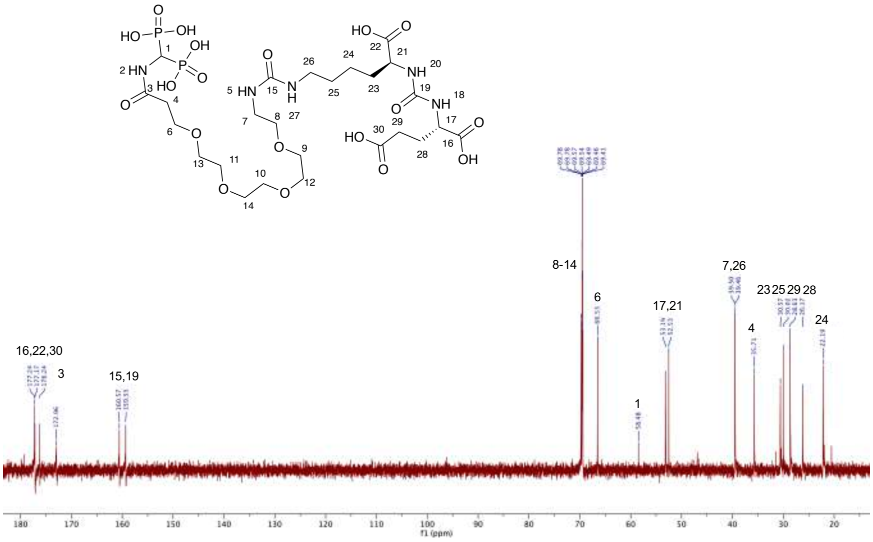

Figure 6.44. $^{31}P\{^{1}H\}$ NMR spectrum (MeOD, 162 MHz) of compound **16**.

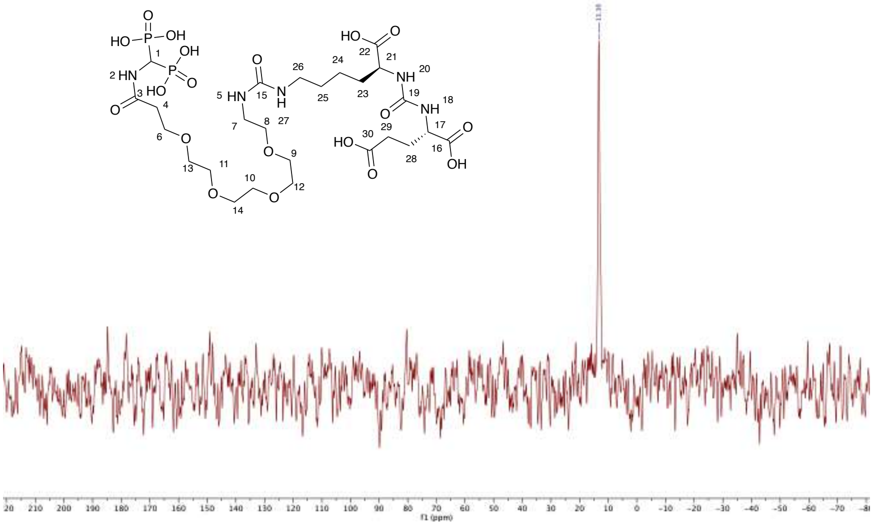

Scheme 6.10. Chemical synthesis of the inactive form of the PSMA binding motif (D-Glu-NH-C(O)-NH-D-Lys).

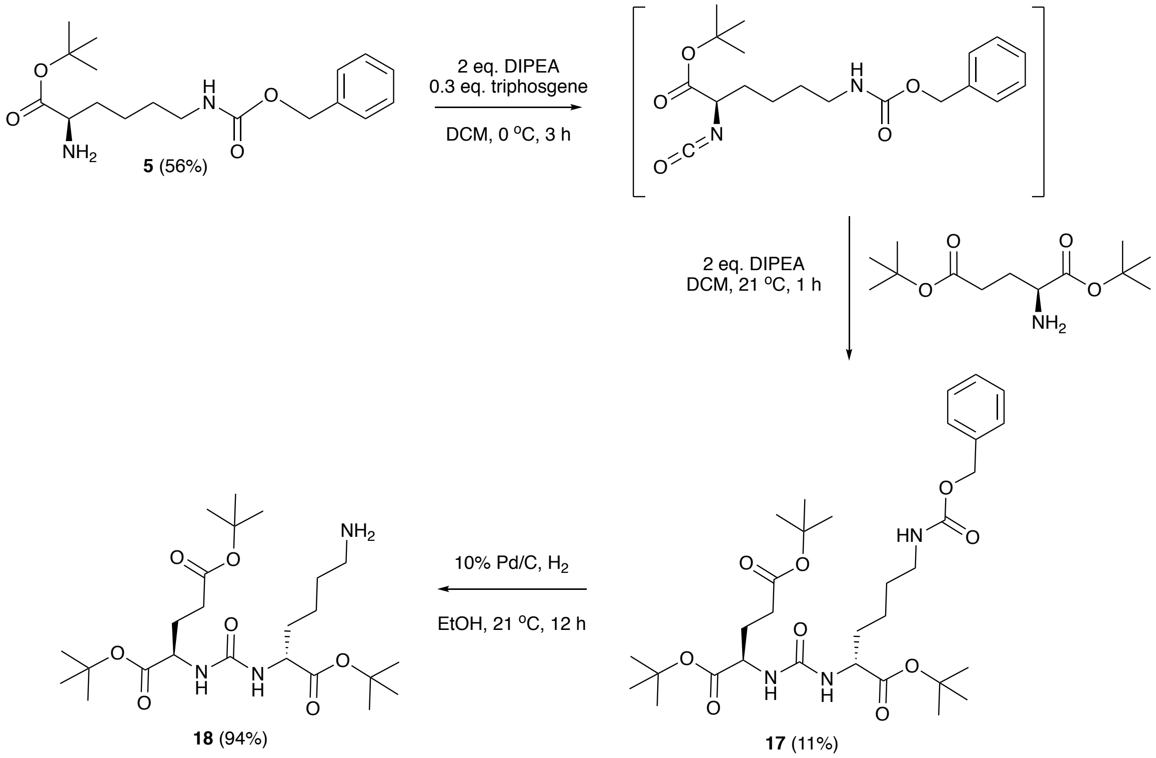

Synthesis of compound **17**

Under an inert atmosphere, a solution of triphosgene (0.61 g, 2.07 mmol) in DCM (50 mL) was cooled to 0 °C and a solution of H-D-Lys(Z)-OtBu (2.11 g, 6.28 mmol) in DCM (10 mL) and DIPEA (1.25 mL) was added dropwise over 2 h. The reaction reached room temperature and a solution of H-D-Glu(OtBu)OtBu·HCl (1.85 g, 6.28 mmol) in DCM (15 mL) and DIPEA (1.25 mL) was added in one portion then stirred for 1 h. The mixture was concentrated to dryness, dissolved in 100 mL EtOAc then washed with 2 M $NaHSO_4$ (2 x 100 mL) and sat. NaCl (aq.). Organic phase was dried over anhydrous $MgSO_4$ and the solvent was removed under reduced pressure. The crude product was purified on silica gel (20-50% EtOAC/Hexane) to isolate compound **17** as a clear oil (438 mg, 0.70 mmol, 11%). ^{1}H NMR (400 MHz, $CDCl_3$) δ 7.41 – 7.29 (m, 5H), 5.20 – 4.97 (m, 5H), 4.38 – 4.29 (m, 2H), 3.20 (q, J = 6.8, 5.9 Hz, 2H), 2.41 – 2.18 (m, 2H), 2.14 – 2.00 (m, 1H), 1.97 – 1.71 (m, 2H), 1.70 – 1.57 (m, 3H), 1.57 – 1.50 (m, 2H), 1.47 – 1.43 (m, 27H), 1.43 – 1.34 (m, 2H). R_f (silica gel, EtOAc:Hexane 1:1) = 0.58. HRMS (ESI+) (m/z): calculated for $C_{32}H_{51}N_3O_9Na^+$ ($[M+Na]^+$): 644.3518; found: 644.3518 (100%).

Figure 6.45. ^{1}H NMR spectrum ($CDCl_3$, 400 MHz) of compound **17**.

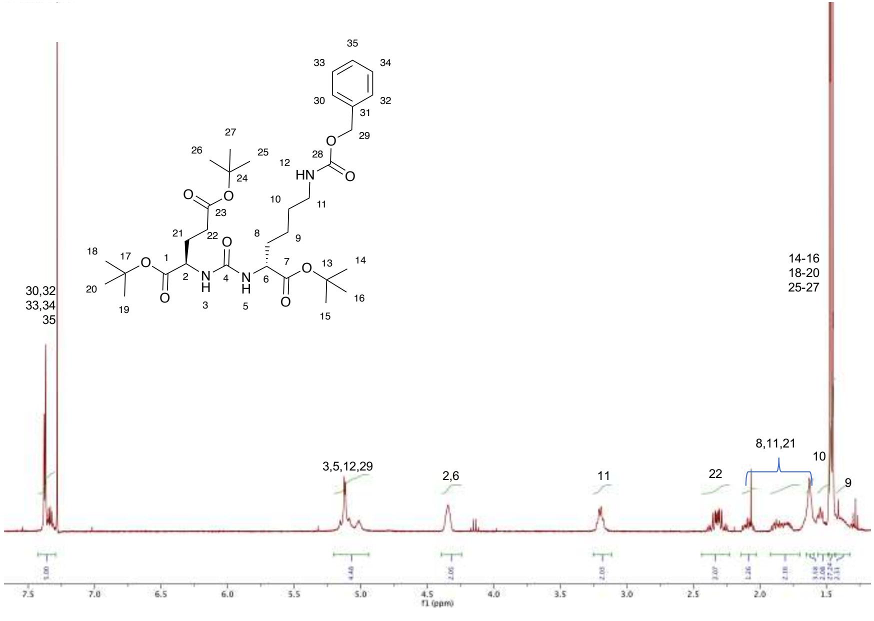

Synthesis of compound 18

To a solution of **17** (430 mg, 0.69 mmol) in EtOH (30 mL), Pd/C (30 mg) was added. The mixture was degassed with N_2, and the system flushed with H_2. The reaction was then stirred for 20 h under an H_2 atmosphere before it was passed through Celite® with excess EtOH. The solvent removed under reduced pressure to yield compound **18** as a yellow oil (318 mg, 0.65 mmol, 94%). ^{1}H NMR (400 MHz,$CDCl_3$) δ 5.22 (s, 1H), 5.20 (s, 1H), 4.39 – 4.31 (m, 2H), 2.73 (t, *J* = 6.7 Hz, 2H), 2.43 – 2.24 (m, 4H), 2.15 – 2.03 (m, 1H), 1.94 – 1.73 (m, 2H), 1.72 – 1.59 (m, 1H), 1.56 – 1.49 (m, 2H), 1.49 (s, 27H), 1.40 – 1.29 (m, 2H). HRMS (ESI+) (m/z): calculated for $C_{24}H_{46}N_3O_7H^+$ ($[M+Na]^+$): 488.3336; found: 488.3327 (100%).

Figure 6.46. ^{1}H NMR spectrum ($CDCl_3$, 400 MHz) of compound **18**.

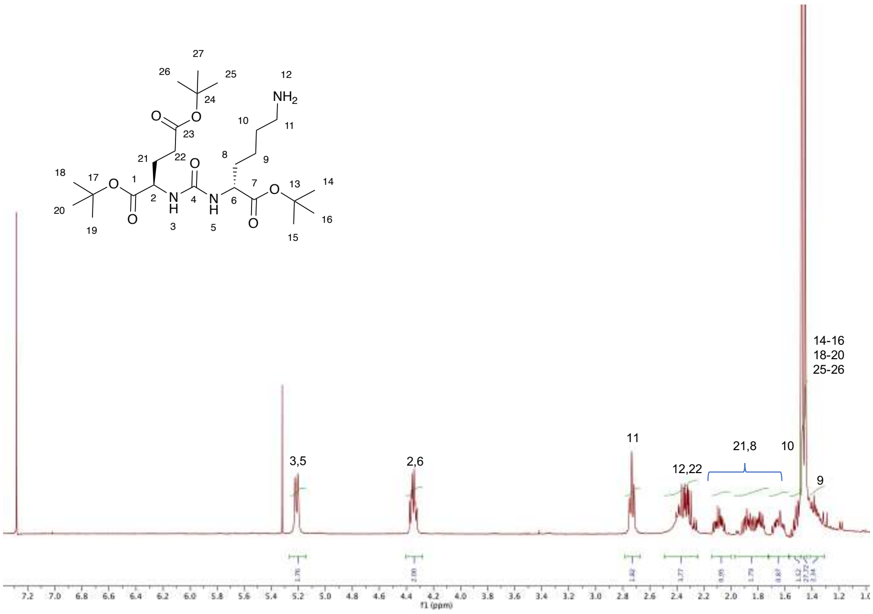

Scheme 6.11. Chemical synthesis of the functionalization of the PEGylated bisphosphonate with the inactive form of the PSMA binding motif (D-Glu-NH-C(O)-NH-D-Lys).

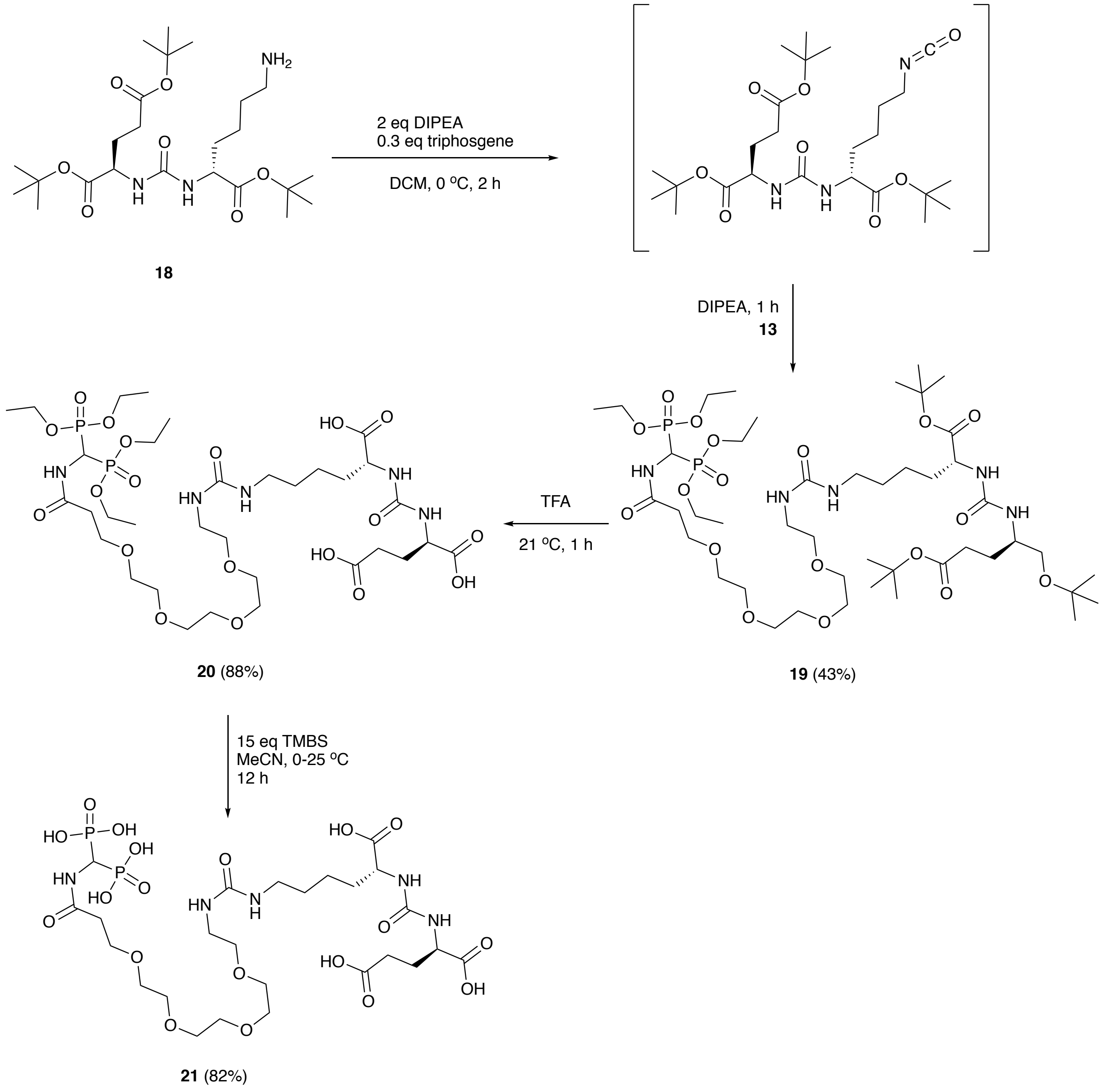

Synthesis of compound **19**

A solution of triphosgene (10 mg, 0.04 mmol) in dry DCM (1.5 mL) was cooled to 0 °C. A solution of **18** (50 mg, 0.11 mmol) in dry DCM (0.5 mL) and DIPEA (50 µL) was added dropwise over 2 h. Compound **13** (58 mg, 0.11 mmol) in DCM (2 mL) and DIPEA (50 µL) then added in one portion and stirred for 1 h at room temperature. Reaction was then washed with water (2 x 5 mL) and brine (5 mL), dried with anhydrous $MgSO_4$ and solvent removed under reduced pressure. The crude product which was purified on silica gel (5-10% MeOH/DCM) to isolate compound **19** as a yellow oil (49 mg, 0.05 mmol, 43%). ^{1}H NMR (400 MHz, $CDCl_3$) δ 6.07 (br s, 4H), 5.07

(td, *J* = 21.9, 10.1 Hz, 1H), 4.30 (br s, 2H), 4.08-4.21 (m, 8H), 3.72 (t, *J* = 6.0 Hz, 2H), 3.65 – 3.56 (m, 12H), 3.53 (td, *J* = 5.2, 2.1 Hz, 2H), 3.38 – 3.30 (m, 2H), 2.56 (t, *J* = 5.8 Hz, 2H), 2.39 – 2.20 (m, 2H), 1.97-2.06 (m, 1H), 1.88 – 1.65 (m, 3H), 1.64 – 1.47 (m, 4H), 1.43 – 1.38 (m, 27H), 1.29 (q, *J* = 7.1 Hz, 12H). $^{31}P\{^1H\}$ NMR (162 MHz, $CDCl_3$) δ 16.50.

Figure 6.47. ^1H NMR spectrum ($CDCl_3$, 400 MHz) of compound **19**.

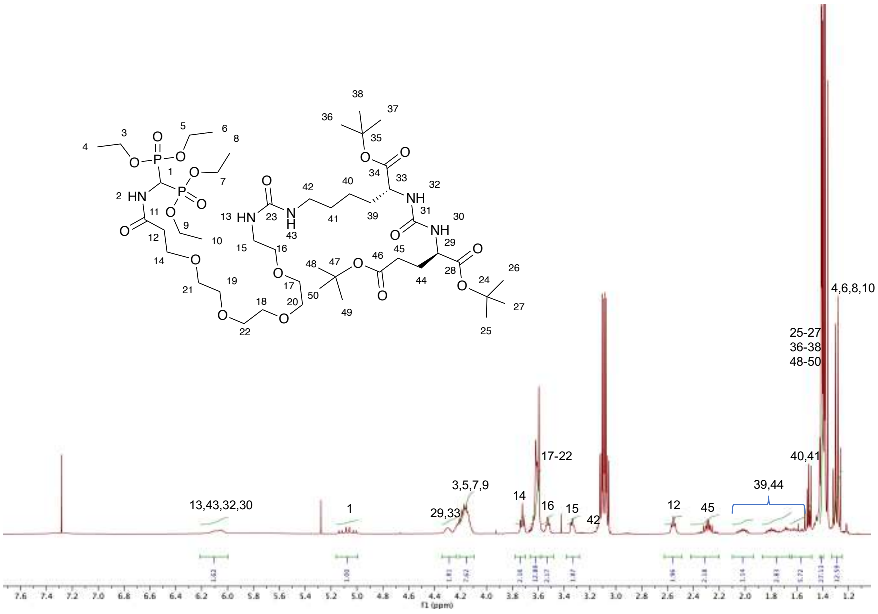

Figure 6.48. $^{31}P\{^1H\}$ NMR spectrum ($CDCl_3$, 162 MHz) of compound **19**.

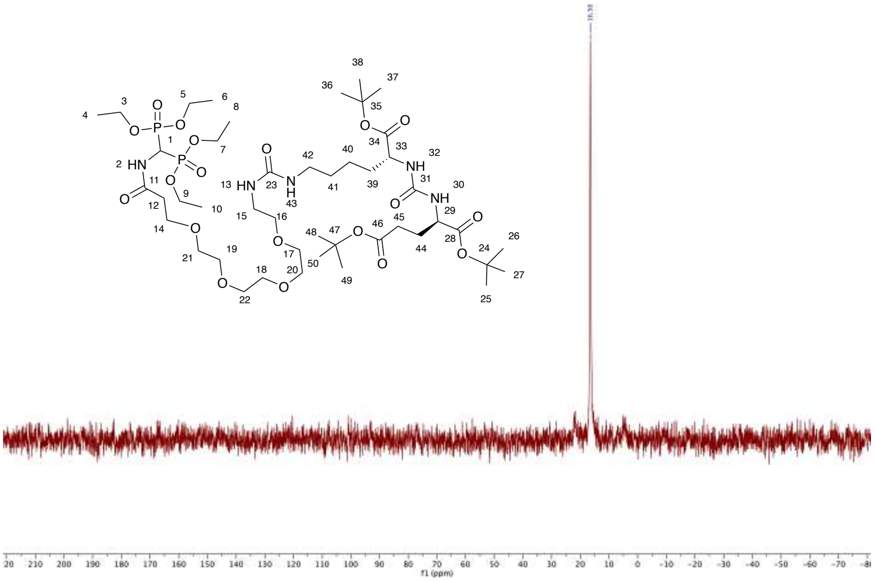

Synthesis of compound **20**

Compound **19** (45 mg, 0.04 mmol) was stirred in TFA (0.5 mL) for 1 h. Et_2O was added (6 mL) and precipitate collect and washed with cold Et_2O (3 x 5 mL) to yield **20** as a white solid (33 mg, 0.04 mmol, 88%). ^1H NMR (300 MHz, MeOD) δ 4.37 – 4.27 (m, 2H), 4.27 – 4.14 (m, 8H), 3.77 (t, *J* = 6.1 Hz, 2H), 3.71 – 3.56 (m, 12H), 3.53 (t, 2H), 3.19 – 3.04 (m, 4H), 2.60 (t, *J* = 5.9 Hz, 2H), 2.42 (t, *J* = 8.1 Hz, 1H), 2.25 – 2.04 (m, 1H), 2.00 – 1.79 (m, 2H), 1.74 – 1.59 (m, 1H), 1.59 – 1.41 (m, 4H), 1.35 (td, *J* = 7.0, 3.7 Hz, 12H). ^{31}P NMR (162 MHz, MeOD) δ 16.51. HRMS (ESI+) (m/z): calculated for $C_{33}H_{63}N_5O_{19}P_2Na^+$ ($[M+Na]^+$): 918.3485; found: 918.3487 (100%).

Figure 6.49. ^1H NMR spectrum (MeOD, 400 MHz) of compound **20**.

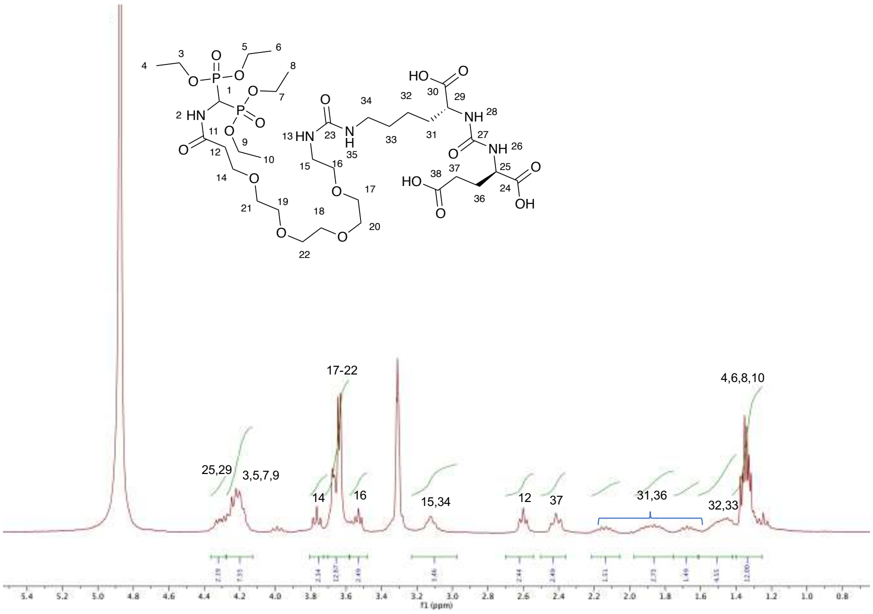

Figure 6.50. $^{31}P\{^1H\}$ NMR spectrum (MeOD, 162 MHz) of compound **20**.

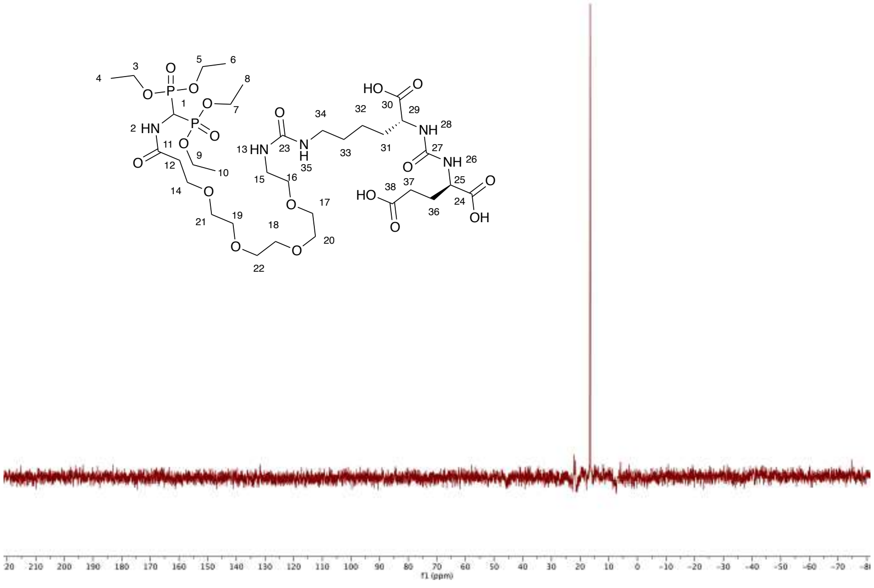

Synthesis of compound 21

Under an N_2 atmosphere, compound **20** (25 mg, 27.9 µmol) was dissolved in dry MeCN (4 mL) and cooled to 0 °C. Trimethylsilylbromide (0.67 mmol, 89 µL) was added dropwise then the reaction was allowed to reach room temperature and stirred for 12 h. Water (3 mL) was added and reaction and stirred for a further 1 h. The reaction was then filtered, wash with DCM (2 x 4 mL) and lyophilised to yield **21** as a white solid (18 mg, 23.0 µmol, 82%). ^{1}H NMR (500 MHz, D_2O) δ 4.62 (t, *J* = 20.9 Hz, 1H), 4.26 (dd, *J* = 9.2, 5.1 Hz, 1H), 4.20 – 4.16 (m, 1H), 3.82 (t, *J* = 6.0 Hz, 2H), 3.71 – 3.66 (m, 12H), 3.58 (t, *J* = 5.3 Hz, 2H), 3.29 (t, *J* = 5.3 Hz, 2H), 3.10 (t, *J* = 6.7 Hz, 2H), 2.65 (t, *J* = 6.2 Hz, 2H), 2.51 (t, *J* = 7.2 Hz, 2H), 2.24 – 2.13 (m, 1H), 2.03 – 1.92 (m, 1H), 1.90 – 1.80 (m, 1H), 1.77 – 1.67 (m, 1H), 1.55 – 1.46 (m, 2H), 1.44 – 1.36 (m, 2H). ^{13}C NMR (126 MHz, D_2O) δ 177.83, 177.75, 176.82, 161.14, 70.35, 70.15, 70.12, 70.07, 70.05, 69.99, 67.10, 53.76, 53.10, 40.10, 40.05, 36.27, 31.14, 30.60, 29.20, 26.74, 22.78. ^{31}P NMR {^{1}H} (162 MHz, D_2O) δ 13.79.

Figure 6.51. ^{1}H NMR spectrum (D_2O, 400 MHz) of compound **21**.

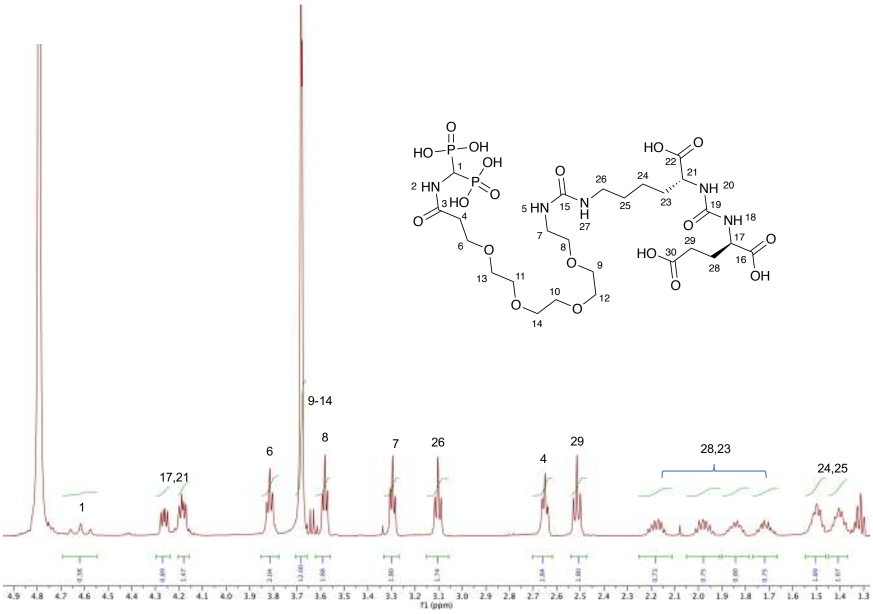

Figure 6.52. $^{13}C\ \{^{1}H\}$ NMR spectrum (D_2O, 126 MHz) of compound **21**.

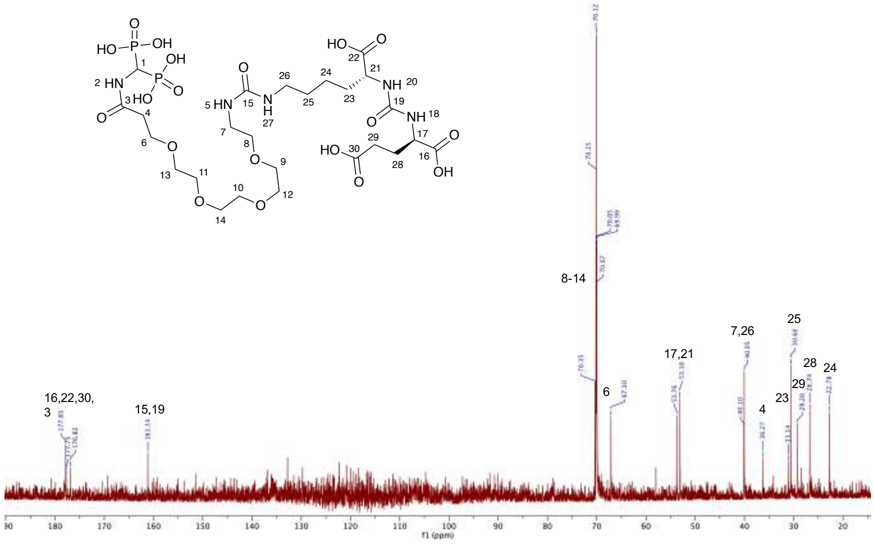

Figure 6.53. $^{31}P\ \{^{1}H\}$ NMR spectrum (D_2O, 162 MHz) of compound **21**.

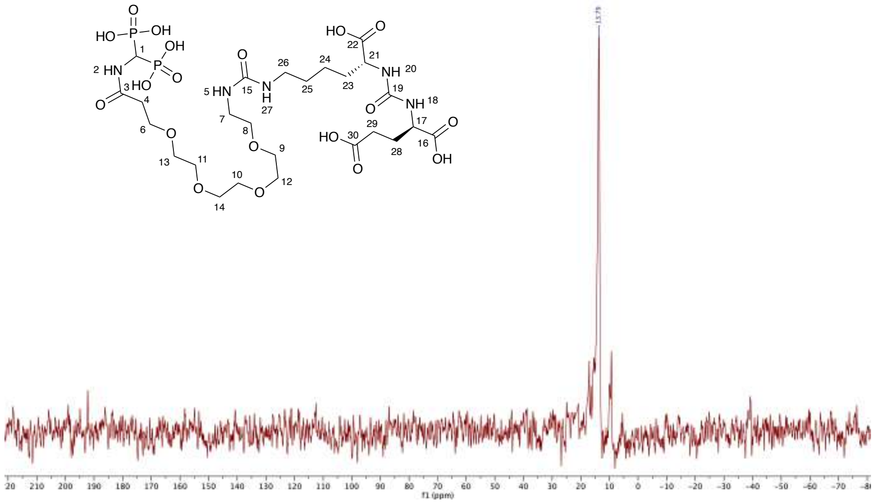

Functionalisation of Feraheme

Determination of concentration of Feraheme particles

The absorbance of known concentrations of Feraheme™ particles was measured at 468 nm. The plot was then used as a reference to calculate concentration of Feraheme™ samples produced in the following procedures.

Figure 6.54. Absorbance of Feraheme™ particles 468 nm at varying concentrations.

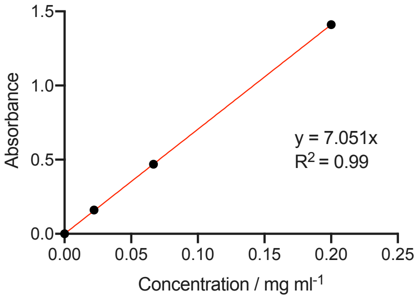

*Functionalisation of particles with compound **16***

A solution of Feraheme™ particles (10 µL, 30 mg ml^{-1}) and compound **6** (10 µL, 11.2 µM) were vortexed for 12 h. The mixture was then loaded onto a PD10-SEC (stationary phase: Sephadex G-25, mobile phase: saline) and the first 2.0 mL was collected and diluted to give a final concentration of 0.13 mg ml^{-1}.

*Functionalisation of particles with compound **21***

Analogous to functionalisation with compound **16**.

*ICP-MS measurement of FH-**16***

Samples measured by UZH ICP-MS service. Nitric acid (3 mL, 2%) was added to samples (0.3 mL, 0.21 mg mL^{-1}) and then a 1:10 dilution was performed before measurements were carried out on an Agilent 8800 ICP-MS. Data was then compared to a phosphorous calibration plot. The phosphorous content was determined to be 2.99 ± 0.11 µg of phosphorous per 1 mg of iron. This was compared to the bare Feraheme™ particles which contain 0.049 ± 0.001 µg of phosphorous per 1 mg of iron.

Radiochemistry

*Synthesis of [^{68}Ga]FH-**16**-Ga and [^{68}Ga]FH-**21**-Ga*

Radiolabelling reactions to prepare [^{68}Ga]FH-**16**-Ga and [^{68}Ga]FH-**21**-Ga were accomplished by addition of an aliquot of [^{68}Ga][Ga(H$_2$O)$_6$]Cl$_3$(aq.) stock solution (ca. 15 MBq) to an aqueous solution of FH-**16** and FH-**21** (13.0 µg) buffered with NaOAc (0.2 M, pH 4.4). After 20 min. at 70 °C a radiochemical conversion (RCC) >98% was found by radio-TLC (R_f [silica gel, 0.1 M citrate buffer] = 0.0-0.2) and >94% for PD10 SEC (saline as eluent).

Stability studies

Reactions were prepared as previously described and then 25 µL was added to PBS, saline or 25 mM EDTA (300 µL) and the samples were incubated (37 °C). RCP was monitored *via* radio-TLC at time points up to 2 h.

Cellular studies

Binding assay

LNCaP cells were plated in 6-well plates with a density of 5 x 10^5 cells/well in 2 mL media. After 24 h, reactions were prepared as described above and diluted in cell media (210-fold). The cell media was removed from the 6-well plates and replaced with the diluted reaction mixture (2 mL, 43 kBq) before incubation (37 °C) for 1.5 h. The plates were then placed on ice and each well washed with ice-cold PBS (2 x 1 mL), 1 M NaOH (1 mL) added and incubated for 10 min. Cells were then collected and their associated radioactivity quantified with the gamma counter. A BCA assay was then used to quantify the protein content of cell samples and this was used to normalise data. Experiments were performed in replicates (*n*=5).

Blocking assay

LNCaP cells were plated in 6-well plates with a density of 8 x 10^5 cells/well in 2 mL media. After 24 h cells, media was removed, cells washed with PBS (2 mL) and the media replaced with either media alone or media containing 0.1% azide (1.8 mL), with the media of blocked wells containing 10 μM 2-PMPA binding motif. Cells were then incubated for 1 h. [^{68}Ga]FH-**16** was prepared as described above, diluted in cell media (60-fold) and added to wells (200 μL, 0.17 MBq) then plates incubated for 1.5 h. Plates were then placed on ice and each well washed with ice-cold PBS (2 x 1 mL), 1 M NaOH (1 mL) added and plates incubated for 10 min. Cells were then collected and their associated radioactivity quantified with the gamma counter. A BCA assay was then used to quantify the protein content of cell samples and this was used to normalise data. Experiments were performed in replicates (*n* = 5).

In vivo studies

[^{68}Ga]FH-**16** was prepared as stated above and diluted with 6-fold with PBS. The tracer was (0.9-1.1 MBq) was injected i.v. *via* the tail vein of mice bearing an LNCaP tumours (168.7 ± 65.6 mm^3; *n*=3). Images were then acquired at 30 mins, 1 h and 2 h (10 min scan). Prior to image acquisition the mouse anaesthetised using an isoflurane dose between 3.0-4.0%. During image acquisition, the respiration rate of the animal was monitored via live video feed and anaesthesia was maintained by an experience animal experimenter by controlling the isoflurane dose between 1.5-2.0%. Images were reconstructed and analysed using VivoQuant^{TM} 3.5 patch 2 software (InviCRO, Boston, MA).

Biodistribution studies

Following the final image at 2 h, the mouse was euthanised and biodistribution studies were performed. A total of 15 tissues (including the tumour) were removed, rinsed in water, dried in air for approx. 2 min., weighed and counted on a calibrated gamma counter for accumulation of activity. Count data were background- and decay-corrected, and the tissue uptake for each sample (determined in units of percentage injected dose per gram [%ID g^{-1}]) was calculated by normalisation to the total amount of activity injected into the animal.

6.4 Experimental methods associated with Chapter 4

6.4.1 Synthesis and characterisation

Synthesis of small molecules for GNF functionalisation

Scheme 6.12. Chemical synthesis of PSMA binding motif PEG derivative (Glu-NH-C(O)-NH-Lys-NH-C(O)-PEG_4-NH_2).

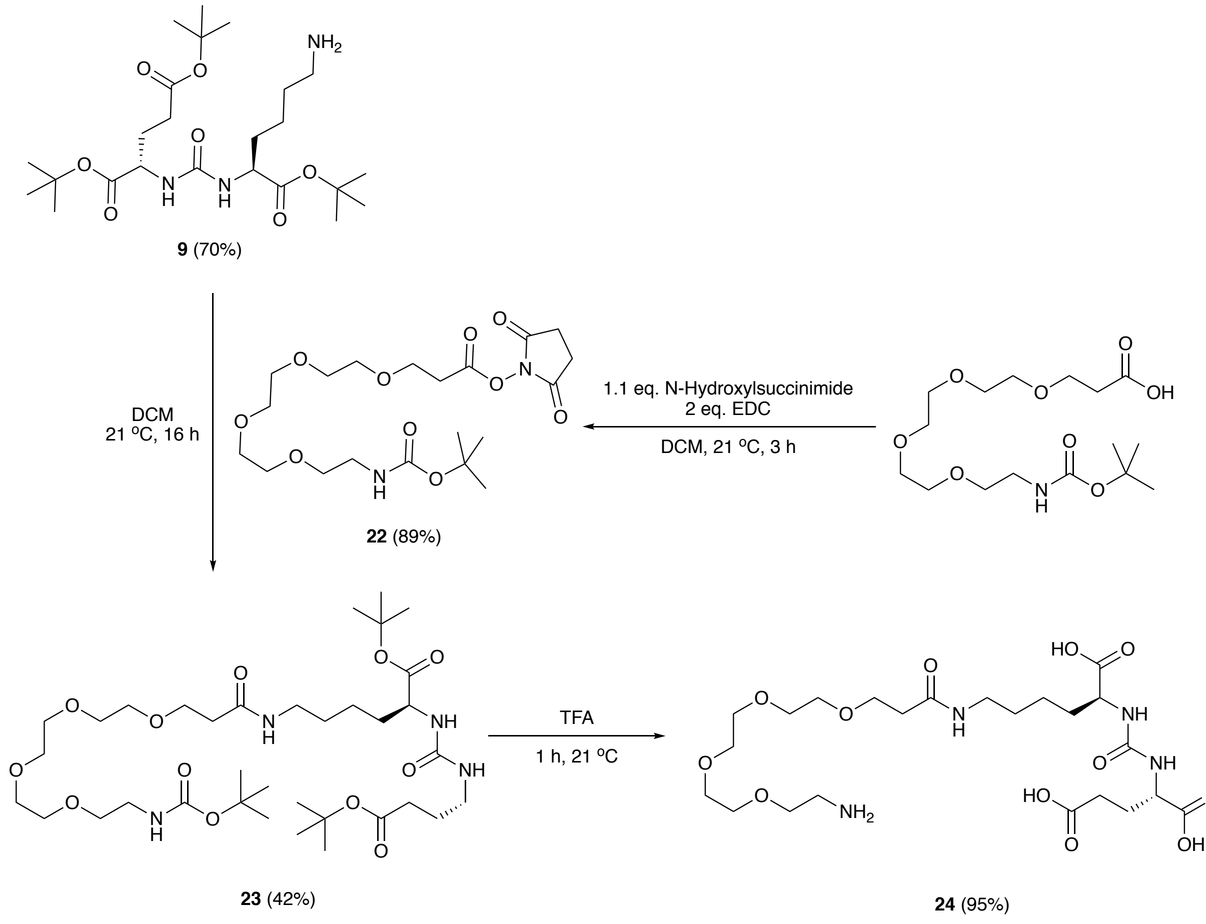

Synthesis of compound **22**

To (Boc-amino)-PEG_4-carboxylic acid (80 mg, 0.21 mmol) in DCM (5 mL), was added NHS (29 mg, 0.25 mmol) and EDC (84 mg, 0.44 mmol) and mixture stirred until TLC showed consumption of product. The reaction mixture was washed with 2.5% $NaHSO_4$ (aq.) (3x10 mL) and brine then the organic phase was dried over anhydrous $MgSO_4$ and solvent removed under reduced pressure to yield compound **22** as a white solid (90 mg, 0.20 mmol, 89%). ^1H NMR (400 MHz, $CDCl_3$) δ (ppm) 5.05 (br, 1H), 3.85 (t, *J* = 6.5 Hz, 2H), 3.69 – 3.58 (m, 12H), 3.53 (t, *J* = 5.1 Hz, 2H), 3.35 – 3.26 (m, 2H), 2.90 (t, *J* = 6.5 Hz, 2H), 2.83 (s, 4H), 1.44 (s, 9H). R_f (silica gel, MeOH:DCM 1:20) = 0.4

Figure 6.55. ^{1}H NMR spectrum ($CDCl_3$, 400 MHz) of compound **22**.

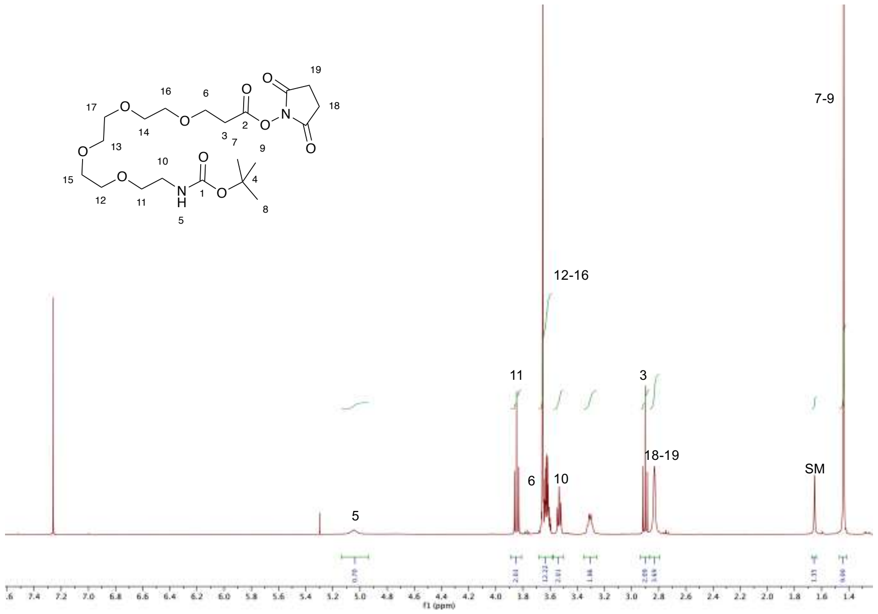

Synthesis of compound **23**

Compound **22** (35 mg, 0.07 mmol) and ammonium formate (45 mg, 0.72 mmol) were dissolved in MeOH (3 mL), stirred for 30 min and the solvent was then removed under reduced pressure. Compound **9** (33 mg, 0.07 mmol) was then added in DCM (8 mL) and TEA (80 µL, 0.57 mmol) and reaction stirred for 16 h. Organic layer was washed with water (3 x 10 mL) and brine (10 mL), then the organic phase was dried over anhydrous $MgSO_4$ and the solvent removed under reduced pressure. Crude product was purified on silica gel (7% MeOH/DCM) to isolate compound **23** as a clear oil (0.2 g, 0.3 mmol, 42%) ^{1}H NMR (400 MHz, $CDCl_3$) δ (ppm) 6.78 (s, 1H), 6.56 (s, 1H), 5.47 (s, 1H), 5.20 (s, 1H), 4.38 – 4.15 (m, 2H), 3.79 – 3.72 (m, 2H), 3.70 – 3.62 (m, 12H), 3.60 – 3.52 (m, 2H), 3.40 – 3.29 (m, 2H), 3.28 – 3.08 (m, 2H), 2.55 – 2.45 (m, 2H), 2.42 – 2.27 (m, 2H), 2.13 – 2.02 (m, 3H), 1.92 – 1.74 (m, 1H), 1.70 – 1.59 (m, 2H), 1.58 – 1.49 (m, 36H), 1.48 – 1.44 (m, 2H).

Figure 6.56. ^{1}H NMR spectrum ($CDCl_3$, 400 MHz) of compound **23**.

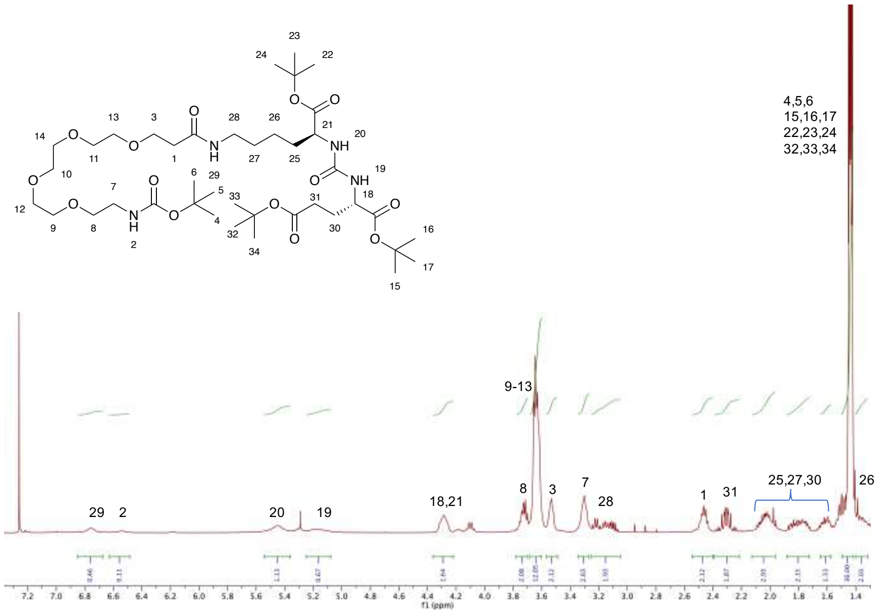

Synthesis of compound 24

Compound **6** (20 mg, 0.02 mmol) was stirred in TFA (500 µL) for 1 h and then precipitated in Et_2O (5 mL). Product was collected by centrifugation, washed with cold Et_2O and dried under reduced pressure to yield compound **24** as a white solid (13.1 mg, 0.02 mmol, 95%) ^{1}H NMR (400 MHz, MeOD) δ (ppm) 4.32 (dd, *J* = 8.6, 5.1 Hz, 1H), 4.26 (dd, *J* = 8.5, 4.9 Hz, 1H), 3.79 – 3.59 (m, 16H), 3.19 (t, *J* = 6.8 Hz, 2H), 3.17 – 3.11 (m, 2H), 2.45 (t, J = 6.0 Hz, 2H), 2.43 – 2.37 (m, 2H), 2.22 – 2.04 (m, 1H), 1.98 – 1.78 (m, 2H), 1.69 – 1.60 (m, 1H), 1.57 – 1.51 (m, 2H), 1.46 – 1.41 (m, 2H). ^{13}C NMR (101 MHz, MeOD) δ (ppm) 175.02, 174.96, 174.42, 172.64, 158.70, 70.01, 69.93, 69.85, 69.82, 69.41, 66.93, 66.40, 52.54, 52.10, 39.11, 38.69, 35.98, 31.79, 29.66, 28.45, 27.51, 22.52. HRMS (ESI+) (m/z): calculated for $C_{24}H_{46}N_3O_7^+$ ($[M+H]^+$): 567.6130; found: 567.2867 (100%).

Figure 6.57. ^1H NMR spectrum (MeOD, 400 MHz) of compound **24**.

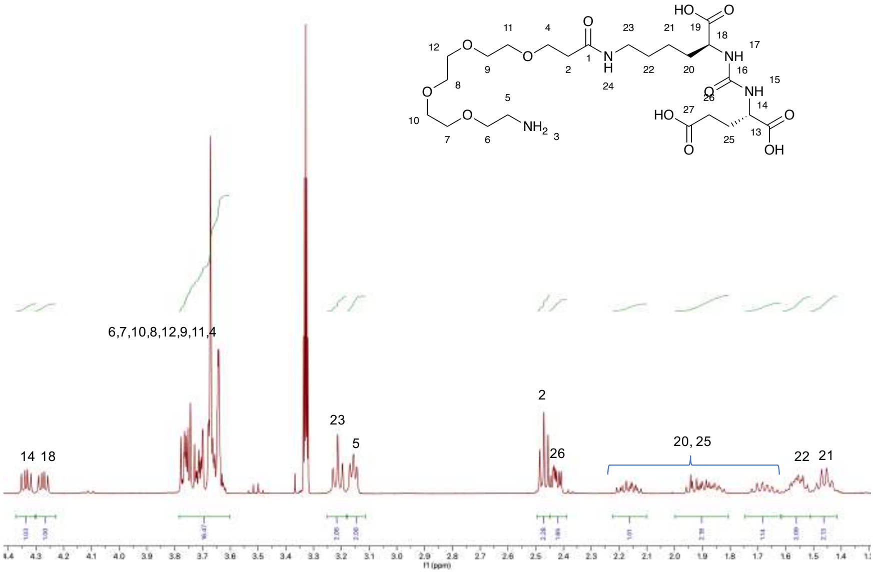

Figure 6.58. $^{13}C\ \{^1H\}$ NMR spectrum (MeOD, 400 MHz) of compound **24**.

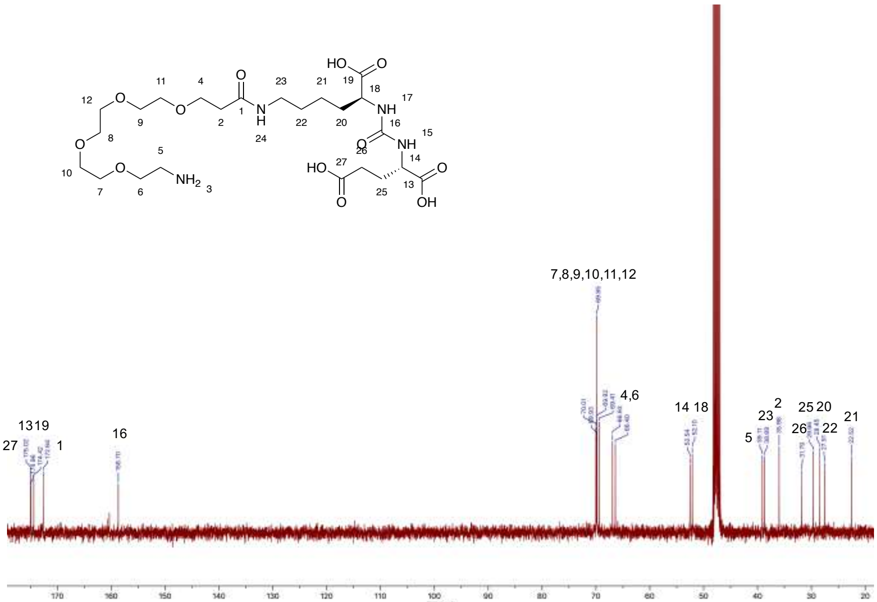

Scheme 6.13. Chemical synthesis of albumin binding motif, compound **26**.

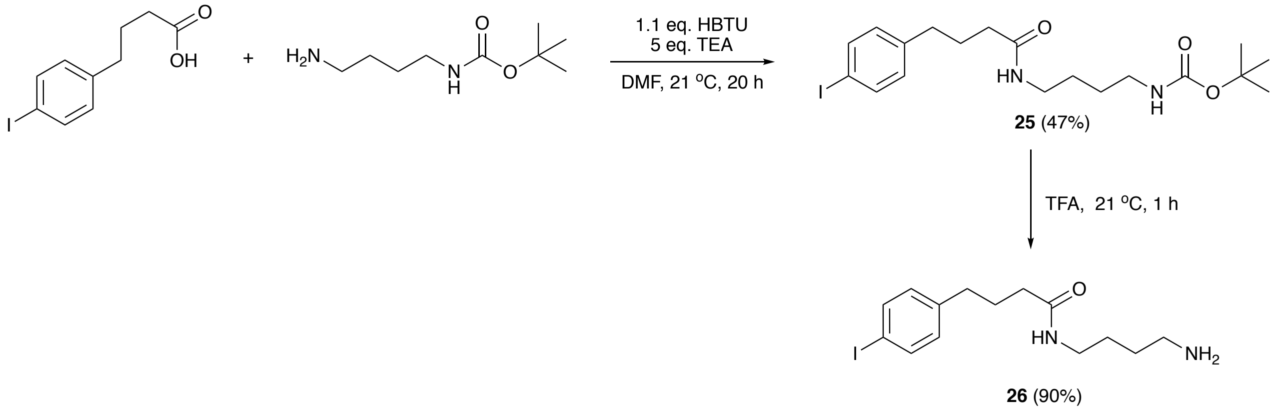

Synthesis of compound **25**

4-(*p*-Iodophenyl)butyric acid (300 mg, 1.03 mmol) in DMF (10 mL) was activated with HBTU (430 mg, 1.12 mmol). Following the addition of *N*-Boc-1,4-butanediamine (194 mg, 1.03 nmol) the reaction was stirred for 20 h. The solvent was removed under reduced pressure and the product re-dissolved in DCM (20 ml) which was washed with 0.1 M NaOH (3 x 20 ml), 0.1 M HCl (3 x 20 mL), and brine (3 x 20 mL). The organic phase was dried over anhydrous $MgSO_4$ and the solvent was removed under reduced pressure. The crude product was purified on silica gel (5-10% DCM/MeOH) to isolate compound **25** as a clear oil (230 mg, 0.49 mmol, 47%). ^{1}H NMR (400 MHz, $CDCl_3$) δ 7.58 (d, *J* = 8.2 Hz, 2H), 6.92 (d, *J* = 8.1 Hz, 2H), 5.76 (s, 1H), 4.62 (s, 1H), 3.30 – 3.21 (m, 2H), 3.17 – 3.06 (m, 2H), 2.58 (t, *J* = 7.5 Hz, 2H), 2.15 (t, *J* = 7.5 Hz, 2H), 1.97 – 1.88 (m, 2H), 1.54 – 1.45 (m, 4H), 1.43 (s, 9H). ^{13}C NMR (101 MHz, $CDCl_3$) δ 172.82, 156.34, 141.29, 137.53, 130.74, 91.11, 79.48, 39.31, 38.82, 35.80, 34.83, 28.54, 27.84, 27.04, 26.69. R_f (silica gel, MeOH:DCM 1:14) = 0.59. HRMS (ESI+) (m/z): calculated for $C_{24}H_{46}N_3O_7^+$ ($[M+Na]^+$): 483.1115; found: 483.1117 (100%).

Figure 6.59. ^{1}H NMR spectrum ($CDCl_3$, 400 MHz) of compound **25**.

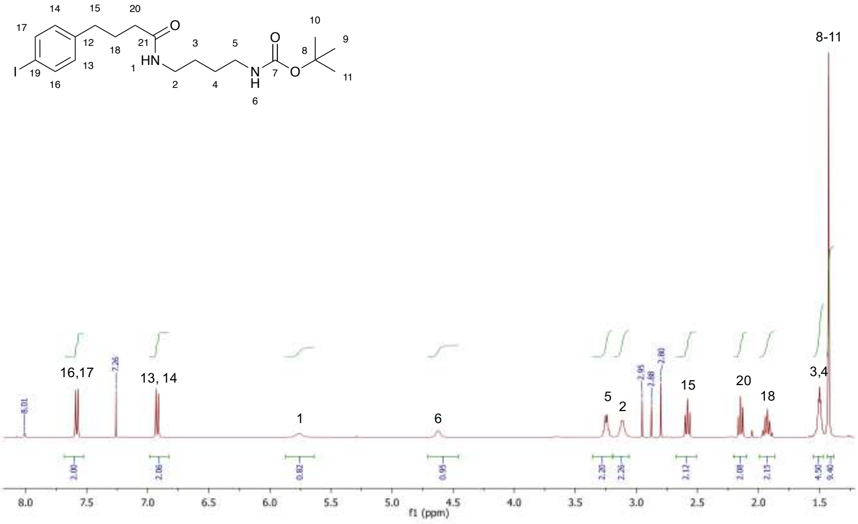

Figure 6.60. ^{13}C {^{1}H} NMR spectrum ($CDCl_3$, 400 MHz) of compound **25**.

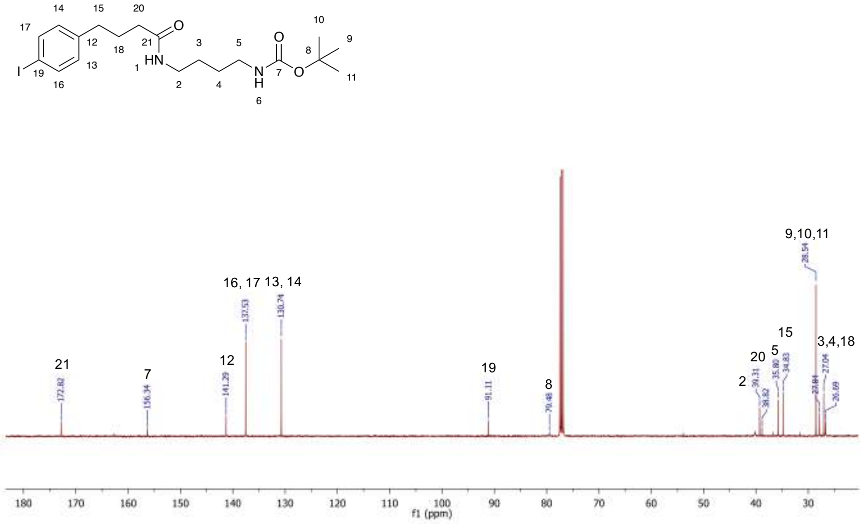

Synthesis of compound **26**

Compound **25** (230 mg, 0.48 mmol) was stirred with TFA (0.5 mL) for 1 h. Toluene was added (10 mL) and solvent removed under reduced pressure. The crude product was then dissolved in DCM (10 mL) and washed with $NaHCO_3$ (0.1 M, 10 mL) and brine (10 mL). The organic phase was dried over anhydrous $MgSO_4$ and the solvent was removed under reduced pressure to yield compound **26** as a yellow solid (161 mg, 0.44 mmol, 90%). ^{1}H NMR (400 MHz, $CDCl_3$) δ (ppm) 7.59 (d, *J* = 8.2 Hz, 2H), 6.93 (d, *J* = 8.1 Hz, 2H), 5.91 (s, 1H), 3.24 (m, 2H), 2.74 (t, *J* = 6.4 Hz, 2H), 2.58 (t, *J* = 7.5 Hz, 2H), 2.16 – 2.12 (m, 2H), 2.07 (s, 2H), 1.98 – 1.86 (m, 2H), 1.65 –

1.43 (m, 4H). ^{13}C NMR (101 MHz, CDCl$_3$) δ (ppm) 172.50, 141.21, 137.41, 130.63, 90.98, 41.45, 39.26, 35.74, 34.68, 30.27, 27.04, 26.89. HRMS (ESI+) (m/z): calculated for $C_{24}H_{46}N_3O_7^+$ ([M+Na]$^+$): 361.0777; found: 361.0772 (100%).

Figure 6.61. ^{1}H NMR spectrum (CDCl$_3$, 400 MHz) of compound **26**.

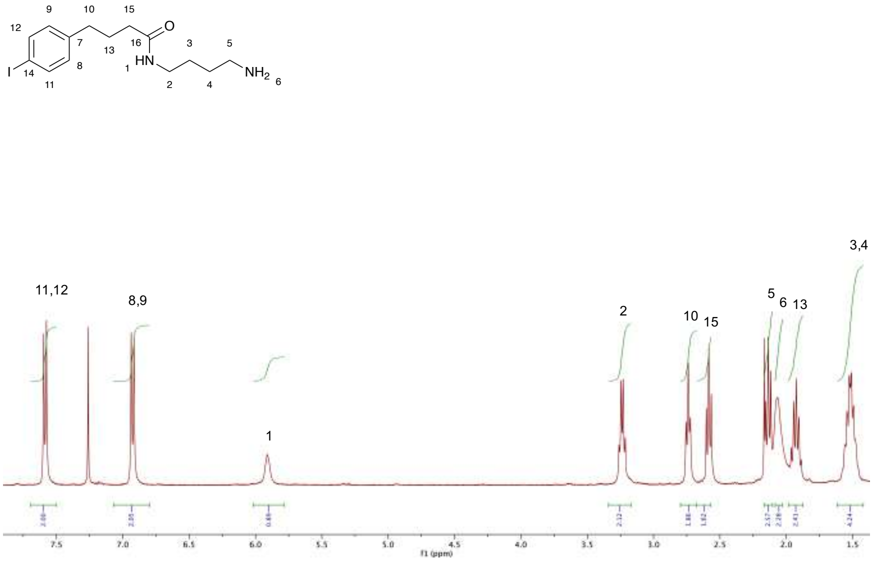

Figure 6.62. ^{13}C{^{1}H} NMR spectrum (CDCl$_3$, 400 MHz) of compound **26**.

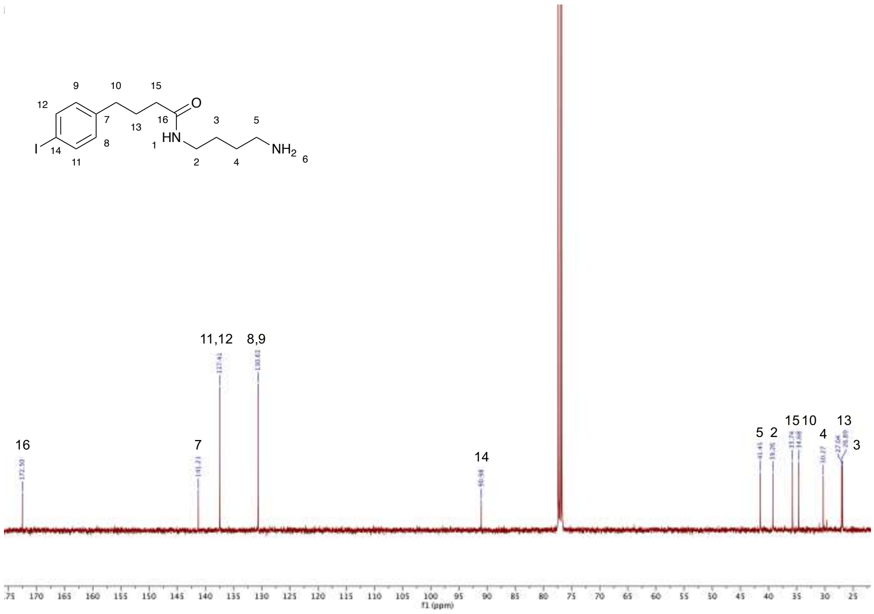

Chemical synthesis of the functionalised GNFs

Synthesis of ***GNF-1***

Scheme 6.14. Chemical synthesis of **GNF-1**.

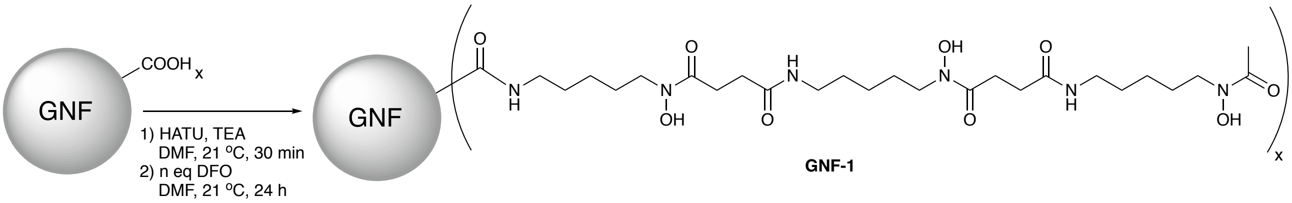

GNFs (4.56 mg) in DMF (1 mL) and TEA (20 μL) were activated with HATU (8.24 mg, 0.02 mmol). Following the addition of DFO (0.40 mg, 0.61 μmol) reaction was vortexed for 24 h. The solvent was removed under reduced pressure and the product purified on silica gel (100% H_2O), after lyophilisation, **GNF-1** was obtained as a black solid (2.13 mg, 42%).

Synthesis of ***GNF-2***

Scheme 6.15. Chemical synthesis of **GNF-2**.

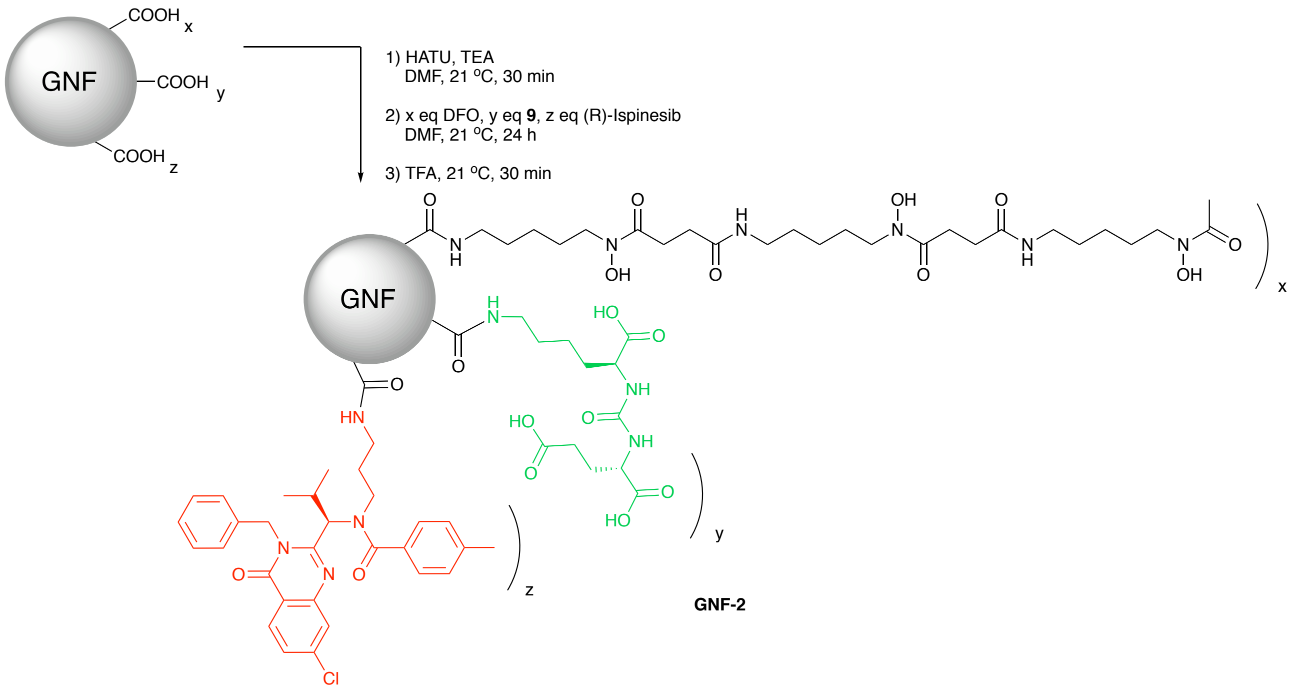

GNFs (4.10 mg) in DMF (1 mL) and TEA (20 μL) were activated with HATU (8.01 mg, 0.02 mmol). Following the addition of DFO (0.50 mg, 0.61 μmol), (*R*)-ispinesib (0.53 mg, 1.03 μmol), and **4** (0.50 mg, 1.03 μmol) reaction was vortexed for 24 h. TFA (0.5 mL) was added and after 1 h the solvent removed under reduced pressure and product purified on silica gel (100% H_2O), after lyophilisation, **GNF-2** was obtained as a black solid (1.84 mg, 36%).

Synthesis of ***GNF-3***

Scheme 6.16. Chemical synthesis of **GNF-3**.

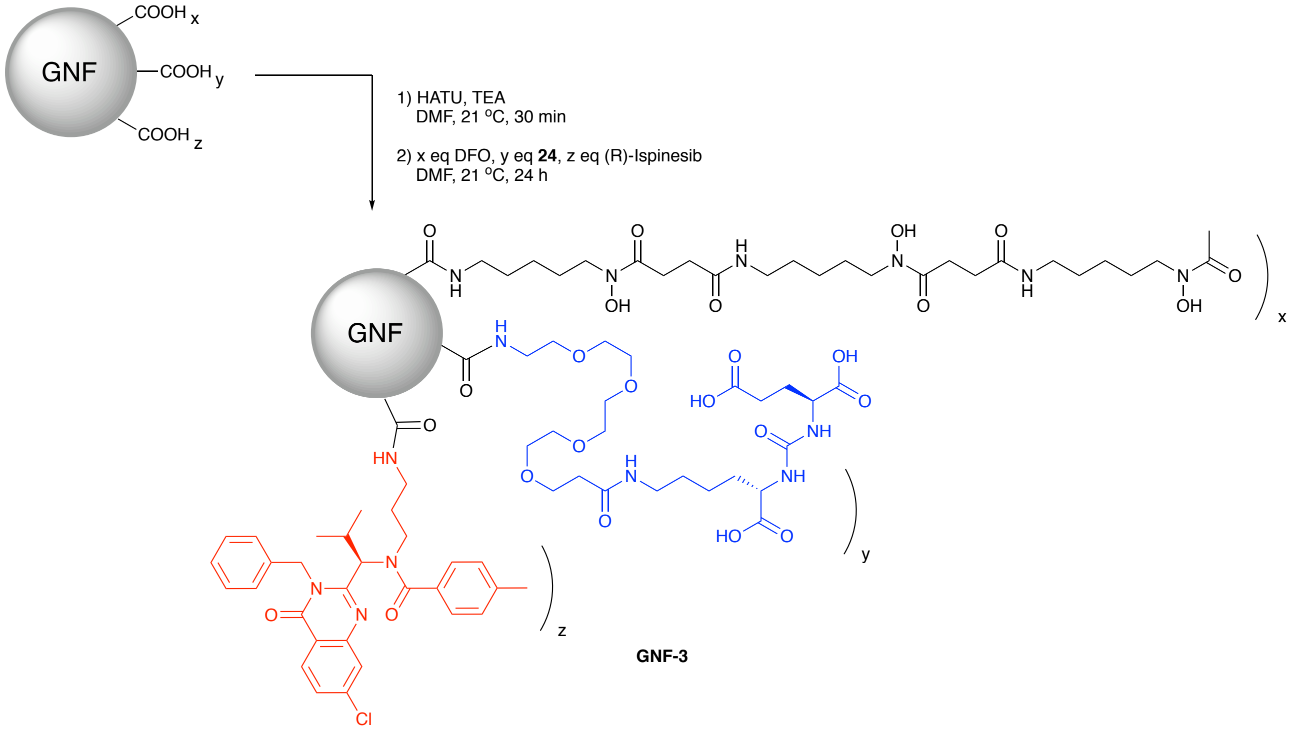

GNFs (4.27 mg) in DMF (1 mL) and TEA (20 µL) were activated with HATU (8.07 mg, 0.02 mmol). Following the addition of DFO (0.47 mg, 0.72 µmol), (*R*)-ispinesib (0.60 mg, 1.16 µmol), and **7** (0.53 mg, 0.93 µmol) reaction was vortexed for 24 h. Solvent was removed under reduced pressure and product purified on silica gel (100% H_2O), after lyophilisation, **GNF-3** was obtained as a black solid (1.72 mg, 29%).

Synthesis of ***GNF-4***

Scheme 6.17. Chemical synthesis of GNF-4.

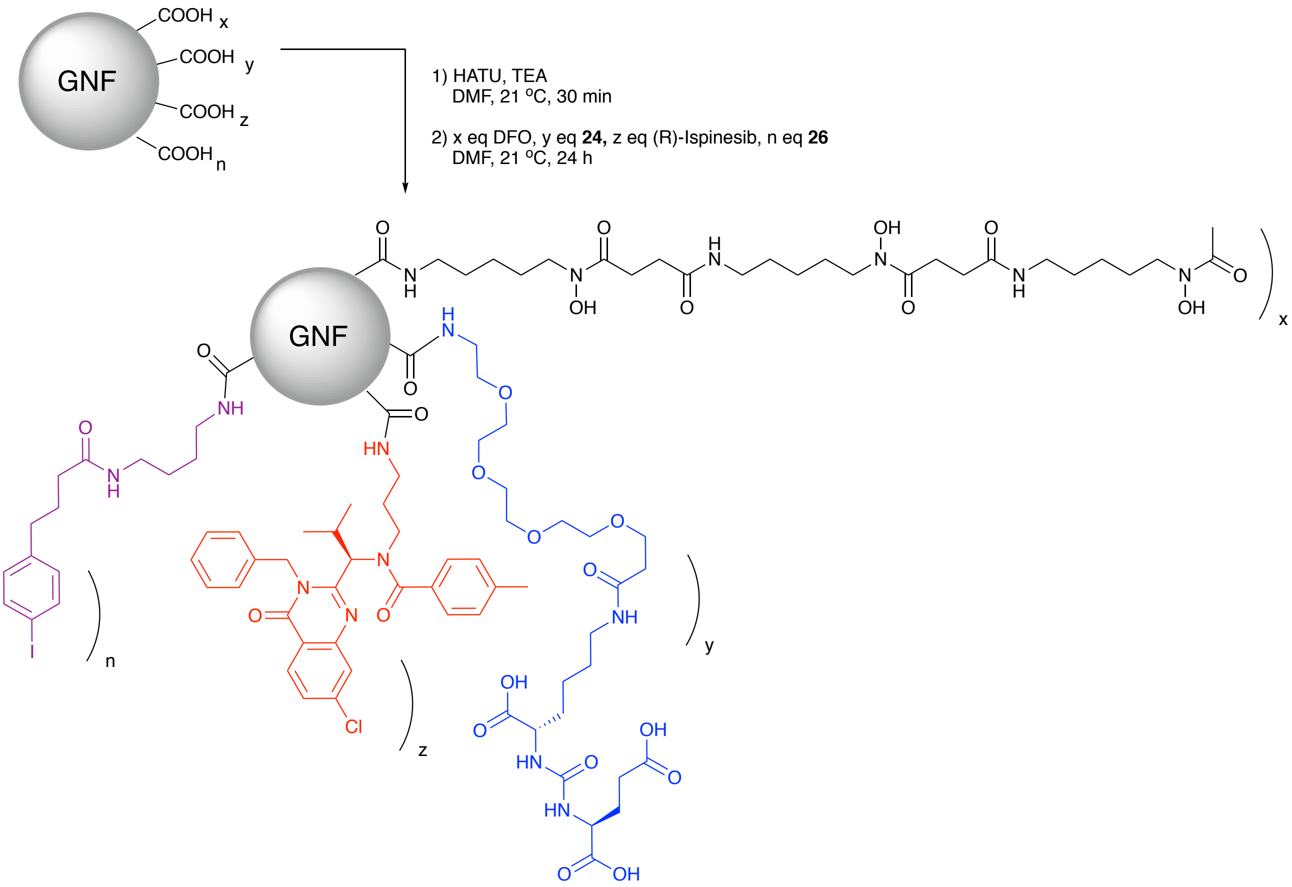

GNFs (4.15 mg) in DMF (1 mL) and TEA (20 μL) were activated with HATU (8.06 mg, 0.02 mmol). Following the addition of DFO (0.47 mg, 0.72 μmol), (*R*)-ispinesib (0.54 mg, 1.04 μmol), **7** (0.56 mg, 0.99 μmol) and **9** (0.31 mg, 0.86 μmol) reaction was vortexed for 24 h. Solvent was removed under reduced pressure and product purified on silica gel (100% H_2O), after lyophilisation, **GNF-4** was obtained as a black solid (1.81 mg, 30%).

Purification of GNF constructs

GNF constructs were purified on silica gel. All starting materials remained at the baseline (R_f = 0.0-0.1) whilst **GNF-1**, **-2**, **-3** and **-4** moved to the solvent from. Compounds which are UV active are visualised using 254 nm, whilst other compounds are visualised using ninhydrin stain (visualising the free amine).

Figure 6.63. TLC separation of GNF constructs and starting materials. Silica gel as stationary phase and 100% H_2O as mobile phase (Visualisation of plates: V = visual observation, N = ninhydrin stain, UV = 254 nm).

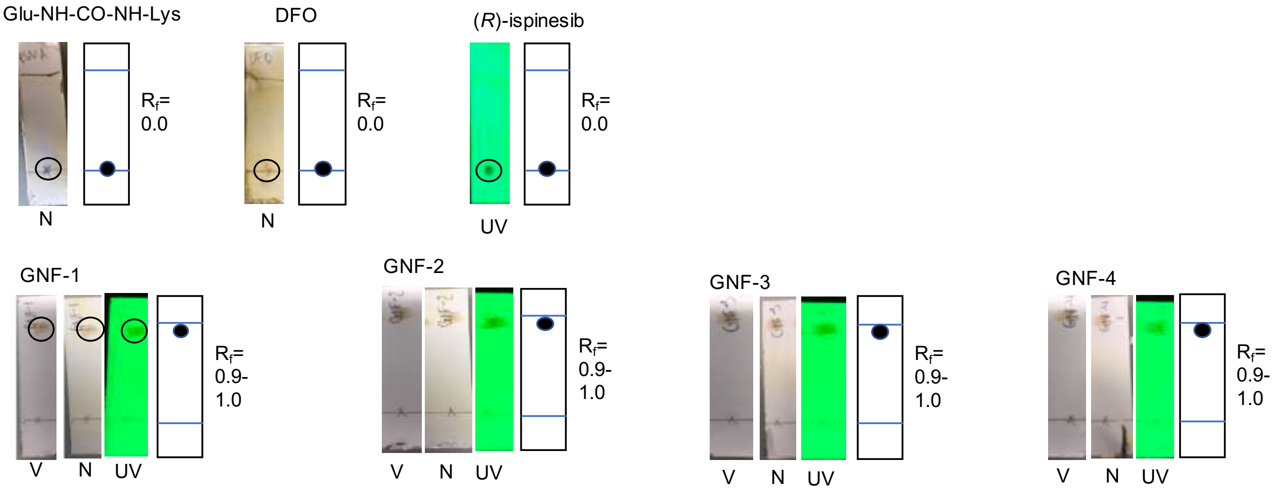

6.4.2 Radiochemistry

General Radiolabeling Conditions

Radiolabelling reactions to prepare [^{68}Ga]**GNF-1**, **-2**, **-3**, and **-4** were accomplished by addition of an aliquot of [^{68}Ga][Ga(H_2O)$_6$]Cl_3(aq.) stock solution (ca. 40 MBq) to an aqueous solution of GNF-1-4 (25 µg) buffered with NaOAc (0.2 M, pH 4.4). The reaction was monitored by using radio-iTLC and was found to be complete after 10 min at 21 °C giving a radiochemical conversions (RCC) >97% (R_f [silica gel, H_2O] = 0.90-1.00).

Quantification of DFO content

[^{68}Ga]**GNF-1**, **-2**, **-3**, and **-4** samples were prepared at a variety of concentrations and buffered with NaOAc (0.2 M, pH 4.4). Aliquots of [^{68}Ga][Ga(H_2O)$_6$]Cl_3(aq.) stock solution (ca. 18 MBq) were added to each sample and after 10 min radio-iTLC was used to gain a RCC. Plots were used in conjunction with the known molar activity of the generator to calculate the amount of DFO (nmol) per mass of GNF (mg).

Lipophilicity measurements

n-Octanol was pre-saturated with PBS for 24 h. Reactions were prepared as described above. Reaction mixture (50 µL) was added to pre-saturated octanol (400 µL) and PBS (350 µL) and shaken for 1 h at 37 °C. Samples were then centrifuged (2000 RPM, 2 min), an aliquot of 50 µL was taken from each phase and the radioactivity of aliquots quantified with the gamma counter. Experiments were performed in triplicate.

Stability Studies

Stability in saline and PBS

Reactions were prepared as previously described and then PBS or saline (300 µL) were added and samples incubated (37 °C). RCP was monitored *via* radio-TLC at time points up to 2 h (*n* = 3, **Table 6.5**, **Table 6.6**).

Table 6.5. Percentage radiochemical purity (RCP) of [^{68}Ga]**GNF-1-4** determined from radio-iTLC following incubation with PBS up to 2 h at 37 °C.

	RCP / %			
Time / min	[^{68}Ga]**GNF-1**	[^{68}Ga]**GNF-2**	[^{68}Ga]**GNF-3**	[^{68}Ga]**GNF-4**
0	99.1 ± 0.7	98.6 ± 0.2	97.4 ± 0.6	97.3 ± 0.4
10	95.2 ± 0.3	97.0 ± 0.3	96.8 ± 0.4	88.1 ± 1.1
20	95.1 ± 1.5	95.3 ± 1.0	90.4 ± 3.5	85.8 ± 2.4
30	96.5 ± 0.6	93.0 ± 0.9	94.5 ± 0.4	88.7 ± 2.3
60	96.5 ± 0.9	92.8 ± 0.3	93.5 ± 0.4	90.7 ± 1.4
120	95.0 ± 0.4	89.3 ± 1.6	93.7 ± 0.5	89.0 ± 0.8

Table 6.6. Percentage radiochemical purity (RCP) of [^{68}Ga]**GNF-1-4** determined from radio-iTLC following incubation with saline up to 2 h at 37 °C.

	RCP / %			
Time / min	[^{68}Ga]**GNF-1**	[^{68}Ga]**GNF-2**	[^{68}Ga]**GNF-3**	[^{68}Ga]**GNF-4**
0	96.6 ± 0.8	98.6 ± 0.2	97.4 ± 0.6	97.3 ± 0.4
10	96.0 ± 2.9	96.6 ± 0.2	93.8 ± 1.0	92.9 ± 0.6
20	91.8 ± 1.5	94.1 ± 1.1	91.5 ± 1.2	89.2 ± 2.8
30	94.7 ± 5.7	89.9 ± 2.4	92.6 ± 2.2	85.0 ± 1.9
60	95.4 ± 1.2	92.1 ± 0.5	88.6 ± 2.2	82.1 ± 1.2
120	95.1 ± 1.0	90.1 ± 0.8	87.6 ± 1.9	83.2 ± 2.2

Stability in human serum albumin

Reactions were prepared as described previously, human serum albumin (300 µL) was added and samples incubated (37 °C). Stability in human serum was monitored *via* radio-SEC (mobile phase: 200 mM arginine in PBS) for time points up to 2.5 h ([^{68}Ga]**GNF-1**: *n* = 3, [^{68}Ga]**GNF-2**, **-3** and **-4**: *n* = 1, **Table 6.7**).

Table 6.7. Percentage radiochemical purity (RCP) of [^{68}Ga]**GNF-1-4** determined from radio-SEC-HPLC following incubation with human serum for up to 2.5 h at 37 °C.

	RCP / %			
Time / min	[^{68}Ga]**GNF-1**	[^{68}Ga]**GNF-2**	[^{68}Ga]**GNF-3**	[^{68}Ga]**GNF-4**
0	95.9 ± 1.6	97.1	98.6	97.3
10	90.7 ± 2.3	95.4	97.5	97.0
80	88.1 ± 2.4	91.3	94.9	95.5
150	84.4 ± 3.6	88.7	93.9	94.4

6.4.3 Cellular assays

In vitro cell proliferation assays

*Treatment with **GNF-2-4***

Cells were plated in 96-well plates with a density of 3000 cells/well in 150 μL media. After 24 h cells were treated with 50 μL compound (1:2 or 1:3 dilution in cell media, 0.25 mg mL^{-1} to 1 pg mL^{-1}) and plates incubated for 48 h then treated with thiazolyl blue tetrazolium bromide (50 μL, 5.0 mg mL^{-1} solution in PBS). Following 3 h incubation in darkness, media was removed, DMSO (100 μL/well) added and after 30 min absorbance was measured at 570 nm (Hidex Sense plate reader). Experiments were performed in triplicate.

Treatment with (R)-ispinesib

Experimental procedure was similar to the above with the addition of 0.2% DMSO in cell media during the treatment period.

Cell Binding Assay

Cells were harvested and distributed in Eppendorf tubes (3 x 10^{6} cells / vial) in media (270 μL) or media with sodium azide (270 μL, 0.1%). Reactions were prepared as previously described and diluted (40-fold) in cell media and then added (30 μl, 75 kBq) to the prepared cells. After mixing for 1.5 h at 37 °C, the samples were centrifuged (2000 rpm, 3 min) and the cell pellet washed with ice-cold PBS (2 x 1 mL) keeping the samples on ice between washes. The radioactivity associated with each sample was quantified using the gamma counter. Experiments were performed in triplicate.

Blocking Assay

LNCaP cells were plated in 6-well plates with a density of 8×10^5 cells / well in 2 mL media. After 24 h cells, media was removed, cells washed with PBS (2 mL) and the media replaced (1.8 mL), with the blocked wells containing media with 5 μM PSMA binding motif. Cells were then incubated for 1 h. Reactions were prepared as described above, diluted in cell media (55-fold) and added to wells (200 μL, 1.4 MBq) then plates incubated for 1.5 h. Plates were then placed on ice and each well washed with ice-cold PBS (2 x 1 mL), 1 M NaOH (1 mL) added and plates incubated for 10 min. Cells were then collected and their associated radioactivity quantified with the gamma counter. Experiments were performed in triplicate.

Confocal Microscopy

Cells were plated in 4 well plates with a density of 8000 cells/well. After 24 h, cells were treated with 1 μg mL^{-1} GNF (**GNF**, **GNF-2**, **-3** or **-4**) and left for 24 h. The media was then removed, wells washed with PBS (3 x 600 μL) and incubated with fixative solution (600 μL, 4% formaldehyde in PBS) for 15 min. Wells were then washed with PBS (3 x 600 μL), incubated with permeabilisation buffer (500 μL, x0.2) for 15 min, washed with PBS (3 x 600 μL) then incubated with 2 drops of Imageit FX. After 30 min, wells washed with PBS (3 x 600 μL), incubated with primary antibody (400 μL, mouse α-tubulin, 1:1000 dilution in blocking buffer) for 2 h, washed with PBS (3 x 600 μL) and incubated with secondary antibody (400 μL, Goat α-mouse Alexa Flour 568 α-tubulin staining, 1:2000 dilution in blocking buffer) for 1.5 h. Following washing with PBS (3 x 600 μL) cells were incubated with Hoeschst 33342 (600 μL, 1:100,000 dilution in H_2O) for 10 min followed by a final washing with H_2O (3 x 600 μL). Slides were drained, dried and wells removed, 1 drop Prolong Gold added and cover slips held in place with nail polish.

Preparation of blocking buffer

A solution of PBS containing 1% BSA and 0.3% Tween-20 was prepared.

Preparation of permeabilisation buffer

A 10x permeabilisation buffer was prepared from 1.54 M NaCl, 15.44 mM KH_2PO_4, 28.58 mM $Na_2HPO_4.7H_2O$ and 5% Triton X-100 in 5 mL H_2O. 40 mL of H_2O added, followed by adjustment of pH to 7.2 before making up to 50 mL creating the 1x permeabilisation buffer. This was stored in the fridge and diluted when needed.

Flow Cytometry

Cells were plated onto 100 mm^2 petri dishes at a cell density of 1.0×10^6 cells/dish. After 24 h cells were treated with 12 ng mL^{-1} and 120 ng mL^{-1} of the compounds (**GNF**, **GNF-2**, **-3** or **-4**) for 36 h, then washed with ice-cold

PBS (4 mL), detached with trypsin-EDTA (2 mL, 0.25%) and collected *via* centrifugation (100 *g*, 10 min) with ice-cold PBS (10 mL). Cell pellet was washed with ice-cold PBS (5 mL) then re-suspended in fixation solution (4 mL, 70 vol% EtOH, 30 vol% H2O) and stored at -20°C for 24 h. Subsequently, ice-cold PBS was added and cells centrifuged (100 xg, 10 min), washed with PBS (10 mL) and re-suspended in staining solution (1 mL) consisting of 0.1 mg/mL RNAse A (Sigma Aldrich), 50 µg/mL propidium iodide (PI) from 2.5 mg/mL stock solution and 0.05% Triton X-100 (Sigma Aldrich) in PBS. After incubation at 37 °C for 40 min the cells were collected by centrifugation (100 xg, 10 min), washed with PBS (10 mL), re-suspended in PBS (2 mL) and samples then analysed on a BD LSR Fortessa cytometry system. Data were analysed by cell-cycle analysis software (FlowJo, TreeStar Inc.).

6.4.4 In vivo studies

Small animal PET imaging

The dynamic scan PET scan (15x2 min scans) was commenced and at t=2 min [^{68}Ga]**GNF-3** or [^{68}Ga]**GNF-4** (~1 MBq, [~27 µCi], in 200 µL sterile PBS) was injected intravenous (i.v.) *via* the tail vein catheter. During image acquisition, the respiration rate of the animal was monitored via live video feed and anaesthesia was maintained by an experience animal experimenter by controlling the isoflurane dose between 1.5 – 2.0%. List-mode data were acquired for 15x2 min and 1x5 min.

Figure 6.64. TACs plotted for the liver, bladder and brain with data extracted from 30 min dynamic PET analysis (15x2min scans) with injection of **(A)** [^{68}Ga]**GNF-3** (*n* = 3) and **(B)** [^{68}Ga]**GNF-4** (*n* = 4) at *t* = 2 min. VOIs were defined and data extracted using the VivoQuant™ software. See main text (**Figure 4.11**) for kidney, tumour, muscle and heart data.

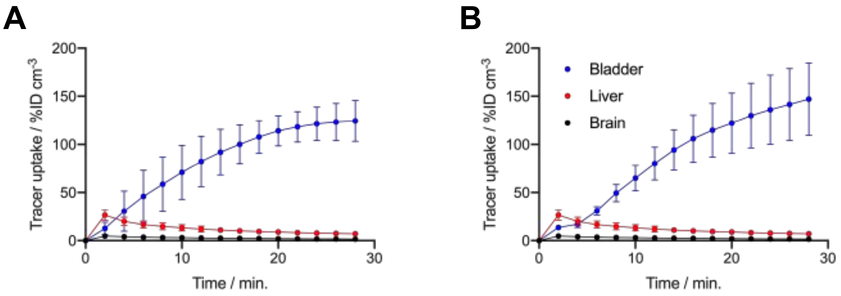

6.5 Experimental methods associated with Chapter 5

6.5.1 Functionalisation of GNFs with a fluorescent BODIPY derivative

Synthesis of small molecules

Scheme 6.18. Chemical synthesis of boron-dipyrromethene (BODIPY) dyes **27** and **28**.

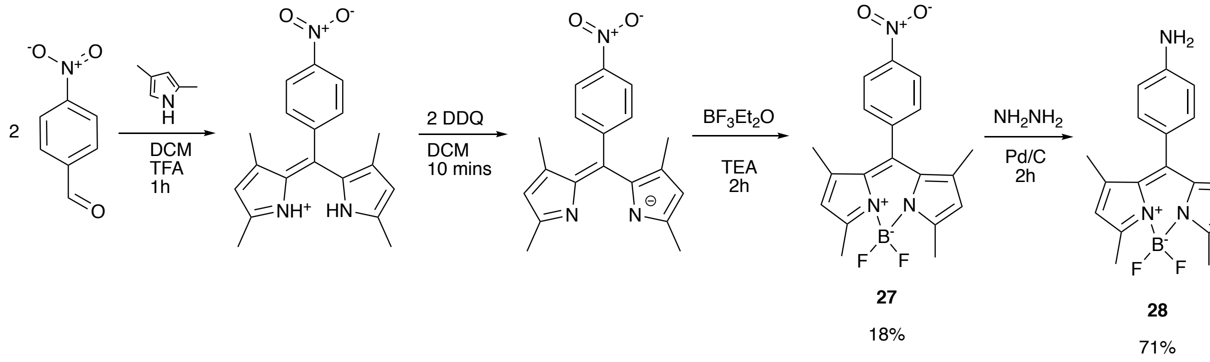

Compounds **27** and **28** were synthesised by using previously published procedures.[382]

Synthesis of compound **27**

Under an N_2 atmosphere, a solution of 2,4-dimethylpyrrole (0.46 mL, 4.50 mmol) and 4-nitrobenzaldehyde (302 mg, 2.00 mmol) in dry DCM (150 mL) is stirred at 21 °C. The reaction was monitored by TLC and once the consumption of 4-nitrobenzaldehyde was confirmed a solution of DDQ (454 mg, 2.00 mmol) in DCM was added. After 10 min TEA (4 mL) and boron trifluoride diethyl etherate (4 mL) were added dropwise and simultaneously and the reaction was stirred for 2 h at room temperature. The reaction was quenched with water (100 mL) and the product was extracted with DCM (3 x 100 mL), dried over anhydrous $MgSO_4$ and the solvent removed under reduced pressure. The crude product was then recrystallized. Briefly, the crude product was dissolved in hot 1:1 ethyl acetate/hexane (25 mL) and the hot solution was filtered. The volume of the filtrate was reduced (15 mL) and left to cool gradually. The resulting crystals were washed with ice cold hexane and dried under vacuum to yield **27** as green crystals (130 mg, 0.35 mmol, 18%). ^{1}H NMR (400 MHz, $CDCl_3$) δ 8.39 (d, *J* = 8.8 Hz, 1H), 7.54 (d, *J* = 8.8 Hz, 1H), 6.02 (s, 1H), 2.57 (s, 3H), 1.37 (s, 3H). HRMS (ESI$^-$) (m/z): calculated for $C_{19}H_{17}N_3O_2^-$ ([M-H]$^-$): 368.1387; found: 368.1386) (100%). R_f (silica gel, EtOAc:Hexane 1:4) = 0.81.

Figure **6.65.** ^{1}H NMR spectrum (CDCl$_3$, 400 MHz) of compound **27**.

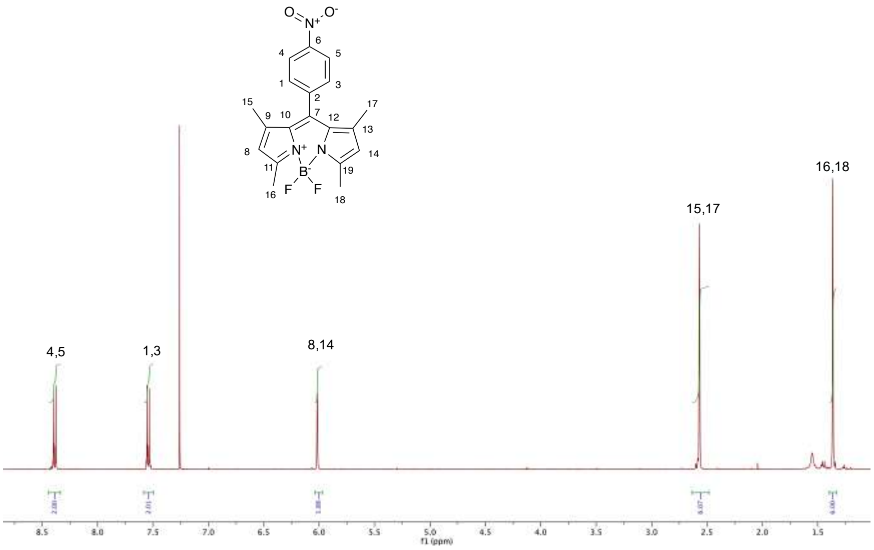

Synthesis of compound **28**

To a solution of compound **27** (15 mg, 40.6 μmol) in dry ethanol (2 mL) palladium on carbon (5 mg) and hydrazine monohydrate (35 μL, 0.71 mmol) were added. The reaction was refluxed for 30 min and then cooled to room temperature. After removing the solids *via* Celite® filtration the solvent was removed under reduced pressure to yield **28** as an orange solid (10 mg, 28.9 μmol, 71%) ^{1}H NMR (400 MHz, CDCl$_3$) δ 7.03 (d, *J* = 8.4 Hz, 2H), 6.80 (d, *J* = 8.4 Hz, 2H), 5.99 (s, 2H), 2.56 (s, 6H), 1.51 (s, 6H). R_f (silica gel, EtOAc:Hexane 1:1 (+1% TEA)) = 0.76.

Figure **6.66.** ^{1}H NMR spectrum ($CDCl_3$, 400 MHz) of compound **28**.

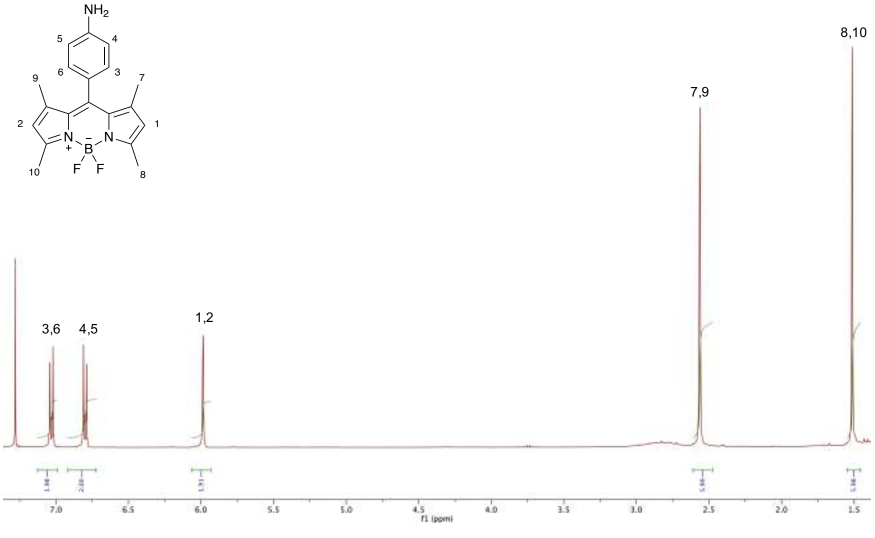

Functionalisation of GNFs with 28

Scheme 6.19. Chemical synthesis of BODIPY-GNF

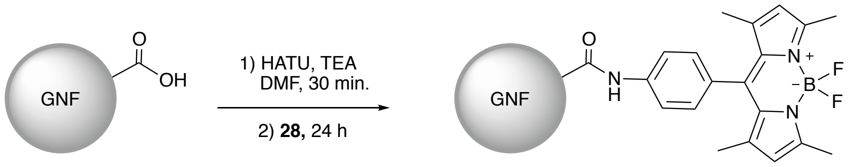

GNFs (1.94 mg) in DMF (1 mL) and TEA (10 μL) were activated with HATU (4.01 mg, 0.01 mmol). Following the addition of **28** (1.19 mg, 3.51 μmol) the reaction was vortexed for 24 h. Solvent was removed under reduced pressure to obtain the crude product which was re-dissolved in water. Non-soluble starting materials were removed and the product was purified on silica gel (100% H_2O). After lyophilisation, BODIPY-GNF was obtained as a red solid (0.76 mg, 39% (mass yield)).

Figure 6.67. TLC separation of GNF constructs and compound **28** (BODIPY). Silica gel as stationary phase and 100% H_2O as mobile phase (Visualisation of plates: V = visual observation, N = ninhydrin stain, UV = 254 nm).

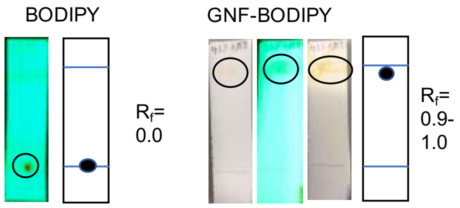

Characterisation of BODIPY-GNF

Absorption/Emission Spectra of BODIPY-GNF

Absorption measurements

Absorption spectra were measure on a Nanodrop^{TM} One^{C} UV-Vis Spectrophotometer using a 50 μg mL^{-1} solution of BODIPY-GNF.

Emission measurements

Emission spectra were measured on a Perkin Elmer LS-50B Luminescence Spectrophotometer with 0.5 μg/mL aqueous solutions of BODIPY-GNF. Excitation at 475 nm, slit width 10 nm.

To measure emission with differing concentrations a Hidex Sense Plate Reader was used. A dilution series was performed and emission was measured at 520 nm was measured following excitation at 475 nm.

Conjugation of BODIPY-GNF to Trastuzumab and Onartuzumab

Synthesis of BODIPY-GNF-trastuzumab

To a solution of BODIPY-GNF (0.1 mg) in MES buffer (200 μL, 50 mM, pH6), EDC (0.6 mg, 1.93 μmol) and NHS (1.2 mg, 10.4 μmol) were added and the solution was mixed for 1.5 h. Pre-purified trastuzumab (0.6 mg) in PBS (800 μL) was added and the solution was mixed for 2.5 h at pH7. The was then purified using PD10-SEC (PBS as eluent) by collecting the first 1.8 mL. The construct was further purified using 100 kDa spin filters (washing with 5 x H_2O, 14,000 g, 2 min). The protein content was determined *via* BCA assay to be 12.97 ± 0.55 mg mL^{-1}. Following a 1:500 dilution emission was measured on the Hidex Sense Plate Reader and found to be 6811 ± 195.

Synthesis of BODIPY-GNF-onartuzumab

To a solution of BODIPY-GNF (0.1 mg) in MES buffer (200 μL, 50 mM, pH6), EDC (0.6 mg, 3.86 μmol) and NHS (1.2 mg, 10.4 μmol) and were added and the solution mixed for 1.5 h. Pre-purified onartuzumab (0.6 mg) in PBS (800 μL) was added and the solution was mixed for 2.5 h at pH7. The crude reaction was then purified using PD10-SEC (PBS as eluent) by collecting the first 1.8 mL. The construct was further purified using 100 kDa spin filters (washing with 5 x H_2O, 14,000 g, 2 min). The protein content was determined *via* BCA assay to be 6.02 ± 0.06 mg mL^{-1}. Following a 1:25 dilution emission was measured on the Hidex Sense Plate Reader and found to be 1997 ± 128.6.

FACS analysis of BODIPY-GNF-trastuzumab

Preparation of FACS buffer

FACS buffer was prepared with the addition of 0.5% BSA and 0.05% sodium azide in PBS.

FACs analysis using BODIPY-GNF-trastuzumab

SK-OV-3 cells were harvested, washed with PBS and distributed in Eppendorf tubes (3 x 10^6 cells / vial) in FACS buffer (270 μL). For treatment of cells a solution of BODIPY-GNF-trastuzumab was prepared in FACS buffer with a protein concentration of 0.1 mg mL^{-1} (BODIPY-GNF concentration of 1.26 μg mL^{-1}). A solution of BODIPY-GNF was prepared in FACS buffer with a concentration of 1.26 μg mL^{-1}. For blocking cells were pre-treated with 1 mg of trastuzumab and incubated at 0 ^{o}C for 30 mins before the addition of further solutions. To the prepared cells BODIPY-GNF-trastuzumab solution (30 μL), BODIPY-GNF solution (30 μL) or the control FACS buffer (30 μL) was added. Cells were incubated with gentle agitation for 30 min, washed with ice-cold PBS (2 x 1 mL) and re-suspended in 1.5 mL FACS buffer. The samples were analysed on a BD LSRFortessa cytometry system (excitation laser: 488 nm, fluorescence detection: 519 nm) and data were analysed using FlowJo, TreeStar Inc**.**

FACS analysis of BODIPY-GNF-onartuzumab

MKN-45 cells were harvested, washed with PBS and distributed in Eppendorf tubes (3 x 10^6 cells / vial) in FACS buffer (270 μL). For treatment of cells a solution of BODIPY-GNF-onartuzumab was prepared in FACS buffer with a protein concentration of 0.1 mg mL^{-1} (BODIPY-GNF concentration of 0.70 μg mL^{-1}). A solution of BODIPY-GNF was prepared in FACS buffer with a concentration of 0.70 μg mL^{-1}. For blocking cells were treated with pre-treated with 1 mg of onartuzumab and incubated at 0 ^{o}C for 30 mins before the addition of further solutions. To the prepared cells BODIPY-GNF-onartuzumab solution (30 μL), BODIPY-GNF solution (30 μL) or the control FACS buffer (30 μL) was added. Cells were incubated with gentle agitation for 30 min, washed with ice-cold PBS (2 x 1 mL) and re-suspended in 1.5 mL FACS buffer. The samples were analysed on a BD LSRFortessa cytometry system (excitation laser: 488 nm, fluorescence detection: 519 nm) and data were analysed using Flowjo, TreeStar Inc.

6.5.2 Conjugation of DFO-GNF (GNF-1) to trastuzumab

Synthesis of DFO-GNF-trastuzumab

To a solution of DFO-GNF (0.1 mg) in MES buffer (100 μL, 50 mM, pH6), EDC (0.60 mg, 1.93 μmol) and NHS (1.20 mg, 10.40 μmol) were added and the solution was mixed for 1.5 h. Pre-purified trastuzumab (0.60 mg) in PBS (800 μL) was added and the solution was mixed for 2.5 h. The reaction was then purified using PD10-SEC (PBS as eluent) by collecting the first 1.8 mL. The construct was further purified using 100 kDa spin filters (washing with 5 x H_2O, 14,000 g, 2 min).

Radiolabelling of DFO-GNF-trastuzumab with ^{89}Zr

To a solution of DFO-GNF-trastuzumab (0.50 mg, 180 μL), Zr^{4+} stock (10 μL, 4.94 MBq) was added and the reaction was incubated at 21 °C for 45 min at pH7. The sample was then purified using 100 kDa spin filters, a portion of the sample (3.99 MBq) was loaded onto the filter and washed with saline (5 x 400 μL, 3 min, 5500 RPM). The purified sample was then recovered (1.10 MBq) giving a RCY of 27.6 %, a RCP of 82% and a protein content (determined by BSA assay) of 0.46 ± 0 .02 mg mL^{-1}.

Lindmo assay using [^{89}Zr]ZrDFO-GNF-trastuzumab

SK-OV-3 cells were harvested and a 1:2 dilution series was performed (in triplicate) in DMEM media. The purified [^{89}Zr]ZrDFO-GNF-trastuzumab (100 ng of protein, 40 Bq) in PBS (100 μL) was added to each cell sample. To determine the non-specific binding, a fourth dilution series was prepared and a 1000-fold excess of cold trastuzumab (100 μg) was added 1 h prior to the addition of the radiotracer. Three samples of radiotracer were prepared to act as standards for the total activity added. Samples were incubated at 37 °C with gentle agitation for 2 h. The cells were then pelleted by centrifugation (2000 RPM, 3 min) and washed with ice-cold PBS (2 x 0.5 mL) whilst on ice. The radioactivity of the cell pellet was measured and the immunoreactive fraction was determined as the reciprocal y-intercept from the Lindmo transformation.

In vivo testing of [^{89}Zr]ZrDFO-GNF-trastuzumab

Small-animal PET imaging

As a pilot study, tumour uptake was investigated in a single mouse. A mouse was injected with cancer cells (2 x 10^6 SK-OV-3 cells) causing the development of a SK-OV-3 tumour with the volume of 113 mm^3 (n = 1 mouse). The tail of the mouse was warmed gently using a warm water bath immediately before administering [^{89}Zr]ZrDFO-GNF-trastuzumab (0.17 MBq, 140 μg of protein, in 200 μL sterile PBS) *via* intravenous (i.v.) tail-vein injection (*t* = 0 h). Images were obtained at 1 h, 6 h and 24 h before the animal was euthanised *via* isoflurane asphyxiation followed by terminal exsanguination.

Biodistribution studies

Following the final image at 24 h, the mouse was euthanised and biodistribution studies were performed. A total of 15 tissues (including the tumour) were removed, rinsed in water, dried in air for approx. 2 min., weighed and counted on a calibrated gamma counter for accumulation of activity. Count data were background- and decay-corrected, and the tissue uptake for each sample (determined in units of percentage injected dose per gram [%ID g^{-1}]) was calculated by normalisation to the total amount of activity injected into the animal.

6.5.3 Functionalisation of GNFs with DOTAGA(Gd) and DFO

Synthesis and characterization of GdDOTAGA-DFO-GNF

Scheme 6.20. Chemical synthesis of GdDOTAGA-PEG$_4$-NH$_2$, **29**.

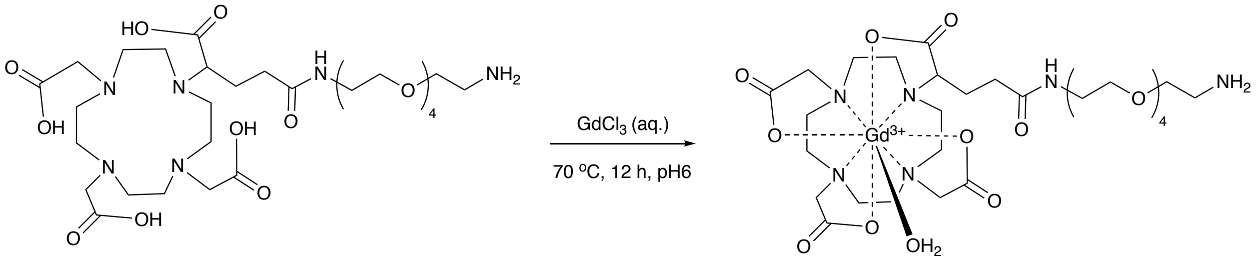

29

61%

Synthesis of compound **29**

DOTAGA-PEG$_4$-NH$_2$ (30 mg, 43 µmol) and $GdCl_3$ (28 mg, 75 µmol) were dissolved in water (1 mL) and heated at 70 °C for 12 h. The solvent was then removed *via* lyophilisation and the crude product was purified using semi-preparative HPLC (5-95% MeOH/H_2O) to obtain **29** as a white solid (61%, 22 mg, 26 µmol). HRMS (ESI+) (m/z): calculated for $C_{29}H_{52}GdN_6O_{13}^{2+}$ ($[M+2H]^{2+}$): 425.1411; found: 425.6454) (100%). RP-HPLC method: A flow rate of 1.0 mL min^{-1} with a linear gradient of A (distilled H_2O containing 0.1% TFA) and B (acetonitrile): *t* = 0 min, 95% A; *t* = 10 min, 5% A; *t* = 12 min, 5% A.

Figure 6.68. Characterisation data for compound **29**. **(A)** HR-ESI-MS data. (**B**) HPLC chromatogram at 220 nm.

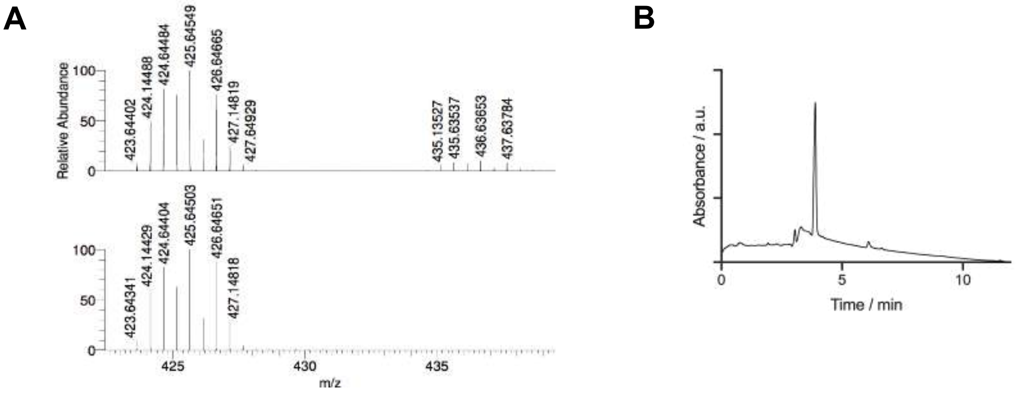

Synthesis of GdDOTAGA-DFO-GNF

GNFs (4 mg) in DMF (1 mL) and TEA (10 μL) were activated with HATU (8 mg, 0.01 mmol). Following the addition of **29** (1.30 mg, 1.52 μmol) and DFO mesylate (0.30 mg, 0.76 μmol) and the reaction was vortexed for 24 h. Solvent was removed under reduced pressure to obtain the crude product which was re-dissolved in water and the product was purified on silica gel (100% H_2O). After lyophilisation, GdDOTAGA-DFO-GNF was obtained as a brown solid (1.37 mg, 34% (mass yield)).

Figure 6.69. TLC separation of GNF constructs and starting materials. Silica gel as stationary phase and 100% H_2O as mobile phase (Visualisation of plates: V = visual observation, N = ninhydrin stain, UV = 254 nm).

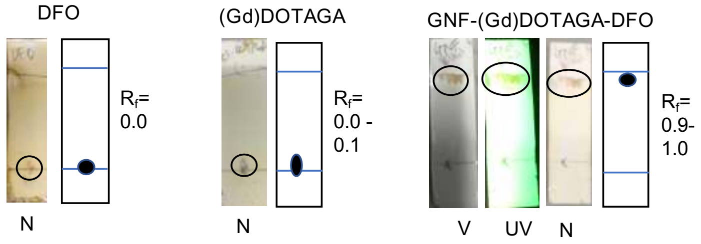

Quantification of DFO content

To a quantify the amount of DFO present on GNF flakes [^{68}Ga]GdDOTAGA-GaDFO-GNF was prepared. GNF-DOTAGA(Gd)-DFO samples were prepared at a variety of concentrations and buffered with NaOAc (0.2 M, pH 4.4). Aliquots of [^{68}Ga][Ga(H_2O)$_6$]Cl_3(aq.) stock solution (ca. 1.2 MBq) were added to each sample after 10 min radio-iTLC was used to determine a RCC. Plots were used in conjunction with the known molar activity of the generator to calculate the amount of DFO (nmol) per mass of GNF (mg) as 13.35 ± 1.78 nmol mg^{-1}.

Figure 6.71. Plot showing RCC when ^{68}Ga is titrated with varying concentrations of GdDOTAGA-DFO-GNF.

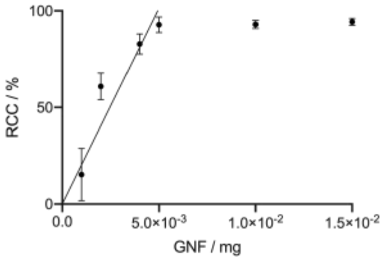

T₁ measurements

T_1 relaxation times for **29,** GdDOTAGA-GaDFO-GNF and GdDOTAGA-DFO-GNF-trastuzumab were measuredusing a Bruker AV-III 11.74 T 500 MHz NMR. By varying concentrations, the r_1 value could be obtained by calculating the gradient of the line when plotting concentration *vs.* $1/T_1$.

Figure 6.70. Reciprocal of T_1 relaxation times with changing concentration of **29**, GdDOTAGA-GaDFO-GNF and GdDOTAGA-DFO-GNF-trastuzumab.

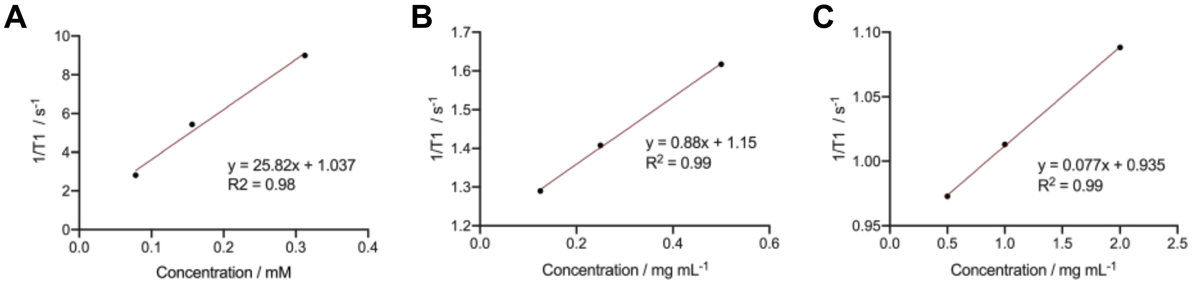

Radiolabelling of GdDOTAGA-DFO-GNF with ^{89}Zr

To a solution of GdDOTAGA-DFO-GNF (40 μg,40 μL), Zr^{4+} stock (10 μL, 6.16 MBq) was added and the reaction is incubated at 21 °C, pH7.9 for 10 min. The product ([^{89}Zr]GdDOTAGA-ZrDFO-GNF) was then characterised using radio-iTLC, PD10-SEC (PBS as eluent) and SEC-HPLC (PBS as eluent) to find a RCC of 97% and a RCP of 98%.

Synthesis of GdDOTAGA-DFO-GNF-trastuzumab

To a solution of GdDOTAGA-DFO-GNF (0.1 mg) in MES buffer (100 μL, 50 mM, pH6), EDC (0.6 mg, 1.93 μmol) and NHS (1.2 mg, 10.4 μmol) were added and the solution was mixed for 1.5 h. Trastuzumab (0.6 mg) in PBS (800 μL) was added and the solution was mixed for 2.5 h. The was then purified using PD10-SEC (PBS as eluent) by collecting the first 1.8 mL. The construct was further purified using 100 kDa spin filters (washing with 5 x H_2O, 14,000 g, 2 min).

Radiolabelling of GNF-DOTAGA(Gd)-DFO-trastuzumab

To a solution of GdDOTAGA-DFO-GNF-trastuzumab (,200 μL), $^{89}Zr^{4+}$ stock (50 μL, 31 MBq) was added and the reaction is incubated at r.t for 2 h at pH7.9. PD10-SEC analysis of the crude product indicated a RCP of 6.3 ± 2.2 % (*n* = 3). Reactions were purified using 100 kDa spin filters and washing with PBS (8 x 400 μL, 3 min, 14000 RPM). The purified sample was then recovered giving [^{89}Zr]GdDOTAGA-ZrDFO-GNF-trastuzumab in a RCY of 9.4 ± 4.5 % (*n* = 3) a RCP of 91.4 ± 1.4 % (*n* = 3). Following combination of reactions, the protein content was determined to be 8.36 ± 0.44 mg mL^{-1}.

Stability study

The stability of [^{89}Zr]GdDOTAGA-ZrDFO-GNF-trastuzumab a with respect to change in radiochemical purity due to loss of radioactivity from the protein fraction was investigated *in vitro*. An aliquot (5 μL) of the purified and formulated radiotracer was added to a solution of DTPA (pH7.1, 50 mM) giving a total reaction volume of 100 μL. The solution was incubated at 37 °C for 24 h and then analysed by radio-iTLC. The stability was monitored by quantifying the radioactivity associated with [^{89}Zr]GdDOTAGA-ZrDFO-GNF-trastuzumab (Elution volume: 0.0-2.0 mL) versus the amount bound to DTPA ([^{89}Zr]Zr-DTPA) (Elution volume 2.0 -8.0 mL). The RCP was found to be 84%.

Figure 6.72. Radioactive PD10-SEC profile of [^{89}Zr]GdDOTAGA-ZrDFO-GNF-trastuzumab following incubation with DTPA (50 mM, pH7.1, 24 h, 37 °C)

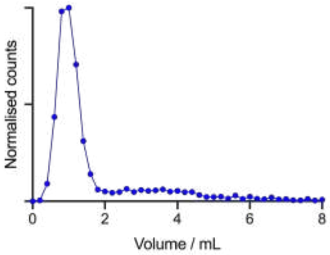

Lindmo assay with [^{89}Zr]GdDOTAGA-ZrDFO-GNF-trastuzumab

SK-OV-3 cells were harvested and a 1:2 dilution series was performed (in triplicate) in DMEM media. The purified [^{89}Zr]GdDOTAGA-ZrDFO-GNF-trastuzumab (100 ng of protein, 200 Bq) in PBS (100 μL) was added to each cell sample. To determine the non-specific binding, a fourth dilution series was prepared and a 1000-fold excess of cold trastuzumab (100 μg) was added 1 h prior to the addition of the radiotracer. Three samples of radiotracer alone were prepared to act as standards for the total activity added. Samples were incubated at 37 °C with gentle agitation for 3 h. The cells were then pelleted by centrifugation (2000 RPM, 3 min) and washed with ice-cold PBS (2 x 0.5 mL) whilst on ice. The radioactivity of the cell pellet was measured and the immunoreactive fraction was determined as the reciprocal y-intercept from the Lindmo transformation.

In vivo testing of [^{89}Zr]GdDOTAGA-ZrDFO-GNF-trastuzumab

Small-animal PET imaging

Mice were injected with cancer cells (2 x 10^6 SK-OV-3 cells) causing the development of a SK-OV-3 tumour with the volume of 192.5 ± 21.7 (*n* = 6 mouse). The tail of the mouse was warmed gently using a warm water bath immediately before administering [^{89}Zr]GdDOTAGA-ZrDFO-GNF-trastuzumab (0.11-0.14 MBq, 65-82 µg of mAb in 200 µL PBS) *via* intravenous (i.v.) tail-vein injection (*t* = 0 h). The blocking formulation contained an additional 15.4-fold (1 mg) of mAb. Images were obtained at 1, 14, 24, 48, 72 and 90 h before the animal was euthanised *via* isoflurane asphyxiation followed by terminal exsanguination.

Figure 6.73. PET images recorded following administration of [^{89}Zr]GdDOTAGA-ZrDFO-GNF-trastuzumab blocking formulation. Study performed in mice bearing SK-OV-3 tumours on the right flank.

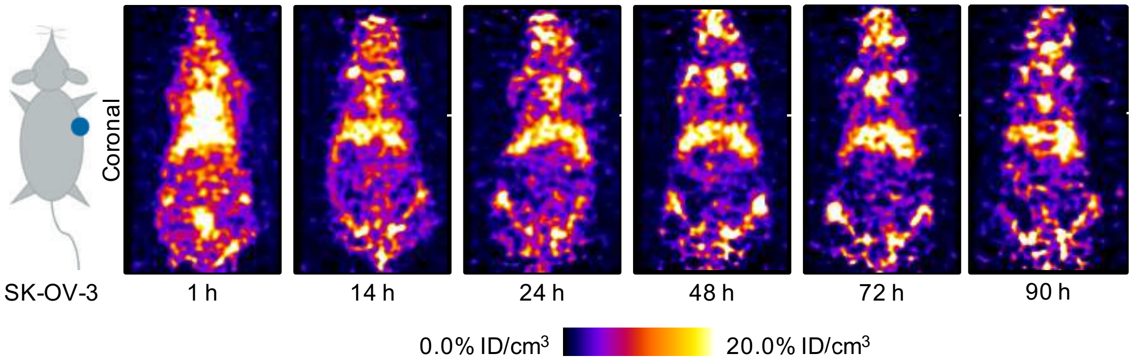

Biodistribution studies

Following the final image at 90 h, the mouse was euthanised and biodistribution studies were performed. A total of 15 tissues (including the tumour) were removed, rinsed in water, dried in air for approx. 2 min., weighed and counted on a calibrated gamma counter for accumulation of activity. Count data were background- and decay-corrected, and the tissue uptake for each sample (determined in units of percentage injected dose per gram [%ID g^{-1}]) was calculated by normalisation to the total amount of activity injected into the animal.

Table 6.8. *Ex vivo* biodistribution tissue uptake data measured at 90 h after i.v. administration of [^{89}Zr]GdDOTAGA-ZrDFO-GNF-trastuzumab (normal (*n* = 4) and blocking (*n* = 4) groups) in female athymic nude mice bearing subcutaneous SK-OV-3 tumours

Tissue	**[^{89}Zr]GdDOTAGA-ZrDFO-GNF-trastuzumab uptake normal group / %ID g^{-1} ± SEM**	**[^{89}Zr]GdDOTAGA-ZrDFO-GNF-trastuzumab uptake block group / %ID g^{-1} ± SEM**
Blood	0.84 ± 0.12	0.89 ± 0.07
Tumour	7.53 ± 0.83	4.21 ± 0.74
Heart	1.61 ± 0.41	1.44 ± 0.23
Lungs	1.36 ± 0.12	1.73 ± 0.13
Liver	20.87 ± 1.98	22.95 ± 1.90
Spleen	6.71 ± 1.34	11.89 ± 1.87
Stomach	0.56 ± 0.12	0.87 ± 0.13
Pancreas	1.07 ± 0.15	0.95 ± 0.12
Kidney	6.68 ± 0.60	8.18 ± 1.01
Sm. Int.	1.06 ± 0.19	1.34 ± 0.12
Large Int.	0.34 ± 0.05	0.61 ± 0.10
Fat	0.39 ± 0.15	0.41 ± 0.09
Muscle	0.56 ± 0.11	0.40 ± 0.05
Bone	10.02 ± 1.73	7.75 ± 2.36
Skin	2.40 ± 0.45	2.58 ± 0.68

Table 6.9. Tumour-to-tissue contrast ratio data extracted form biodistribution data following the administration of [^{89}Zr]GdDOTAGA-ZrDFO-GNF-trastuzumab (normal (*n* = 4) and blocking (*n* = 4) groups) in female athymic nude mice bearing subcutaneous SK-OV-3 tumours.

Tissue	**[^{89}Zr]GdDOTAGA-ZrDFO-GNF-trastuzumab normal group, tumour-to-tissue contrast ratio ± SEM**	**[^{89}Zr]GdDOTAGA-ZrDFO-GNF-trastuzumab block group, tumour-to-tissue contrast ratio ± SEM**
Blood	9.68 ± 1.53	5.13 ± 1.01
Tumour	1.00	1.00
Heart	6.08 ± 1.40	3.53 ± 0.60
Lungs	5.69 ± 0.70	2.62 ± 0.58
Liver	0.38 ± 0.06	0.19 ± 0.03
Spleen	1.32 ± 0.28	0.42 ± 0.17
Stomach	15.52 ± 3.09	6.13 ± 1.78
Pancreas	7.53 ± 1.00	5.14 ± 1.09
Kidney	1.15 ± 0.13	0.58 ± 0.11
Sm. Int.	8.22 ± 1.53	3.32 ± 0.53
Large Int.	27.50 ± 1.57	8.24 ± 1.07
Fat	34.28 ± 12.02	13.72 ± 2.25
Muscle	15.47 ± 2.89	10.08 ± 1.46
Bone	0.69 ± 0.18	0.75 ± 0.21
Skin	2.85 ± 0.55	3.15 ± 0.16

Figure 6.74. Tumour-to-tissue contrast ratios derived from the biodistribution data.

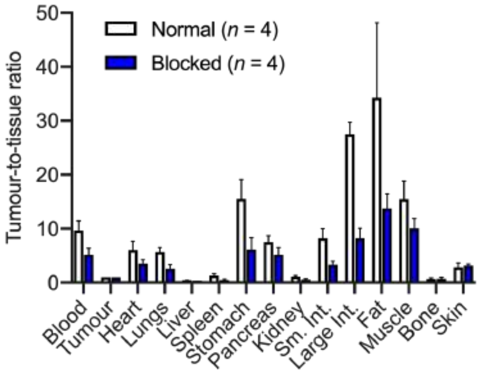

Bibliography

1 World Health Organisation, *Press release no. 263: Latest global cancer data*, 2018.

2 J. Ferlay, M. Ervik, F. Lam, M. Colombet, L. Mery, M. Piñeros, A. Znaor, I. Soerjomataram and F. Bray, Global Cancer Observatory: Cancer Tomorrow. Lyon, France: International Agency for Research on Cancer., https://gco.iarc.fr/tomorrow, (accessed 9 February 2020).

3 C. Mathers, G. A. Stevens, W. R. Mahanani, D. M. Fat and D. Hogan, *WHO methods and data sources for country-level causes of death*, 2018.

4 NCI biomarker definition, https://www.cancer.gov/publications/dictionaries/cancer-terms/def/biomarker, (accessed 15 February 2020).

5 J. A. Ludwig and J. N. Weinstein, *Nat. Rev. Cancer*, 2005, **5**, 845–856.

6 C. L. Sawyers, *Nat. Publ. Gr.*, 2008, **452**, 548–552.

7 G. A. Ulaner, C. C. Riedl, M. N. Dickler, K. Jhaveri, N. Pandit-taskar and W. Weber, *J. Nucl. Med.*, 2016, **57**, 53–60.

8 J. Ferlay, M. Colombet, I. Soerjomataram, T. Dyba, G. Randi, M. Bettio, A. Gavin, O. Visser and F. Bray, *Eur. J. Cancer*, 2018, **103**, 356–387.

9 W. J. Catalona, D. S. Smith, T. L. Ratliff, K. M. Dodds, D. E. Coplen, J. J. Yuan, J. A. Petros and G. L. Andriole, *N. Engl. J. Med.*, 1991, **324**, 1156–1161.

10 M. K. Samplaski, W. Heston, P. Elson, C. Magi-Galluzzi and D. E. Hansel, *Mod. Pathol.*, 2011, **24**, 1521–1529.

11 B. T. Ristau, D. S. O'Keefe and D. J. Bacich, *Urol. Oncol.*, 2014, **32**, 272–279.

12 C. Barinka, P. Šácha, J. Sklenár, P. Man, K. Bezouška, B. S. Slusher and J. A. N. Konvalinka, *Protein Sci.*, 2004, **13**, 1627–1635.

13 W. D. W. Heston, *Urology*, 1997, **49**, 104–112.

14 A. Ghosh and W. D. W. Heston, *J. Cell. Biochem.*, 2004, **91**, 528–539.

15 N. Tan, N. Bavadian, J. Calais, U. Oyoyo, J. Kim, I. B. Turkbey, E. Mena and M. S. Davenport, *J. Urol.*, 2019, **202**, 231–240.

16 D. A. Silver, I. Pellicer, W. R. Fair, W. D. Heston and C. Cordon-Cardo, *Clin. Cancer Res.*, 1997, **3**, 81–85.

17 J. L. Kasperzyk, S. P. Finn, R. Flavin, M. Fiorentino, R. Lis, W. K. Hendrickson, S. K. Clinton, H. D. Sesso, L. Edward, M. J. Stampfer, M. Loda and L. A. Mucci, *Cancer Epidemiol Biomarkers Prev.*, 2013, **22**, 2354–2363.

18 R. Sokoloff, K. C. Norton, C. L. Gasior, K. M. Marker and L. S. Grauer, *Prostate*, 2000, **43**, 150–157.

19 J. R. Mesters, C. Barinka, W. Li, T. Tsukamoto, P. Majer, B. S. Slusher, J. Konvalinka and R. Hilgenfeld, *Eur. Mol. Biol. Organ.*, 2006, **25**, 1375–1384.

20 M. I. Davis, M. J. Bennett, L. M. Thomas and P. J. Bjorkman, *PNAS*, 2005, **102**, 5981–5986.

21 C. Barinka, M. Rovenska, P. Mlcochovà, K. Hlouchova, A. Plechanovovà, P. Majer, T. Tsukamoto, B. S. Slusher, J. Konvalinka and J. Lubkowski, *J. Med. Chem.*, 2007, **50**, 3267–3273.

22 C. Barinka, J. Starkova, J. Konvalinka and J. Lubkowski, *Acta Cryst.*, 2007, **63**, 150–153.

23 V. Klusák, C. Bařinka, A. Plechanovová, P. Mlčochová, J. Konvalinka, L. Rulíšek and J. Lubkowski, *Biochemistry*, 2009, **48**, 4126–4138.

24 C. Barika, C. Rojas, B. Slusher and M. Pomper, *Curr. Med. Chem.*, 2012, **19**, 856–870.

25 T. Wüstemann, W. Mier, U. Haberkorn and J. Babich, *Med. Res. Rev.*, 2019, **39**, 40–69.

26 P. F. Jackson, D. C. Cole, B. S. Slusher, S. L. Stetz, L. E. Ross, B. A. Donzanti and D. A. Trainor, *J. Med. Chem.*, 1996, **39**, 619–622.

27 D. Vitharana, J. E. France, D. Scarpetti, G. W. Bonneville, P. Majer and T. Tsukamoto, *Tetrahedron: Asymmetry*, 2002, **13**, 1609–1614.

28 S. Son, H. Kwon, H. Ahn, H. Nam, K. Kim, S. Nam, D. Choi, H. Ha, I. Minn and Y. Byun, *Bioorg. Med. Chem. Lett.*, 2020, **30**, 126894.

29 H. F. Schmitthenner, D. E. Dobson, K. G. Jones, N. Akporji, D. Q. M. Soika, K. L. Nastiuk and J. P. Hornak, *Chem. Eur. J.*, 2019, **25**, 13848–13854.

30 Y. Chen, C. A. Foss, Y. Byun, S. Nimmagadda, M. Pullambhatla, J. J. Fox, M. Castanares, S. E. Lupold, J.

W. Babich, R. C. Mease and M. G. Pomper, *J. Med. Chem.*, 2008, **51**, 7933–7943.

31 M. L. T. Cossio, L. F. Giesen, G. Araya, M. L. S. Pérez-Cotapos, R. L. VERGARA, M. Manca, R. A. Tohme, S. D. Holmberg, T. Bressmann, D. R. Lirio, J. S. Román, R. G. Solís, S. Thakur, S. N. Rao, E. L. Modelado, A. D. E. La, C. Durante, U. N. A. Tradición, M. En, E. L. Espejo, D. E. L. A. S. Fuentes, U. A. De Yucatán, C. M. Lenin, L. F. Cian, M. J. Douglas, L. Plata and F. Héritier, *Bioconjug. Chem.*, 2012, **23**, 81–87.

32 S. M. Hillier, K. P. Maresca, F. J. Femia, J. C. Marquis, C. A. Foss, N. Nguyen, C. N. Zimmerman, J. A. Barrett, W. C. Eckelman, M. G. Pomper, J. L. Joyal and J. W. Babich, *Cancer Res*, 2009, **69**, 6932–6941.

33 S. S. Chang, *Rev. Urol.*, 2004, **6**, S13-8.

34 H. Liu, P. Moy, S. Kim, Y. Xia, A. Rajasekaran, V. Navarro, B. Knudsen and N. H. Bander, *Adv. Br.*, 1997, **57**, 3629–3634.

35 J. Wu, D. Han, S. Shi, Q. Zhang, G. Zheng, M. Wei, Y. Han, G. Li, F. Yang, D. Jiao, P. Xie, L. Zhang, A.-G. Yang, A. Zhao, W. Qin and W. Wen, *Mol. Cancer Ther.*, 2019, **18**, 1289–1302.

36 S. S. Chang, V. E. Reuter, W. D. W. Heston, N. H. Bander, L. S. Grauer and P. B. Gaudin, *Cancer Res.*, 1999, **59**, 3192–3198.

37 S. T. Tagawa, S. Vallabhajosula, Y. Jhanwar, K. V Ballman, A. Hackett, L. Emmerich, J. Babich, A. O. Sartor, L. C. Harshman, H. Beltran, A. M. Molina, D. M. Nanus and N. H. Bander, *J. Clin. Oncol.*, 2018, **36**, 399.

38 M. I. Milowsky, D. M. Nanus, L. Kostakoglu, S. Vallabhajosula, S. J. Goldsmith and N. H. Bander, *J. Clin. Oncol.*, 2004, **22**, 2522–2531.

39 S. T. Tagawa, M. I. Milowsky, M. Morris, S. Vallabhajosula, N. P. Taskar, H. I. Scher, N. H. Bander and D. M. Nanus, *Clin. Cancer Res.*, 2013, **19**, 5182–5191.

40 N. Pandit-taskar, J. A. O. Donoghue, J. C. Durack, S. K. Lyashchenko, S. M. Cheal, V. Beylergil, R. A. Lefkowitz, J. A. Carrasquillo, D. F. Martinez, A. M. Fung, S. B. Solomon, G. Heller, M. Loda, D. M. Nanus, S. T. Tagawa, J. L. Feldman, J. R. Osborne, J. S. Lewis, V. E. Reuter, W. A. Weber, N. H. Bander, H. I. Scher, S. M. Larson and M. J. Morris, *Clin. Cancer Res.*, 2015, **21**, 5277–5286.

41 D. J. George, M. R. McDevitt, E. Barendswaard, D. Ma, L. Lai, M. J. Curcio, G. Sgouros, A. M. Ballangrud, W. H. Yang, R. D. Finn, V. Pellegrini, J. Geerlings, M. Lee, M. W. Brechbiel, N. H. Bander, C. Cordon-Cardo and D. A. Scheinberg, *Prostate J.*, 2000, **3**, 1.

42 M. Eder, M. Eisenhut, J. Babich and U. Haberkorn, *Eur. J. Nucl. Med. Mol. Imaging*, 2013, **40**, 819–823.

43 C. Barinka, Y. Byun, C. L. Dusich, S. R. Banerjee, Y. Chen, M. Castanares, A. P. Kozikowski, R. C. Mease, M. G. Pomper and J. Lubkowski, *J. Med. Chem.*, 2008, **51**, 7737–7743.

44 D. J. Slamon, G. M. Clark, S. G. Wong, W. J. Levin, A. Ullrich and W. L. Mcguire, *Science*, 1987, **235**, 177–182.

45 M. L. Disis and K. Schiffman, *Semin. Oncol.*, 2001, **28**, 12–20.

46 N. E. Hynes and H. A. Lane, *Nat. Rev. Cancer*, 2005, **5**, 341–354.

47 J. Baselga, *Oncologist*, 2002, **7**, 2–8.

48 P. V Elizalde, R. I. C. Russo, M. F. Chervo and R. Schillaci, *Endocr. Rel. Can.*, 2016, **23**, 243–257.

49 A. Citri and Y. Yarden, *Nat .Rev. Mol. Cell Bio.*, 2006, **7**, 505–516.

50 D. Harari and Y. Yarden, *Oncogene*, 2000, **19**, 6102–6114.

51 J. Wang and B. Xu, *Signal Transduct. Target. Ther.*, 2019, **4**, 1–22.

52 C. L. Arteaga, M. X. Sliwkowski, C. K. Osborne, E. A. Perez, F. Puglisi and L. Gianni, *Nat. Clin. Oncol.*, 2012, **9**, 16–32.

53 M. C. Franklin, K. D. Carey, F. F. Vajdos, D. J. Leahy, A. M. de Vos and M. X. Sliwkowski, *Cancer Cell*, 2004, **5**, 317–328.

54 H. A. Burris, G. Giaccone, S.-A. Im, T. M. Bauer, D.-Y. Oh, S. F. Jones, J. L. Nordstrom, H. Li, D. A. Carlin, J. E. Baughman, R. J. Lechleider and Y.-J. Bang, *J. Clin. Oncol.*, 2015, **33**, 523.

55 J. Baselga, *Eur. J. Cancer J Can*, 2001, **37**, 18–24.

56 H. Cho, K. Mason, K. X. Ramyar and A. M. Stanley, *Nat. Publ. Gr.*, 2003, **421**, 756–760.

57 C. A. Hudis, *N. Engl. J. Med.*, 2007, **357**, 39–51.

58 J. Baselga and J. Albanell, *Ann. Oncol.*, 2001, **12**, S35–S41.

59 A. V. F. Massicano, B. V Marquez-nostra and S. E. Lapi, *Mol. Imaging*, 2018, **17**, 1–11.

60 M. J. W. D. Vosjan, L. R. Perk, G. W. M. Visser, M. Budde, P. Jurek, G. E. Kiefer and G. A. M. S. Van Dongen, *Nat. Protoc.*, 2010, **5**, 739–743.

61 E. C. Dijkers, J. G. Kosterink, A. P. Rademaker, L. R. Perk, G. A. van Dongen, J. Bart, J. R. De Jong, E. G. E. De Vries and M. N. L. Hooge, *J. Nucl. Med.*, 2009, **50**, 974–982.

62 M. A. Deri, S. Ponnala, P. Kozlowski, B. P. Burton-pye, H. T. Cicek, C. Hu, J. S. Lewis and L. C. Francesconi, *Bioconjug. Chem.*, 2015, **26**, 2579–2591.

63 M. Patra, S. Klingler, S. Larissa and J. P. Holland, *iScience*, 2019, **13**, 416–431.

64 G. A. Ulaner, D. M. Hyman, D. S. Ross, A. Corben, S. Chandarlapaty, S. Goldfarb, H. Mcarthur, J. P. Erinjeri, S. B. Solomon, H. Kolb, S. K. Lyashchenko, J. S. Lewis and J. A. Carrasquillo, *J. Nucl. Med.*, 2016, **57**, 1523–1529.

65 E. C. Dijkers, T. H. O. Munnink, J. G. Kosterink, A. H. Brouwers, P. L. Jager and J. R. De Jong, *Clin. Pharmacol. Ther.*, 2010, **87**, 586–592.

66 G. Gebhart, L. E. Lamberts, Z. Wimana, C. Garcia, P. Emonts, L. Ameye, S. Stroobants, M. Huizing, P. Aftimos, J. Tol, W. J. G. Oyen, D. J. Vugts, O. S. Hoekstra, C. P. Schröder, C. W. Menke-van der Houven van Oordt, T. Guiot, A. H. Brouwers, A. Awada, E. G. E. de Vries and P. Flamen, *Ann. Oncol.*, 2016, **27**, 619–624.

67 G. A. Ulaner, D. M. Hyman, S. K. Lyashchenko, J. S. Lewis and J. A. Carrasquillo, *Clin. Nucl. Med.*, 2017, **42**, 912–917.

68 B. Peruzzi and D. P. Bottaro, *Clin. Cancer Res.*, 2006, **12**, 3657–3661.

69 K. M. Weidner, N. Arakakit, G. Hartmann, J. Vandekerckhove, S. Weingart, H. Rieder, C. Fonatsch, H. Tsubouchi, T. Hishida, Y. Daikuharat and W. Birchmeier, *Proc. Natl. Acad. Sci. USA*, 1991, **88**, 7001–7005.

70 G. Maulik, A. Shrikhande, T. Kijima, P. C. Ma, P. T. Morrison and R. Salgia, *Cytokine Growth Factor Rev.*, 2002, **13**, 41–59.

71 V. S. Hughes and D. W. Siemann, *Trends Cancer.*, 2018, **4**, 94–97.

72 H. Y. Zou, Q. Li, J. H. Lee, M. E. Arango, S. R. Mcdonnell, S. Yamazaki, T. B. Koudriakova, G. Alton, J. J. Cui, P. Kung, M. D. Nambu, G. Los, S. L. Bender, B. Mroczkowski and J. G. Christensen, *Cancer Res.*, 2007, **67**, 4408–4418.

73 H. Luo, H. Hong, M. R. Slater, S. A. Graves, S. Shi, Y. Yang, R. J. Nickles, F. Fan and W. Cai, *J. Nucl. Med.*, 2015, **56**, 758–764.

74 D. R. Spigel, M. J. Edelman, K. O. Byrne, L. Paz-ares, S. Mocci, S. Phan, D. S. Shames, D. Smith, W. Yu, V. E. Paton and T. Mok, *J. Clin. Oncol.*, 2017, **35**, 412–420.

75 E. M. Jagoda, L. Lang, V. Bhadrasetty, S. Histed, M. Williams, G. Kramer-marek, E. Mena, L. Rosenblum, J. Marik, J. N. Tinianow, M. Merchant, L. Szajek, C. Paik, F. Cecchi, K. Raffensperger, D. P. Bottaro and P. Choyke, *J. Nucl. Med.*, 2012, **53**, 1592–1601.

76 R. Weissleder, *Science*, 2006, **312**, 1168–1172.

77 D. Mankoff, *J. Nucl. Med.*, 2007, **48**, 18.

78 J. D. Wagner, D. S. Schauwecker, D. Davidson, S. Wenck, S. H. Jung and G. Hutchins, *J. Surg. Oncol.*, 2001, **77**, 237–242.

79 V. Ambrosini, S. Nicolini, P. Caroli, C. Nanni, A. Massaro, M. C. Marzola, D. Rubello and S. Fanti, *Eur. J. Radiol.*, 2012, **81**, 988–1001.

80 M. E. Seaman, G. Contino, N. Bardeesy and K. Kimberly, *Expert Rev. Mol. Med.*, 2011, **12**, 1–24.

81 J. P. Holland, *Chimia (Aarau).*, 2016, **70**, 787–795.

82 P. Oehr, H.-J. Biersack and E. Coleman, *PET and PET-CT in Oncology*, 2004.

83 G. B. Saha, *Basics of PET Imaging*, Springer Science, 2005.

84 C. L. Melcher, *J. Nucl. Med,* 2000, **41**, 1051–1056.

85 A. Nassalski, M. Kapusta, T. Batsch, D. Wolski, D. Möckel, W. Enghardt and M. Moszyński, *IEEE*, 2005, 2823–2829.

86 H. Zhang, N. T. Vu, Q. Bao, R. W. Silverman, B. N. Berry-Pusey, A. Douraghy, D. A. Williams, F. R. Rannou, D. B. Stout and A. F. Chatziioannou, *IEEE Trans Nucl. Sci.*, 2010, **57**, 1038–1044.

87 R. E. Schmitz, A. M. Alessio and P. E. Kinahan, *The Physics of PET / CT scanners*, 2019.

88 T. K. Lewellen, *Phys. Med. Biol.*, 2008, **53**, 287–317.

89 T. G. Turkington, *J. Nucl. Med. Technol.*, 2001, **29**, 1–8.

90 F. A. Mettler and M. J. Guiberteau, *Essentials of Nuclear Medicine Imaging*, 2012.

91 M. F. Kijewski, *Positron Emission Tomography (PET) and Single-Photon Emission Computed Tomography (SPECT) Physics*, 2016.

92 P. Zanzonico, *Semin. Nucl. Med.*, 2004, **34**, 87–111.

93 L. L. Corrigan, *EANM Technolgists Guide - Radiopharmacy: An update*, 2019.

94 T. Ido, C. Wan, V. Casella, J. Fowler, A. Wolf, M. Reivich and D. Kuhl, *J. Label. Compd. Radiopharm.*, 1978, **14**, 175–183.

95 K. Hamacher, H. H. Coenen and G. Stocklin, *J. Nucl. Med.*, 1986, **27**, 235–239.

96 J. S. Fowler and T. Ido, *Semin. Nucl. Med.*, 2002, **32**, 6–12.

97 A. Rahmim, M. A. Lodge, N. A. Karakatsanis, V. Y. Panin, Y. Zhou, A. Mcmillan, S. Cho, H. Zaidi, M. E. Casey and R. L. Wahl, *Eur. J. Nucl. Med. Mol. Imaging*, 2018, **46**, 501–518.

98 I. Human, T. Xenogrcrfts, P. Tomography, R. L. Wahl, G. D. Hutchins, D. J. Buchsbaum, M. Liebert, H. B. Grossman and S. Fisher, *Cancer*, 1991, **67**, 1544–1550.

99 R. R. Edelman, *Radiology*, 2014, **273**, 181–200.

100 T. Ai, J. N. Morelli, X. Hu, D. Hao, F. L. Goerner, B. Ager and V. M. Runge, *Invest. Radiol.*, 2012, **47**, 725–740.

101 E. E. DeLange and John P Mugler, *Essentials of body MRI. Ch1-Basic MR physics*, 2012.

102 G. B. Chavhan, P. S. Babyn, B. Thomas, M. M. Shroff and E. M. Haacke, *RadioGraphics*, 2009, **29**, 1434–1449.

103 E. L. Hahn, *Phys. Rev.*, 1950, **80**, 580–564.

104 D. B. Plews, *RadioGraphics*, 1994, **14**, 1389–1404.

105 R. A. Pooley, *RadioGraphics*, 2005, **25**, 1087–1099.

106 A. O. Rodriguez, *Rev. Mex. Fis.*, 2004, **50**, 272–286.

107 E. F. Jackson, L. E. Ginsberg, D. F. Schemer and N. E. Leeds, *Surg. Neurol.*, 1997, **3019**, 185–199.

108 R. Bitar, G. Leung, R. Perng, S. Tadros, A. R. Moody, J. Sarrazin, C. McGregor, M. Christakis, S. Symons, A. Nelson and T. P. Roberts, *RadioGraphics*, 2006, **26**, 513–537.

109 F. Mattrey, *Prog. Radiol.*, 1989, **152**, 247–252.

110 E. A. Tanifum, C. Pate, M. E. Liaw, R. G. Pautler and A. V Annapragada, *Nat. Sci. Reports*, 2018, **8**, 1–8.

111 D. Pan, A. H. Schmieder, S. A. Wickline and G. M. Lanza, *Tetrahedron*, 2011, **67**, 8431–8444.

112 P. Hermann, V. Kubicek, J. Kotek and I. Luke, *Dalt. Trans.*, 2008, **9226**, 3027–3047.

113 H.-J. Weinmann, R. C. Brasch, W. R. Press and G. E. Wesbey, *AJR*, 1984, **142**, 619–624.

114 E. L. Que and C. J. Chang, *Chem. Soc. Rev.*, 2010, **39**, 51–60.

115 K. N. Raymond and V. C. Pierre, *Bioconjug. Chem.*, 2005, **16**, 3–8.

116 H. Bin Na, I. C. Song and T. Hyeon, *Adv. Mater.*, 2009, **744**, 2133–2148.

117 K. M. Krishnan, *IEEE Trans. Magn.*, 2010, **46**, 2523–2558.

118 M. G. Harisinghani, J. Barentsz, P. F. Hahn, W. M. Deserno, S. Tabatabaei and R. Weissleder, *N. Engl. J. Med.*, 2003, **348**, 2491–2499.

119 Y. Jun, Y. Huh, J. Choi, J. Lee, H. Song, S. Kim, S. Yoon, K. Kim, J. Shin, J. Suh and J. Cheon, *J. Am. Chem. Soc.*, 2005, **127**, 5732–5733.

120 G. Kandasamy and D. Maity, *Int. J. Pharm.*, 2015, **496**, 191–218.

121 W. Baaziz, B. P. Pichon, S. Fleutot, Y. Liu, C. Lefevre, J. Greneche, M. Toumi, T. Mhiri and S. Begin-colin, *J. Phys. Chem. C*, 2014, **118**, 3795–3810.

122 B. H. Kim, N. Lee, H. Kim, K. An, Y. Il Park, Y. Choi, K. Shin, Y. Lee, S. G. Kwon, H. Bin Na, J. Park, T. Ahn, Y. Kim, W. K. Moon, S. H. Choi and T. Hyeon, *J. Am. Chem. Soc.*, 2011, **133**, 12624–12631.

123 M. W. Marashdeh, B. Ababneh, O. M. Lemine, A. Alsadig, K. Omri, L. El Mir, A. Sulieman and E. Mattar, *Results Phys.*, 2019, **15**, 102651.

124 A. Alipour, Z. Soran-erdem, M. Utkur, V. K. Sharma, O. Algin, E. U. Saritas and H. V. Demir, *Magn. Reson. Imaging*, 2018, **49**, 16–24.

125 Y. C. Park, J. B. Smith, T. Pham, R. D. Whitaker, C. A. Sucato, J. A. Hamilton, E. Bartolak-suki and J. Y.

Wong, *Colloids Surfaces B Biointerfaces*, 2014, **119**, 106–114.
126 D. Evanko, *Nat. Methods*, 2008, **5**, 377.
127 R. F. Muzic and F. P. Difilippo, *Semin. Roentgenol*, 2014, **49**, 242–254.
128 M. S. Judenhofer, H. F. Wehrl, D. F. Newport, C. Catana, S. B. Siegel, M. Becker, A. Thielscher, M. Kneilling, M. P. Lichy, M. Eichner, K. Klingel, G. Reischl, R. E. Nutt, K. Uludag, S. R. Cherry, S. Widmaier, M. Ro, C. D. Claussen and B. J. Pichler, *Nat. Med.*, 2008, **14**, 459–465.
129 S. A. Esfahani, S. Salcedo, P. Heidari, O. A. Catalano, R. Pauplis, J. F. Kronauge and U. Mahmood, *Am. J. Nucl. Med. Mol. Imaging*, 2017, **7**, 53–62.
130 C. Spick, K. Herrmann and J. Czernin, *J. Nucl. Med.*, 2016, **57**, 420–431.
131 T. A. Hope, M. H. Pampaloni, E. Nakakura, H. Vanbrocklin, J. Slater, S. Jivan, C. M. Aparici, J. Yee and E. Bergsland, *Abdom. Imaging*, 2015, **40**, 1432–1440.
132 L. Frullano, C. Catana, T. Benner, A. D. Sherry and P. Caravan, *Angew. Chemie - Int. Ed.*, 2010, **49**, 2382–2384.
133 X. Shi and L. Shen, *J. Inorg. Biochem.*, 2018, **186**, 257–263.
134 C. Yang, K. K. Ghosh, P. Padmanabhan, O. Langer, J. Liu, D. Ng, C. Eng, C. Halldin and B. Gulyás, *Theranostics*, 2018, **8**, 6210–6232.
135 G. Frielander, J. W. Kennedy, E. S. Maciacs and J. M. Miller, *Nuclear and Radiochemistry*, 1981.
136 K. H. Lieser, *Nuclear and Radiochemistry*, .
137 W. A. Volkert and T. J. Hoffman, *Chem. Rev.*, 1999, **99**, 2269–2292.
138 C. J. Anderson and M. J. Welch, *Chem. Rev.*, 1999, **99**, 2219–2234.
139 X. Sun and C. J. Anderson, *Methods Enzymol.*, 2004, **386**, 237–261.
140 D. A. Scheinberg and M. R. Mcdevit, *Curr. Radiopharm.*, 2011, **4**, 306–320.
141 D. Van Der Born, A. Pees, A. J. Poot, A. D. Windhorst and D. J. Vugts, *Chem. Soc. Rev.*, 2017, **46**, 4709–4773.
142 M. A. Deri, B. M. Zeglis, L. C. Francesconi and J. S. Lewis, *Nucl Med Biol.*, 2013, **40**, 3–14.
143 S. M. Qaim, *Radiochim. Acta*, 2001, **89**, 297–302.
144 M. Dahlbom, *Physics of PET and SPECT Imaging.*, 2017.
145 S. R. Banerjee and M. G. Pomper, *Appl. Radiat. Isot.*, 2013, **0**, 2–13.
146 E. Schönfeld, Ga-68 Data sheet, http://www.nucleide.org/DDEP_WG/Nuclides/Ga-68_tables.pdf, (accessed 8 April 2020).
147 F. Roesch and P. J. Riss, *Curr. Top. Med. Chem.*, 2010, 1633–1668.
148 F. Roesch, *Appl. Radiat. Isot.*, 2013, **24**, 24–30.
149 F. Roesch, *Curr. Radiopharm.*, 2012, **5**, 202–211.
150 P. Brisset and G. U. Din, *Radiotracer Generators for Industrial Applications*, 2013.
151 M. Fani, J. P. André and H. R. Maecke, , DOI:10.1002/cmmi.232.
152 A. Koers, D. J. Berry, Y. Ma, J. R. Ballinger, R. Tavare, K. Sunassee, T. Zhou, S. Nawaz, G. E. D. Mullen, C. Hider and P. J. Blower, *Chem. Commun.*, 2011, **47**, 7068–7070.
153 M. I. Tsionou, C. E. Knapp, C. A. Foley, C. R. Munteanu, A. Cakebread, C. Imberti, T. R. Eykyn, J. D. Young, B. M. Paterson, P. J. Blower and M. T. Ma, *RSC Adv.*, 2017, **7**, 49586–49599.
154 J. Šimeček, O. Zemek, P. Hermann, O. Notni and H.-J. Wester, *Mol. Pharm.*, 2014, **11**, 3893–3903.
155 A. Evers, R. D. Hancock, A. E. Martell and R. J. Motekaitis, *Inorg. Chem.*, 1989, **27**, 2189–2195.
156 Jean-Francois and E. Toth, *Inorg. Chem.*, 2011, **50**, 10371–10378.
157 A. L. Nichols, Zr-89 data sheet, http://www.nucleide.org/DDEP_WG/Nuclides/Zr-89_tables.pdf, (accessed 8 April 2020).
158 Y. Zhang, H. Hong and W. Cai, *Curr Radiopharm.*, 2011, **4**, 131–139.
159 A. Kasbollah, P. Eu, S. Cowell and P. Deb, *J. Nucl. Med. Technol.*, 2013, **41**, 35–42.
160 S. A. Gravesa, C. Kutyreffb, K. E. Barrettb, R. Hernandezc, P. A. Ellisonb, S. Happeld, E. Aluicio-Sarduyb, T. E. Barnhartb, R. J. Nickles and and J. W. Engleb, *Nucl Med Biol.*, 2018, **64**, 1–7.
161 J. P. Holland, *Inorg. Chem.*, 2020, **59**, 2070–2082.
162 J. P. Holland, V. Divilov, N. H. Bander, P. M. Smith-Jones, S. M. Larson and J. S. Lewis, *J. Nucl. Med.*, 2010, **51**, 1293–1300.

163 J. R. Dilworth and S. I. Pascu, *Chem. Soc. Rev.*, 2018, **47**, 2554–2571.
164 B. Gutfilen, S. A. L. Souza and G. Valentini, *Drug Des. Devel. Ther.*, 2018, **12**, 3235–3245.
165 J. S. Lewis, R. Laforest, T. L. Buettner, S. Song, Y. Fujibayashi, J. M. Connett and M. J. Welch, *PNAS*, 2000, **98**, 1206–1211.
166 B. A. Gingras, T. Suprunchuk and C. H. Bayley, *Can. J. Chem.*, 1962, **40**, 1053–1059.
167 J. P. Holland, J. H. Giansiracusa, S. G. Bell, L.-L. Wong and J. R. Dilworth, *Phys. Med. Biol.*, 2009, **54**, 2103–2119.
168 R. I. Maurer, P. J. Blower, J. R. Dilworth, C. A. Reynolds, Y. Zheng and G. E. D. Mullen, *J. Med. Chem.*, 2002, **45**, 1420–1431.
169 R. G. Helmer, Cu-64 Data Sheet, http://www.nucleide.org/DDEP_WG/Nuclides/Cu-64_tables.pdf.
170 V. P. Chechev, In-111 Data sheet, http://www.nucleide.org/DDEP_WG/Nuclides/In-111_tables.pdf, (accessed 8 April 2020).
171 M. Brom, L. Joosten, W. J. G. Oyen, M. Gotthardt and O. C. Boerman, *EJNMMI Res.*, 2012, **2**, 1–11.
172 S. Bhattacharyya and M. Dixit, *Dalt. Trans.*, 2011, **40**, 6112–6128.
173 M. Conti and L. Eriksson, *EJNMMI Phys.*, 2016, **3**, 1–17.
174 R. Feynman, *Eng. Sci. Mag.*, 1960, 22–36.
175 C. Toumey, *Nat. Publ. Gr.*, 2016, **11**, 306–307.
176 A. L. Porter and J. Youtie, *Nat. Nanotechnol.*, 2009, **4**, 534–536.
177 V. Wagner, A. Dullaart, A. Bock and A. Zweck, *Nat. Biotechnol.*, 2006, **24**, 1211–1217.
178 N. Fernandes, C. F. Rodrigues, A. F. Moreira and I. J. Correia, *Biomater. Sci.*, 2020, **8**, 2990–3020.
179 J. Conde, G. Doria and P. Baptista, *J. Drug Deliv.*, 2012, **2012**, 1–12.
180 N. Lee and T. Hyoen, *Chem. Soc. Rev.*, 2012, **41**, 2575–2589.
181 X. Huang and M. A. El-sayed, *J. Adv. Res.*, 2010, **1**, 13–28.
182 C. Shi, H. Yu, D. Sun, L. Ma, Z. Tang, Q. Xiao and X. Chen, *Acta Biomater.*, 2015, **18**, 68–76.
183 E. Boros, A. M. Bowen, L. Josephson and J. P. Holland, *Chem. Sci.*, 2015, **6**, 225–236.
184 S. E. McNeil, *WIREs Nanomedicine and Nanobiotechnology*, 2009, **1**, 264–271.
185 A. E. Nel, L. Mädler, D. Velegol, T. Xia, E. M. V. Hoek, P. Somasundaran, F. Klaessig, V. Castranova and M. Thompson, *Nat. Mater.*, 2009, **8**, 543–557.
186 H. Wang, C. A. Thorling, X. Liang, K. R. Bridle, Y. Zhu, D. H. G. Crawford, P. Xu and M. S. Roberts, *J. Mater. Chem.*, 2015, **3**, 939–958.
187 E. Blanco, H. Shen and M. Ferrari, *Nat. Biotechnol.*, 2015, **33**, 941–951.
188 Y. Zhang, W. Poon, A. J. Tavares, I. D. Mcgilvray and W. C. W. Chan, *J. Control. Release*, 2016, **240**, 332–348.
189 G. V Lowry, R. J. Hill, S. Harper, A. F. Rawle, C. O. Hendren, F. Klaessig, U. Nobbmann, P. Sayre and J. Rumble, *Environ. Sci. Nano*, 2016, **3**, 953–965.
190 S. E. Mcneil, *Characterization of Nanoparticles Intended for Drug Delivery*, 2011.
191 C. M. Goodman, C. D. Mccusker, T. Yilmaz and V. M. Rotello, *Bioconjug. Chem.*, 2004, **15**, 897–900.
192 J. Lamb and J. P. Holland, *J. Nucl. Med.*, 2018, **59**, 382–390.
193 A. E. Nel, L. Mädler, D. Velegol, T. Xia, E. M. V Hoek, P. Somasundaran, F. Klaessig, V. Castranova and M. Thompson, *Nat. Mater.*, 2009, **8**, 543–557.
194 D. Kalyane, N. Raval, R. Maheshwari, V. Tambe, K. Kalia and R. K. Tekade, *Mater. Sci. Eng. C*, 2019, **98**, 1252–1276.
195 R. K. Jain and T. Stylianopoulos, *Nat. Publ. Gr.*, 2010, **7**, 653–664.
196 S. Goel, F. Chen, E. B. Ehlerding and W. Cai, *Small*, 2014, **10**, 3825–3830.
197 S. Guerrero, J. R. Herance, S. Rojas, J. F. Mena, J. D. Gispert, G. A. Acosta, F. Albericio and M. J. Kogan, *Bioconjug. Chem.*, 2012, **23**, 399–408.
198 R. Torres Martin de Rosales, R. Tavaré, A. Glaria, G. Varma, A. Protti and P. J. Blower, *Bioconjug. Chem.*, 2011, **22**, 455–465.
199 D. L. J. Thorek, D. Ulmert, N.-F. M. Diop, M. E. Lupu, M. G. Doran, R. Huang, D. S. Abou, S. M. Larson and J. Grimm, *Nat. Commun.*, 2014, **5**, 1–9.
200 M. Zhou, R. Zhang, M. Huang, W. Lu, S. Song, M. P. Melancon, M. Tian, D. Liang and C. Li, *J. Am.*

Chem. Soc. Chem Soc., 2010, **132**, 15351–15358.

201 O. Hahn, *Applied Radiochemistry*, 1936.

202 K. C. L. Black, Y. Wang, H. P. Luehmann, X. Cai, W. Xing, B. Pang, Y. Zhao, C. S. Cutler, L. V Wang, Y. Liu and Y. Xia, *ACS Nano*, 2014, **5**, 4385–4394.

203 Y. Wang, Y. Liu, H. Luehmann, X. Xia, D. Wan, C. Cutler and Y. Xia, *Nano Lett.*, 2013, **13**, 581–585.

204 Y. Yang, Y. Sun, T. Cao, J. Peng, Y. Liu, Y. Wu, W. Feng, Y. Zhang and F. Li, *Biomaterials*, 2013, **34**, 774–783.

205 J. Zeng, B. Jia, R. Qiao, C. Wang, L. Jing, F. Wang and M. Gao, *Chem. Commun.*, 2014, **50**, 2170–2172.

206 J. Pellico, J. Ruiz-Cabello, M. Saiz-Alía, G. del Rosario, S. Caja, M. Montoya, L. Fernández de Manuel, M. P. Morales, L. Gutiérrez, B. Galiana, J. A. Enríquez and F. Herranz, *Contrast Media Mol. Imaging*, 2016, **11**, 203–210.

207 L. Yang, G. Sundaresan, M. Sun, P. Jose, D. Hoffman, P. R. McDonagh, N. Lamichhane, C. S. Cutler, J. M. Perez, J. Zweit, X. Chen, U. Banin, A. M. Wu, R. Sinclair, S. Weiss and S. S. Gambhir, *J. Mater. Chem. B*, 2013, **1**, 1421.

208 W. Guo, X. Sun, O. Jacobson, X. Yan, K. Min, A. Srivatsan, G. Niu, D. O. Kiesewetter, J. Chang and X. Chen, *ACS Nano*, 2015, **9**, 488–495.

209 X. Sun, X. Huang, X. Yan, Y. Wang, J. Guo, O. Jacobson and D. Liu, *ACS Nano*, 2014, **8**, 8438–8446.

210 Y. Zhao, D. Sultan, L. Detering, S. Cho, G. Sun, R. Pierce, K. L. Wooley and Y. Liu, *Angew. Chemie - Int. Ed.*, 2014, **53**, 156–159.

211 R. M. Wong, D. A. Gilbert, K. Liu and A. Y. Louie, *ACS Nano*, 2012, **6**, 3461–3467.

212 M. Zhou, R. Zhang, M. Huang, W. Lu, S. Song, M. P. Melancon, M. Tian, D. Liang and C. Li, *J. Am. Chem. Soc.*, 2010, **132**, 15351–15358.

213 F. Chen, P. A. Ellison, C. M. Lewis, H. Hong, Y. Zhang, S. Shi, R. Hernandez, M. E. Meyerand, T. E. Barnhart and W. Cai, *Angew. Chemie - Int. Ed.*, 2013, **52**, 13319–13323.

214 R. Sharma, Y. Xu, S. W. Kim, M. J. Schueller, D. Alexoff, S. D. Smith, W. Wang and D. Schlyer, *Nanoscale*, 2013, **5**, 7476.

215 X. Cui, D. Mathe, N. Kovács, I. Horváth, M. Jauregui-Osoro, R. Torres Martin De Rosales, G. E. D. Mullen, W. Wong, Y. Yan, D. Krüger, A. N. Khlobystov, M. Gimenez-Lopez, M. Semjeni, K. Szigeti, D. S. Veres, H. Lu, I. Hernández, W. P. Gillin, A. Protti, K. K. Petik, M. A. Green and P. J. Blower, *Bioconjug. Chem.*, 2016, **27**, 319–328.

216 Y. Sun, M. Yu, S. Liang, Y. Zhang, C. Li, T. Mou, W. Yang, X. Zhang, B. Li, C. Huang and F. Li, *Biomaterials*, 2011, **32**, 2999–3007.

217 T. M. Shaffer, M. A. Wall, S. Harmsen, V. A. Longo, C. M. Drain, M. F. Kircher and J. Grimm, *Nano Lett.*, 2015, **15**, 864–868.

218 P. A. Ellison, F. Chen, S. Goel, T. E. Barnhart, R. J. Nickles, O. T. DeJesus and W. Cai, *ACS Appl. Mater. Interfaces*, 2017, **9**, 6772–6781.

219 S. Shi, C. Xu, K. Yang, S. Goel, H. F. Valdovinos, H. Luo, E. B. Ehlerding, C. G. England, L. Cheng, F. Chen, R. J. Nickles, Z. Liu and W. Cai, *Angew. Chemie - Int. Ed.*, 2017, **56**, 2889–2892.

220 S. Goel, F. Chen, S. Luan, H. F. Valdovinos, S. Shi, S. A. Graves, F. Ai, T. E. Barnhart, C. P. Theuer and W. Cai, *Adv. Sci.*, 2016, **3**, 1–11.

221 T. Liu, S. Shi, C. Liang, S. Shen, L. Cheng, C. Wang, X. Song, S. Goel, T. E. Barnhart, W. Cai, Z. Liu, S. Materials, S. N. Science, C. F. Materials, M. S. Program, M. Physics, U. States, W. Carbone and U. States, *ACS Nano*, 2015, **9**, 950–960.

222 R. Chakravarty, H. F. Valdovinos, F. Chen, C. M. Lewis, P. A. Ellison, H. Luo, M. E. Meyerand, R. J. Nickles and W. Cai, *Adv. Mater.*, 2014, **26**, 5119–5123.

223 K. P. Raven, A. Jain and R. H. Loeppert, *Environ. Sci.Technol.*, 1998, **32**, 344–349.

224 R. Torres Martin de Rosales, R. Tavaré, R. L. Paul, M. Jauregui-Osoro, A. Protti, A. Glaria, G. Varma, I. Szanda and P. J. Blower, *Angew. Chemie - Int. Ed.*, 2011, **50**, 5509–5513.

225 H. Lee, Z. Li, K. Chen, A. R. Hsu, C. Xu, J. Xie, S. Sun and X. Chen, *J. Nucl. Med.*, 2008, **49**, 1371–1379.

226 O. Clément, N. Siauve, C. A. Cuénod and G. Frija, *Top. Magn. Reson. Imaging*, 1998, **9**, 167—182.

227 S. Moon, B. Y. Yang, Y. J. Kim, M. K. Hong, Y. Lee, D. S. Lee, J. Chung and J. M. Jeong, *Nanomedicine*

Nanotechnology, Biol. Med., 2016, **12**, 871–879.

228 X. Yang, H. Hong, J. J. Grailer, I. J. Rowland, A. Javadi, S. A. Hurley, Y. Xiao, Y. Yang, Y. Zhang, R. J. Nickles, W. Cai, D. A. Steeber and S. Gong, *Biomaterials*, 2011, **32**, 4151–4160.

229 M. Yang, K. Cheng, S. Qi, H. Liu, Y. Jiang, H. Jiang, J. Li, K. Chen, H. Zhang and Z. Cheng, *Biomaterials*, 2013, **34**, 2796–2806.

230 S. Kim, M. K. Chae, M. S. Yim, I. H. Jeong, J. Cho, C. Lee and E. K. Ryu, *Biomaterials*, 2013, **34**, 8114–8121.

231 N. Gholipour, M. Akhlaghi, A. Mokhtari, P. Geramifar and D. Beiki, *Int. J. Biol. Macromol.*, 2020, **148**, 932–941.

232 B. P. Burke, N. Baghdadi, A. E. Kownacka, S. Nigam, G. S. Clemente, M. M. Al-yassiry, J. Domarkas, M. Lorch, M. Pickles, P. Gibbs, R. Tripier, C. Cawthorne and S. J. Archibald, *Nanoscale*, 2015, **7**, 14889–14896.

233 M. Brandt, J. Cardinale, I. Rausch and T. L. Mindt, *J. Label Compd. Radiopharm.*, 2019, **62**, 541–551.

234 C. M. Lewis, S. A. Graves, R. Hernandez, H. F. Valdovinos, T. E. Barnhart, W. Cai, M. E. Meyerand, R. J. Nickles and M. Suzuki, *Theranostics*, 2015, **5**, 227–239.

235 J. Zhu, H. Li, Z. Xiong, M. Shen, P. S. Conti, X. Shi and K. Chen, *ACS Appl. Mater. Interfaces*, 2018, **10**, 34954–34964.

236 Y. Zhan, E. B. Ehlerding, S. Shi, S. A. Graves, S. Goel, J. W. Engle, J. Liang and W. Cai, *J. Biomed. Nanotechnol.*, 2018, **14**, 900–909.

237 J.-L. Bridot, a.-C. Faure, S. Laurent, C. Riviere, C. Billotey, B. Hiba, M. Janier, V. Josserand, J.-L. Coll, L. VanderElst, R. Muller, S. Roux, P. Perriat and O. Tillement, *J. Am. Chem. Soc.*, 2007, **129**, 5076–5084.

238 F. Ai, S. Goel, Y. Zhan, H. F. Valdovinos, F. Chen, T. E. Barnhart and W. Cai, *Am. J. Transl. Res.*, 2016, **8**, 5591–5600.

239 R. Massart, *IEEE Trans. Magn.*, 1981, **17**, 1247–1248.

240 M. J. Williams, E. Sánchez, E. Aluri, F. Douglas, D. A. Maclaren, O. Collins, E. Cussen, J. Budge, L. Saunders, M. Michaelis, M. Smales, J. Cinatl Jr., S. Lorrio Gonzalez, D. Kruger, R. T. M. de Rosales and S. Corr, *RSC Adv.*, 2016, **6**, 83520–83528.

241 A. Spepi, C. Duce, C. Ferrari, J. González-Rivera, Z. Jagličić, V. Domenici, F. Pineider and M. R. Tiné, *RSC Adv.*, 2016, **6**, 104366–104374.

242 and G. L. Shouheng Sun, Hao Zeng, David B. Robinson, Simone Raoux, Philip M. Rice, Shan X. Wang, *J.Am.Chem.Soc.*, 2004, **126**, 273–279.

243 I. Karimzadeh, M. Aghazadeh, M. R. Ganjali, T. Doroudi and P. H. Kolivand, *J. Magn. Magn. Mater.*, 2017, **433**, 148–154.

244 R. A. Bini, R. F. C. Marques, F. J. Santos, J. A. Chaker and M. Jafelicci, *J. Magn. Magn. Mater.*, 2012, **324**, 534–539.

245 I. Djerdj, D. Arcon, Z. Jaglicic and M. Nedererberger, *J. Phys. Chem. C*, 2007, **111**, 3614–3623.

246 H. Bin Na, J. H. Lee, K. An, Y. Il Park, M. Park, I. S. Lee, D. H. Nam, S. T. Kim, S. H. Kim, S. W. Kim, K. H. Lim, K. S. Kim, S. O. Kim and T. Hyeon, *Angew. Chemie - Int. Ed.*, 2007, **46**, 5397–5401.

247 J. M. Rosenholm, R. M. Korpi, E. Lammentausta, S. Lehtonen, P. Lehenkari, R. Niemi, W. Xiao, J. Zhang, D. Lindberg, H. Gu, C. Sahlgren and R. Blanco Sequeiros, *Inorg. Chem. Front.*, 2015, **2**, 640–648.

248 R. Bazzi, M. A. Flores-Gonzalez, C. Louis, K. Lebbou, C. Dujardin, A. Brenier, W. Zhang, O. Tillement, E. Bernstein and P. Perriat, *J. Lumin.*, 2003, **102**–**103**, 445–450.

249 A. Akbarzadeh, R. Rezaei-sadabady, S. Davaran, S. W. Joo, N. Zarghami, Y. Hanifehpour, M. Samiei, M. Kouhi and K. Nejati-Koshki, *Nanoscale Res. Lett.*, 2013, **8**, 1–9.

250 J. Malinge, B. Géraudie, P. Savel, V. Nataf, A. Prignon, C. Provost, Y. Zhang, P. Ou, K. Kerrou, J.-N. Talbot, J.-M. Siaugue, M. Sollogoub and C. Ménager, *Mol. Pharm.*, 2017, **14**, 406–414.

251 D. S. Abou, D. L. J. Thorek, N. N. Ramos, M. W. H. Pinkse, H. T. Wolterbeek, S. D. Carlin, B. J. Beattie and J. S. Lewis, *Pharm. Res.*, 2013, **30**, 878–888.

252 A. R. Menjoge, R. M. Kannan and D. A. Tomalia, *Drug Discov. Today*, 2010, **15**, 171–185.

253 Y. Li, T. Lin, Y. Luo, Q. Liu, W. Xiao, W. Guo, D. Lac, H. Zhang, C. Feng, S. Wachsmann-hogiu, J. H. Walton, S. R. Cherry, D. J. Rowland, D. Kukis, C. Pan and K. S. Lam, *Nat. Commun.*, 2014, **5**, 4712.

254 H. Y. Mao, S. Laurent, W. Chen, O. Akhavan, M. Imani, A. A. Ashkarran and M. Mahmoudi, *Chem. Rev.*, 2013, **113**, 3407–3424.
255 S. Shi, K. Yang, H. Hong, H. F. Valdovinos, T. R. Nayak, Y. Zhang, C. P. Theuer, T. E. Barnhart, Z. Liu and W. Cai, *Biomaterials*, 2013, **34**, 3002–3009.
256 S. Jang, Y. Oh, A. T. E. Vilian, I. Lee, Y. Han, J. H. Park and C. Roh, *Int. J. Nanomedicine*, 2018, **13**, 221–234.
257 C. Xu, S. Shi, L. Feng, F. Chen, S. A. Graves, E. B. Ehlerding, S. Goel, H. Sun, C. G. England, R. J. Nickles, Z. Liu, A. Wang and W. Cai, *Nanoscale*, 2016, **8**, 12683–12692.
258 B. T. Cisneros, J. J. Law, M. L. Matson, A. Azhdarinia, E. M. Sevick-Muraca and L. J. Wilson, *Nanomedicine*, 2014, **9**, 2499–2509.
259 S. K. Smart, A. I. Cassady, G. Q. Lu and D. J. Martin, *Carbon N. Y.*, 2006, **44**, 1034–1047.
260 A. M. Schrand, H. Huang, C. Carlson, J. J. Schlager and O. Eiji, *J. Phys. Chem. B*, 2007, **111**, 2–7.
261 L. M. Manus, D. J. Mastarone, E. A. Waters, X. Q. Zhang, E. A. Schultz-Sikma, K. W. MacRenaris, D. Ho and T. J. Meade, *Nano Lett.*, 2010, **10**, 484–489.
262 S. Rojas, J. D. Gispert, R. Martin, S. Abad, C. Mench, D. Pareto, V. M. Vıctor, M. Alvaro, H. Garcıa and J. R. Herance, *ACS Nano*, 2011, **5**, 5552–5559.
263 J. Luo, J. D. Wilson, J. Zhang, J. I. Hirsch, H. C. Dorn, P. P. Fatouros and M. D. Shultz, *Appl. Sci.*, 2012, **2**, 465–478.
264 S. R. Kumar, S. Priyatharshni, V. N. Babu, D. Mangalaraj, C. Viswanathan, S. Kannan and N. Ponpandian, *J. Colloid Interface Sci.*, 2014, **436**, 234–242.
265 F. Chen, H. Hong, Y. Zhang, H. F. Valdovinos, S. Shi, G. S. Kwon, C. P. Theuer, T. E. Barnhart and W. Cai, *ACS Nano*, 2013, **7**, 9027–9039.
266 H. Zolata, H. Afarideh and F. Abbasi-Davani, *J. Radioanal. Nucl. Chem.*, 2014, **301**, 451–460.
267 S. Li, B. Goins, L. Zhang and A. Bao, *Bioconjug. Chem.*, 2012, **23**, 1322–1332.
268 M. Liang, K. Fan, M. Zhou, D. Duan, J. Zheng, D. Yang, J. Feng and X. Yan, *PNAS*, 2014, **111**, 14900–14905.
269 X. Lin, J. Xie, G. Niu, F. Zhang, H. Gao, M. Yang, Q. Quan, M. A. Aronova, G. Zhang, S. Lee, R. Leapman and X. Chen, *ACS Nano*, 2011, **11**, 814–819.
270 S. S. Lucky, K. C. Soo and Y. Zhang, *Chem. Rev.*, 2015, **115**, 1990–2042.
271 C. Xu, J. Nam, H. Hong, Y. Xu and J. J. Moon, *ACS Nano*, 2019, **13**, 12148–12161.
272 J. Shi, L. Wang, J. Gao, Y. Liu, J. Zhang, R. Ma, R. Liu and Z. Zhang, *Biomaterials*, 2014, **35**, 5771–5784.
273 Y. Wang, F. Yang, H. X. Zhang, X. Y. Zi, X. H. Pan, F. Chen, W. D. Luo, J. X. Li, H. Y. Zhu and Y. P. Hu, *Cell Death Dis.*, 2013, **4**, 1–10.
274 R. Vankayala, Y. K. Huang, P. Kalluru, C. S. Chiang and K. C. Hwang, *Small*, 2014, **10**, 1612–1622.
275 T. Murakami, H. Nakatsuji, M. Inada, Y. Matoba, T. Umeyama, M. Tsujimoto, S. Isoda, M. Hashida and H. Imahori, *J. Am. Chem. Soc.*, 2012, **134**, 17862–17865.
276 C. Wang, S. Cao, X. Tie, B. Qiu, A. Wu and Z. Zheng, *Mol. Biol. Rep.*, 2011, **38**, 523–530.
277 D. Jaque, L. Martínez Maestro, B. Del Rosal, P. Haro-Gonzalez, A. Benayas, J. L. Plaza, E. Martín Rodríguez and J. García Solé, *Nanoscale*, 2014, **6**, 9494–9530.
278 M. Zhou, S. Song, J. Zhao, M. Tianb and C. Li, *J. Mater. Chem. B*, 2015, **3**, 8939–8948.
279 B. Cheng, H. He, T. Huang, S. S. Berr, J. He, D. Fan, J. Zhang and Ap. Xu, *J. Biomed. Nanotechnol.*, 2017, **12**, 435–449.
280 AMAG Pharmaceuticals, *FULL PRESCRIBING INFORMATION: Fereheme(R)*, 2009.
281 J. P. Bullivant, S. Zhao, B. J. Willenberg, B. Kozissnik, C. D. Batich and J. Dobson, *Int. J. Mol. Sci.*, 2013, **14**, 17501–17510.
282 W. Wu, Q. He and C. Jiang, *Nanoscale Res. Lett.*, 2008, **3**, 397–415.
283 W. Wu, Z. Wu, T. Yu, C. Jiang and W.-S. Kim, *Sci. Technol. Adv. Mater.*, 2015, **16**, 23501.
284 H. A. Eivari and A. Rahdar, *World Appl. Program.*, 2013, **3**, 52–55.
285 J. C. Aphesteguy, G. V Kurlyandskaya, J. P. De Celis, A. P. Safronov and N. N. Schegoleva, *Mater. Chem. Phys.*, 2015, **161**, 243–249.
286 L. Li, K. Y. Mak, C. W. Leung, K. Y. Chan, W. K. Chan, W. Zhong and P. W. T. Pong, *Microelectron. Eng.*,

2013, **110**, 329–334.
287 S. Sun and H. Zeng, *Am. Chem. Soc.*, 2002, **124**, 8204–8205.
288 M. Instruments, Dynamic Light Scattering: An Introduction in 30 Minutes, www.malvern.co.uk, (accessed 9 May 2020).
289 J. T. Woods and M. G. Mellon, *Ind. Eng. Chem.*, 1942, **13**, 551–554.
290 B. J. Von Hoene, R. G. Charles and W. M. Hickam, *J. Phys. Chem.*, 1958, **62**, 1098–1101.
291 A. Lak, T. Kahmann, S. J. Schaper, J. Obel, F. Ludwig, P. Mu and J. Lipfert, *ACS Appl. Mater. Interfaces*, 2020, **12**, 217–226.
292 S. G. Kwon and T. Hyeon, *Small*, 2011, **7**, 2685–2702.
293 X. Cui, S. Belo, D. Krüger, Y. Yan, R. T. M. de Rosales, M. Jauregui-Osoro, H. Ye, S. Su, D. Mathe, N. Kovács, I. Horváth, M. Semjeni, K. Sunassee, K. Szigeti, M. A. Green and P. J. Blower, *Biomaterials*, 2014, **35**, 5840–5846.
294 S. Eustis, M. A. El-sayed and M. Kasha, *Chem. Soc. Rev.*, 2006, **35**, 209–217.
295 W. Haiss, N. T. K. Thanh, J. Aveyard and D. G. Fernig, *Anal. Chem.*, 2007, **79**, 4215–4221.
296 E. W. Price and C. Orvig, *Chem. Soc. Rev.*, 2014, **43**, 260–290.
297 T. J. Wadas, E. H. Wong, G. R. Weisman and C. J. Anderson, *Chem. Rev.*, 2010, **110**, 2858–2902.
298 E. W. Price, J. F. Cawthray, G. A. Bailey, C. L. Ferreira, E. Boros, M. J. Adam and C. Orvig, *J. Am. Chem. Soc.*, 2012, **134**, 8670–8683.
299 J. P. Holland, V. Divilov, N. H. Bander, P. M. Smith-Jones, S. M. Larson and J. S. Lewis, *J Nucl Med*, 2010, **51**, 1293–1300.
300 N. Wu, C. S. Kang, I. Sin, S. Ren, D. Liu, V. C. Ruthengael, M. R. Lewis and H.-S. Chong, *J. Biol. Inorg. Chem.*, 2016, **21**, 177–184.
301 W. C. Cole, S. J. Denardo, C. F. Meares, M. J. Mccall, G. L. Denardo, A. L. Epstein, H. A. O. Brien and M. K. Moi, *J. Nucl. Med.*, 1987, **28**, 83–90.
302 V. Kubíček, Z. Böhmová, R. Ševčíková, J. Vaněk, P. Lubal, Z. Poláková, R. Michalicová, J. Kotek and P. Hermann, *Inorg. Chem.*, 2018, **57**, 3061–3072.
303 S. Shi, C. Xu, K. Yang, S. Goel, H. F. Valdovinos, H. Luo, E. B. Ehlerding, C. G. England, L. Cheng, F. Chen, R. J. Nickles, Z. Liu and W. Cai, *Angew. Chem. Int. Ed*, 2017, **56**, 2889–2892.
304 R. Madru, T. A. Tran, J. Axelsson, C. Ingvar, A. Bibic, F. Ståhlberg, L. Knutsson and S.-E. Strand, *Am. J. Nucl. Med. Mol. Imaging*, 2014, **4**, 60–69.
305 R. Chakravarty, H. F. Valdovinos, F. Chen, C. M. Lewis, P. A. Ellison, H. Luo, E. Meyerand, R. J. Nickles and W. Cai, *Adv Mater*, 2014, **26**, 5119–5123.
306 P. S. Patrick, L. K. Bogart, T. J. Macdonald, P. Southern, M. J. Powell, M. Zaw-Thin, N. H. Voelcker, I. P. Parkin, M. F. Lythgoe, T. L. Kalber, Q. A. Pankhurst and J. C. Bear, *Chem. Sci.*, 2019, **10**, 2592–2597.
307 J. A. Dougan, C. Karlsson, W. E. Smith and D. Graham, *Nucleic Acids Res.*, 2007, **35**, 3668–3675.
308 R. G. Nuzzo, B. R. Zegarski and L. H. Dubois, *J. Am. Chem. Soc.*, 1987, **109**, 733–740.
309 A. Cossaro, R. Mazzarello, R. Rousseau, L. Casalis, A. Verdini, A. Kohlmeyer, L. Floreano, S. Scandolo, A. Morgante and G. Scoles, *Science*, 2008, **321**, 943–947.
310 Y. Wang, Q. Chi, N. S. Hush, J. R. Reimers, J. Zhang and J. Ulstrup, *J. Phys. Chem. C*, 2009, **113**, 19601–19608.
311 S. Knoppe and T. Bürgli, *Acc. Chem. Res.*, 2014, **47**, 1318–1326.
312 I. Dolamic, B. Varnholt and T. Bürgli, *Nat. Commun.*, 2015, **6**, 1–7.
313 S. Si, C. Gautier, J. Boudon, R. Taras, S. Gladiali and T. Bürgli, *J. Phys. Chem. C*, 2009, **113**, 12966–12969.
314 P. Carro and R. C. Salvarezza, *Nanoscale*, 2019, 19341–19351.
315 M. Patra, L. S. Eichenberger, G. Fischer and J. P. Holland, *Angew. Chemie - Int. Ed.*, 2019, **58**, 1928–1933.
316 L. S. Eichenberger, M. Patra and J. P. Holland, *Chem. Commun.*, 2019, **55**, 2257–2260.
317 R. Fay, M. Gut and J. P. Holland, *Bioconjug. Chem.*, 2019, **30**, 1814–1820.
318 F. Benyettou, I. Chebbi, L. Motte and O. Seksek, *J. Mater. Chem.*, 2011, **21**, 4813–4820.
319 E. Boros, A. M. Bowen, L. Josephson, N. Vasdev and J. P. Holland, *Chem. Sci.*, 2015, **6**, 225–236.

320 B. Zhang, G. Salassa and T. Bürgi, *Chem. Commun.*, 2016, **52**, 9205–9207.

321 B. Zhang, O. V. Safonova, S. Pollitt, G. Salassa, A. Sels, R. Kazan, Y. Wang, G. Rupprechter, N. Barrabés and T. Bürgi, *Phys. Chem. Chem. Phys.*, 2018, **20**, 5312–5318.

322 M. Eder, O. Neels, M. Müller, U. Bauder-Wüst, Y. Remde, M. Schäfer, U. Hennrich, M. Eisenhut, A. Afshar-Oromieh, U. Haberkorn and K. Kopka, *Pharmaceuticals*, 2014, **7**, 779–796.

323 E. Gourni, L. Del Pozzo, M. Bartholoma, Y. Kiefer, P. T. Meyer, H. R. Maecke, J. P. Holland and D. Phil, *Mol. Imaging*, 2017, **16**, 1–11.

324 M. Eder, M. Scha, U. Bauder-wu, W. Hull and C. Wa, *Bioconjug. Chem.*, 2012, **23**, 688–697.

325 C. P. Leamon, J. A. Reddy, A. Bloomfield, R. Dorton, M. Nelson, M. Vetzel, P. Kleindl, S. Hahn, K. Wang and I. R. Vlahov, *Bioconjug. Chem.*, 2019, **30**, 1805–1813.

326 D. R. Lide, *CRC Handbook of Chemistry and Physics, 84th Edition*, 2003.

327 M. Borzenkov, G. Chirico, L. D. Alfonso, L. Sironi, M. Collini, E. Cabrini, G. Dacarro, C. Milanese, P. Pallavicini, A. Taglietti, C. Bernhard and F. Denat, *Langmuir*, 2015, **31**, 8081–8091.

328 T. Bürgi, *Nanoscale*, 2015, **7**, 15553–15567.

329 V. Amendola, R. Pilot, M. Frasconi, O. M. Marago and M. Antonia lati, *J. Phys. Condes. Matter*, 2017, **29**, 1–48.

330 R. García-álvarez, M. Hadjidemetriou, A. Sánchez-iglesias, L. M. Liz-marzán and K. Kostarelos, *Nanoscale*, 2018, **10**, 1256–1264.

331 B. M. P. Brigham, W. H. Stein and S. Moore, *J Clin Invest.*, 1960, **39**, 1633–1638.

332 A. Banjac, T. Perisic, H. Sato, A. Seiler, S. Bannai, N. Weiss, P. Ko, K. Tschoep, R. D. Issels, P. Daniel, M. Conrad and G. W. Bornkamm, *Oncogene*, 2008, **27**, 1618–1628.

333 L. Turell, R. Radi and B. Alvarez, *Free Radic. Biol. Med.*, 2013, **65**, 244–253.

334 G. P. M. J S Horoszewicz, E Kawinski, *Antcancer Res.*, 1987, **7**, 927–935.

335 B. Demoro, F. Caruso, M. Rossi, D. Benítez, M. González, H. Cerecetto, M. Galizzi, L. Malayil, R. Docampo, R. Faccio, Á. W.Mombrú, D. Gambino and L. Otero, *Dalt. Trans.*, 2012, **41**, 6335–6349.

336 R. Torres, M. De Rosales, R. Tavar, A. Glaria, G. Varma, A. Protti and P. J. Blower, *Bioconjug. Chem.*, 2011, **22**, 455–465.

337 G. Olive and A. Jacques, *Phosphorus, Sulfur Silicon Relat. Elem.*, 2003, **178**, 33–46.

338 S. Priyadarsini, S. Mohanty, S. Mukherjee, S. Basu and M. Mishra, *J. Nanostructure Chem.*, 2018, **8**, 123–137.

339 M. Kurzawski and M. Droz, *Chem. Phys. Lett.*, 2013, **569**, 151–156.

340 J. Chen, S. Chen, X. Zhao, L. V Kuznetsova, S. S. Wong and I. Ojima, *J.Am.Chem.Soc.*, 2008, **130**, 16778–16785.

341 A. Ramachandra, K. Sasikala, R. G. Thomas, A. R. Unnithan, B. Saravanakumar and Y. Y. Jeong, *Nat. Publ. Gr.*, 2016, **6**, 1–14.

342 K. Yang, *Chem. Soc. Rev.*, 2013, **42**, 530–547.

343 J. Johns and M. Hersam, *Acc Chem Res*, 2014, **46**, 77–86.

344 B. C. G. Salzmann, S. A. Llewellyn, G. Tobias, M. A. H. Ward, Y. Huh and M. L. H. Green, *Adv Mater*, 2007, **19**, 883–887.

345 J. Zhu, J. Hiltz, M. A. Mezour, V. Bernard-gauthier, R. B. Lennox and R. Schirrmacher, *Chem. Mater*, 2014, **26**, 5058–5062.

346 D. C. Marcano, D. V Kosynkin, J. M. Berlin, A. Sinitskii, Z. Sun, A. Slesarev, L. B. Alemany, W. Lu and J. M. Tour, *ACS Nano*, 2010, **4**, 4086–4814.

347 S. Stankovich, D. A. Dikin, R. D. Piner, K. A. Kohlhaas, A. Kleinhammes, Y. Jia and Y. Wu, *Carbon N. Y.*, 2007, **45**, 1558–1565.

348 C. G. Salzmann, V. Nicolosi and M. L. H. Green, *J. Mater. Chem.*, 2010, **20**, 314–319.

349 M. Rosillo-lopez, J. Lee, M. Bella, M. Hart and C. G. Salzmann, *RSC Adv.*, 2015, **5**, 104198–104202.

350 A. Evers, R. D. Hancock, A. E. Martell and R. J. Motekaitis, *Inorg. Chem.*, 1989, **27**, 2189–2195.

351 J. P. Holland, M. W. Jones, S. Cohrs, R. Schibli and E. Fischer, *Bioorg. Med. Chem.*, 2013, **21**, 496–507.

352 V. Sarli and A. Giannis, *Clin Cancer Res*, 2008, **14**, 7583–7588.

353 S. Tru, C. Dumelin, K. Frey, A. Villa, F. Buller and D. Neri, *Bioconjug. Chem.*, 2009, **20**, 2286–2292.

354 E. Gourni, L. Del Pozzo, M. Bartholoma, Y. Kiefer, P. T. Meyer, H. R. Maecke, J. P. Holland and D. Phil, *Mol. Imaging*, 2017, **16**, 1–11.

355 L. Lacerda, M. A. Herrero, K. Venner, A. Bianco, M. Prato and K. Kostarelos, *Small*, 2008, **4**, 1130–1132.

356 C. E. Dumelin, S. Trüssel, F. Buller, E. Trachsel, F. Bootz, Y. Zhang, L. Mannocci, S. C. Beck, M. Drumea-Mirancea, M. W. Seeliger, C. Baltes, T. Müggler, F. Kranz, M. Rudin, S. Melkko, J. Scheuermann and D. Neri, *Angew. Chemie - Int. Ed.*, 2008, **47**, 3196–3201.

357 T. M. Gorges, S. Riethdorf, O. von Ahsen, P. Nastaly, K. Röck, M. Boede, S. Peine, A. Kuske, E. Schmid, C. Kneip, F. König, M. Rudolph and K. Pantel, *Oncotarget*, 2016, **7**, 34930–34941.

358 M. Venere, C. Horbinski, J. F. Crish, X. Jin, A. Vasanji, J. Major, A. C. Burrows, C. Chang, J. Prokop, Q. Wu, P. A. Sims, P. Canoll, M. K. Summers, S. S. Rosenfeld and J. N. Rich, *Sci. Transl. Med.*, 2015, **7**, 1–12.

359 L. Lad, L. Luo, J. D. Carson, K. W. Wood, J. J. Hartman, R. A. Copeland and R. Sakowicz, *Biochemistry*, 2008, **47**, 3576–3585.

360 A. Afshar-Oromieh, A. Malcher, M. Eder, M. Eisenhut, H. G. Linhart, B. A. Hadaschik, T. Holland-Letz, F. L. Giesel, C. Kratochwil, S. Haufe, U. Haberkorn and C. M. Zechmann, *Eur. J. Nucl. Med. Mol. Imaging*, 2013, **40**, 486–495.

361 A. Afshar-oromieh, J. W. Babich, C. Kratochwil, F. L. Giesel, M. Eisenhut, K. Kopka and U. Haberkorn, *J. Nucl. Med.*, 2016, **57**, 79–89.

362 K. Kopka, M. Benesova, C. Ba, U. Haberkorn and J. W. Babich, *J. Nucl. Med.*, 2019, **58**, 17–26.

363 R. Al, R. Henry, A. S. Biris, R. Sleezer and G. J. Salamo, *J. Appl. Toxicol.*, 2017, **37**, 1346–1353.

364 V. Castagnola, W. Zhao, L. Boselli, M. C. Lo Giudice, J. N. Coleman, K. A. Dawson, K. R. Paton and C. Backes, *Nat. Commun.*, 2018, **9**, 1–9.

365 H. Carol, R. Lock, P. J. Houghton, C. L. Morton, E. A. Kolb, R. Gorlick, C. P. Reynolds, M. John, S. T. Keir, C. A. Billups and M. A. Smith, *Pediatr. Blood Cancer*, 2009, **53**, 1255–1263.

366 J. Lamb, E. Fischer, M. Rosillo-Lopez, C. G. Salzmann and J. P. Holland, *Chem. Sci.*, 2019, **10**, 8880–8888.

367 P. Chakravarty, R. Marches, N. S. Zimmerman, A. D. E. Swafford, P. Bajaj, I. H. Musselman, P. Pantano, R. K. Draper and E. S. Vitetta, *PNAS*, 2008, **105**, 8697–8702.

368 Y. Li, Q. Lu, H. Liu, J. Wang, P. Zhang, H. Liang, L. Jiang and S. Wang, *Adv. Mater.*, 2015, **27**, 6848–6854.

369 M. R. McDevitt, D. Chattopadhyay, B. J. Kappel, J. S. Jaggi, S. R. Schiffman, C. Antczak, J. T. Njardarson, R. Brentjens and D. A. Scheinberg, *J. Nucl. Med.*, 2007, **48**, 1180–1189.

370 E. Heister, V. Neves, C. Tîlmaciu, K. Lipert, V. S. Beltrán, H. M. Coley, S. R. P. Silva and J. McFadden, *Carbon N. Y.*, 2009, **47**, 2152–2160.

371 C. Spinato, A. Perez Ruiz De Garibay, M. Kierkowicz, E. Pach, M. Martincic, R. Klippstein, M. Bourgognon, J. T. W. Wang, C. Ménard-Moyon, K. T. Al-Jamal, B. Ballesteros, G. Tobias and A. Bianco, *Nanoscale*, 2016, **8**, 12626–12638.

372 S. Srivastava, V. Kumar, K. Arora, C. Singh, M. A. Ali, N. K. Puri and B. D. Malhotra, *RSC Adv.*, 2016, **6**, 56518–56526.

373 C. Loftus, M. Saeed, D. M. Davis and I. E. Dunlop, *Nano Lett.*, 2018, **18**, 3282–3289.

374 K. Yang, L. Feng, H. Hong, W. Cai and Z. Liu, *Nat. Protoc.*, 2013, **8**, 2392–2403.

375 A. Ruggiero, C. H. Villa, J. P. Holland, S. R. Sprinkle, C. May, J. S. Lewis and M. R. Mcdevitt, *Int. J. Nanomedicine*, 2010, **5**, 783–802.

376 G. Ulrich, R. Ziessel and A. Harriman, *Angew. Chemie - Int. Ed.*, 2008, **47**, 1184–1201.

377 A. Paulus, P. Desai, B. Carney, G. Carlucci, T. Reiner, C. Brand and W. A. Weber, *EJNMMI Res.*, 2015, **5**, 1–9.

378 M. Ceulemans, K. Nuyts, W. M. De Borggraeve and T. N. Parac-Vogt, *Inorganics*, 2015, **3**, 516–533.

379 J. A. Hendricks, E. J. Keliher, D. Wan, S. A. Hilderbrand, R. Weissleder and R. Mazitschek, *Angew. Chemie*, 2012, **124**, 4681–4684.

380 N. Kondo, T. Temma, J. Deguchi, K. Sano, M. Ono and H. Saji, *J. Control. Release*, 2015, **220**, 476–483.

381 H. S. Hendrickson, E. K. Hendrickson, I. D. Johnson and S. A. Farber, *Anal. Biochem.*, 1999, **276**, 27–35.

382 A. Cui, X. Peng, J. Fan, X. Chen, Y. Wu and B. Guo, *J. Photochem. Photobiol. A Chem.*, 2007, **186**, 85–92.

383 A. V. Vorontsov and E. V. Tretyakov, *Phys. Chem. Chem. Phys.*, 2018, **20**, 14740–14752.

384 T. Lindmo, E. Boven, F. Cuttitta, J. Fedorko and P. A. Bunn, *J. Immunol. Methods*, 1984, **72**, 77–89.

385 J. M. Mattes, *Int. J. Cancer*, 1995, **61**, 286–288.

386 S. Konishi, K. Hamacher, S. Vallabhajosula, P. Kothari, D. Bastidas, N. Bander and S. Goldsmith, *Cancer Biother. Radiopharm.*, 2004, **19**, 706–715.

387 R. Dux, A. Kindler-Röhrborn, K. Lennartz and M. F. Rajewsky, *J. Immunol. Methods*, 1991, **144**, 175–183.

388 R. P. Junghans, *Immunol. Today*, 1999, **5699**, 401–406.

389 R. Rielly, *Cancer Biother Radiopharm.*, 2004, **19**, 669–672.

390 T. J. Clough, L. Jiang, K. L. Wong and N. J. Long, *Nat. Commun.*, 2019, **10**, 1–14.

391 X. Wang, T. Jin, V. Comblin, A. Lopez-Mut, E. Merciny and J. F. Desreux, *Inorg. Chem.*, 1992, **31**, 1095–1099.

392 D. S. Abou, T. Ku and P. M. Smith-Jones, *Nucl. Med. Biol.*, 2011, **38**, 675–681.

393 P. Zanzonico, *J. Nucl. Med.*, 2008, **49**, 1114–1131.

394 B. Bai, M. Dahlbom, R. Park, L. Hughes, G. Dagliyan, L. P. Yap and P. S. Conti, *2012 IEEE Nuclear Science Symposium and Medical Imaging Conference Record (NSS / MIC 2012) 27 October – 3 November 2012*, 2012.

Curriculum Vitae

JENNIFER LAMB

Email: lambjennifer4@gmail.com **Date of Birth:** 10.02.1994 **Tel:** +41786773050

Current Employment

August 2016-August 2020: PhD candidate under the supervision of Prof. Jason Holland, Department of Chemistry, University of Zurich, CH

Thesis title: *Nanomaterials as multi-modal imaging agents*

Key skills implemented:

- Chemical synthesis of small molecules and analysis *via* **mass spectrometry**, **NMR spectroscopy**, **UV-visible spectroscopy** and **HPLC analysis**.
- The synthesis of nanomaterials and analysis using **dynamic light scattering** (DLS), **X-ray diffraction** (XRD) and **transmission electron microscopy** (TEM).
- **Antibody conjugation** and analysis using **size exclusion chromatography**.
- **Radiochemical synthesis** of compounds using ^{89}Zr, ^{68}Ga, ^{111}In and ^{64}Cu.
- Evaluation of synthesised constructs *in vitro* and *in vivo* using **cellular uptake and blocking assays**, **FACS analysis**, **cellular anti-proliferation assays**, and **small animal PET imaging** in tumour bearing mice following **xenograft implantation** (**LTK1 qualified**).

Academic Qualifications

September 2012-July 2016: MChem Chemistry (1st class honours), University of Sheffield, UK

BSc level GPA: 71% MChem level GPA: 77%
Awarded the Ray Charlesworth Scholarship in recognition of academic achievements.

2008-2012: Westcliff High School for Girls, Westcliff-on-sea, Essex, UK

A-levels: Mathematics (A), Biology (A) and Chemistry (B)
GCSEs: 11 A*-B grade GCSE's including Maths and English.

Other Research Experience

September 2015- June 2016: Master Research Project under the supervision of Prof. Jim Thomas, Bio-inorganic Chemistry Laboratory, University of Sheffield, UK

- Research focused on the use of coordination chemistry to synthesise a new dppz based ruthenium complex.
- A large proportion of the project involved organic and inorganic synthesis, with characterisation of compounds using various techniques.
- The DNA “light-switch” effect was measured using a temperature controlled fluorimeter by monitoring emission whilst titrating calf thymus DNA.

Publications

Journal articles:

- J. Lamb, E. Fischer, M. Rosillo-Lopez, C. G. Salzmann and J. P. Holland, Multi-functionalised graphene nanoflakes as tumour-targeting theranostic drug-delivery vehicles, *Chem. Sci.* 2019, 10, 8880-8888
- J. Lamb and J. P. Holland, Advanced Methods for Radiolabelling Multimodality Nanomedicines for SPECT/MRI and PET/MRI, *J. Nucl. Med.,* 2018, 59, 382-389

Conference abstracts:

- J. Lamb, M. Rosillo-Lopez, C. G. Salzmann and J. P. Holland, Graphene nanoflake antibody conjugates for multi-modal imaging, Swiss Chemical Society Fall Meeting, 2020, Abstract ID: IC-014.
- J. Lamb, M. Yaffee, and J. P. Holland, Au@Fe_2O_3 nanoparticles as multi-modal imaging agents targeting cancer, European Society for Molecular Imaging, 2020, Abstract ID: PW-09.
- J. Lamb, E. Fischer, M. Rosillo-Lopez, C. G. Salzmann and J. P. Holland, Functionalised graphene nanoflakes as potential theranostic agents, International Society of Radiopharmaceutical Sciences, 23rd International Symposium, 2019, Abstract ID: 424.
- J. Lamb, E. Fischer, M. Rosillo-Lopez, C. G. Salzmann and J. P. Holland, Multi-functionalised graphene nanoflakes as tumour-targeted theranostic agents, 19th International Conference on Biological Inorganic Chemistry, 2019, Abstract ID: P260.
- J. Lamb and J. P. Holland, A comparison of radiolabelling methods for iron oxide nanoparticles, Swiss Chemical Society Fall Meeting, 2019, Abstract ID: IC-127.